DEPARTAMENTO DE ASTROFISICA

Universidad de La Laguna

AN INTEGRAL VIEW ON BAR-DRIVEN SECULAR EVOLUTION AND ITS INFLUENCE ON BULGES

Memoria que presenta
MARJA KRISTIN SEIDEL
para optar al grado de
Doctora en Astrofísica.

INSTITUTO DE ASTROFISICA DE CANARIAS
septiembre de 2015

Examination date: 16th October 2015
Thesis supervisor: Dr. Jesús Falcón-Barroso

Some of the material included in this document has been already published in *The Monthly Notices of the Royal Astronomical Society.*

To life.

The best thing that ever happened to me.

All truths are easy to understand
once they are discovered;
the point is to discover them.[1]
Galileo Galilei

[1] ... and to enjoy the discovery

Abstract

Since the dawn of *extragalactic astrophysics* in the 1930s thanks to the work of Edwin Hubble assuring that our galaxy was just one amongst billions, the study of the formation and evolution of galaxies has been an active field in astrophysical research. Enormous efforts have been undertaken trying to understand the multitude of sizes and shapes of galaxies and their origin. In this thesis we will focus on nearby galaxies with a barred structure. These structures are present in about 2/3 of the local population of disc galaxies, which is illustrating the necessity to better understand this component. Former studies have already investigated bars, but their predicted influence as major drivers of secular evolution has not been observationally revealed. Studies of integrated quantities in fact have shown practically no differences between barred and unbarred galaxies. With this thesis, we want to investigate bars in great detail. Our aim is to quantify the influence of the bar on its host galaxy, in particular in the context of the build-up of bulges.

We therefore created our own sample, BaLROG (Bars in Low Redshift Optical Galaxies), composed of 16 early- and late-type galaxies building large mosaics (54 pointings of 1-2h each) with the integral field unit SAURON on the William-Herschel Telescope in La Palma. These observations allow us to study bars in unprecedented spatial resolution and determine their impact in different regions on their host galaxies.

We first develop a new technique to measure the strength of bars, only based on the observed stellar kinematics and intrinsic galaxy parameters. We compare this measurement to existing techniques using photometric observations, in our case from the *Spitzer Space Telescope* as part of the Spitzer Survey of Stellar Structure in Galaxies (S^4G). This comparison results in a good agreement and is backed up with a large set of numerical simulations analysed with the same methods. We establish the bar strength as a yard stick to further test if stronger bars produce stronger predicted effects in kinematics or stellar populations.

We characterise the stellar and gas kinematics as well as determine the stellar population parameters based on line-strength indices of the BaLROG sample. We find important clues on where bars can influence their host galaxies: i) in *inner regions* and ii) *along the bar major axis*. Both are found in kinematics and populations. Hence, our results point towards a common influence of bars. These findings help to guide larger statistical studies in terms of where to search for bar-driven evolution and set at the same time important limitations to the possible influence caused by bar-driven secular evolution. Concretely:

i) Is reflected by dips in the stellar velocity and stellar angular momentum profiles at 0.2±0.1 bar length (or humps interior to this value), anti-correlations between Gauss-Hermite moment h_3 and V/σ within 0.1 bar lengths, inner features in velocity and velocity dispersion profiles that increase with bar strength, breaks in the index and single stellar population (SSP) profiles at 0.13±0.06 bar length and a correlation between very high central metallicities and a stronger h_3-$V/\sigma_{stellar}$ anticorrelation. All these results indicate that bars seem to significantly alter a certain part in the inner regions, likely by funneling material towards them and triggering star formation, leading to the build-up of inner components. However, they seem to not reach the nucleus, only the *circumcentral* regions.

ii) Is revealed in particular in the populations, where we find a flattening of the Fe5015 and Mg*b* indices along the bar major axis compared to the minor axis and an unbarred control sample. This translates into a flattening of the metallicity in the same areas. A mild flattening of the stellar velocity dispersion gradient with increasing bar strength is also observed, along both bar axes. The flattening of stellar population parameters along the bar major axis compared to other axes or unbarred galaxies holds important clues on the structure of the bar itself. Instead of strongly modifying the entire galaxy, bars seem to be self-contained structures with stars being locked on barred orbits. Through the interplay of creating new structures, hence stars forming from an enriched medium, and orbital mixing along the bar, the flattening along this structure could be achieved.

In order to better understand the relation of bars to bulges, we complement the BaLROG study with a very high spectral resolution study using the integral field unit WiFeS at Siding Spring Observatory to observe three bulges. The analysis of their star formation histories yields overall old ages of the majority of the stellar mass within our field of view, despite young star-forming regions. Explicitly, we find that at least 50% of the stellar mass already existed 12 Gyr ago. Furthermore, we detect a younger component (age between ∼1 to ∼8 Gyr) whose present day distribution seems to be affected much more strongly by morphological structures, especially bars, than the older one. In the BaLROG study, we detected a similarity between bulges and bars as opposed to their surrounding discs. In particular a number of early-type old bars seemed to reside inside a star-forming disc, suggesting that these bars have formed long ago and survived until the present day.

Both studies hence agree that the onset of bar-driven secular evolution occurred already long ago, although most probably below redshift∼2, meaning after the estimated peak of the history of cosmic star formation. This implies that any possible effects of bar-driven secular evolution will largely depend on the already formed mass in the proto-galaxy and explains the lack of significant global effects of bars. These results are an important piece of the puzzle of galaxy evolution and will help to constrain galaxy formation models as well as motivate future observations tailored to detecting this onset of bar-driven evolution and its effects at high redshift.

Resumen

Desde el comienzo de la *astrofísica extragaláctica* en los años 30 - gracias al trabajo de Edwin Hubble quien constató que nuestra galaxia era solamente una entre millones - el estudio de la formación y evolución de galaxias se ha convertido en un sector muy estudiado dentro de la investigación astrofísica. Se han hecho enormes esfuerzos para entender la multitud de tipos y tamaños de las galaxias y sus orígenes. En esta tesis, nos centramos en las galaxias cercanas con estructura barrada. Estas estructuras están presentes en aproximadamente 2/3 de la población local de las galaxias de disco, lo que ilustra la necesidad de entender mejor esta componente. En estudios anteriores ya se han investigado las barras pero su esperada influencia como actores destacados de la evolución secular no se ha podido verificar observacionalmente. De hecho, estudios de las propriedades integradas no han mostrado diferencia alguna entre galaxias barradas y no barradas. Con esta tesis, queremos investigar las barras de manera muy detallada. Nuestro objetivo es cuantificar la influencia de las barras sobre sus galaxias anfitrionas, particularmente en el contexto de la formación de los bulbos.

Para ello hemos creado nuestra propria muestra, BaLROG (Bars in Low Redshift Optical Galaxies), compuesta de 16 galaxias de tipo temprano y tardío, constituyendo mosaicos grandes (54 apuntados de 1-2horas cada uno en total) con el espectrógrafo de campo integral SAURON ubicado en el telescopio William-Herschel Telescope en La Palma. Estas observaciones nos permiten estudiar barras en una resolución espacial sin precedente y determinar su impacto en diferentes regiones dentro de sus galaxias anfitrionas.

Primero desarrollamos una nueva técnica para medir la fuerza de barras, basada únicamente en la cinemática estelar observada y en los parámetros intrínsecos de la galaxia. Comparamos esta medida con técnicas existentes utilizando observaciones fotométricas del telescopio Spitzer Space Telescope como parte del sondeo Spitzer Survey of Stellar Structure in Galaxies (S4G). Esta comparación revela una buena concordancia entre los datos, siendo reforzada por una gran cantidad de simulaciones numéricas analizadas según el mismo método. La fuerza de la barra nos sirve de referencia para examinar si barras más fuertes producen efectos predichos más fuertes en la cinemática y las poblaciones estelares.

Caracterizamos la cinemática estelar y la del gas y determinamos los parámetros de las poblaciones estelares basándonos en un análisis de índices de fuerza de las líneas espectrales de la muestra BaLROG. Encontramos evidencias importantes

en cuanto a la cuestión dónde las barras influyen sus galaxias anfitrionas: i) *en las regiones internas* y ii) *a lo largo del eje mayor de la barra*. Ambos se encuentran en la cinemática y en las poblaciones. Nuestros resultados apuntan, por lo tanto, hacia una influencia común de las barras. Estas evidencias ayudan a guiar estudios estadísticos más extensos indicando dónde se puede buscar la evolución inducida por barras y, a la vez, establecen limitaciones importantes en la posible influencia de la evolución secular causada por barras. En concreto:

i) Se refleja por los dips en los perfiles de la velocidad estelar y del momento angular estelar a 0.2±0.1 de la longitud de la barra (o picos interiores a este valor), anticorrelaciones entre el momento Gauss-Hermite h_3 y V/σ dentro de 0.1 longitud de barra, propiedades internas en los perfiles de velocidad y de dispersión de velocidad que aumentan con la fuerza de barra, rupturas (breaks) en los perfiles de índice y de poblaciones estelares singulares (Single Stellar Population, SSP) a 0.13±0.06 longitud de barra y una correlacion entre metalicidades centrales muy elevadas y una anticorrelación más fuerte de h_3-$V/\sigma_{stellar}$. Todos estos resultados indican que las barras pueden alterar significativamente una parte determinada en las regiones internas, probablemente llevando material hacia esas zonas y provocando así la formación de estrellas, culminando en la formación de componentes internas. No obstante, parece que no llegan hacia el núcleo, solamente hacia las regiones *circumnucleares*.

ii) Se revela en particular en las poblaciones, donde encontramos un aplanamiento de los índices Fe5015 y Mg*b* a lo largo del eje mayor de la barra comparado con el eje menor y una muestra de control no-barrada. Esto se traduce en un aplanamiento de la metalicidad en las misma areas. Asímismo, se observa un aplanamiento suave del gradiente de la dispersion de velocidad estelar a medida que aumenta la fuerza de barra, a lo largo de ambos ejes. El aplanamiento de los parámetros de poblaciones estelares a lo largo del eje mayor de la barra comparado con otros ejes o galaxias no-barradas contiene informacion importante acerca de la estructura de la barra en sí misma. En vez de modificar gravemente la galaxia entera, las barras parecen ser estructuras autónomas con las estrellas fijadas en las órbitas de la barra. El aplanamiento a lo largo de esta estructura podría lograrse mediante la interacción de la creación de nuevas estructures, estrellas que por lo tanto se forman en un medio enriquecido, y la mezcla de órbitas a lo largo de la barra.

Para entender mejor la relación entre barras y bulbos, complementamos el estudio de BaLROG con un estudio de muy alta resolución espectral utilizando la unidad de campo integral WiFeS en el observatorio Siding Spring Observatory para observar tres bulbos. El análisis de sus respectivas historias de formación estelar revela edades viejas en la mayoría de la masa estelar en nuestro campo de vista, a pesar de la presencia de regiones de formación estelar reciente. A saber, encontramos que por lo menos 50% de la masa estelar ya existía hace 12 Gyr. Asímismo, detectamos una componente más jóven (edad entre ∼1 a ∼8 Gyr) cuya distribución hoy en día parece ser afectada mucho más notablemente por las estructuras morfológicas, en particular por las barras, que la vieja. En el estudio de BaLROG, ya detectamos una similitud entre bulbos y barras en oposición a sus discos. En particular, un número de barras viejas de tipos tempranos parece residir en un disco que forma estrellas, lo que sugiere que estas barras se formaron hace mucho tiempo y que han sobrevivido hasta

el día de hoy.

Ambos estudios concuerdan en que el comienzo de la evolución secular inducida por barras ocurrió hace mucho tiempo, aunque muy probablemente fuese después de redshift$\sim$2, esto es, después del pico estimado de la historia de formación estelar cósmica. Ello implica que cualquier efecto posible de la evolución secular inducida por barras va a depender considerablemente de la masa que ya se formó en la proto-galaxia, y así también se explica la ausencia de efectos globales significativos de las barras. Estos resultados son una pieza muy importante del puzzle de la evolución de galaxias y nos ayudarán a restringir los modelos de formación de galaxias y motivarán futuras observaciones destinadas a detectar el comienzo de la evolución inducida por barras y sus efectos a alto redshift.

Contents

List of Figures

Acronyms

ANU - *Australian National University*

BaLROG - *Bars in Low Redshift Optical Galaxies*

CR - *Corotation*

ESA - *European Space Agency*

IFU - *Integral Field Unit*

ILR - *Inner Lindblad Resonance*

IMACS - *Inamori Magellan Areal Camera and Spectrograph*

IMF - *Initial Mass Function*

GTO - *Guaranteed Time Observations*

HST - *Hubble Space Telescope*

ΛCDM model - *Cold Dark Matter (cosmological) model*

LIS-8.4 Å - *Line Index System at 8.4 Å*

LOSVD - *Line-Of-Sight Velocity Distribution*

LS - *Line Strength*

MILES - *Medium-resolution Isaac Newton Telescope library of empirical spectra*

MUSE - *Multi Unit Spectroscopic Explorer*

MW - *Milky Way*

NASA - *National Aeronautics and Space Administration*

OLR - *Outer Lindblad Resonance*

PA - *Position Angle*

RSAA - *Research School of Astronomy & Astrophysics*

S^{4}G - *Spitzer Survey of Stellar Structure in Galaxies*

SAURON - *Spectral Area Unit for Research on Optical Nebulae*

SDSS - *Sloan Digital Sky Survey*

SFH - *Star Formation History*

S/N - *Signal- to-Noise ratio*

SSP - *Single Stellar Population*

VLT - *Very Large Telescope*

WiFeS - *Wide Field Spectrograph*

1

Introduction

I would rather have questions
that can't be answered
than answers that can't be questioned.
Richard Feynman

Have you already spent a night outside the city, maybe even somewhere remote in the mountains, in the desert or on a beach shore, far away from illuminated areas (that otherwise turn night into day, unless you are lucky enough to experience a temporary blackout)? And have you switched off your lamps, tilted your head upwards and experienced the magic of the star-strewn sky above you, realizing your place on this small rocky planet inside a seemingly infinite Universe? And have you ever pondered about the distribution of stars, have you consciously grasped that you are sitting inside a spiral arm in the outskirts of our Galaxy, the Milky Way, only one of billions of galaxies out there?

1.1 A brief history of *Extragalactic Astrophysics*

On a clear, moonless night, the band of the Milky Way can clearly be appreciated across the sky, as illustrated in Fig. 1.1 showing the night sky above the *El Teide* volcano in Tenerife. Already the ancient Greeks distinguished it as a confined structure. They coined the root of the term 'Galaxy', which originates from the Greek work 'galakt', meaning 'milk', alluding to the fuzzy fluid they perceived. Later on, the Romans elaborated this term to 'Via Lactea', meaning 'Milky Way' - the name of our home galaxy which remains until today. While the European world was caught in the Middle Ages, the Arabic and Persian world had translated astronomy works from Greek, Indian and Persian into Arabic and also made huge efforts in observational astronomy (Ballay, 1990; Micheau, 1996). In fact, Isfahan astronomers already had distinguished our neighbour galaxy Andromeda very likely before 905 AD. Abd al-Rahman al-Sufi (Azophi) in the 10th century however, was the first to describe and illustrate Andromeda, calling it 'a little cloud', as well as record observations of the Large Magellanic Cloud, another neighbouring galaxy (e.g. Glyn Jones, 1968;

Strohmaier, 1984; Hafez, 2010). Nevertheless, it took about 500 years longer to really identify, what even the cloudy fluid-like band of the Milky Way was made up of.

FIGURE 1.1: The Milky Way above *El Teide* as seen from Chipeque. While the moon is already illuminating the mountain, light pollution can clearly be seen on the horizon. Image taken in August 2015, credit to Carmen Negrín Mata, José-Ángel Estévez Armas and José Juan Pérez Gutiérrez.

Only in 1610, Galileo was able to resolve the mystic fluid into stars thanks to advances in technology that had developed the telescope (e.g. Feigelson, 2012). A century later, people started to explore the sky by telescopes. In particular Charles Messier dedicated his time to collect and classify a large amount of objects, most being comets or stellar clusters and as such part of our own Galaxy. But some also were objects outside of our galaxy, such as the Andromeda or Sombrero Galaxy. In the 19th century, the Herschels performed a more systematic search on nebulae. The 5079 objects found were published in the *General Catalogue of Galaxies* in 1864 by John Herschel. Only about 20 years later, Dreyer published an updated version containing about 15000 objects. The nomenclature used in this *New General Catalogue of Nebulae and Clusters of Stars* and two supplementary *Index Catalogues* is still used today - in fact all galaxies studied in this thesis have *NGC* numbers.

However, it was not observational, but philosophical (genius) intuition that led Immanuel Kant to the idea of 'island Universes'. He suspected that the Milky Way was only one amongst many systems whose presence could only be seen as fuzzy patches on the sky, the so-called 'nebulae' at the time - as Messier really could not resolve any stars in his objects. Kant thought that they were composed of stars similar to the Milky Way, just positioned at a much larger distance and hence could only be seen as a 'patch of fluid' again (as the Milky Way before the telescope invention). He further speculated that the stars of

the Milky Way were gravitationally bound similar to the solar system, building up a rotating structure (for more details please see Seidengart 1996; Bracher 1994).

As these ideas could not be tested observationally (yet), the controversy about these fuzzy objects and about our own Galaxy, our position in it and altogether the scale of the Universe itself, remained a mystery for still a long time. In 1920, two of the experts in the field, Harlow Shapley and Herber Curtis, discussed these ideas officially leading to a historical dialogue in astronomy which later became well-known as the 'Great Debate'. Both researchers had very opposite points of view. Curtis had performed observations of novae in the Andromeda galaxy and derived from their much fainter brightness that this system must be significantly further away in order to make it its own galaxy, distinct from the Milky Way. Shapley however thought that all nebulae belonged to the Milky Way. His opinion was based on research from van Maanen who claimed to have observed rotation in the Andromeda galaxy. If this was true, coupled with the distance measurements of Curtis, the rotation speeds would be so high, exceeding the speed of light, which would be an unphysical result and hence impossible. Shapley was however correct in stating that the Milky Way was much larger than previously thought and the Sun's position away from the center. So, both Curtis and Shapley, were correct and mistaken at distinct aspects, but changed and challenged the understanding of our place in the Universe and the large structures, galaxies, that are our home and surround us (for more details and reviews see, e.g., Shapley & Curtis 1921; Hetherington 1970; Berendzen, Hart & Seeley 1976; Trimble 1995).

The doubts about the 'nebulae' were only settled with studies by Edwin Hubble. He managed to resolve individual stars in the Andromeda galaxy, identified Cepheid stars and doubtlessly measured their distances (Hubble, 1929). Through this work, he could prove that the Andromeda galaxy was indeed an extragalactic system such as many of the nebulae found by Messier, the Herschels and Dreyer.

It was a long way for the field of 'extragalactic astrophysics' to be born, but from then onwards, *galaxy evolution* developed into one of the strongest fields in astrophysics. Immense research efforts have been undertaken to better understand the formation and evolution of galaxies and yet, numerous questions remain unanswered. We will discuss and dive into more details in the following section.

1.2 Galaxy evolution

1.2.1 Initial classifications and interpretation attempts

Since the unequivocal confirmation of the existence of external galaxies by Edwin Hubble, the formation and evolution of galaxies has been widely studied. Hubble himself already tried to develop an evolutionary diagram based on his classifications (Hubble, 1926, 1927). This so-called *Hubble tuning fork diagram*

is shown in Fig. 1.2 in its original form (Hubble, 1936) and illustrated with Sloan Digitial Sky Survey (SDSS) *gri*- and Hubble Space Telescope (HST) images[1]. It is important to note that it does not show an evolutionary path, but serves as a classification scheme. It is separated into two families: elliptical galaxies (E) and spiral galaxies - the latter subdivided into normal spirals (S) and barred spirals (SB). Lenticular galaxies (S0) in between comprise another subgroup, containing a disc, but no spiral arms. Based on the evoked evolutionary trend by Hubble, ellipticals (and S0s) are referred to as *early types* while spirals (no matter if barred or unbarred) fall under the term *late types*. Subscripts such as 'a', 'b' or 'c' indicate the compactness of the spiral arms going from tightly wound (a) to open and loose (c). The size of the bulge -the central round region in spirals (see more in section 1.4), decreases from 'a' to 'c', while gas and star formation increases. For ellipticals, the subscript is a number and refers to the degree of ellipticity (from round to very elliptical).

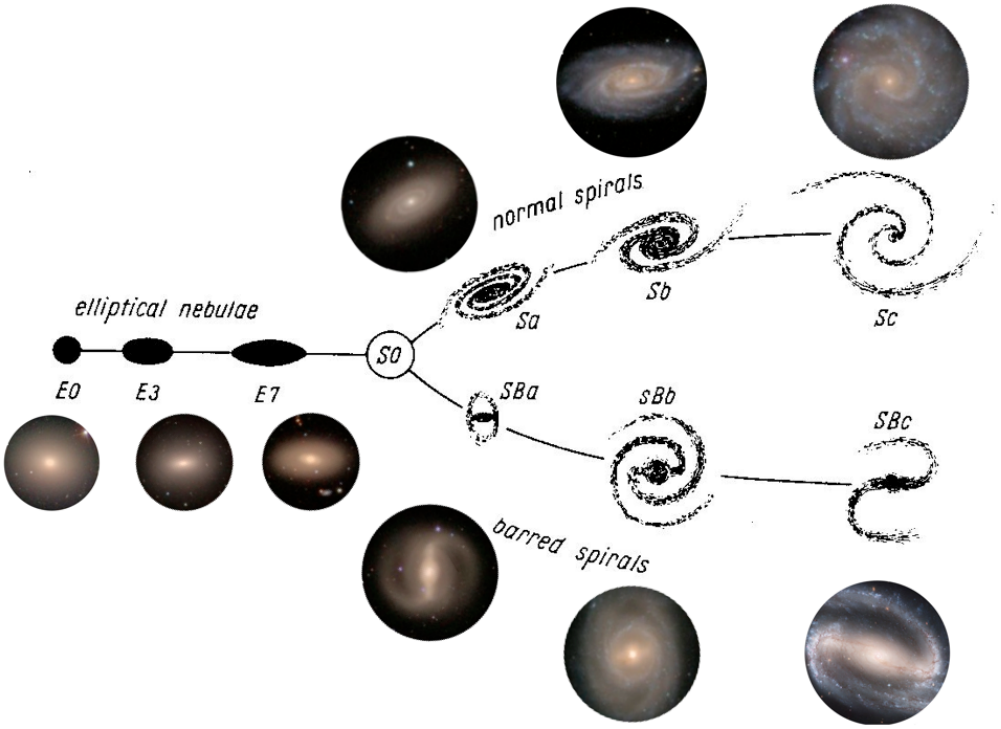

FIGURE 1.2: The Hubble Tuning Fork diagram. We show the original tuning fork developed by Hubble (1936) and illustrated with SDSS *gri*- and HST images.

Thanks to technological advances, higher resolution could be achieved that also allowed a more detailed classification. Hence other authors developed refined versions of Hubble's *Tuning Fork*, distinguishing substructures such as rings or other features, while barred galaxies always remained a separate group (Holmberg, 1958; de Vaucouleurs, 1959; van den Bergh, 1960b,a; Morgan, 1971; de

[1]inspired by Karen Masters, http://www.galaxyzooforum.org

Vaucouleurs, 1974). Figure 1.3 depicts the increasing complexity of the classification with the de Vaucouleurs diagram from 1959. This diagram already included irregular galaxies, denoted as Sm and Im.

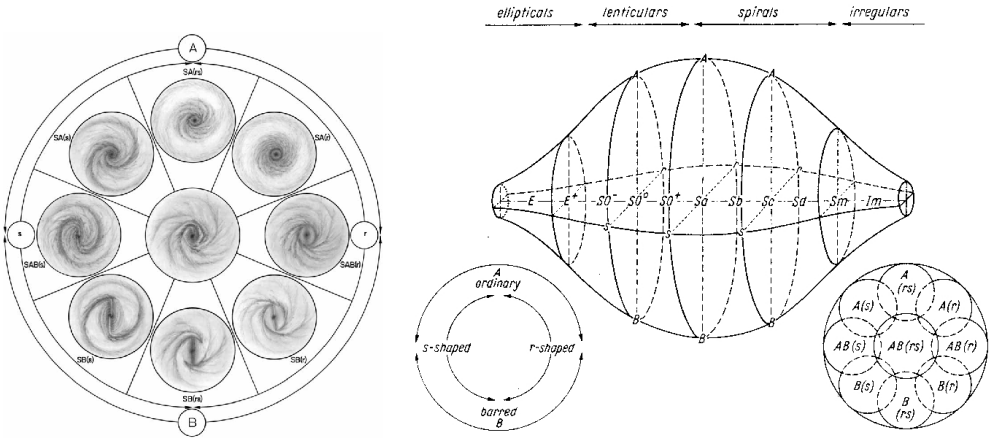

FIGURE 1.3: The de Vaucouleurs classification diagram (de Vaucouleurs, 1959).

Although all these classifications have only used morphology as the deciding factor, other parameters were found to correlate with these classes, e.g. the stellar kinematics and content shows a systematic variation from elliptical to spiral systems (Sandage, Freeman & Stokes, 1970). The former are mainly pressure supported, i.e. by random motions of the stars, while the latter consist of flattened discs mainly supported by rotation. The dynamical properties, also measuring and taking into account stellar angular momentum profiles or other intrinsic properties along with the galaxy morphology were later used to attempt new classification schemes (e.g. van den Bergh, 1976; Kormendy & Bender, 1996; Cappellari et al., 2011b; Kormendy & Bender, 2012).

While we do know that the evolution of galaxies does not happen according to the sequence shown in the Hubble diagram we are far from a complete understanding of the different formation and evolutionary scenarios even today, despite the attempts to re-order the diagram. Nevertheless, there have been enormous efforts trying to disentangle the distinct parameters involved in the evolution of a galaxy, from the possibility of an early *collapse* and/or *mergers*, *star formation* to the evolution of the *dynamics*, the stellar orbital parameters and gas movement, up to the changing *chemical composition* over the galaxys' life time. In the following subsections we will try to summarize the different scenarios proposed in the literature and in particular discuss the importance of *secular evolution*.

1.2.2 Fast versus slow processes - competing or coacting

According to the state-of-the-art astrophysics, galaxies formed in dark matter haloes which developed in the early universe due to a Gaussian random field of tiny density fluctuations (Bardeen et al., 1986), summarized now as the cold dark matter cosmological model (ΛCDM model, Blumenthal et al. 1984; Davis et al. 1985; Springel, Frenk & White 2006; Planck Collaboration et al. 2014; Genel et al. 2014; Schaye et al. 2015). Self-gravity caused the overdensities to

grow further and develop a cosmic web of clumps, filaments and voids, whose structure was adapted by the baryonic matter. Gas accumulated in the overdense regions and started to spin up forming rotationally supported discs inside the dark matter haloes where star formation initiated the growth of the first galaxies. Since then, galaxies continuously evolve together with the Universe itself. The latter, the evolution of the Universe and in particular its expansion, causes alterations in the processes that drive galactic evolution.

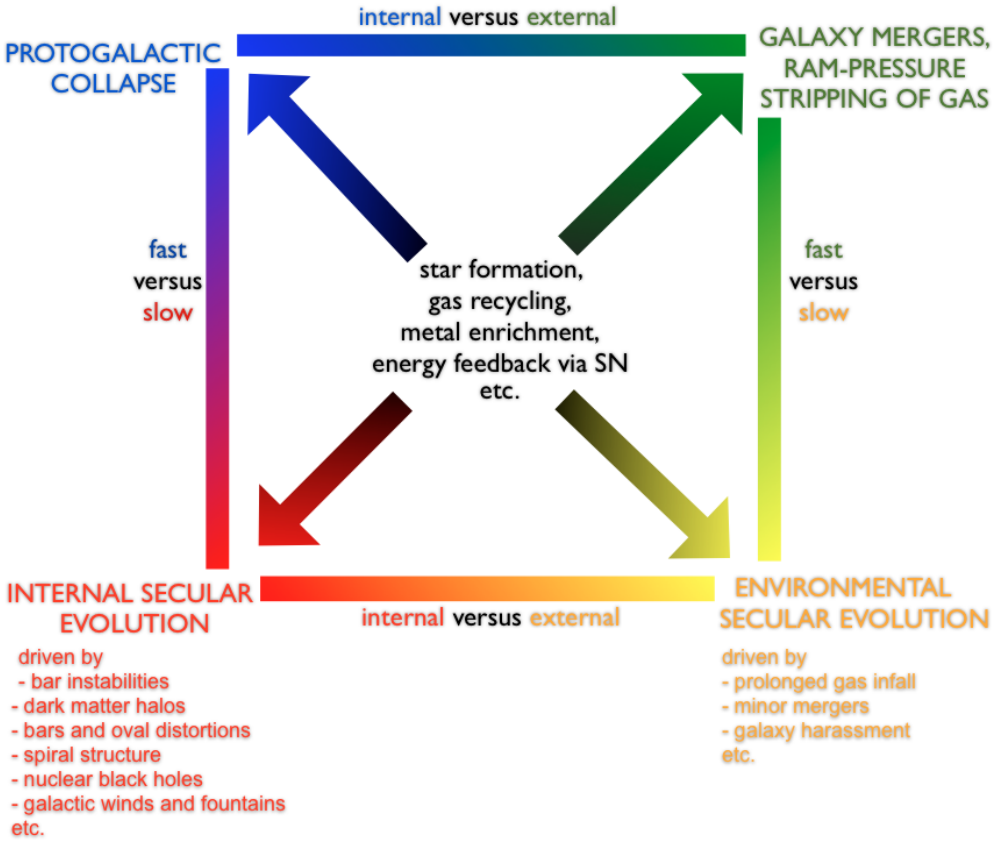

FIGURE 1.4: Morphological box (Zwicky, 1957) of processes of galactic evolution, taken from Kormendy & Kennicutt (2004), which is an updated version of Kormendy (1982a). The top half considers fast evolution processes while the bottom considers slow processes; on the left, the evolution is internal while on the right the effects of the environment are included.

The morphological box, developed originally by Zwicky (1957) and then revised by Kormendy (1982a) is shown in Fig. 1.4. It summarizes very nicely the different processes that can drive the formation and evolution of a galaxy. In the early Universe, the dominating processes were fast, as structures were very close to each other and frequent mergers continued changing their gravitational potential (upper part of Fig. 1.4) (Barnes & Hernquist, 1992).

Historically, two different scenarios have been proposed during the early formation phase:

- **monolithic collapse**
- **hierarchical clustering**

In the first case, the main criterium is, that the formation occurs on a rapid time-scale. Through the complete and violent collapse of the protogalactic cloud, the spheroids building elliptical galaxies or bulges of spiral galaxies are directly formed. This model has been proposed by Eggen, Lynden-Bell & Sandage (1962) a long time ago and since then been backed up by numerous studies confirming several of its predictions: spheroids are metal-rich in the centers and exhibit negative metallicity gradients; they are old and have shallow positive age gradients (centers might be slightly younger); and their stellar abundance ratios are supersolar with positive gradients (e.g. Larson, 1974; Larson & Tinsley, 1974; Terlevich et al., 1981; van Albada, 1982; Carlberg, 1984a,b; Madau, Pozzetti & Dickinson, 1998; Terlevich et al., 1999; Moore et al., 1999; Kuntschner, 2000; Matteucci, 2003). Nevertheless, many of these predictions can also be reconciled with the second, alternative scenario which is compatible with the framework of the current ΛCDM model, while the monolithic collapse scenario is not (e.g. van Dokkum et al. 2008 and see below).

The scenario of **hierarchical clustering**, already briefly outlined above with the ΛCDM model, was proposed only later, but has been supported by numerous studies since then (e.g. Toomre & Toomre, 1972; Press & Schechter, 1974; Toomre, 1977; White & Negroponte, 1982; Blumenthal et al., 1984; Frenk et al., 1988; Kauffmann, 1996; Kormendy & Kennicutt, 2004). The idea is a hierarchical assembly of a galaxy via interactions and clustering of smaller objects accumulating to bigger galaxies (bottom-up formation). This process is strongly dependent on the interacting candidates. Therefore predictions are more complex to establish, but still can be given concerning the global properties of the resulting galaxies. These predictions are mainly based on cosmological simulations which are established within the ΛCDM model (e.g. Cole, 1991; Lacey & Cole, 1993; Kauffmann, White & Guiderdoni, 1993; Kauffmann & White, 1993; Navarro, Frenk & White, 1995, 1996; De Lucia et al., 2006; Navarro et al., 2010; Vogelsberger et al., 2014; Schaye et al., 2015). Amongst others, these simulations predict that more massive galaxies tend to have higher metallicities (mass-metallicity relationship) while less massive ones will have more extended star formation histories over time resulting in positive correlations of stellar population properties (i.e. age, metallicity and abundances) with velocity dispersion. For the same reason, early mergers will lead to super solar abundances [α/Fe], while later, more recent mergers will result in solar and rather flat abundance profiles. Overall the environment and mass density is found to have a crucial influence on the stellar population properties (e.g. Bower et al., 1990; Guzman et al., 1992; Rose et al., 1994; Terlevich et al., 1999; Poggianti & van Gorkom, 2001).

Based on this second, nowadays more accepted scenario, two groups of galaxies formed: the red sequence of galaxies (mainly ellipticals) in which most gas was heated considerably such that not enough cool gas remains to settle later and restart active star formation; and the blue cloud (spirals) consisting of galaxies where the center hosts a bulge but with enough cool gas to continue to form stars in an underlying and growing disc (Kauffmann & Charlot, 1998). A long time ago, Butcher & Oemler (1978) already tried to observe a morphological evolution and found that the fraction of elliptical galaxies remains almost constant over cosmic time, while spiral galaxies decrease and S0s increase (Butcher-

Oemler effect, but see also, e.g., Couch et al. 1994; Dressler et al. 1994, 1997; Oemler, Dressler & Butcher 1997). A natural explanation would be that S0s form by merging of spiral galaxies, which also could account for the existence of features attributed to interactions such as tidal tails or shells in a number of early-type galaxies (e.g. Schweizer, 1982; Kormendy, 1984; Moore et al., 1996; van Dokkum et al., 1999; Serra et al., 2006).

While interactions and mergers still continue to happen in today's Universe, they do depend on a certain proximity and rather dense environments. As these were the conditions of the early Universe, in the past, the evolution time was short and of the order of the free fall time $t_{ff} = t_{dyn} \approx (G\rho)^{-\frac{1}{2}}$, G being the gravitation constant and ρ the mean density of the object produced (Kormendy & Kennicutt, 2004). Fast processes, as shown in the top of Fig. 1.4, dominated the evolution of galaxies as outlined above. But the Universe continuously evolves and expands and hence the number of mergers and major interactions decreases (Toomre, 1977; Conselice et al., 2003) and other processes take over and start driving galactic evolution.

This slower evolution, determined by the galaxy structure itself or minor environmental influences only, is called **secular evolution** and started to gain attention only in the 1980s, mainly due to works by e.g., Kormendy 1979, 1982a,b and Kormendy & Illingworth 1982. It refers to the redistribution of energy and mass within the galaxy. This rearrangement can be achieved by an interplay of internal structures such as bars, triaxial halos, oval discs or simply the galaxy's spiral structure (see Kormendy & Kennicutt 2004 for a review and the bottom part of Fig. 1.4 for more examples). In general, these (slow) processes need to last much longer than t_{dyn} for them to have a visible impact on the internal structure of the host galaxy. Given the evidence of hierarchical clustering, secular evolution processes have not been regarded as important for the evolution of galaxies until recently. However, important evidence for its existence has been found, such as a substantial number of galaxies which consist of discs only (e.g. van der Kruit & Freeman, 2011). Their state suggests that they have not (recently) undergone major merger events compared to bulges (and ellipticals) which are assumed to have been built up by mergers (Toomre, 1977). Even bulges with disc-like properties are found, suggesting the possibility to have formed via secular evolution influences instead of interactions (e.g. Kormendy & Kennicutt, 2004; Sheth et al., 2005; Fisher & Drory, 2008). While certain processes, such as quasar fueling, still require the influence of mergers (e.g. Hopkins et al., 2008), a crucial influence of secular evolution has already been detected at higher redshifts, e.g. up to z$\sim$2 (e.g. Genzel et al., 2008).

Right now, both types of processes - rapid and slow - are taking place in today's Universe. However, their relative importance now and in the past are not fully understood. In the future, as distances between most galaxies tend to increase further, galaxy evolution is predicted to be dominated by slow secular evolution. Therefore the impact of galaxy morphology, dynamical structures, intrinsic dark matter distributions and other properties intrinsic to the galaxy is crucial and has not been completely characterized yet. One of the major drivers of internal secular evolution, also possibly responsible for the build-up of inner structures such as bulges, are bars. They are the focus of this work

and will be reviewed in the following chapter.

1.3 Barred galaxies as major drivers of secular evolution

Bars are ubiquitous in spiral galaxies, being present in at least 2/3 of the disc population in the nearby Universe (e.g. Eskridge et al., 2000; Knapen, Shlosman & Peletier, 2000; Whyte et al., 2002; Marinova & Jogee, 2007; Menéndez-Delmestre et al., 2007; Barazza, Jogee & Marinova, 2008; Aguerri, Méndez-Abreu & Corsini, 2009; Méndez-Abreu, Sánchez-Janssen & Aguerri, 2010; Masters et al., 2011; Méndez-Abreu et al., 2014; Cisternas et al., 2014), but also at least up to redshift$\sim$1 (e.g., Abraham et al., 1996; Elmegreen, Elmegreen & Hirst, 2004; Jogee et al., 2004; Simmons et al., 2014) (more details on bar fractions in Chapter 1.3.5). Because of their significant departure from axisymmetry and the associated torques, bars are likely to play a key role in disc galaxy evolution via numerous processes. That bar-driven secular evolution of discs happens is confirmed (e.g., Sheth et al., 2005; Gadotti & de Souza, 2006; Laurikainen et al., 2007; Buta et al., 2010; Laurikainen et al., 2011; Pérez & Sánchez-Blázquez, 2011; Sánchez-Blázquez et al., 2011, 2014b; Kim et al., 2014), but it has been hard to quantify.

In the following chapters we will introduce the different properties of bars and illustrate their importance with respect to the evolution of their host galaxies. As they are prominent optical features, we will start with a visual overview of the photometric properties and then briefly look into bar formation scenarios. After, we will dive into the dynamical and stellar population properties that have been predicted and found in observations. We finish with a summary on bar fractions to illustrate the omnipresence and a deeper look into the bar strength measurements as these form an integral part of this thesis.

1.3.1 Photometric properties

As illustrated in Chapter 1.2.1, bars were distinguished as distinct structures early on and barred galaxies constitute one of the major classification arms in the *Hubble tuning fork* and other classifications. Doubtlessly, bars are very prominent seen in the photometry as revealed by one of the spectacular images of the Hubble Space Telescope (HST) showing a composite image of NGC 1300, depicted in Fig. 1.5[2]. Instead of reaching to the center, the spiral arms of the disc seem to connect to the ends of the bar, which is commonly the case in barred spirals.

Although barred and unbarred galaxies are both mainly composed of an approximately axisymmetric disc described by an exponential law (Freeman, 1970b) and usually a central bulge (see Chapter 1.4 for details on bulges), light profiles of barred galaxies are often found to be broken compared to the exponentially declining profiles of unbarred galaxies (e.g. Freeman, 1970a). The fraction of the total luminosity of a galaxy in the bar can be as high as $\sim$30% (Sellwood & Wilkinson, 1993). And if bars are ignored, luminosity profiles fail to recover the true fraction of the bulge luminosity, because it would be contaminated by light from the bar (Laurikainen, Salo & Buta, 2005; Laurikainen et al., 2006).

[2]Figure from *http* : *//apod.nasa.gov/apod/ap*050112.*html*

FIGURE 1.5: Composite image of the barred spiral galaxy NGC 1300. Image credit to the Hubble Heritage Team, ESA and NASA.

Therefore, the barred structure characterized by its large ellipticity, flat surface brightness profile along the major axis and steep along the minor axis (Binney, Kormendy & White, 1982), has long been introduced in image decomposition of galaxies. Models of a bar are usually based on concentric, generalized ellipses (Athanassoula et al., 1990; Binney, 1999). Furthermore, there are several descriptions that try to capture the surface brightness profile of the bar. One of the first was a Freeman law (Freeman, 1966). Then a Ferrers bar or ellipsoid was developed - usually referred to as a projected surface density of a prolate Ferrers bar (Binney & Tremaine, 1987; Laurikainen, Salo & Buta, 2005). Also a flat profile (Prieto et al., 1997) has been used and very commonly a Sérsic function (Sersic, 1968; Caon, Capaccioli & D'Onofrio, 1993) similar to the bulge:

$$\mu_{bar}(r) = \mu_{e,bar} + c_{n,bar}\left[\left(\frac{1}{r_{e,bar}}\right)^{\frac{1}{n_{bar}}} - 1\right] \tag{1.1}$$

where $\mu_{0,bar}$ is the central surface brightness of the bar, $r_{e,bar}$ corresponds to the effective radius of the bar, i.e. the radius that contains half of its light, $\mu_{e,bar}$ to the bulge effective surface brightness, i.e. the surface brightness at $r_{e,bar}$, n_{bar} to the Sérsic index, which defines the shape of the profile and $c_{n,bar}$ = 2.5(0.868n_{bar}-0.142). The last description is used in the work of Gadotti (2008) illustrated as an example for a two-dimensional image decomposition in Fig. 1.6 and corresponding radial profiles in Fig. 1.7[3]. Both figures clearly illustrate the necessity of the barred component in order to fit the total model.

[3]Figures from *http://www.sc.eso.org/∼dgadotti/budda.html*

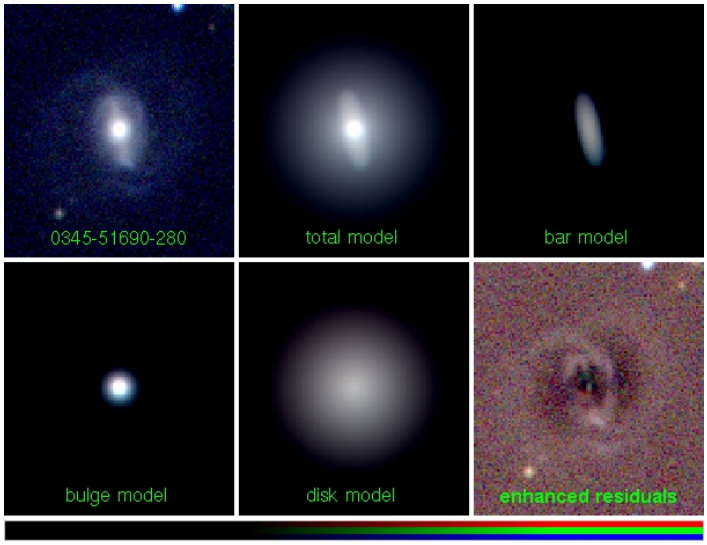

FIGURE 1.6: Photometric decomposition of a barred galaxy at z=0.06 within the sample of SDSS galaxies analysed by Gadotti (2008). The top row shows: left: the gri colour composite of the original galaxy image, middle: the total model obtained with BUDDA, right: only the model for the bar; Bottom row: left: only the bulge model, middle: only the disc model, right: enhanced residuals of the image after model subtraction.

The motivation for using the Sérsic function over the Ferrers bar is the possiblility of using a suitable Sérsic index to better adapt to late-type spirals that often exhibit an exponential luminosity profile, even in the bar, compared to the flatter profiles of early-type spirals or lenticulars.

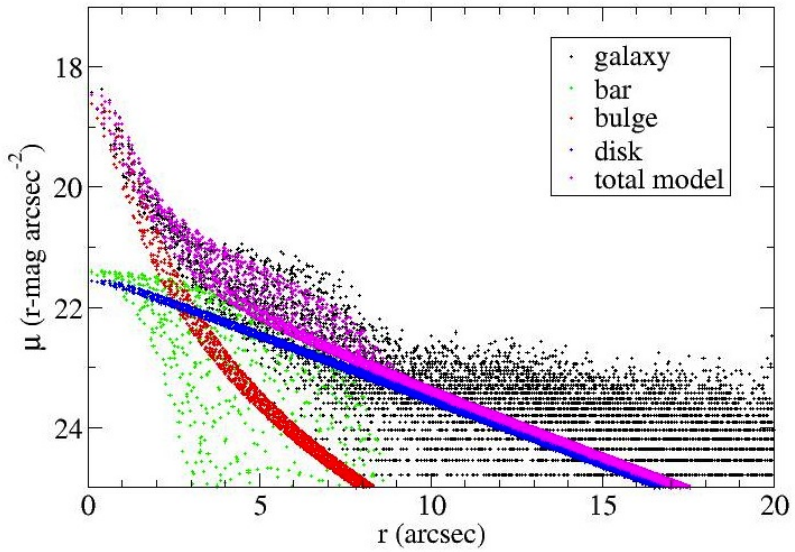

FIGURE 1.7: The radial profiles for the galaxy above showing the different model contributions.

Photometrically, bars reveal two other characteristic parameters, namely their *length* and *strength*. The latter will be described in detail in Chapter 1.3.6. Together with the *pattern speed* (refer to Chapter 1.3.3) these properties provide a detailed description of a barred system.

There is no universal way to measure the length of a bar. The most straightforward method is simply by visual inspection of optical images, optionally choosing to take spiral arms, outer rings or other substructures as the outer bar limits (e.g., Kormendy, 1979; Martin, 1995). Apart from this manual measurement, there is a variety of techniques that can partly be automatised. This includes the analysis of variations in the slope of the luminosity profiles along the bar major axis (Chapelon, Contini & Davoust, 1999). The intrinsic elliptical shape of bars motivates the method of measuring the location of the maximum of the isophotal ellipticity within the bar region - also fixed visually (Wozniak & Pierce, 1991; Wozniak et al., 1995; Jungwiert, Combes & Axon, 1997; Márquez et al., 1999; Laine et al., 2002; Sheth et al., 2003; Marinova & Jogee, 2007; Aguerri, Méndez-Abreu & Corsini, 2009). This method provides a lower limit and is frequently used as a first indication or in conjunction with the visual estimate (e.g. Aguerri, Debattista & Corsini, 2003). Using the difference between the bar and disc position angles or the minimum ellipticity outside the bar region are variations of this method (Erwin & Sparke, 2002; Erwin, 2004, 2005). A third possibility is based on the direct structural decomposition of the surface brightness distribution of the galaxy, via a Fourier or other decomposition techniques (e.g. Prieto et al., 1997; Aguerri et al., 2000; Prieto et al., 2001; Aguerri et al., 2001; Aguerri, Debattista & Corsini, 2003; Aguerri et al., 2005; Laurikainen, Salo & Buta, 2005; Laurikainen et al., 2007; Gadotti, 2008; Weinzirl et al., 2009; Laurikainen et al., 2009; Gadotti, 2011).

The ellipticity criterion is not often double-checked without reason via a visual measurement: both simulations and observations have shown that bars can be more complex and not follow pure elliptical isophotes, let alone the variations introduced by different orientations and inclinations (Sparke & Sellwood, 1987; Combes et al., 1990; Athanassoula et al., 1990; Martinez-Valpuesta, Shlosman & Heller, 2006). In particular ansae, illustrated in Fig. 1.8 are often located at the ends of the bar.

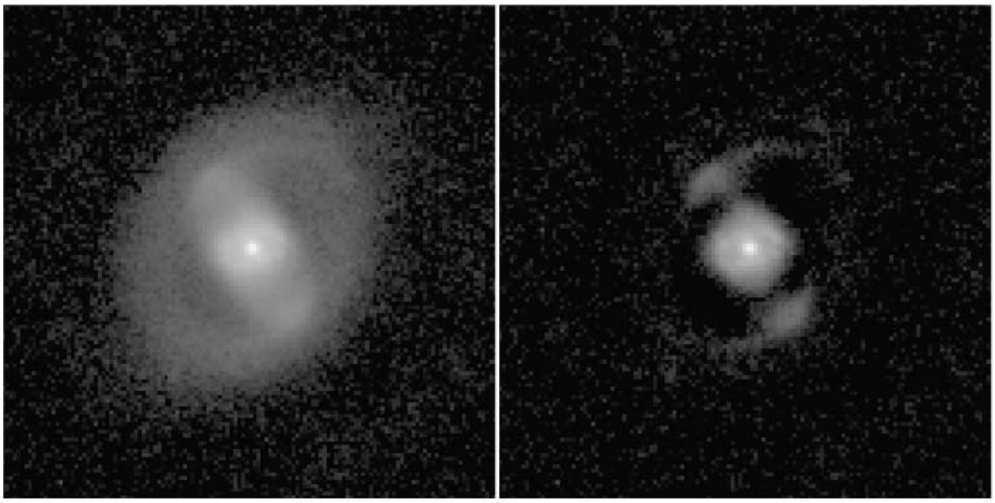

FIGURE 1.8: An H-band image of the early-type barred spiral ESO 565-11 obtained with the CTIO 1.5 m telescope (Buta, Crocker & Byrd, 1999) can be seen on the left and on the right its unsharp mask revealing the ansae at the end of the bar. Figure from Martinez-Valpuesta, Knapen & Buta (2007).

They are observed commonly in early-type barred galaxies (Athanassoula et al., 1984; Buta et al., 2015). Martinez-Valpuesta, Knapen & Buta (2007) in fact find ansae in 40% of a sample of early-types. These structures can have a significant effect on the deviation of elliptical isophotes and other properties (Buta et al., 1995; Buta, Purcell & Crocker, 1995; Martinez-Valpuesta, Knapen & Buta, 2007; Fragkoudi et al., 2015). Recent studies further show that the chosen waveband influences both, the measured length and ellipticity such that bluer bands result in longer and thinner bars (Menéndez-Delmestre, Sheth & S4G Team, 2015).

Despite the lack of a uniform method and projected differences in the measurements of bar lengths of the order of up to ∼35% (Athanassoula & Misiriotis, 2002), former studies agree on a relation between bar length and Hubble type such that bars in late-type galaxies tend to be shorter. Early-types (SB0 to SBb galaxies) exhibit a typical bar radius of 3-4 kpc (e.g. Marinova & Jogee, 2007) while the late-type systems (SBc-SBd galaxies) show a significantly lower value of ∼1.5 kpc (Erwin, 2005). Within the early types, lenticulars exhibit the longest bars overall (Elmegreen & Elmegreen, 1985; Aguerri, Méndez-Abreu & Corsini, 2009; Masters et al., 2011). Apart from the Hubble-type, other dependencies of bar length exist. Increasing bar length seems to be coupled to increasing galaxy size, disc scale length, galaxy colour towards redder colours and more prominent bulges (e.g., Aguerri et al., 2005; Marinova & Jogee, 2007; Gadotti, 2011; Hoyle et al., 2011).

1.3.2 Bar formation and evolution

According to N-body simulations bars can form spontaneously from instabilities in the galactic disc as a result of the swing-amplification mechanism (Toomre, 1964, 1981; Goldreich & Tremaine, 1979; Combes & Sanders, 1981; Sellwood & Wilkinson, 1993; Polyachenko, 2013; Saha & Naab, 2013). This process of swing-amplification is based on the lack of an inner Lindblad resonance (see section 1.3.3) in the disc prior to the bar formation which allows the onset of a feedback loop. A strong swing-amplification of gravitationally unstable m=2 bar modes in the stellar disc requires further a Toomre parameter of $Q < 2$ and X_2 parameter of the disc between $1 < X_2 < 3$ (Julian & Toomre, 1966; Toomre, 1981)[4]. In Fig. 1.9, we illustrate the formation of a bar based on Athanassoula (2013).Three time steps are shown, at the start, middle and end of the simulation illustrating numerous effects of the bar: the initially thin disc thickens, an inner ring surrounds the bar, the peanut-shape can be appreciated side-on while the end-on view could lead to the mistaken interpretation of a bulge and not a bar. Hence, simulations help us to better understand the effect of viewing angles in observations.

An alternative criterion for bar instability using observationally-derived quantities was proposed by Efstathiou, Lake & Negroponte (1982) and revisited by Foyle, Courteau & Thacker (2008). They define a stability threshold ϵ_m as a measure of the importance of self-gravity of the disc.

[4]The Toomre's Q number gives a criterion whether the system is unstable or not for an axisymmetric perturbation. The X_2 is the swing-amplification parameter.

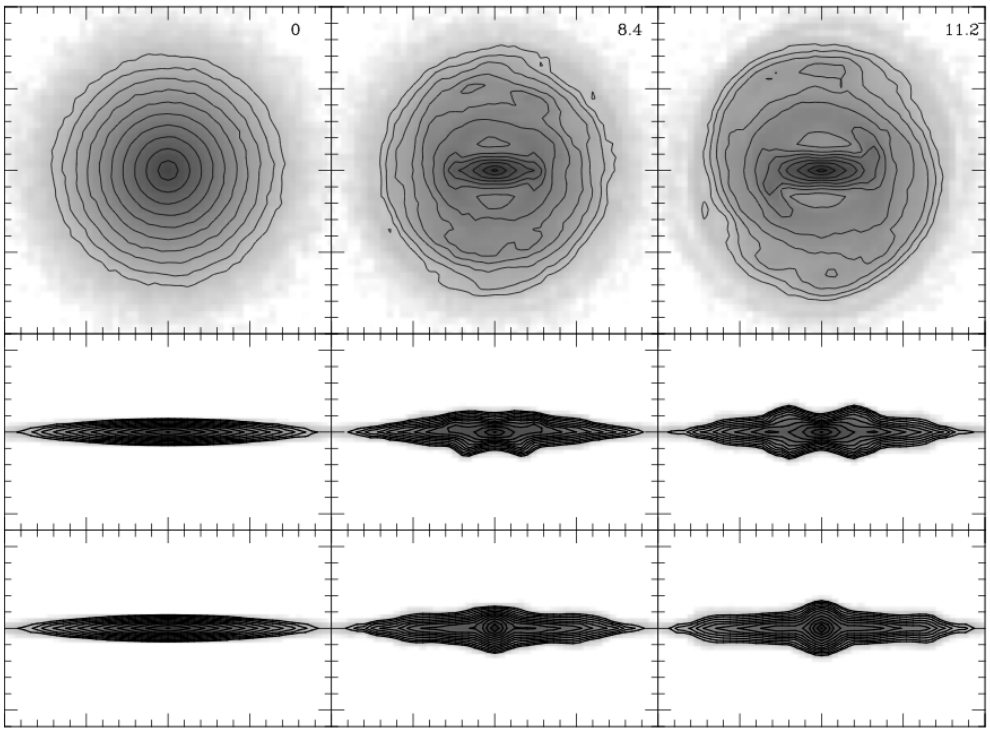

FIGURE 1.9: Formation and evolution of a bar from an instability in an exponential disc, increasing in time from left to right (time in Gyr given in the top right panels of each column). From top to bottom, different angles are shown: face-on, side-on and end-on. This figure is taken from Athanassoula (2013).

This parameter is based on their N-body simulations of exponential discs embedded in various halos and suggests that stellar discs remain stable against the bar mode as long as (Efstathiou, Lake & Negroponte, 1982; Mo, van den Bosch & White, 2010):

$$\epsilon_m \equiv \frac{V_{max}}{(GM_d/R_d)^{\frac{1}{2}}} \gtrsim 1.1 \tag{1.2}$$

where V_{max} is the maximum rotation velocity of the disc, G the gravitational constant, M_d the disc mass and R_d the radius of the disc. The same criterion applied to gaseous discs leads to a threshold of $\epsilon_m \gtrsim 10.9$ (Christodoulou, Shlosman & Tohline, 1995). A typical value of an isolated exponential disc is $\epsilon_m \approx 0.63$ meaning that it is unstable. However, V_{max} can increase due to the influence of an extended halo and lead to stability. This was already suggested early on by simulations of Ostriker & Peebles (1973) only using 500 particles. Later on, simulations further revealed a more complex influence of the halo, also differentiating different halo types (e.g., Athanassoula 2003, Athanassoula, Machado & Rodionov 2013 and mentioned in the review of Courteau et al. 2014). Triaxial haloes for example have significantly different influences than spherical ones: first they promote bar formation and later soften the resulting bar strengths.

In addition, other processes have been investigated that could lead to bar formation. These studies find that bars can also be triggered by mergers and

galaxy interactions in otherwise stable discs (Noguchi, 1987; Barnes & Hernquist, 1992; Miwa & Noguchi, 1998). Considering the high merger rate in the hierarchical evolution model, it is likely that some bars might be the result of these processes. Furthermore, Earn & Lynden-Bell (1996) propose bar formation through the cooperation of orbital streams.

After the first instability and initial bar formation, a lot of parameters determine the type of bar that develops. Athanassoula, Machado & Rodionov (2013) for example test the effect of gas and distinct halos on the growth of bars. We illustrate their results in Fig. 1.10 as an example.

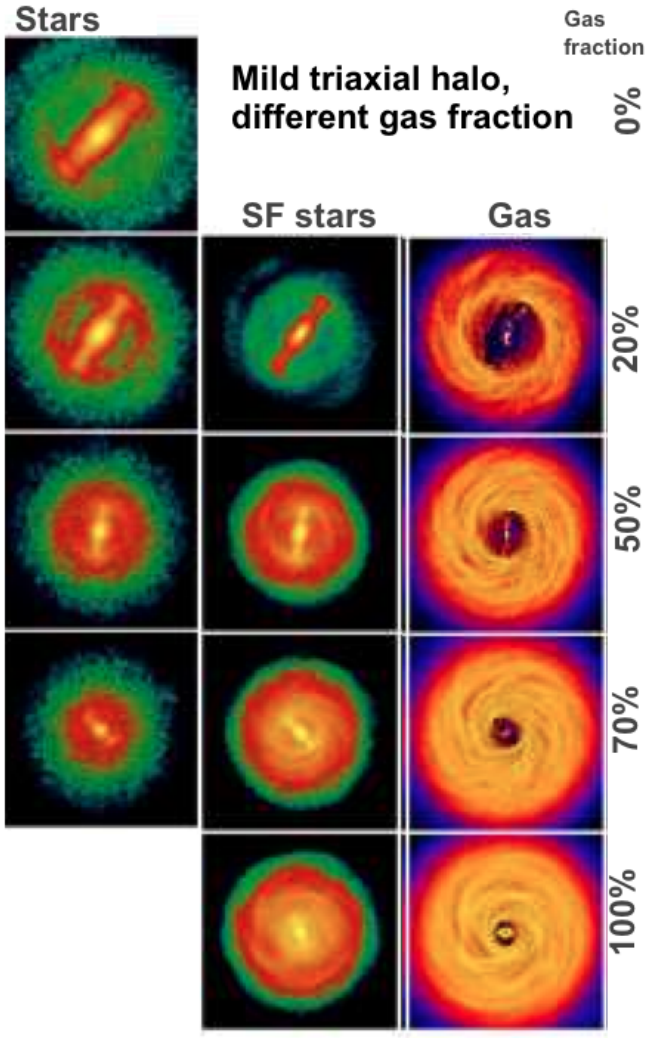

FIGURE 1.10: The influence of the gas fraction on the evolution of the bar. Each column shows different parts of this simulation using a mild triaxial halo, from left to right: initial stars, stars formed during the simulation, gas. Each row represents a different gas fraction. This figure composition based on results of Athanassoula, Machado & Rodionov (2013).

Their work and the figure show that the amount of gas is crucial such that gas-rich galaxies form smaller bars and need longer timescales to develop strong bars. This could mean for instance a difference of bars in early- and late-type

galaxies, as suggested by observational work, but is still not fully quantified.

In general, there seem to be several conditions (not only the Efstathiou, Lake & Negroponte 1982 – criterion) - maybe even in interplay - that lead to the stabilization of a disc against non-axisymmetric perturbations (Sánchez-Janssen & Gadotti, 2013). Numerous studies (e.g. Athanassoula & Sellwood, 1986; Athanassoula, 2003; Sellwood & Evans, 2001; Sellwood, 2010) suggest the following conditions as possibilities leading to the stabilization of the disc: high stellar velocity dispersion (kinematically hot discs), central mass concentrations, rather unresponsive dark matter haloes or even steeply rising inner rotation curves (independent of the dark matter content).

In order to better understand the dynamical processes involved, we will provide a brief overview in the following section.

1.3.3 Dynamical properties

Due to their significant departure from axisymmetry, bars are supposed to act as major dynamical drivers in disc galaxies (although their relative mass might play a crucial role with respect to their expected dynamical influence). While spiral arms are also suggested to drive galaxy dynamics, they are supposed to be linked and driven by bars rather than vice versa (Kormendy, 1979; Kormendy & Norman, 1979). Nonetheless, barred and unbarred galaxies share the same large-scale dynamical properties, i.e. they both belong to the same Tully-Fisher relations (Courteau et al., 2003). This is important as it hints to a similar baryon/dark matter global distribution, implying that secular evolution should be a *local* phenomenon.

Bars, as elliptical galaxies, are triaxial stellar systems, but differ significantly from each other due to their non-axisymmetric shape. The orbits of stars in a barred potential can be described by two fundamental frequencies: i) Ω, the circular angular velocity and ii) $\kappa = 2\Omega[1 + \frac{1}{2}\frac{R}{\Omega}\frac{d\Omega}{dR}]^{1/2}$, the epicyclic frequency, describing free oscillations. The third important parameter is the bar pattern speed Ω_p (see below). Already the presence of a weak bar in a differentially rotating disc provokes resonances and an associated pattern speed such that a perturbed orbit in its potential takes the following form (Binney & Tremaine, 1987):

$$R = R_0 + C_1 cos[\kappa\phi/(\Omega - \Omega_p) + \alpha] + C_2 cos(m\phi)/[\kappa^2 - m^2(\Omega - \Omega_p)^2] \quad (1.3)$$

where C_1 and C_2 are constansts, ϕ the angle and $m \geq 0$ is an integer. The C_2 terms contain the resonances which are

- Corotation Resonance (CR): $\Omega(r) = \Omega_p$
- Inner Lindblad Resonance (ILR): $\Omega - \Omega_p = \kappa/2$
- Outer Lindblad Resonance (OLR): $\Omega - \Omega_p = -\kappa/2$
- Inner 4:1 Resonance (I4R): $\Omega - \Omega_p = \kappa/4$
- Outer 4:1 Resonance (I4R): $\Omega - \Omega_p = -\kappa/4$

Furthermore, the inner Lindblad Resonance can be subdivided into two resonances in some galaxies: the Inner Inner Lindblad Resonance (IILR) and Outer Inner Lindblad Resonance (OILR). Depending on the circular velocity curve, the number of ILRs varies between zero and two (Mo, van den Bosch & White, 2010). This is not the case for the Outer Lindblad Resonance, where only one exists. Of course, this theoretical picture is simplified because the orbits of stars in a real galaxy are also susceptible to the potential of the entire disc and structures within it. Nonetheless, these resonance regions are particularly populated by stars remaining on these closed resonant bar orbits. This results in visual differences in the morphology of real galaxies as depicted in Fig. 1.11.

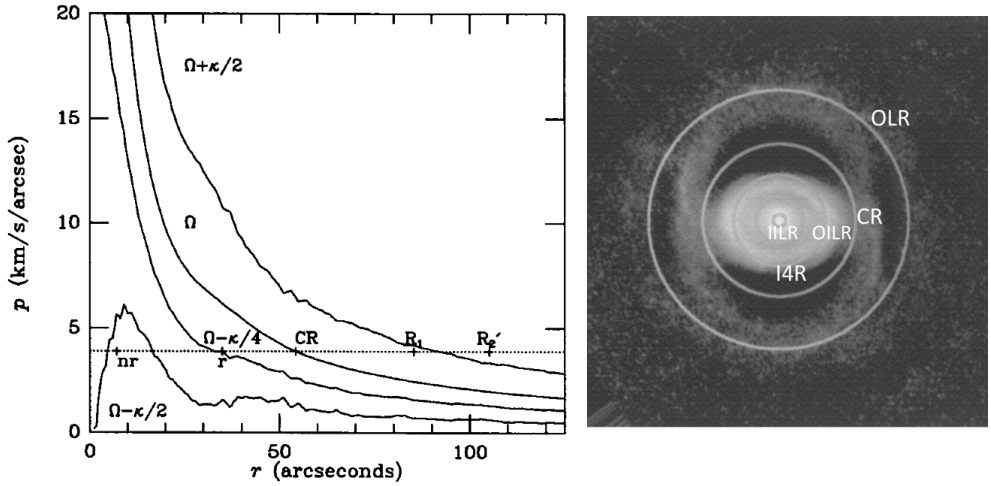

FIGURE 1.11: An analysis of the rotation curve reveals the precession frequencies for NGC 3081, shown in the left panel. The dotted line is the determined pattern speed locating the resonance regions, indicated on the right panel on top of the galaxy image (disc-subtracted, deprojected and rotated B-band image, in logarithmic units from 19 - 29 mag arcsec^{-1}). Figures are from Buta & Purcell (1998) and Buta (2013a) .

This figure shows the results of a study by Buta & Purcell (1998) on NGC 3081. They obtained the rotation curve from the velocity field of a Fabry-Perot and computed the angular velocity along with the precession frequencies. They also determined the pattern speed (shown as a dotted line on the left panel) which locates the resonance regions coinciding with the rings as seen on the right panel.

Hence, the pattern speed, usually parametrized by the ratio $\mathcal{R} = R_{CR}/a_b$ and therefore unit-less, is another important parameter of the bar (Mo, van den Bosch & White, 2010). Here, R_{CR} is the corotation radius and a_b is the bar semi-major axis. As seen from the equation above, the pattern speed is closely linked to the CR. This in fact is usually obtained via the pattern speed and not vice versa. The CR is key in a barred system because it defines where the angular velocity of the stars equals the angular rotation velocity of the bar. In order to obtain the pattern speed and hence the resonance points, the Tremaine & Weinberg (1984) method is commonly used. It is based on obtaining the slope of the linear correlation between the luminosity-weighted averages of the line of sight velocity <V> and different positions <X>. This slope is defined by $\Omega_p \sin i$, i being the inclination of the galaxy. In combination with the rotation

curve, the CR can be found.

The parametrized value of the pattern speed is furthermore used to differentiate between fast and slow bars, such that fast bars show a value of $\mathcal{R} \approx 1$ while slow bars need to have $\mathcal{R} >> 1$. This is based on dynamical arguments showing that weak bars cannot extend beyond corotation (Mo, van den Bosch & White, 2010). So finally, a connection between the length of bars, their strength (weakness) and pattern speeds is established. Numerous studies further suggest the presence of only fast bars throughout SB0, SB0/a and spiral galaxies finding values between $1.0 \lesssim \mathcal{R} \lesssim 1.4$ (e.g., Merrifield & Kuijken, 1995; Gerssen, Kuijken & Merrifield, 1999; Debattista & Williams, 2001; Debattista, Corsini & Aguerri, 2002; Gerssen, Kuijken & Merrifield, 2003; Corsini, 2011).

Alternative ways to obtain the corotation radius are usually less accurate than the Tremaine-Weinberg approach. They include the comparison with morphological structures such as rings or with areas of distinct (inhibited) star formation (Cepa & Beckman, 1990; Pérez, Aguerri & Méndez-Abreu, 2012). Although the prerequisite to apply the Tremaine-Weinberg method is normally limited to tracers that satisfy the continuity equation (i.e. old stellar populations), it has been successfully applied to CO (e.g., Zimmer, Rand & McGraw, 2004) and Hα observations (e.g., Hernandez et al., 2005; Fathi et al., 2009).

Apart from the above mentioned frequencies and resonances, there are several other important orbit families associated to bars. One of the most significant ones are the x1 orbits that populate the area along the bar major axis and form to a large fraction the ILR (Athanassoula, 2003), always remaining within the CR radius (Contopoulos & Papayannopoulos, 1980). They are part of the periodic orbits (Contopoulos & Grosbol, 1989) and contribute majorly to the appearance of the bar. Their counterpart are the x2 orbits, which are found perpendicular to the bar major axis and located between the two ILRs (if they exist) (Buta & Combes, 1996).

Apart from the intrinsic dynamics of the barred system itself, bars are supposed to influence the kinematics of gas and stars of their host galaxy. This influence has so far only been detected in local changes as bars do not seem to alter the global rotation pattern (i.e. the kinematic major axis remains almost constant as a function of radius, e.g., Barrera-Ballesteros et al. 2014). Nevertheless, in some barred galaxies subtle twists in the line-of-nodes of the velocity field have been found, which are attributed to the bar (e.g., Maciejewski, Emsellem & Krajnović, 2012). Furthermore, so-called double-hump rotation curves (local inner maximum followed by a slight drop and further rise) are predicted by simulations (Bureau & Athanassoula, 2005) and so far mainly confirmed in edge-on systems (e.g., Chung & Bureau 2004, see Fig. 1.12). The presence of $\sigma-$drops or plateaus in stellar velocity dispersion maps is another kinematic feature also predicted by simulations of barred galaxies (e.g., Wozniak et al., 2003) and partially found in the same observations, illustrated in Fig. 1.12.

Peanut-shaped bulges in barred galaxies are further predicted to show a kinematic signature in the Gauss-Hermite moment h_4 when taking profiles along the bar major axis (e.g., Debattista et al., 2005). So far, only a few studies (e.g., Méndez-Abreu et al., 2008, 2014) have confirmed this prediction.

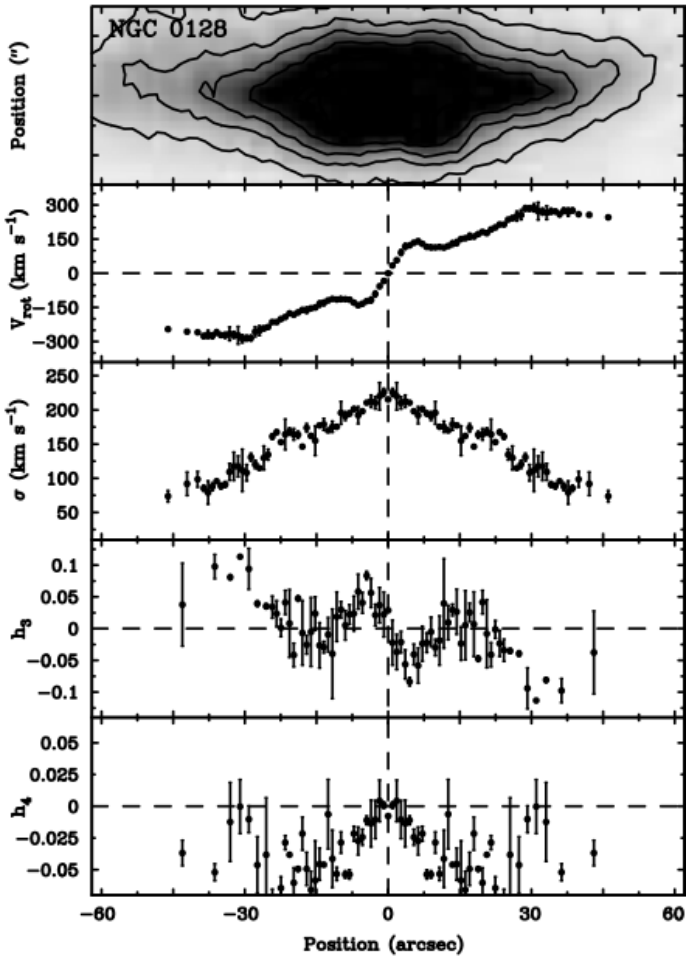

FIGURE 1.12: From top to botttom: optical image of the Digitilized Sky Surveys, kinematic profile of stellar velocity, velocity dispersion and Gauss-Hermite moments h_3 and h_4. This galaxy, NGC 128, is part of the observations of boxy/peanut bulges of a work by Chung & Bureau (2004). They are examples of bars seen edge-on, and show some of the predicted properties such as a double-hump rotation curve. Figure adapted from Chung & Bureau (2004).

Overall, the kinematic influence of bars, despite their own complex dynamics, has not been fully characterised, in particular in observations. Therefore, we analyse the stellar and gas kinematics of a representative sample of barred galaxies in the nearby Universe systematically and in great detail in Chapter 4.

1.3.4 Stellar populations in bars

Bars are predicted to have a crucial influence on their host galaxies due to their ability to redistribute angular momentum as well as gas, which can lead to a central mass concentration or build-up of bulges and influence the present and new stellar populations (e.g., Combes & Sanders, 1981; Martin & Roy, 1994; Bureau & Freeman, 1999; Bureau & Athanassoula, 1999; Sakamoto et al., 1999; Knapen et al., 1995; Fathi & Peletier, 2003; Chung & Bureau, 2004; Bureau & Athanassoula, 2005). And yet, there is no consensus among studies of central regions and bulges in barred and unbarred galaxies in terms of their stellar

population and metal content. Another drawback is that only very few studies have investigated these regions in a spatially resolved way (see below).

Simulations and observations mostly agree on the influence on the gas phase, such as an increase of the gaseous metallicity in the bulge (e.g., Friedli, Benz & Kennicutt, 1994; Friedli & Benz, 1995; Martel, Kawata & Ellison, 2013). Concerning the stellar metallicity however, authors find different results. Some find that it remains unchanged in the central parts (e.g., Friedli, Benz & Kennicutt, 1994; Coelho & Gadotti, 2011; Williams, Bureau & Kuntschner, 2012; Cacho et al., 2014), while others find a mild increase (e.g., Moorthy & Holtzman, 2006; Pérez & Sánchez-Blázquez, 2011) or even a significantly higher metallicity for barred galaxies (e.g., Ellison et al., 2011). Simulations furthermore predict that in the absence of star formation, both stellar and gas metallicities of bulges in barred galaxies are supposed to decrease because lower metallicity stars and gas are funneled towards the center and thus dilute the initial negative metallicity gradient (e.g., Di Matteo et al., 2013).

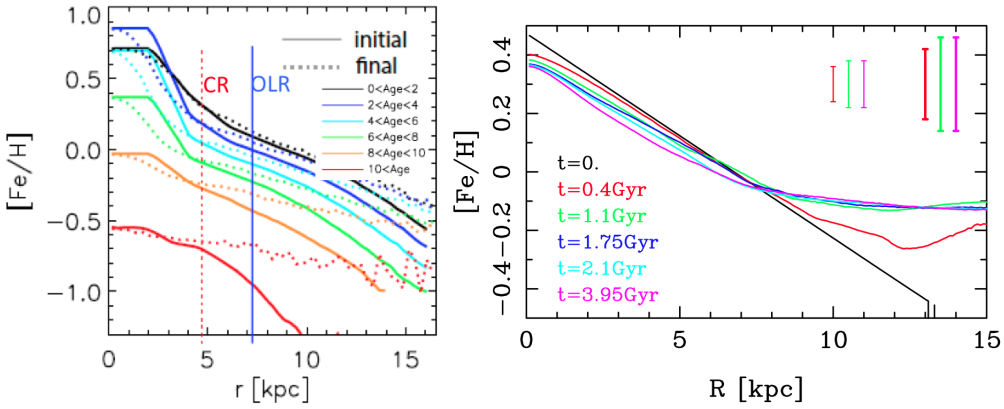

FIGURE 1.13: Results of two distinct numerical simulations predicting a flattening of the metallicity gradients due to the influence of bars - in particular for old stellar populations, but also appreciable for younger ones, in the center and outer parts. The left figure is from Minchev et al. (2012) and the right one from Di Matteo et al. (2013).

The disagreement also exists for the bulge ages, where Coelho & Gadotti (2011) found a difference between barred and unbarred galaxies (although only for the most massive spirals) while others did not (Pérez & Sánchez-Blázquez, 2011; Williams, Bureau & Kuntschner, 2012; Cacho et al., 2014). Furthermore, numerous studies suggest that bars do not seem to alter AGN activity or be related to its presence (e.g., Ho, Filippenko & Sargent, 1997; Oh, Oh & Yi, 2012; Cisternas et al., 2014; Cheung et al., 2015b).

Apart from their influence on the central parts, there is evidence for bars being responsible for a redistribution of the stellar component (e.g., Gadotti & dos Anjos, 2001). Due to their non-axisymmetric structure, bars have been predicted to increase radial motions and thus to act as agents reshuffling the stellar content resulting in a flattening of radial gradients (e.g., Minchev & Famaey, 2010; Kubryk, Prantzos & Athanassoula, 2013; Di Matteo et al., 2013), shown in Fig. 1.13.

In particular, large-scale bars are proposed as a major driver of radial mixing

for a long time (e.g., Friedli & Benz, 1993), not only in the inner regions but especially throughout the disc. In combination with spiral arms (e.g., Sellwood & Binney, 2002), they can create a resonance overlap (e.g., Minchev & Famaey, 2010; Shevchenko, 2011; Minchev et al., 2012) which can lead to a further increase of radial mixing. Similarly to the lack of consensus found for the central values in barred and unbarred galaxies, former studies disagree once more on the stellar population gradients. Pérez, Sánchez-Blázquez & Zurita (2009, 2007) find a variety of age and metallicity gradients and no systematic difference for barred galaxies. A deeper analysis of 2 of them by Sánchez-Blázquez et al. (2011) however shows tentatively flatter age and more distinct flatter metallicity gradients *along the bar* compared to those along the disc, illustrated in Fig. 1.14. This is confirmed by flatter gradients in boxy/peanut-shaped bulges (indicative for the presence of a bar (Athanassoula, 2005) compared to unbarred early-type galaxies (Williams, Bureau & Kuntschner, 2012).

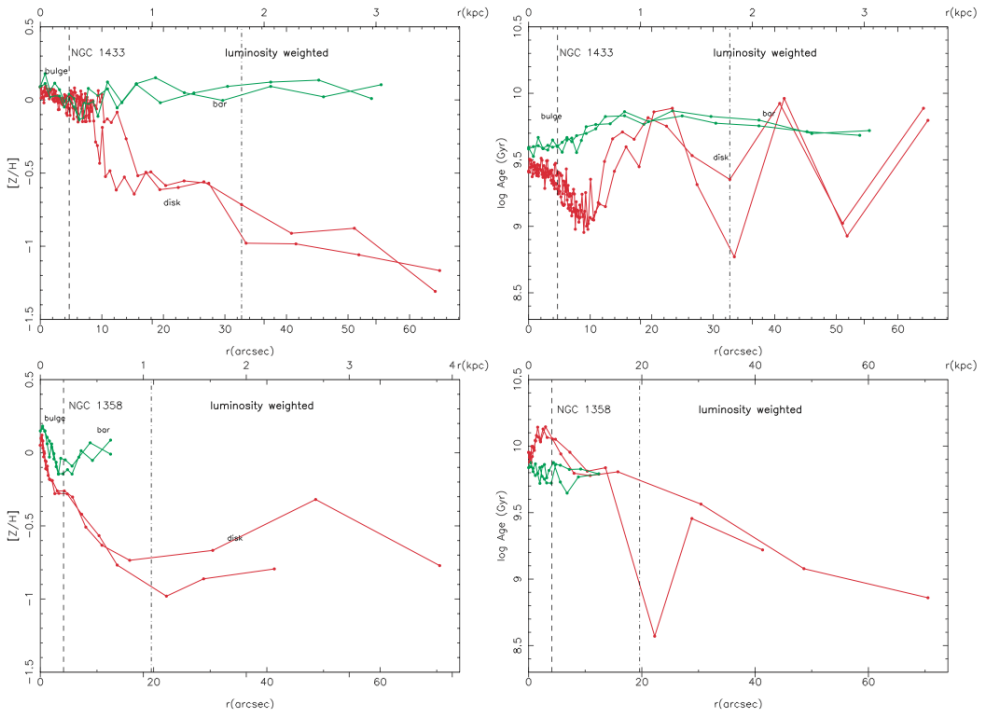

FIGURE 1.14: The comparison of major axis and bar axis age and metallicity gradients for two galaxies reveals flatter gradients along the bar than along the major axis, in particular in the metallicity. Figure from Sánchez-Blázquez et al. (2011).

Simulations of the Milky Way bulge (boxy) confirm this trend (Martinez-Valpuesta & Gerhard, 2013). Recent studies using large statistics by means of the CALIFA (Sánchez et al., 2012) and Sloan Digital Sky Survey (SDSS, Strauss et al. 2002; Abazajian et al. 2009) however find no difference between the stellar population gradients of barred and unbarred galaxies (Sánchez-Blázquez et al. 2014b and Cheung et al. 2015a respectively). The reason for these discrepancies might be the result of sample selections or bar identification, but also could be due to the resolution and methodology of those studies which are significantly different to the former ones.

In Chapter 5, we present the analysis of the stellar populations in bars using the BaLROG sample.

1.3.5 Bar fraction

The amount of bars found in the local Universe and at higher redshifts gives an indication of how relevant their contribution to the overall evolution of galaxies might be. Numerous studies have tried to measure bar fractions and arrived at similar results. In the optical, about half of the local population of disc galaxies are found to be barred (e.g. Whyte et al., 2002; Marinova & Jogee, 2007; Menéndez-Delmestre et al., 2007; Barazza, Jogee & Marinova, 2008; Aguerri, Méndez-Abreu & Corsini, 2009; Méndez-Abreu, Sánchez-Janssen & Aguerri, 2010; Masters et al., 2011; Cisternas et al., 2014). Moving to near infrared (NIR) wavelengths in order to avoid dust extinction and obscuration, this fraction rises to nearly two thirds (e.g. Knapen, Shlosman & Peletier, 2000; Eskridge et al., 2000; Barway, Wadadekar & Kembhavi, 2011). The size of those bars detected is often significantly smaller as illustrated in Fig. 1.15. It shows the same galaxy, M101, once in the optical (HST image[5])and once in the near infrared (Spitzer image[6]). In the latter, a small nuclear bar can be distinguished, as the NIR shows weak bars more strongly (e.g. Buta et al., 2010; Sánchez-Janssen & Gadotti, 2013).

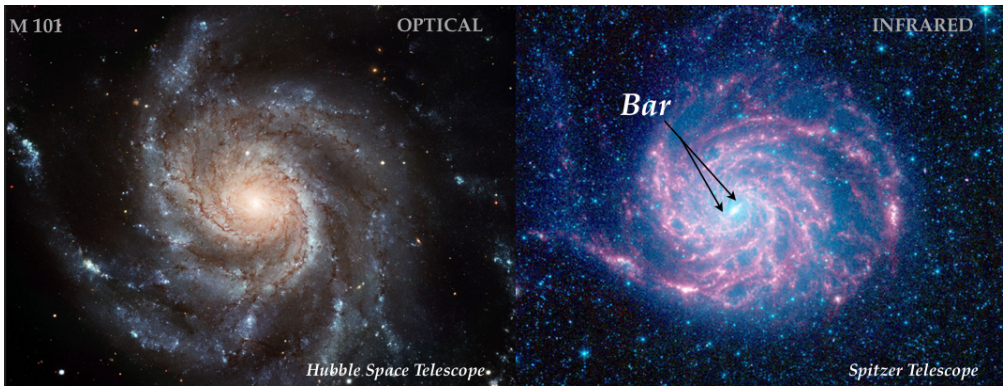

FIGURE 1.15: M101 - on the left seen with the HST and on the right seen through Spitzer. In the near infrared, the nuclear bar is revealed. Figure adapted from original images.

Of course, the near infrared does not only reveal nuclear bars, but also traces much better any type of bar. As this waveband is also a tracer of the disc mass, large bars imply a substantial non-axisymmetric distortion of the disc's mass distribution (Binney & Tremaine, 1987). And yet, compared to their prominence in light, their mass fraction compared to that of the entire disc is rather small. The bar contribution to the total disc potential as found by hydrodynamical simulations ranges only about 10-20% (England, Gottesman & Hunter, 1990; Laine & Heller, 1999; Lindblad, Lindblad & Athanassoula, 1996; Aguerri et al., 2001).

Apart from the high fraction overall found in the local Universe, our own galaxy,

[5]taken from *https* : *//www.spacetelescope.org/news/heic*0602/
[6]taken from *http* : *//apod.nasa.gov/apod/ap*080725.*html*

the Milky Way, also hosts a bar (e.g. Blitz & Spergel, 1991). Already more than half a century ago, its presence was suggested (Johnson, 1957; de Vaucouleurs, 1964), but due to our limited edge-on view, this could not be supported observationally with a high probability until recently. Large spectroscopic surveys detecting prominent cylindrical rotation (e.g. BRAVA Howard et al. 2009, ARGOS Ness et al. 2013) coupled with near-infrared surface photometry, the measurement of HI and molecular gas kinematics in the central few kpc, gravitational microlensing and star counts (Gerhard, 2002; Merrifield, 2004) now confirm this suggestion with overwhelming evidence. The competing scenario of a triaxial bulge instead of a bar nonetheless exists and the contribution of a possible bar and/or classical bulge are still under discussion (e.g. Nakada et al., 1991; Portail et al., 2015; Di Matteo et al., 2015). Also two of the satellites of the Milky Way, the Large and Small Magellanic Clouds, are both barred dwarf irregular galaxies.

But what about higher redshift? When does bar formation start? Simulations predict the formation of bars through dynamical instabilities (e.g. Combes & Sanders, 1981; Efstathiou, Lake & Negroponte, 1982; Pfenniger, 1984; Pfenniger & Friedli, 1991) in the discs once those discs supported by rotation have formed. All recent simulations also agree on the continuous longevity of bars (e.g. Debattista & Sellwood, 2000; Athanassoula, 2002; Athanassoula & Misiriotis, 2002; Martinez-Valpuesta, Shlosman & Heller, 2006; Athanassoula, Machado & Rodionov, 2013) which suggests their presence over large cosmic epochs as they could survive since they formed in the first systems. Indeed, bars have been found at higher redshifts (e.g., Abraham et al., 1996; Elmegreen, Elmegreen & Hirst, 2004; Jogee et al., 2004; Simmons et al., 2014), but their fraction seems to be less than in the local Universe, e.g., 15% at z=1 (Sheth et al., 2008), but this number is still under debate (e.g., Sheth et al., 2008; Nair & Abraham, 2010). The recent work of Simmons et al. (2014) even finds bars up to redshift$\sim$2, strong bars at $z \sim$1.5 and no evolution of the bar fraction between the redshift range 0.5<z<2. These results are however limited to massive discs and might imply that their dynamics are stable over a long timeframe.

In fact, it is important to distinguish galaxy types and environments when comparing bar fractions. Apart from spontaneous disc instabilities, bars are also predicted to be triggered by interactions (e.g., Noguchi, 1987). Studies on bars in different environments indeed detect differences between clusters and fields such that the majority of barred galaxies in clusters are found in the high mass and luminosity regime while the field barred galaxies are rather fainter and less massive (e.g., Barazza et al., 2009; Méndez-Abreu, Sánchez-Janssen & Aguerri, 2010; Méndez-Abreu et al., 2010; Marinova et al., 2012). Furthermore, bars among S0 galaxies seem to be more frequent in clusters than in the field (Barway, Wadadekar & Kembhavi, 2011), suggesting that interactions indeed could catalyse bar formation. Nonetheless, other studies (e.g. Aguerri & González-García, 2009) also suggest interactions as mechanisms that lead to weaker bars or even to their destruction.

As already mentioned, the two Magellanic clouds as Milky Way dwarf galaxy satellites are both barred irregular galaxies. Nevertheless, the barred structures in dwarfs are still little explored, although already found in scarce studies (e.g.,

Lisker, Grebel & Binggeli, 2006)

1.3.6 Bar strength measurements

One of the most important characteristics of a bar is its strength. One of our major aims in this study will be the quantification of the influence of the bar on the host galaxy. Therefore, we will start with a detailed determination of its strength in order to establish a yard stick. Calibrated this way, we hope to identify in our sample common features, as found in previous works and discussed above, that correlate with the strength of the bar. If these features are mainly due to the bar, we would expect stronger alterations with increasing bar strength, unless other factors are equally or more important and hence reducing the possible influence of a bar.

In the past, numerous attempts have been made in order to define a bar strength parameter. One of the first works, by Martinet & Friedli (1997) uses the bar axis ratio. An axis ratio (b/a) larger or smaller than 0.6 would mean a strong or weak bar respectively. In their study they find strong bars to be long and exhibit higher star formation (SF). Another study (Aguerri, Beckman & Prieto, 1998) relates the amplitude of m=2 and m=0 components in order to measure the bar strength. Here they find a tentative but shallow correlation of the bar strength with the ratio of the corotation radius to the bar length. Abraham et al. (1999) also base their criterion on the physical axial ratio of the bar, similar to Martinet & Friedli (1997) . They introduce the value of $(b/a)^2_{bar}$ in order to identify barred systems in the Hubble deep field. This criterion is thus used mainly for identification and is supported by the fact that galaxies recognized by eye as being barred show systematically larger values of $(b/a)^2_{bar}$ than unbarred galaxies.

The maximum value of the ratio of the tangential force to the mean axisymmetric radial force in a barred disc galaxy, denoted as Q_g (or later Q_b), as a quantitative measure of the strength of the bar is first used in Buta & Block (2001). This value goes away from the physical parameters such as bar ellipticities or bar shape but tries to quantify the effect of the bar inside the disc. In Fig. 1.16 we show an illustration based on Buta, Block & Knapen (2003); Buta (2013a).

This method has been widely used, e.g. in Laurikainen & Salo (2002), on the one hand taking the scale height into account and concluding that thin discs show stronger bars than thick discs and on the other hand probing nuclear activity fueling with the result of strongest bars being embedded in non-active galaxies, i.e. galaxies with weak bar strengths host nuclear activity.

The simulations of Athanassoula (2003) use a similar measure for bar strength and find correlations with the angular momentum exchange, mass and velocity dispersion. In her later simulations (Athanassoula, 2005), she finds that a central mass concentration will decrease the bar strength but does not lead to the full destruction of the bar. After a former disagreement on the effect of gas inflows based mainly on different dissolution time scales and the resulting central mass concentration (CMC) enabling to fully destroy the bar, Bournaud, Combes & Semelin (2005) do agree with the results by Athanassoula (2005), such that CMCs will weaken the bar strength but not fully destroy it.

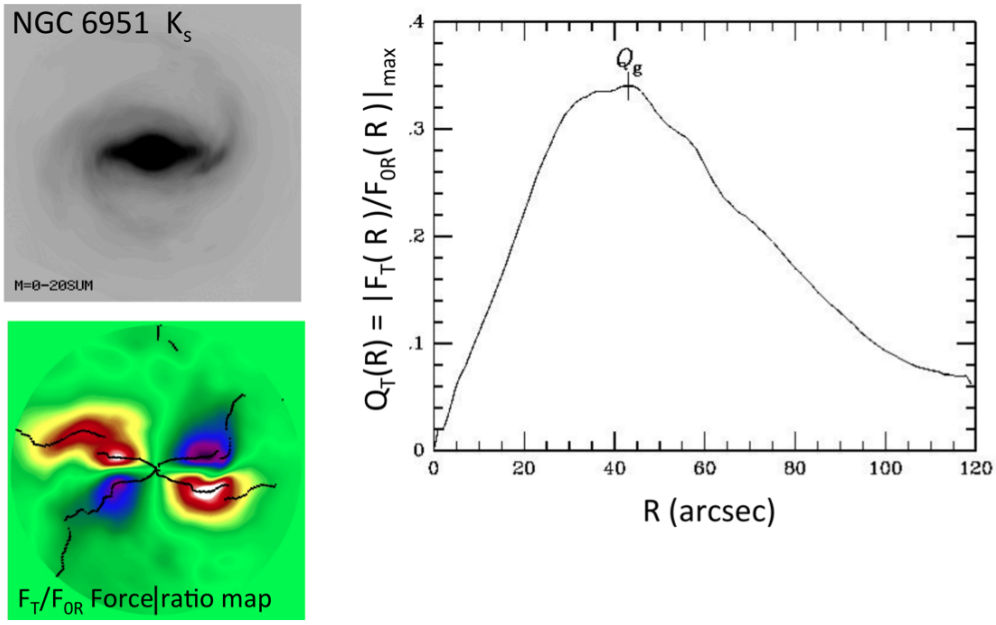

FIGURE 1.16: Measurement of the bar strength Q_g for NGC 6951. The top left panel shows the 2.1μm image of NGC 6951, the bottom left panel the colour-coded ratio maps of the tangential force to the mean axisymmetric radial force (red shows positive and blue negative forces) and the right panel shows the ratio, Q_T, as a function of radius, where the maximum value, Q_g is indicated. Figure from Buta, Block & Knapen (2003); Buta (2013a).

In more recent observational studies, Block et al. (2004) find that the bar strength, again measured in Q_b from near infrared K-band images, correlates with spiral arm strength. They interpret this result as a common disc instability where the PA of the outer bar and inner spiral coincide. This result is supported by the OSUBUGS survey (Buta et al., 2005) where strong bars are found along with strong spirals. However, at the same time, strong bars seem to live shorter than weak ones, assuming recurrent bar formation.

The GEMS Survey (Jogee et al., 2004) shows that the bar strength might evolve within the last 8 Gyrs, but conclude that bars are long lived structures in galaxies, supporting the findings of the former simulations.

Bars are furthermore often associated with dust lanes and Peeples & Martini (2006) try to quantify this relation correlating bar strength (Q_b) with circumnuclear dust morphology. They investigate the central regions and find an increasing presence of circumnuclear rings in strongly barred galaxies; but not all strong bars seem to be equally efficient in fueling the central regions.

A different set of simulations by Kim et al. (2012) uses hydrodynamical simulations to test the relationship of gas structures with bar strength and in Kim & Stone (2012), even magnetic fields are taken into account and their effect on bar substructures (dust lanes, nuclear rings) is probed. Magnetic stress is found to further remove angular momentum from the gas leading to e.g. smaller rings.

Finally, recent N-body simulations even track the bar strength in a dwarf galaxy (Łokas et al., 2014), measuring the maximum of the bar mode. They find that tidal torques decrease the bar strength and length over time.

As the most commonly used method for the determination of the bar strength in observations is the measure of Q_b relating radial and tangential forces, our aim is to compare this method using radial and tangential velocities from the stellar velocity field which can be obtained by a method developed by Maciejewski, Emsellem & Krajnović (2012). This will provide an independent view and check the assumptions made when using only the photometry. Our analysis and results can be found in Chapter 4.

1.4 Bulges

Bulges, as a 'central spheroid', are one of the keys to study galaxy formation and evolution processes, and yet many details of their origin remain unresolved. Hubble was once again one of the first who distinguished them as a morphologically distinct component in his work, calling them 'the nucleus' or 'dominating non-stellar nuclei' (Hubble, 1927, 1936). Nowadays, the word 'nucleus' refers only to the very central component found in galaxies, while bulges contain the central spheroid. However, bulges turn out to be not only a simple spheroidal accumulation of stars. Instead, significant differences found between bulges hint to different formation and evolution scenarios. In the following chapters, we will give a brief overview of the properties of bulges and proposed formation scenarios.

1.4.1 Properties of bulges

Bulges are defined photometrically as the excess of light of an inner component which seems to be superimposed on the exponential disc (e.g., Wyse, Gilmore & Franx, 1997; Fathi & Peletier, 2003; Kormendy, 2015). Originally, they were thought to follow an $r^{1/4}$ de Vaucouleurs (1948) law, similar to elliptical galaxies (Binney, Kormendy & White, 1982). Ongoing research however revealed that there is a clear difference between bulges of early- and late-type galaxies. The former could better be adjusted to an elliptical-type profile with n$\sim$4, while the latter show lower indices (e.g., Courteau et al., 1993; Andredakis & Sanders, 1994). In general, the bulge surface brightness profile can be described by a Sérsic function (Sersic, 1968; Caon, Capaccioli & D'Onofrio, 1993):

$$\mu_b(r) = \mu_e + c_n \left[\left(\frac{r}{r_e} \right)^{\frac{1}{n}} - 1 \right] \tag{1.4}$$

where r_e corresponds to the effective radius of the bulge, μ_e to the bulge effective surface brightness, n to the Sérsic index, which defines the shape of the profile and $c_n = 2.5(0.868n\text{-}0.142)$ (e.g., Gadotti, 2008).

Bulges can also be distinguished dynamically. While discs are rotation-supported structures, bulges are supposed to be more pressure-supported. This means that dispersion velocities are higher than in the disc and often bulges are approximated with an almost isotropic velocity distribution (Kormendy & Kennicutt, 2004; Graham, 2012, 2015b; Kormendy, 2015; Graham, 2015a). Nevertheless, bulges do exhibit rotation, already found long ago (Pease, 1918; Babcock, 1938)

and confirmed in numerous studies (Rubin, Ford & Krishna Kumar, 1973; Pellet, 1976; Bertola & Capaccioli, 1977; Mebold et al., 1979; Kormendy & Illingworth, 1982). The analysis of the specific stellar angular momentum λ_R (defined in Emsellem et al. 2007) instead of measures of v_{max}/σ led to the distinction of fast and slow rotating galaxies and to the conclusion that bulges are in fact anisotropic (Cappellari et al. 2007 and Falcón-Barroso 2015 for a review).

Kormendy & Kennicutt (2004) argue that the disc-like behaviour of some bulges could be attributed to the influence of the bar on the bulge properties leading to this observed disc-like rotation. Early simulations already managed to produce these rotating, exponential-like bulges due to an influence of a bar (e.g., Bardeen, 1975; Hohl, 1975). Bars in fact have been found to significantly alter the position-velocity-diagram (Kuijken & Merrifield, 1995), if they are present. Especially in edge-on systems, they cannot be detected photometrically. However, peanut-shaped bulges seen in highly inclined galaxies have been suggested to be related to the presence of a bar. The projected orbits for edge-on systems as predicted by the work of Kuijken & Merrifield (1995) are shown in Fig. 1.17. The kinematic signatures due to the barred potential can clearly be seen: double-peaked line-of-sight velocity distributions with a characteristic 'figure-of-eight' variation with radius.

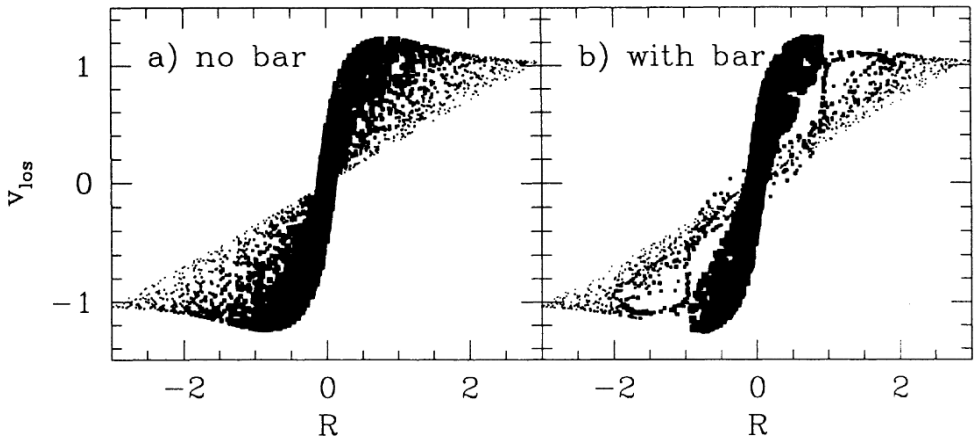

FIGURE 1.17: Predicted Position-Velocity Diagram for a galaxy without a bar and with a bar, both at an intermediate position angle. The figure is from Kuijken & Merrifield (1995).

The same study already included observations that pointed towards a verification, but in the work of Bureau & Freeman (1999), shown in Fig. 1.18, this evidence becomes clearer. They studied the bulges of 15 edge-on spiral galaxies and found the predicted eight-shape figure in the gas emission lines. This was an excellent diagnostic of the presence of multiple orbit families within a bar, and hence an important evidence of the close relation between bars and peanut-shaped bulges.

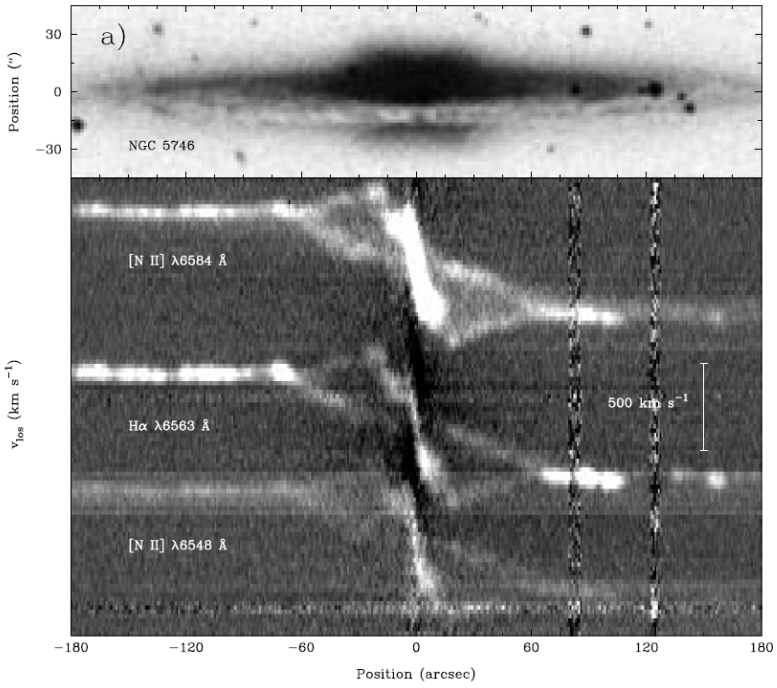

FIGURE 1.18: Observed Position-Velocity Diagram of a barred galaxy The figure is from Bureau & Freeman (1999).

The stellar content of early-type galaxies and classical bulges was once assumed to be characterised by single stellar populations whose stars formed long ago on short timescales (e.g. Hernquist, 1990; Trager et al., 2000). In fact, first bulge studies focused on early-types (to avoid the gas) and compared bulges to elliptical galaxies (e.g. Sansom, Proctor & Reid, 1998; Proctor & Sansom, 2002). However, modern detailed population analyses of bulge systems (e.g. Moorthy & Holtzman, 2006; Jablonka, Gorgas & Goudfrooij, 2007; Morelli et al., 2008; MacArthur, González & Courteau, 2009), largely based on well-resolved spectroscopy, have revealed a more complex picture of star formation history occurring at both early and later times. Especially the analysis of more complex secularly driven structures which formed over longer periods had to be revised. For this analysis, inversion algorithms (e.g. `STARLIGHT`: Cid Fernandes et al. 2005; `STECKMAP`: Ocvirk et al. 2006a,b; `FIT3D`: Sánchez et al. 2006; `ULySS`: Koleva et al. 2009) were developed to perform full-spectral fitting of the data comparing it with a set of synthetic model spectra for a range of ages and metallicities.

Only very few studies have investigated galactic bulges in this great detail up to date and only few have used integral-field spectroscopy (e.g. Ganda et al., 2007; Yoachim, Roškar & Debattista, 2012; Sánchez-Blázquez et al., 2014a). Ocvirk, Peletier & Lançon (2008) demonstrated that a young and cold stellar population could be distinguished from an old and hot bulge using age - line-of-sight-velocity-distribution (LOSVD) diagrams. More recent attempts in the literature to achieve similar goals (using different techniques) are very scarce and usually restricted to very few, well-known multiple component systems (e.g. van der Laan et al., 2013b; Coccato et al., 2011, 2013; Johnston et al., 2013).

Despite great progress, especially with the advent of large spectroscopic surveys (e.g. ATLAS3D, Cappellari et al., 2011a), we are still far from understanding galactic bulges and their subcomponents, both kinematically and from the stellar population point of view.

The next section will now differentiate between different bulge types and their possible formation scenarios.

1.4.2 Different types of bulges and their formation scenarios

The different formation scenarios brought forward during the last decades describe mainly two bulge types:

- **merger-driven** and so-called **classical bulges**
- **secularly evolved disc-like bulges**, which are also often called **boxy/peanut bulges** or **pseudobulges** and which are the result from secular and/or internal evolution (e.g. Kormendy & Kennicutt 2004 and references therein).

Figure 1.19[7] shows an illustration of both types in different orientations.

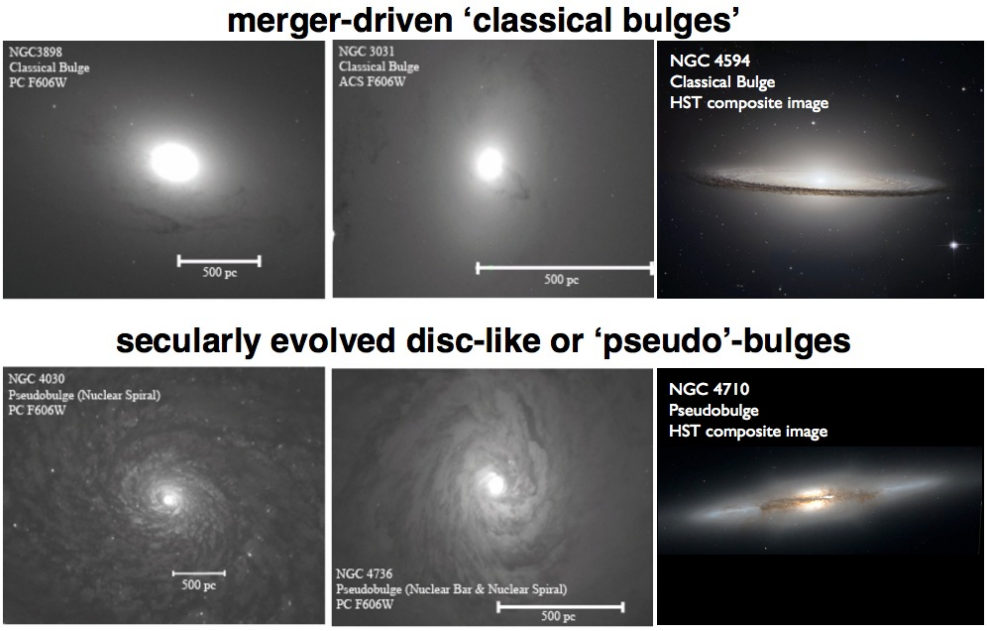

FIGURE 1.19: Examples of merger-driven 'classical' (first row) and secularly evolved disc-like or 'pseudo'-bulges (second row) in spiral galaxies in different orientations, the last column showing an edge-on view in both cases. The first row shows (from left to right) NGC 3898 (HST, F606W), NGC 3031 (HST, F606W) and NGC 4504 (HST composite), also known as M104 or Sombrero galaxy. This last example is commonly a prototype for a classical bulge, but recent work showed that it also could host a disc-like component (Gadotti & Sánchez-Janssen, 2012). Second row: NGC 4030 (M31) (HST, F606W), NGC 4736 (HST, F606W) and NGC 4710 (HST composite). The first two images of each row are taken from Fisher & Drory (2010), the edge-on images are HST images from *http://hla.stsci.edu/*. The entire figure is inspired by Buta (2013b).

[7] inspired by Buta (2013b)

Increasingly detailed studies in the last years have revealed the presence of rich substructures within those bulges which cannot be fully attributed to one common evolution scenario. Athanassoula (2005) redefined the classes based on numerical simulations into: *classical bulges* being results of mergers or monolithic collapse, *boxy/peanut bulges* formed via the natural evolution of barred galaxies (see also Combes & Sanders, 1981; Di Matteo et al., 2014) and *disc-like bulges* resulting from the inflow of gas to the centre-most parts triggering star formation. The latter two bulge types are both results from secular processes within the host galaxy, so that the division by physical origin remains to be i) classical and ii) secularly evolved bulges.

Based on cosmological simulations, mergers are necessary to produce classical bulges (e.g. Hernquist, 1992; Bournaud, Jog & Combes, 2005) and disc-like-bulges are produced via secular evolution (e.g. Pfenniger, 1984; Athanassoula, 2005). Earlier studies already report a strong influence of environment on the resulting bulge types (e.g. Kormendy et al., 2009), such that high density environments produce rather classical bulges than low density environments, hence supporting the above scenarios.

However, Hopkins et al. (2009) report that also bulges with disc-like properties can be a merger product. So far, observations indicate that disc-like bulges are not merger-driven. However, mergers dominated in the early Universe and a large fraction of observed bulges in the present day Universe are found not be fully classical. This could mean that certain mergers (e.g., minor mergers with higher gas fractions) could lead to bulges with disc-like properties rather than to classical bulges. In several simulations these scenarios have been tested and Eliche-Moral et al. (2011) find that minor mergers can create rotationally supported stellar inner components (rings, discs, spiral patterns). Hopkins et al. (2010) furthermore show that major mergers mainly contribute to L_* bulge and spheroid formation while minor mergers are more important in lower mass systems.

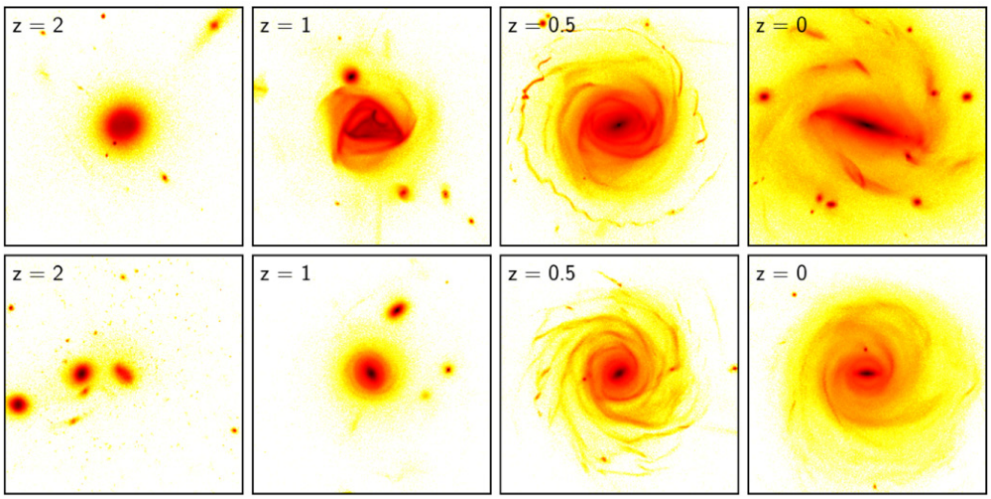

FIGURE 1.20: Transition from an early violently unstable phase to the stable secular phase shown for cosmological zoom-in simulations. The top row shows a violent disc instability, while the bottom shows major mergers. The figure is based on Martig et al. (2012).

Very recently, a third scenario, compatible with both mergers and secular evolution, has arisen. Due to violent disc instabilities at high redshift, giant gas clumps can migrate to the centers of galaxies and merge, leading to bulge structures, that have properties of classical, merger-built bulges (see Bournaud 2015 and Kormendy 2015 and references therein). Observations of kpc-size star-forming clumps in high redshift gas-rich galaxies support this scenario (e.g. Elmegreen, Elmegreen & Ferguson, 2005; Elmegreen et al., 2007, 2009; Bournaud, Elmegreen & Elmegreen, 2007; Genzel et al., 2011; Förster Schreiber et al., 2011). This violent disc instability is widely found in simulations (e.g., Martig et al., 2012) and we show an example in the top row of Fig. 1.20.

This figure also illustrates the transition from an early violently unstable phase (at around z>1) to the secular phase where bars and spiral arms become apparent (at around z<1) for two of their cosmological zoom-in simulations. However, the transition seems to depend on stellar mass. High mass galaxies appear to transit earlier while lower mass galaxies experience the disc instabilities later. This is confirmed by observations that find a predominance of barred spiral morphologies in high-mass galaxies at higher redshift (Sheth et al., 2008; Kraljic, Bournaud & Martig, 2012). Indeed, Martig et al. (2012) find that the bulges with the highest Sérsic index (more classical) show commonly intense gas accretion histories coupled with disc instabilites instead of an active merger history. Nevertheless, after this early formation phase - active mergers and/or collapse of clumps - a secular evolution phase begins and is predicted to influence inner regions and bulges.

Pioneering research and recent discoveries show a variety of different bulges with and without rich substructures hinting to secular evolution - not only bar-driven. Disentangling these different components can be resolved in different ways: (i) Photometric observations allow us to study the morphological features and substructures, e.g. bulge-disc decomposition, through their light distribution (e.g. de Souza, Gadotti & dos Anjos, 2004; Laurikainen et al., 2007) and the derived broad-band colours can already give us an idea of the present stellar populations (e.g. Bell & de Jong, 2000; MacArthur et al., 2004; Gadotti & de Souza, 2006; Muñoz-Mateos et al., 2007; Roediger et al., 2012); abundant photometric studies also relate star formation rates and stellar masses to distinct bulge types (e.g. Fisher & Drory, 2011) (ii) Spectroscopic observations provide us with the kinematic properties (e.g. Falcón-Barroso et al., 2006; Ganda et al., 2006) and distribution of stellar populations in these galaxies (e.g. Trager et al., 2000; Kuntschner, 2000; MacArthur, González & Courteau, 2009; Sánchez-Blázquez et al., 2011).

In this thesis, we will make use of two-dimensional spectroscopy, namely integral field units (described in Chapter 3) in order to better understand the interplay of bars, bulges and other substructures and their influence on the evolution of galaxies.

1.5 Aim and Outline of this Thesis

Secular evolution of galaxies has only recently captured the attention of extragalactic research. **Bars**, as the **major driver of secular evolution**, have been studied extensively in simulations and observations, but mainly photometrically. Thanks to the advent of **integral field spectroscopic units**, this novel technology allows us now to better characterise non-axisymmetric structures such as bars and really quantify their impact on the evolution of their host galaxy. During the last decade, several studies have already begun to investigate the nature of bars, but their predicted major influence, in particular on the stellar component, has not been detected in observations yet. This thesis uses spectroscopy to study **barred galaxies in unprecedented detail**, in particular spatially, based on a **representative sample of bars in the local Universe**. Furthermore, we complement this study with an **extremely high spectral resolution study of bulges** in barred and unbarred galaxies in order to unravel their formation and evolution scenarios in the context of **bar-driven secular evolution**.

The nucleus of this thesis is composed of the **BaLROG sample** (Bars in Low-Redshift Optical Galaxies), which we built in numerous observing runs wih the integral field unit SAURON at the William-Herschel telescope. Building mosaics of up to 7 pointings per galaxies, we achieve to map the bars in unprecedented spatial detail, about **10 times better than large ongoing IFU surveys**. This allows the in depth study of the kinematics altered by bars and allows us to develop a **new technique of calculating bar strength using the kinematics**. This analysis is furthermore complemented with a **large number of numerical simulations**. Within the kinematic analysis, we **quantify** for the first time the subtle **influence of bars on the kinematics**. We aim to correlate the magnitude of certain features, such as humps in the rotation curves (not only in edge-on galaxies), with increasing bar strength.

The **lack of consensus amongst prior research on stellar populations in barred galaxies** also lead us to study the population parameters in great detail. The novelty of our approach is to explore the two-dimensional maps with sufficient spatial resolution as well as trends along different axes of the galaxy. As outlined in Sec. 1.3.4, major efforts have already been undertaken to identify the **influence of bars on the chemical evolution of galaxies**, but **no consensus has been reached**. Thanks to technical developments within the last decade, stellar and gas contributions in the spectra could be separated (e.g., Sarzi et al., 2006) and improved instrumentation enabled the distinction of fainter (sub-)structures (e.g., MacArthur, González & Courteau, 2009; Pérez & Sánchez-Blázquez, 2011; Sánchez-Blázquez et al., 2011; Seidel et al., 2015a). On the one hand, these technical improvements enabled analyses of details and substructures. On the other hand, recent surveys have improved the statistics of stellar population results (e.g., Sánchez-Blázquez et al., 2014b; McDermid et al., 2015), but without the capability to resolve a similar level of detail as achieved in the previous studies mentioned. The **BaLROG sample tries to reconcile the two extremes by providing a small and yet representative sample of barred galaxies in the local Universe covering**

different bar morphologies and strengths (see Chapter 4), while sampling them in unprecedented spatial detail, necessary to detect and quantify the effects of bars.

The high spectral resolution study on bulges of barred and unbarred galaxies finally complements this prior analysis. It allows us to **investigate the build-up of bulges** through cosmic time and **unravel the mass and light distribution of their populations**. This analysis helps us to understand fundamental processes and evolutionary stages in the formation of bulges. It also allows us to **characterise the influence of bars on the build-up of bulges** and other **central substructures** and the point in time of its beginning.

The principal objectives of the thesis are:

- *Development of a bar strength parameter based on the dynamical properties of barred galaxies*
  In order to quantify the influence of bars on the kinematics or populations, we first have to establish a yard stick. Usually the bar strength is determined from photometric images, but these methods are strongly model-dependent. Therefore, it is necessary to assure these methods using the kinematics with a large enough sample, in particular as the bar's influence is predicted to alter the kinematics. The description and use of this method can be found in Chapter 4.

- *Characterization of the kinematics of a representative sample of barred galaxies in the local Universe*
  A full characterization of the stellar and gas kinematics in context of the bar strength is given in Chapter 4. The influence of bars, in particular on the stellar component, had not been fully characterised yet and in particular our high spatial resolution allows us to detect the subtle, but noticeable influence of the bars. Notes and results on individual galaxies including maps are presented in the Appendix.

- *Characterization of the stellar populations of a representative sample of barred galaxies in the local Universe*
  Studying the stellar populations in great detail and along different axes as well as with our full maps, we try to resolve some of the discrepancies among the literature. We present our analysis and results in Chapter 5 determining ages, metallicities and abundances via line-strength indices, as well as stellar population gradients.

- *Understanding the formation histories of bulges in the context of secular evolution versus early formation scenarios*
  Analysing the ensemble of stellar and gas kinematics, classic line-strength indices and the novel approach of full-spectrum-fitting techniques we study the formation histories of three distinct bulges in Chapter 6. The extremely high spectral resolution allows an exhaustive use of the full-spectral fitting code allowing us to distinguish between different forma-

tion redshifts of the populations in mass and light, helping us to constrain their formation.

- *The influence of bars on the bulge component*
  We further characterise the influence of bars on the central substructures and composition of bulges, also presented in in Chapter 6.The obtention of star formation histories allows us to constrain the point in time when bars might have started to act on their host galaxy.

Throughout this work, the cosmological parameters used are $H_0 = 67\,\mathrm{km\,s^{-1}\ s^{-1}\,Mpc^{-1}}$, $\Omega_\Lambda = 0.7$ and $\Omega_m = 0.3$ (Planck Collaboration et al., 2014) .

2

Data

I have to put up with two or three caterpillars
if I want to know butterflies.
Antoine de Saint-Exupéry, The Little Prince

Our approach in trying to better understand the secular processes that act in galaxy evolution is focused on observations. We use **integral field spectroscopy** to derive the stellar and gas kinematics as well as stellar population parameters over the full two-dimensional extend of the galaxies. In our study, spatial (and spectral) resolution is of utmost importance. Therefore we concentrate on high quality data rather than quantity. We use two different instruments:

- the **SAURON integral field** unit at the William-Herschel telescope at the Roque de los Muchachos Observatory in La Palma, Spain in order to build our sample of barred galaxies
- the **WiFeS integral field** unit at the 2.3m-telescope in Siding Spring Observatory, Australia, to perform a pilot study on bulges and the influence of secular processes, in particular bars on their build-up

The principle of integral field spectroscopy as well as both instruments are described in the following chapter. The observation campaigns along with their reduction process will be discussed in Sections 2.2 and 2.3 respectively.

Observations alone of course cannot lead to a comprehensive understanding of the physics that drive galaxy evolution. That is why we first of all compare our results with numerous theoretical models and simulations. In addition we also run our own simulations, in particular for the determination of a new bar strength parameter (see Sec. 4.1.2).

We note that part of this chapter is based on our work already published in MNRAS (Seidel et al., 2015a,c) and submitted (Seidel et. al, 2015d).

2.1 Integral Field Spectroscopy

Spectroscopy is one of the most powerful tools in astrophysics which allows us to learn about the dynamics and chemical composition of stars. Up until the mid 19th century, this was still believed to be an impossible goal. Integral field spectroscopy even extends the possibilities of classical long-slit spectroscopy, where information can only be recovered along the axis of the slit. The use of integral-field units (IFU) allows to disperse the light of an object creating a spectrum, while maintaining its spatial information. The outcome is a 3-dimensional datacube with two spatial axes and one spectral dimension. Hence, instead of the information of only a single line across a galaxy, we obtain spectra at each and every point of the galaxy. This is crucial in galaxy research as galaxies are extremely complex objects that can show different features their extent.

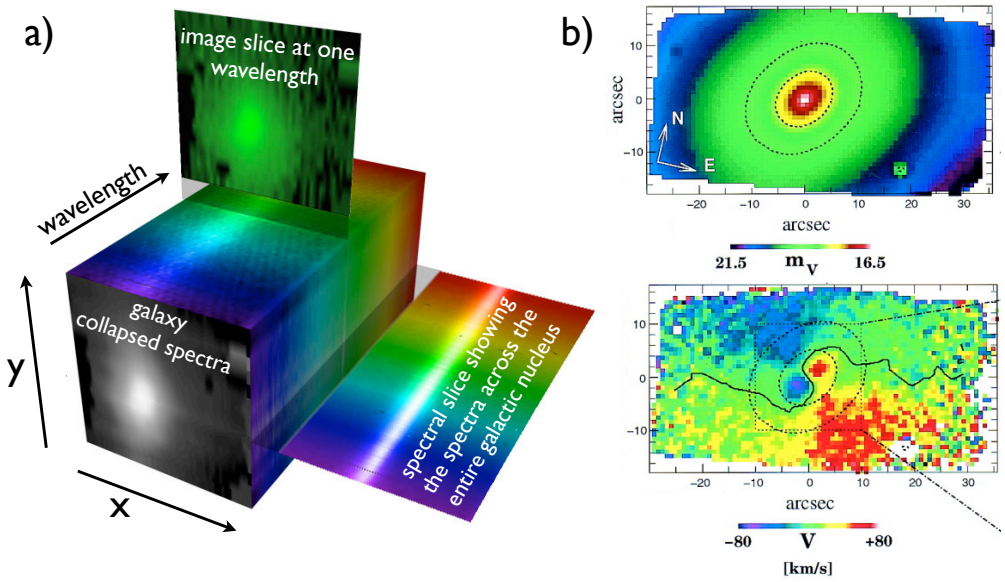

FIGURE 2.1: The principle and importance of integral field units. *a)*: Illustration of the three dimensional data cube: in front, the gray scale image shows the galaxy integrated in wavelength; on top is one image at a single wavelength - it is one of hundreds that add up to the gray scale image; to the right is a slice where the image is collapsed along the y-direction showing the spectrum across the nucleus of the galaxy. *b)*: The necessity of IFUs is illustrated with this galaxy investigated by Davies et al. (2001): the smooth integrated intensity (top) does not reveal anything suspicious about this galaxy while the complexity is doubtlessly revealed in the stellar kinematic map below: a clear kinematically decoupled core sits in the center of the galaxy which probably would not have been detected by only placing a long-slit across the major kinematic axis.

The principle of a 3-D datacube is illustrated in Fig. 2.1 panel a) which shows an adapted figure from the *United Kingdom Infrared Telescope webpage*[1] and the necessity for these observations is depicted in panel b), an adapted figure from the *SAURON webpage*[2] based on the work by Davies et al. (2001). The top panel

[1] http://www.ukirt.hawaii.edu/instruments/uist/ifu/PARAMETERS.html
[2] https://www.strw.leidenuniv.nl/sauron/

of Fig. 2.1 b) shows the integrated light for NGC 4365. Its distribution does not reveal any dramatic twists that would call the observer's attention. In the panel below however, the stellar velocity map clearly unravels a kinematically decoupled core. This feature would have been difficult to detect only using a long-slit observation across the major kinematic axis of this galaxy. Cases like these are of course extreme, however, if we already observe such complex dynamics in a galaxy whose light distribution appears to be very smooth, we must expect even more complex patterns for objects with a more irregular shaped intensity.

One of the first works exploring the concept of IFUs placed an array of optical fibers at the entrance of a classical long-slit spectrograph transforming the bidimensional field into a pseudo-slit (Vanderriest, 1980). A couple of years later, microlense arrays were proposed to spatially sample the data (Courtes, 1982) and TIGER (Bacon et al., 1995) was the first to implement this concept at the Canada-France-Hawaii Telescope on Hawaii. At this time, the integral field units, like `OASIS`, based on the TIGER principle, only possessed a rather small field of view, sufficient for the proposed science aim to study galactic nuclei. Studies of the large-scale stellar kinematics were only made possible with an increase of the field of view a few years later, thanks to the construction of SAURON.

2.1.1 SAURON

SAURON stands for **S**pectrographic **A**real **U**nit for **R**esearch on **O**ptical **N**ebulae and is based on a lenslet array. A detailed description can be found in Bacon et al. (2001) and de Zeeuw et al. (2002). The light first passes through a filter selecting the wavelength range, then through an enlarger until it hits the lenslet array which acts as hundreds of micropupils. After, the light passes a collimator, leading it to a grism to disperse it into spectra which are then imaged on a CCD. The wavelength range and field of view vary with the resolution mode which can be selected between high and low resolution. For our study, we used the low resolution mode which amounts to a wavelength range of 4800 to 5400 Å. Several emission lines to constrain the gas kinematics, namely H$\beta\lambda\lambda$4861, the doublets [OIII]$\lambda\lambda$4959, 5007 and [NI]$\lambda\lambda$5200, 5202 Å can be found in this range. Furthermore it allows the study of stellar absorption line features such as the Mgb band, Hβ and the Fe5015 line. In the employed low-resolution mode, this instrument has a field of view of $33'' \times 41''$, spatial sampling of $0\farcs94 \times 0\farcs94$ per lenslet (1431 in total) and a spectral resolution of full width at half maximum (FWHM) of 3.9 Å. A summary of the instrument specifications in the low-resolution mode is given in table 2.1

In addition SAURON possesses 146 sky lenslets which allows a simultaneous observation of the sky. They are positioned 1'.9 away from the lenslet array imaging the object. Hence a total of 1577 spectra are densely packed on the CCD per SAURON exposure. The data reduction must then be tailored to carefully remove the instrumental signature in the spectra whilst retaining the contribution from the individual lenslets.

TABLE 2.1: Instrument specifications of SAURON in the low-resolution mode.

Characteristics	LR mode
Field-of view	41"×33"
Spatial sampling	0.94"
Spectral resolution (FWHM)	4.2 Å
instrumental dispersion	108 kms^{-1}
spectral sampling	1.1 Å $pixel^{-1}$
Spectral window	4810-5350 Å
emission features	H_β, [OIII], [NI]
absorption features	H_β, Fe5015, Mgb

2.1.2 WiFeS

The Wide Field Spectrograph (WiFeS) is a slightly more recent IFU than SAURON. It was commissioned in May 2009 and its detailed description can be found in Dopita et al. (2007, 2010). Its design is based on former works on the Dual-Beam Spectrograph (DBS) by the Research School of Astronomy & Astrophysics (RSAA) combined with the concentric image-slicer concept of the Near-infrared Integral-Field Spectrograph (NIFS) for the Gemini Observatory planned and constructed by the RSAA of the Australian National University (ANU) College of Physical & Mathematical Sciences.

The WiFeS IFU provides a $38\times25\,\mathrm{arcsec}^2$ field-of-view with 1×1 arcsec per spatial element. WiFeS can be used across the full optical wavelength range, depending on the gratings that are chosen. The instrument's dichroic allows observations with two gratings simultaneously and two separate cameras designed and optimized to operate for a particular part of the wavelength range, register the obtained spectra. Using the RT615 dichroic, we chose the two high resolution gratings B7000 and I7000. The B7000 grating results in a wavelength coverage of 4180 to 5580 Å with a spectral resolution (σ) of 43 km/s, more details for our data in section 2.3.5. The I7000 grating ranging from 6800 to 8900 Å supplies the information on the Calcium triplet region. We list the general instrument specifications as well as the special ones applied to our data in table 2.2.

WiFeS does not offer a simultaneous observation of the sky, but a nod-and-shuffle mode. Due to our observing strategy outlined below, we did not choose this method though, but performed a point-and-stare strategy instead.

TABLE 2.2: General instrument specifications of WiFeS and our applied settings.

Characteristics	Values
Field-of view	38"×25"
Pixel size	15 microns
Pixel scale	1" (slitlet width)×0.5" (spatial sampling along slitlets)
Wavelength coverage overall	330 - 900 nm
Gratings chosen	B7000 and I7000
Wavelength per grating	4180 - 5580 Å ; 6800 - 8900 Å
Spectral resolution (FWHM)	1 Å
instrumental dispersion	43 kms^{-1}
emission features	H_β, [OIII], [NI]
absorption features	H_β, Fe5015, Mgb

2.2 The BaLROG sample for barred galaxies

2.2.1 Sample selection

The parent sample from which our target galaxies are drawn is the S^4G survey of nearby galaxies (Sheth et al., 2010). We restricted our initial choice to barred galaxies with inclinations below 70° and brighter than $M_B = -18.0\,\mathrm{mag}$ to ensure high quality data. As we took our sample from the S^4G survey, we were naturally constrained to those galaxies with $cz \leq 3000\,\mathrm{km\,s^{-1}}$ so that important spectral features (Hβ, Mgb) remain within the wavelength range probed by SAURON. This instrument is mounted on the William Herschel Telescope (WHT) in La Palma at the Observatorio del Roque de los Muchachos. Therefore, galaxies with sky declinations between $-2° \leq \delta \leq 60°$ were chosen to achieve optimal visibility. The entire exercise resulted in a large number of galaxies ($\sim$100), most of which were located in the vicinity of or within the Virgo Cluster. Full 2D spectroscopic analysis of a large sample was beyond our capabilities in terms of observing time. We thus carefully inspected different sets of numerical simulations and images of the S^4G survey and selected those galaxies with prominent bars in different apparent stages of their evolution and with different morphologies. In addition, we selected both early-type and late-type galaxies and those with inclinations below 60° to reduce uncertainties (e.g. in the Q_b determination).

Our target sample consists of 16 galaxies (see Fig. 2.2), a number that provides a reasonable representation of different types of bars. The number of SAURON pointings greatly exceeds this number: the dataset for each galaxy is a mosaic of several pointings (up to seven individual IFU pointings) allowing us to reach the spatial detail that we aimed for while also covering the bars out to the beginning of their surrounding discs. The limitations of the size of our sample are obvious. And although our selection of barred galaxies is representative of the local population concerning different bar strengths, it is slightly biased towards early-types. However, while large integral field surveys such as CALIFA, SAMI or MaNGA provide large enough samples for statistics, they lack the detailed

spatial sampling provided by this work (e.g. we sample at typically 100 pc, even maintained with our Voronoi-binning (within the bar region) which is in most cases at least a factor 10 better than the larger surveys). Table 2.3 gives the entire list of observed targets and basic properties.

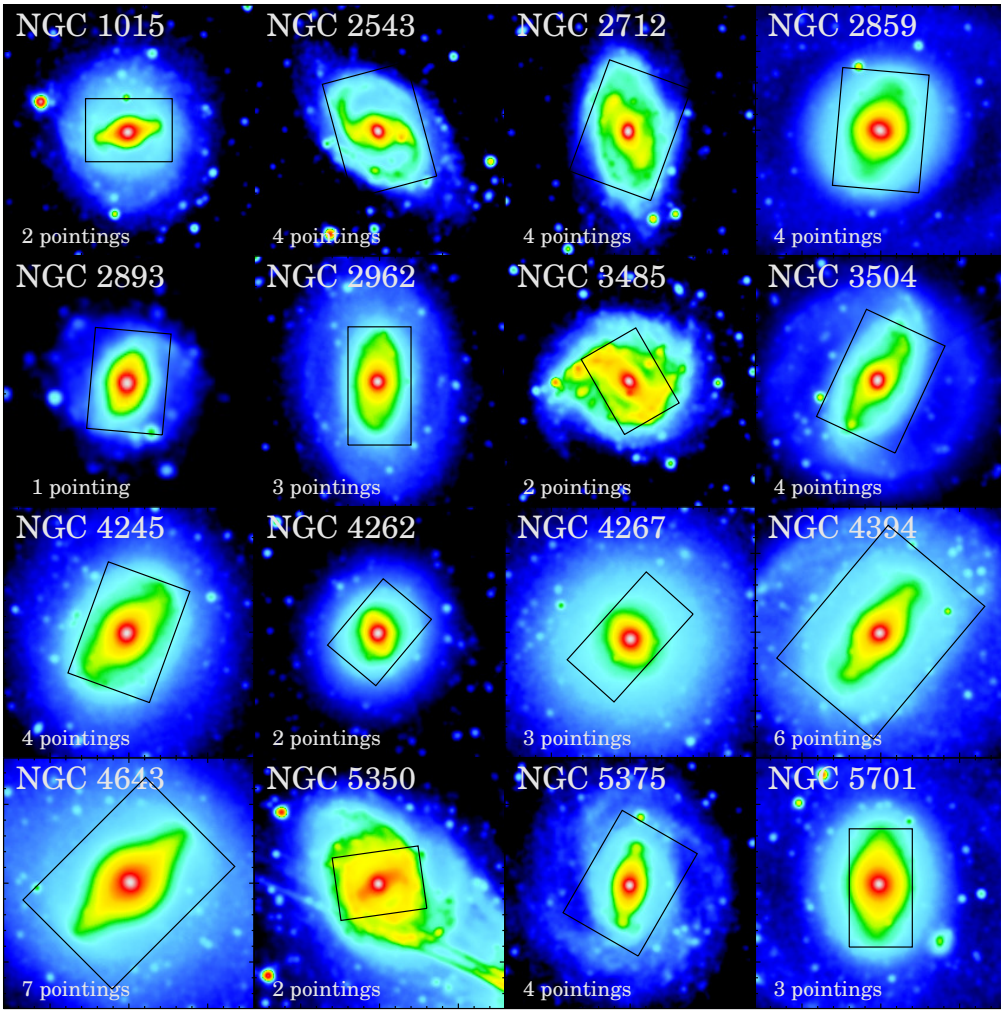

FIGURE 2.2: *Spitzer* images drawn from the S^{4}G survey of nearby galaxies (Sheth et al., 2010) of our sample observed with SAURON. The number of IFU pointings is indicated in the left lower part for each galaxy. The final SAURON mosaic, composed of individual pointings of 30×40 arcsec FoV, is shown on top of the images. North is up and East is towards the left in all cases. The extensions of the S^{4}G fields shown here (squares with indicated mosaic on top) are 160 × 160 arcsec, except for NGC 2893 where it is only 100×100 arcsec.

2.2.2 Observations

The observations were carried out in four consecutive runs in March 2012, January 2013, April 2013 and January 2014 at the WHT in La Palma with the SAURON integral field unit (Bacon et al., 2001). In the employed low-resolution mode, this instrument has a field of view of $33'' \times 41''$, spatial sampling of $0\farcs94 \times 0\farcs94$ per lenslet (1431 in total) and a spectral resolution of full width at half maximum (FWHM) of 3.9 Å. Its wavelength coverage ranges from 4760 Å to 5300 Å, leading to the above mentioned redshift limitations chosen to include

TABLE 2.3: Galaxy Sample. - (1) Galaxy name, (2) Hubble type, (3, 4) J2000 coordinates (right ascension, declination), (5) systemic velocity, (6) inclination, (7) bar length, (8) position angle, (9) bar position angle, (10) effective radius (r_e). Objects belonging to the Virgo cluster are marked with a small *v* next to their name. Notes. - All morphological classifications, coordinates and V_{sys} are from the *NASA Extragalactic Database (NED)*, http://ned.ipac.caltech.edu/. All inclinations, PAs and effective radii of the galaxy (r_e) are from the S^4G P4 (Salo et al. 2015, accepted to ApJS) while bar lengths and bar PAs are determined by Herrera-Endoqui et al. (2015, submitted) (here the ones by visual inspection).

Galaxy	Hubble Type	RA (hh mm ss.ss)	Dec (dd mm ss.ss)	V_{sys} (km s^{-1})	Inclination (deg)	Bar Length (arcsec)	PA (degrees)	PA_{bar} (degrees)	r_e (arcsec)
(1)	(2)	(3)	(4)	(5)	(6)	(7)	(8)	(9)	(10)
NGC 1015	SBa	02 38 11.56	-01 19 07.3	2628	30.5	21.5	−8.3	101.4	19.73
NGC 2543	SB(s)b	08 12 57.92	+36 15 16.7	2471	59.9	14.9	37.0	105.5	26.56
NGC 2712	SBb	08 59 30.47	+44 54 50.0	1815	60.5	20.5	3.6	22.6	25.09
NGC 2859	(R)SB0$^+$(r)	09 24 18.53	+34 30 48.6	1687	37.2	34.4	1.8	169.6	22.41
NGC 2893	SB0-a	09 30 16.96	+29 32 23.9	1703	17.4	12.0	88.1	164.1	4.58
NGC 2962	SB0-a	09 40 53.93	+05 09 56.9	1960	49.0	30.7	8.3	172.7	20.50
NGC 3485	SBb	11 00 02.38	+14 50 29.7	1436	20.4	21.0	−64.6	40.6	26.38
NGC 3504	SBab	11 03 11.21	+27 58 21.0	1539	12.8	37.1	−41.7	148.3	11.13
NGC 4245	SB0/a(r)	12 17 36.77	+29 36 28.8	886	33.3	36.3	0.5	131.0	23.52
NGC 4262^v	SB0$^-$(s)	12 19 30.57	+14 52 39.6	1359	24.5	13.4	−6.0	26.5	5.99
NGC 4267^v	SB0$^-$	12 19 45.24	+12 47 53.8	983	11.9	16.9	−27.5	34.0	21.07
NGC 4394^v	(R)SB(r)b	12 25 55.53	+18 12 50.6	922	30.4	41.4	−57.6	143.4	36.79
NGC 4643	SB0/a(rs)	12 43 20.14	+01 58 41.8	1330	36.8	49.9	56.0	133.3	24.22
NGC 5350	SBbc	13 53 21.63	+40 21 50.2	2321	50.3	15.2	7.9	120.8	28.06
NGC 5375	SBab	13 56 56.00	+29 09 51.7	2386	29.8	27.2	−9.4	171.1	24.35
NGC 5701	(R)SB0/a(rs)	14 39 11.08	+05 21 48.5	1505	15.2	39.0	52.0	174.9	25.97

important emission and stellar absorption line features.

We observed up to 7 SAURON pointings per galaxy to build a large mosaic. The final maps extend along the bars up until the start of the disc, allowing us to probe radial dependencies within and outside the bar, while also resolving great spatial detail. This strategy was quite costly in time: for the small sample of 16 galaxies we invested 54 pointings in total, each of 1–2 hours depending on the galaxy's surface brightness. Table 2.4 summarises the number of pointings and the total exposure times for each galaxy. Figure 2.2 shows the final extent of the mosaic overlaid on top of the S^{4}G images.

Apart from the large pointing offsets, we introduced small dithers within each pointing of typically 1 to 2″. This helps us to account for a couple of bad columns in the CCD and to improve our sampling. The orientation of the field of view (FoV) of SAURON was such that the 146 sky lenslets always pointed away from the galaxy's centre. They are 1.9 arcmin from the main FoV and thus ensure a simultaneous sky exposure during the object exposure.

We took a calibration frame using a Neon lamp before and after each science frame. Skyflats were taken at dusk and dawn, as well as continuum lamp exposures with a Tungsten lamp. For the flux calibration we observed several spectrophotometric standard stars. For further spectral calibration, we also observed a broad range of stars with different spectral types from the MILES database[3] (Sánchez-Blázquez et al., 2006b).

2.2.3 Data reduction

The reduction was performed with the available SAURON pipeline XSauron described in detail in Bacon et al. (2001). The preprocessing of raw frames includes overscan and bias subtraction. The evaluation of dark frames showed that the dark current is negligible: less than $1\,\mathrm{e^-pixel^{-1}h^{-1}}$. All frames were preprocessed in this same way. After that, a model mask was created to extract the spectra. This mask builds a table indicating corresponding positions by relating the pixels on the CCD to their associated wavelengths and lenslets. The outcome is a set of three-dimensional data cubes (α, δ, λ). Wavelength calibration was achieved with the arc (neon) lamp exposures. A cross-correlation function between the neon frames taken before and after the science exposure and the one of the extraction mask defines potential slight offsets between the science frame and the mask. This analysis is based on 11 emission lines which can be seen in the wavelength range of SAURON.

The flat-fields were created with a combination of twilight and continuum lamp (tungsten) exposures. The former calibrates the spatial component, while the latter is responsible for the spectral coordinates. We used for each run a representative twilight and continuum flat exposure investigating counts and distributions of all flat exposures. On a case-by-case basis, we also chose night-dependent flats, but for the vast majority and thanks to our bright objects, the former method proved to work well. Cosmic rays were removed before the sky subtraction, where the median of the 146 dedicate sky lenslet values was computed and subtracted from the science frame spectra. Flux calibration was

[3] http://miles.iac.es

TABLE 2.4: Summary of the observations: (1) NGC number, (2) Run number, (3) Pointing number, (4) Total exposure time, in seconds.

Galaxy (1)	Run (2)	# P (3)	T_{exp} (4)
NGC 1015	2	2	12×1800
NGC 2543	1,2	3	10×1800
NGC 2712	4	4	8×1800
NGC 2859	1	4	16×1800
NGC 2893	3	1	8×1800
NGC 2962	4	3	9×1800
NGC 3485	4	2	4×1800
NGC 3504	3	4	12×1800
NGC 4245	2	4	16×1800
NGC 4262	1	2	8×1800
NGC 4267	1	3	12×1800
NGC 4394	2	6	24×1800
NGC 4643	3	7	23×1800
NGC 5350	2	2	8×1800
NGC 5375	4	4	16×1800
NGC 5701	1	3	12×1800

done using the spectrophotometric standards. Their flux correction curve was extracted comparing the observed curve with a reference spectrum. The resulting correction curve was used to calibrate all science frames. The merging and mosaicking of the individual data cubes was achieved with the XSAURON software using the integrated intensity contours in comparison with those of a *g*-band SDSS image. The entire mosaic was constructed with the obtained offsets and scalings between each image.

2.2.4 S^{4}G data

We complement our SAURON mosaics with *Spitzer* 3.6μm images from the S^{4}G (Sheth et al., 2010). As the *Spitzer* images are very deep, the outer isophotes are typically close to or beyond the 3.6 = 25.5 mag/arcsec^2 in the AB magnitude system, the position angles (PA) and ellipticities (ℓ) are taken from the S4G pipeline 4 (Salo et al. 2015, accepted to ApJ). Global galaxy parameters such as the effective radii of the galaxies (r_e) are from Muñoz-Mateos et al. (2015, submitted) and the barlength measurements are from Herrera-Endoqui et al. (2015, submitted). In addition, we used the *Spitzer* images to compute bar strengths, Q_b, for our sample as described in Section 4.1.1. The Q_b measurements for the complete S^{4}G are given in Díaz-García et al. (2015, submitted).

2.3 The WiFeS sample for bulges

2.3.1 Target selection

The target selection aimed at providing galaxies with distinct properties and level of morphological substructure seen in the photometry in their inner regions in order to quantify the importance of the different stellar populations present in each system. Therefore we chose galaxies with three distinct galactic bulges in barred, unbarred and ringed galaxies, spanning a very different level of complexity in stellar populations based on the literature. We selected bright, prominent bulges to maximize the quality of the data while reducing the required observing time. The sample was selected from the Carnegie-Irvine Galaxy Survey (Ho et al., 2011) and the catalogue of inner disks and rings (Erwin & Sparke, 2002), with extensive ancillary photometric decompositions (Weinzirl et al., 2009; Li et al., 2011). Detailed descriptions of each galaxy can be found in the following Chapter 2.3.2. Despite the obvious limitations of a sample of only three galaxies, this pilot study allows us to compare these systems and still detect significant similarities, see e.g. §6.3.3, helping us to understand common fundamental formation and evolution mechanisms throughout bulges in disk galaxies.

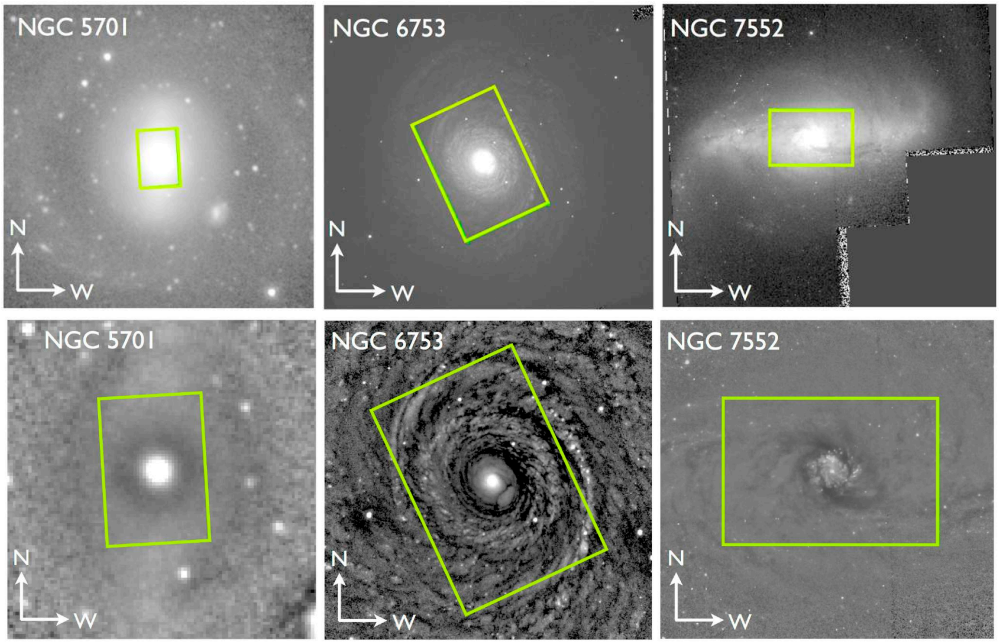

FIGURE 2.3: (*Top row*) Sample of galaxies observed with the WiFeS spectrograph. Spitzer 3.6μm imaging from the S^{4}G survey is shown for NGC 5701 (left), while HST imaging in the F814W filter is presented for NGC 6753 (middle) and NGC 7552 (right). The green rectangle marks the footprint of the WiFeS FoV (25×38 arcsec). (*Bottom row*) Unsharp mask images for our sample of galaxies. See §2.3.3 for details.

We retrieved *Hubble Space Telescope* (HST) Wide Field Planetary Camera 2 archival data, in the F814W filter, for NGC 6753 and NGC 7552 from the Hub-

ble Legacy Archive[4]. For NGC 5701, we used S^{4}G imaging[5] (Sheth et al., 2010) given that no HST data were available (see Fig. 2.3). The basic characteristics, taken from HyperLeda[6], are listed in Table 2.5. The table also contains bulge characteristics determined by Weinzirl et al. (2009) via two-dimensional surface brightness decomposition as well as central (circular aperture of 1.5 arcsec) velocity dispersions and line-strength values extracted from our own analysis.

2.3.2 Details on each galaxy

NGC 5701 is an early-type galaxy with a rather smooth bulge. According to the De Vaucouleurs Atlas Description, it shows a well-defined bar imbedded in a strong inner lens, one of the best-defined examples of this phenomenon. In the centre and bar region, this galaxy does not seem to exhibit star formation nor dust. According to Erwin & Sparke (2002), this galaxy (being part of the WIYN Sample) has no inner structures apart from a nuclear spiral. Therefore, here we expect to have one dominant old population with possibly a weak younger population in the centre. Furthermore, we can test the hypothesis brought forward by Gadotti & de Souza (2003) to be a disk-lacking galaxy.

NGC 6753 is also an early-type galaxy but with more substructure. The dominant feature here is a bright inner ring which lies at the rim of a fairly uniform inner disk zone. This inner disk zone is filled with H-alpha emission (Crocker, Baugus & Buta, 1996). Outside the inner ring, a broad oval zone includes complex and partially flocculent spiral structure. Beyond the broad oval zone, a well-defined, and mostly detached outer ring is found. For this project, mostly the inner parts are of importance and here we now expect to find more substructures than in NGC 5701. In particular, we aim to detect signatures of an inner ring both in the kinematics and stellar population parameters.

NGC 7552 is mostly defined by a complex, dusty bar and is best known for its central starburst, which is associated with a nuclear ring. The bar is prominent, and numerous HII regions are scattered within the disk in an asymmetric pattern. The 1 kpc starburst ring is best visible in radio wavelengths and reveals numerous supernova remnants (Forbes et al., 1994; Forbes, Kotilainen & Moorwood, 1994). Nevertheless, it does not present very strong nuclear activity which simplifies studies of the circumnuclear ring. The classification of this object seemed difficult amongst the literature: The presence of giant HII regions near the corotation radius lead Bonatto, Bica & Alloin (1989) to the conclusion to deal with an H II galaxy, whereas Durret & Bergeron (1988) classified it as a LINER due to the detection of a weak [OI] λ 6300 line. The dusty bar morphology is very unusual (the De Vaucouleurs Atlas Description). As a member of the Grus triplet, the galaxy may be affected by an interaction that has disturbed its morphology. In fact, Claussen & Sahai (1992) report high molecular gas concentrations in the centre and signatures of tidal disturbance deduced from the observed asymmetries in their CO line profiles. Additionally, Feinstein et al. (1990) discovered two weaker rings (of radii 1.9 kpc and 3.4

[4]http://hla.stsci.edu, based on observations made with the NASA/ESA HST, obtained from the European Southern Observatory (ESO)/ST-ECF Science Archive Facility.

[5]http://irsa.ipac.caltech.edu/data/SPITZER/S4G/

[6]http://leda.univ-lyon1.fr/

TABLE 2.5: Galaxy sample properties. The columns show the following: (1) NGC number; (2) Hubble type (RC3; de Vaucouleurs et al. 1995); (3) - (6) J2000 coordinates (right ascension, declination), absolute B-band magnitude and inclination (taken from HyperLeda); (7) and (8) bulge effective radius and bulge Sérsic index (taken from Weinzirl et al. 2009); (9) - (13) Hβ and Mgb line strength indices in Å and mag as determined from our data in a central circular aperture of radius of 1.5 arcsec.

Galaxy	RC3 Type	RA	Dec	M_B	incl.	Bulge r_e	Bulge n	$\sigma_{\rm cen}$	Hβ	Hβ	Mgb	Mgb
		(h, m, s)	(d, m, s)	(mag)	(deg)	(arcsec)		(km s^{-1})	(Å)	(mag)	(Å)	(mag)
(1)	(2)	(3)	(4)	(5)	(6)	(7)	(8)	(9)	(10)	(11)	(12)	(13)
NGC 5701	(R)SB(rs)0/a	14 39 11.1	+05 21 49	-19.99	40.6	11.13	2.41	112	1.95	0.076	3.82	0.136
NGC 6753	(R)SA(r)b	19 11 23.6	-57 02 58	-21.65	30.1	1.50	0.94	214	1.60	0.062	4.80	0.174
NGC 7552	(R')SB(s)ab	23 16 10.8	-42 35 05	-20.52	23.6	2.70	0.64	89	5.00	0.208	1.20	0.041

kpc). Hameed & Devereux (1999) investigate NGC 7552 via Hα, while Forbes, Kotilainen & Moorwood (1994) focuse on the ring, revealing yet another inner ring of the size of only 1 kpc in the radio. Schinnerer et al. (1997) concentrate as well on this central feature showing among others Brγ images, also tracing gas ionized by recently formed massive stars and distinguish different star formation histories (SFH) for the nucleus and the ring. Furthermore, based on NIR and HST V-band continuum maps, they postulate the existence of in inner bar located inside the nuclear ring and perpendicular to the outer east-west oriented large bar. Pan et al. (2013) discuss in detail the circumnuclear starburst ring and the related formation of dense molecular gas and stars in that region.

2.3.3 Level of substructure from unsharp masking

In our galaxies certain substructures are already evident from the photometric images shown in the upper row of Fig. 2.2. Nevertheless, we have produced unsharp masked images, following Erwin (2004) and Lisker et al. (2006), to reveal any small-scale structures or structures with no radial symmetries that may be present. This method relies on the presence of a smooth and symmetric overall light distribution which can be modeled by the `gauss` task of IRAF[7] (Tody, 1993). Then the original image can be divided by the smooth model to obtain the unsharp mask. For NGC 6753 and NGC 7552, we used a value of $\sigma_{mask} = 20$ for the Gaussian convolution and $\sigma_{mask} = 5$ for NGC 5701. We determined the ellipticity and PA values from our own reconstructed images (i.e. intensity images extracted from WiFeS datacubes). The results are presented in the bottom row of Fig. 2.2. The different substructures stand out very clearly. NGC 5701 shows a rather smooth distribution with a strong central feature. The rectangle indicating the WiFeS FoV exacerbates the proper visualization of its large scale bar, which can be seen rather faint here. NGC 6753 also exhibits a prominent central component, but with significant flocculent spiral structure throughout the FoV, but mainly concentrated in the inner ring. In NGC 7552, the dust lanes are very evident, along with the bright circumnuclear ring with star forming regions of different intensities.

2.3.4 Observations

The observations were taken in July and September 2013 at the 2.3m telescope at Siding Spring Observatory (SSO) in Australia. We used the WiFeS IFU which provides a $38\times25\,\mathrm{arcsec}^2$ field-of-view with 1×1 arcsec per spatial element. It was commissioned in May 2009 and its detailed description can be found in Dopita et al. (2007, 2010). The instrument's dichroic allows observations with two gratings simultaneously. Using the RT615 dichroic, we chose the two high resolution gratings B7000 and I7000. The B7000 grating results in a wavelength coverage of 4180 to 5580 Å with a spectral resolution (σ) of 43 km/s, more details for our data in §2.3.5. The I7000 grating ranging from 6800 to 8900 Å supplies the information on the Calcium triplet region. The good instrumental resolution allowed us to measure the lowest expected velocity dispersions while the large spectral coverage still ensures a meaningful

[7]IRAF is distributed by the National Optical Astronomy Observatory, which is operated by the Association of Universities for Research in Astronomy, Inc., under cooperative agreement with the National Science Foundation.

full-spectral fitting analysis.

The central surface brightness for the bulges in our sample is $\mu \simeq 18$ mag arcsec^{-2} (Li et al., 2011). A minimum S/N per resolution element of S/N$\approx$ 20 is required to characterize the kinematics and stellar populations of each separate stellar components (e.g. Johnston et al., 2013). We aimed at 4 hour integration times for each galaxy in order to achieve that S/N and still maintain the maximum spatial sampling provided by the instrument (i.e. 1×1 arcsec). We obtained 4800 seconds (4×20 min exposures) each for NGC 5701 and NGC 7552 and 14400 seconds (12×20 min exposures) for NGC 6753. Although we lost observation time on the first two targets due to weather conditions, their data are still very useful, just with somewhat coarser binning. The average seeing was around 1.5 arcsec, September being slightly better than July.

We observed one single pointing per galaxy centred on the bulge dominated region (see Fig. 1). Nonetheless, the large FoV allowed us to reach disk dominated regions. We took calibration frames (bias, flats and arc) before dawn and after dusk, and sky flats during twilight. The observational strategy was to "point-and-stare", i.e. to observe in blocks of object−sky−object, calibration frames and calibration stars. This strategy was designed to have sky and calibrations near each science frame to avoid temporal effects. We decided to adopt this method rather than the nod-and-shuffle method available for WiFeS since it maximized the exposure time on the science frames. Instead of taking the same amount of time on the sky and object frames, we decided to increase the time spent on the object frames to increase the signal, and at the expense of slightly larger noise level (i.e. increase by the square root of 2).

2.3.5 Data reduction

We reduced and calibrated our data using the new pipeline designed for this instrument, PyWiFeS[8]. The pipeline performs a typical reduction on each single WiFeS frame which consists of 25 slit spectra being 1 arcsec wide and 38 arcsec long. The reduction includes bias subtraction, flatfielding, distortion correction, wavelength calibration, sky (and additional telluric correction for the red arm) subtraction, sensitivity curve correction and datacube generation. Details can be found in Childress et al. (2014).

For the wavelength calibration of our frames, we had to devise a non-standard solution. This was done using neon and argon arc lamp spectra which were taken close to the science exposures during the entire night. Since this lamp had not been used before with the B7000 and I7000 high resolution gratings, we created our own reference files from the arc lamp measurements and calibrated them with the line values given, relative to air, on the NIST webpage[9]. We ensured the accuracy of this calibration by reducing arc lamp spectra as well as sky frames and checking the position of the arc and sky lines. This resulted in an uncertainty of $\Delta\approx$0.1 Å. The datacubes were flux calibrated with the help of flux standard stars observed: HIP71453, EG131 and Feige110, to achieve a relative flux calibration. For the red-arm spectra, the removal of telluric lines was achieved using observations of featureless white dwarfs, taken close to the

[8]http://www.mso.anu.edu.au/mjc/wifes.html
[9]http://www.nist.gov/pml/data/index.cfm

science frames and at similar air masses as the object.

The data reduction is run separately for the blue and red arm frames. After finding the offsets, we use the iraf `imcombine` routine to merge the individual cubes to a single datacube sampled to a common spatial grid. The blue spectra span from 4100 Å to 5500 Å with a spectral sampling of 0.347 Å per pixel and a spectral resolution (Full Width Half Maximum, FWHM) of FWHM$\simeq$0.9 Å. The red spectra cover the range from 6808 Å to 8930 Å with a spectral sampling of 0.5665 Å per pixel and a spectral resolution of FWHM$\simeq$1.5Å. In both cases the spectral resolution was not constant along the frame and therefore we convolved the spectra in each case to the highest measured FWHM values, setting the final spectral resolution to FWHM$\simeq$1.0 Å and FWHM$\simeq$1.6 Å for the blue and red setups respectively.

3

Methods

Some people feel the rain.
Others just get wet.
Roger Miller

This chapter presents the multitude of techniques, methods and analysis tools used throughout this work. The basic tools are the same for the two samples and only differ in their configuration due to the distinct properties of the data, mainly due to the wavelength range and the spectral resolution. Here we summarise the methods to derive the i) stellar and gas kinematics and ii) stellar populations. In particular, the same kinematic analysis has been performed on both the BaLROG and WiFeS data sets while the stellar population analysis differed slightly between the two samples. In the following we explain the necessary steps and theoretical background of the techniques in detail.

3.1 Signal-to-Noise constraints

A detailed analysis of the stellar and gas kinematics requires a minimum signal-to-noise ratio (S/N) (e.g., van der Marel & Franx, 1993). In our analysis of kinematics and stellar populations of the BaLROG sample, we adopted the Voronoi binning scheme of Cappellari & Copin (2003) and applied it to our data. For the kinematic study we chose to reach a minimum S/N≈40 per pixel for all galaxies. The central spectra remained unbinned in all cases and exceeded this S/N level (e.g. S/N>100). While a S/N of 40 ensures high-quality spectra for the extraction of the mean stellar velocity, velocity dispersion as well as Gauss-Hermite moments h_3 and h_4, it is also low enough to preserve the spatial substructures in the galaxies, as seen in the resulting maps (see Appendix A). Before we binned, we also ensured that we would not contaminate our measurements by poor quality spaxels. Therefore we excluded those spaxels with a S/N below 3 and then limited the data to an isophote with at least this average S/N level. The resulting extensions of the maps are hence due to the combined mosaic and this additional S/N minimum threshold.

The stellar population analysis of the BaLROG sample required a slightly elevated S/N. We chose in this case a minimum S/N of ≈80 per pixel for all

galaxies, which is double than that for the kinematic analysis. The central spectra remained unbinned nevertheless in all cases and exceeded this S/N level (e.g., S/N>100). The reason to elevate the S/N for this work is the delicacy of the extraction of absorption line strengths (connected with the emission line removal). Before the binning, we also excluded spaxels with a S/N below 3 in order to avoid contamination by poor quality measurements. The extensions of the maps are therefore not only given by the mosaic, but also by this imposed S/N minimum threshold, as for the kinematic analysis.

For the analysis of the WiFeS data, we also adopted a Voronoi binning scheme (Cappellari & Copin, 2003) to reach the desired S/N levels. We chose to bin our data for NGC 5701 and NGC 7552 to S/N≈20 and for NGC 6753 to S/N≈40. This choice ensures a meaningful analysis while maximizing the spatial sampling, which is important to resolve substructures present in our maps. The S/N are lower in this sample than in the BaLROG sample as we profit from a much higher spectral resolution and larger wavelength coverage which is crucial and helps us in the different analysis technique (full-spectral fitting) that we focus on with this sample. The extension of the field is the WiFeS FoV, however bins of too low signal (less than S/N=3) have been left out, similar to the BaLROG sample.

3.2 Stellar and gas kinematics

3.2.1 Stellar kinematics

In order to obtain kinematical information from galaxy spectra, one needs to recover the line-of-sight velocity distribution (LOSVD). A galactic spectrum can be approximated by a stellar spectrum - given as a template - convolved with the velocity distribution of the stars along the line-of-sight, i.e. LOSVD (e.g Gerssen, 2000):

$$\textsc{Galaxy} = \textsc{Template} \otimes \textsc{Losvd} \tag{3.1}$$

In all datasets, we extracted the stellar kinematics using the pPXF – penalized pixel fitting – code developed by Cappellari & Emsellem (2004). The routine fits each galaxy spectrum with a combination of template spectra from a given library.

For the BaLROG sample, we used a subset of Medium-resolution Isaac Newton Telescope library of empirical spectra (MILES; Sánchez-Blázquez et al. 2006b) single stellar population (SSP) model spectra (Vazdekis et al., 2010) with a range of ages and metallicities of 0.1 Gyr to 17.8 Gyr and -0.40<[Z/H]<+0.22, respectively. Their mean resolution is of FWHM = 2.51 Å (Falcón-Barroso et al., 2011) and before the fitting process, we matched the spectral resolution of the models to that of our data.

For the WiFeS dataset, we extracted the stellar kinematics from the blue and red arm separately. For simplicity, we will present the results from the blue spectra only. Both sets of maps agree within the uncertainties. Here, we used a subset of PEGASE high resolution model spectra `PEGASE-HR` with R≈10000 (Le Borgne et al., 2004) spanning a wide range of ages and metallicities in order to minimize the impact of template mismatch. Before the fitting process, we

also matched the spectral resolution of those models to that of our data.

Throughout this work we assume a Kroupa initial mass function (IMF, Kroupa, 2001). The result of pPXF is a line-of-sight velocity distribution described by a Gauss-Hermite parametrisation (Gerhard, 1993; van der Marel & Franx, 1993) allowing the measurement of the velocity (V), velocity dispersion (σ) and higher order Gauss-Hermite moments (h_3 and h_4). Figure 3.1 shows a spectrum of the disc region of NGC 4394 and the pPXF analysis. The top-panel illustrates the determination of the stellar kinematics, where blue columns show the masked regions where contamination of emission lines are expected. The red model spectra fit very well the black data. The residuals, shown in green, indicate the goodness of the fit. The obtained parameters for this spectrum are given on the top left in the top panel.

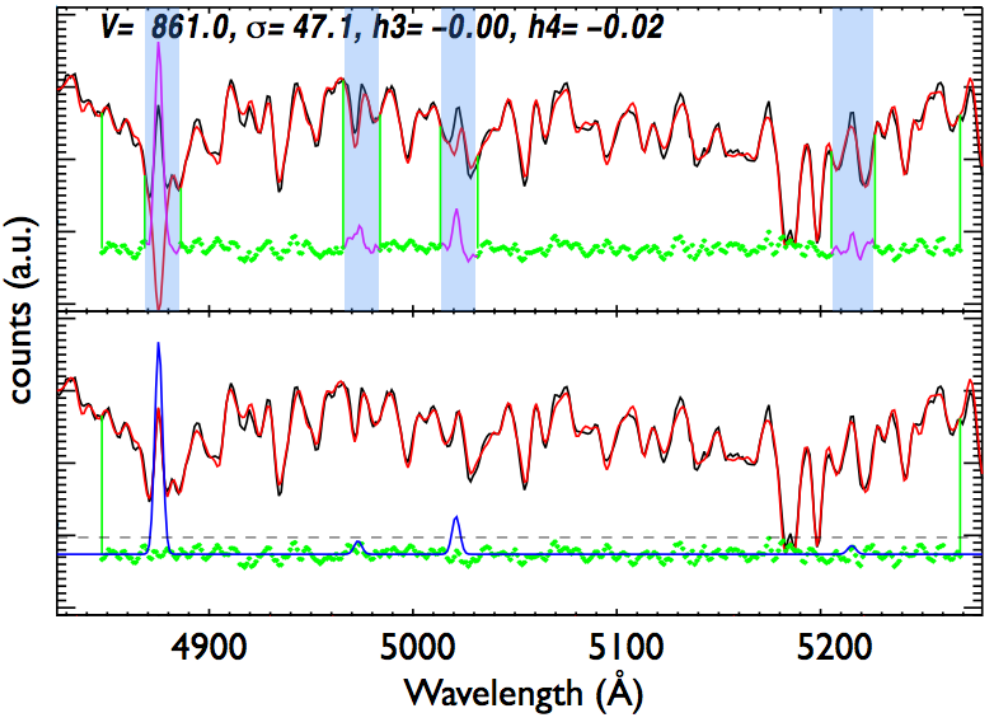

FIGURE 3.1: A spectra of the disc region of NGC 4394 is shown to illustrate the process of pPXF. The top panel shows the spectrum of the galaxy (black), a model fit (red), residuals of the areas fitted (green) and indications of the masked areas where emission lines are present (marked with pink lines and blue transparent columns). The obtained parameter for stellar velocity (including the systemic velocity), velocity dispersion and Gauss-Hermite moments are given on the left. The panel below shows the fits of the emission lines using `GANDALF` (see section 3.2.2 for details). The emission lines are shown as additional gaussians in blue, the rest remains the same.

For the BaLROG sample, we also calculated the value of the specific stellar angular momentum λ_R (Emsellem et al. 2007; and see equation 4.4 in section 4.2.3) from the stellar velocity and velocity dispersion. This calculation was done radially but also integrated within $1\,r_e$. Using the code developed by Maciejewski, Emsellem & Krajnović (2012), we furthermore obtained the radial and tangential velocities V_r and V_t for a subset of our sample (see Section 4.1.2 for more details).

3.2.2 Emission lines

The measurement of the stellar population parameters requires the removal of the ionised emission present in the spectra. This is particularly important in the Balmer lines (i.e. Hγ and Hβ) present in our wavelength range, which are the key features determining the age of the stellar population.

We use the Gas AND Absorption Line Fitting (`GANDALF`) package by Sarzi et al. (2006) and Falcón-Barroso et al. (2006) to obtain the ionised-gas distribution and kinematics. The emission lines are treated as additional Gaussian templates on top of the stellar continuum and the code iteratively looks for the best match of their velocities and velocity dispersions.

The SAURON wavelength range allows us to measure the emission line of H$\beta\lambda$4861 and the doublets [OIII]$\lambda\lambda$4959, 5007 and [NI]$\lambda\lambda$5200, 5202. The WiFeS spectra contain the same and a few additional lines. For the blue-arm spectra, we could measure the following emission lines: H$\gamma\lambda$4341, H$\beta\lambda$4861 and the doublets [OIII]$\lambda\lambda$4959, 5007 and [NI]$\lambda\lambda$5200, 5202.

In both cases, we tyed spectral lines kinematically to lower the number of free parameters given to `GANDALF`. For the BaLROG sample, we always chose to tye spectral lines to the [OIII] doublet. For the WiFeS data, we chose the strongest lines in each case: in NGC 5701, we fixed the kinematics of the emission lines to the [OIII] doublet and in NGC 6753 and NGC 7552, we fixed the emission line kinematics to the Hβ line instead. We checked that leaving them free resulted in a consistent outcome.

Furthermore, we imposed known relative flux relations to constrain the freedom of the doublet lines during the fitting process. For the BaLROG sample the only relation was: $F([\mathrm{OIII}]_{4959}) = 0.350 \cdot F([\mathrm{OIII}]_{5007})$. For the WiFeS dataset, we also used the following equation relating the two Balmer lines: $F(\mathrm{H}_\gamma) = 0.469 \cdot F(\mathrm{H}_\beta)$ (Osterbrock & Ferland, 2006).

An illustration of the resulting emission lines to clean the spectra is given in Fig. 3.1 in the bottom panel. The clean spectrum can be seen in Fig. 3.2.

We thus used our results from `GANDALF` to *clean* the spectra of our galaxies and produce emission-line-free datacubes for our stellar population analysis.

3.3 Stellar populations

While resolving stellar populations would be ideal (instead of integrated light), this is limited to only a few galaxies within the Local Group (e.g. Tolstoy, Hill & Tosi, 2009; Frebel et al., 2010). Therefore integrated spectra and especially colours are usually employed. Thanks to technical developments during the last decade, the separation of stellar and gas contributions in the spectra could be achieved (e.g. Sarzi et al., 2006) and due to better instrumentation, fainter (sub-)structures could be revealed (e.g. MacArthur, González & Courteau, 2009; Pérez & Sánchez-Blázquez, 2011; Sánchez-Blázquez et al., 2011). Furthermore, major developments in stellar population analysis techniques coupled with the improved calibration and extension of spectral stellar libraries (e.g., STELIB, Le Borgne et al. 2003; MILES, Sánchez-Blázquez et al. 2006b; Indo-US, Valdes et al. 2004; CaT, Cenarro et al. 2001a,b) have pushed stellar population analyses forward.

In our work with the BaLROG sample, we will use the classical method of line-strength indices to derive single stellar population (SSP) parameters. The analysis of the WiFeS dataset will also benefit from this technique and even go a step further. For this study, we also chose to use a full-spectrum fitting technique described in Sec. 3.3.3.

3.3.1 Line-strength indices

To start analysing the stellar content we focus on the classical approach of using absorption line-strength (LS) indices measured on observed spectra. These indices can be compared with those computed via single stellar population (SSP) models in order to derive stellar population parameters from integrated spectra (e.g., Faber, 1973; Davies, Sadler & Peletier, 1993; Worthey et al., 1994; Vazdekis, 1999; Thomas et al., 2005; Sánchez-Blázquez et al., 2006a; Kuntschner et al., 2006; MacArthur, González & Courteau, 2009; McDermid et al., 2015).

The most commonly used method to probe the luminosity-weighted age, metallicity and abundance ratios of specific elements is the measurement of Lick/IDS indices in the Lick system. This system suffers, however, from intrinsic uncertainties due to a multi-object and multi-instrument approach leading to an inhomogeneous spectral resolution (Vazdekis et al., 2010). To avoid those and profit from flux-calibrated spectra with a constant resolution as a function of wavelength, we chose to measure the absorption line strengths in the Line Index System at 8.4 Å (LIS-8.4Å) (Vazdekis et al., 2010). For several galaxies however (namely NGC 2859, NGC 2962, NGC 4262, NGC 4267 and NGC 4643 for BaLROG and NGC 6753 in the WiFeS dataset), a few central spectra reach up to ≈9 Å which exceeds the 8.4 Å value. Testing the resulting effect, we found that this would lead to a shift of ≈0.02 Å in Hβ and ≈0.05 Å in Mgb. This corresponds to a difference of 1.5 Gyr in age from our measured value which is well within our uncertainties for old populations. Given this small effect, and for simplicity, we chose to not convolve the data further and use the models at 8.4 Å. We made sure that this is not affecting any of our conclusions.

Within the wavelength range of SAURON we can detect the following lines and measure their strengths: Hβ as an age indicator, Mgb and Fe5015 as proxies for metallicity. Figure 3.2 shows a disc spectrum of NGC 4394, emission-line-cleaned and broadened to 8.4 Å. The three bandpasses are indicated.

In addition, we also combine the Mgb and Fe5015 indices to obtain the [MgFe50]' index following Kuntschner et al. (2010):

$$[\mathrm{MgFe50}]' = \frac{0.69 \times \mathrm{Mg}b + \mathrm{Fe5015}}{2} \tag{3.2}$$

This combined iron-magnesium index is almost insensitive to the [Mg/Fe] overabundance (e.g., Kuntschner et al., 2010). For our analysis, we relate the index measurements to MILES model predictions (Sánchez-Blázquez et al., 2006b; Vazdekis et al., 2010; Falcón-Barroso et al., 2011).

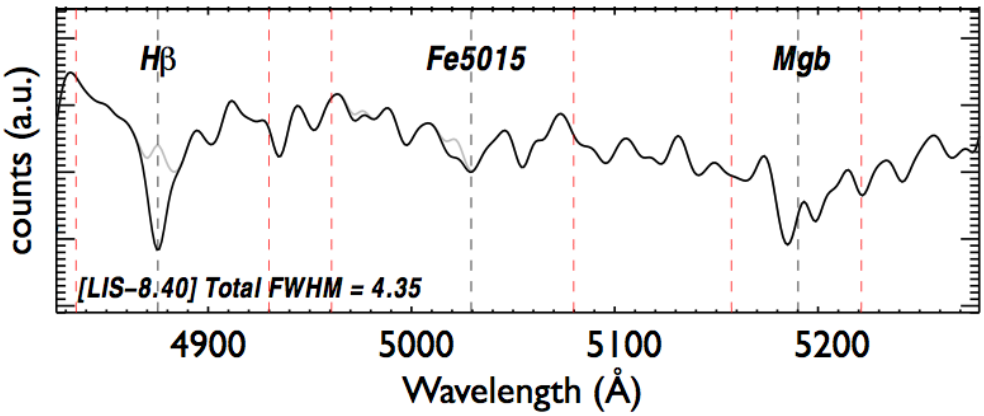

FIGURE 3.2: The line-strength measurements are computed from the emission-line-cleaned spectra. This is the same spectrum as shown in Fig. 3.1, but brought to 8.4Å (as indicated in the lower left corner, along with the maximum FWHM detected for this spectrum before raising it to 8.4Å). The central bandpasses for H_β, Fe5015 and Mg*b* are shown as gray dashed lines and their continuum areas as red dashed lines. The parts where corrections for emission lines have been made are shown as gray lines deviating from the galaxy spectrum (black).

In the study with WiFeS, we were able to measure more indices due to a larger wavelength and two arms. The following indices could be investigated only from the blue grating: Ca4227, G4300, HγA, HγF, Fe4383, Ca4455, Fe4531, Fe4668, Hβ, Hβ_o (Cervantes & Vazdekis, 2009), Fe5015, Fe5270, Mg*b*, Fe5270, Fe5335 and Fe5406. From the red grating, we also determined indices following Cenarro et al. (2001a): CaT, CaT*, and PaT with Ca1($\lambda\lambda$8484.0-8515.0), Ca2($\lambda\lambda$8522.0-8562.0), Ca3($\lambda\lambda$8642.0-8682.0), Pa1($\lambda\lambda$8461.0-8474.0), Pa2($\lambda\lambda$8577.0-8619.0) and Pa3($\lambda\lambda$8730.0-8772.0). While we only made use of some of them to derive our results, we provide a summary of all maps for each galaxy for BaLROG and WiFes, in both gratings, in the appendix.

In the presentation of our results for the WiFeS dataset in Chapter 6, we only use the Hβ_o, Mg*b*, Fe5270 and Fe5335 index maps to determine the stellar population parameters. Further, we specifically combine the Mg*b*, Fe5270 and Fe5335 indices to obtain the [MgFe]' index (e.g. Thomas, Maraston & Bender, 2003), which is almost insensitive to [Mg/Fe] variations.

We obtain the mean luminosity-weighted age and metallicity by employing the `rmodel`[1] code (Cardiel et al., 2003). Here we use the Hβ index as a proxy for age (Hβ_o for the WiFeS data) and we implemented the combined iron-magnesium index, as given above, as a proxy for metallicity. We represent our results in index-index diagrams with the MILES SSP models for different ages and metallicities overlaid, compute gradients and average values for different regions in the galaxy. Throughout this work we assume a Kroupa initial mass function (IMF, Kroupa, 2001).

In the BaLROG study, we use the difference of the metallicities of magnesium and iron (denoted as [Z_{Mg}-Z_{Fe}] in our work) to determine a proxy of the overabundance [Mg/Fe]. Even though a linear relation between [Mg/Fe] and [Z_{Mgb}-Z_{Fe5015}] exists (Peletier et al., 2007; Vazdekis et al., 2010), the absolute

[1] http://www.ucm.es/info/Astrof/software/rmodel/rmodel.html

value of our measurements cannot be compared directly with literature values because most other authors take combined iron indices into account. Due to the limited SAURON spectral range, we are however restricted to the above proxy (which has been successfully used in former SAURON and ATLAS3D studies). For the WiFeS study, we could indeed implement other iron indices and the details of this study are presented in Sec. 6.2.2.

We are conscious about the simplification and hence introduced bias when representing the stellar populations by an SSP (e.g., Serra & Trager, 2007). Therefore, this method has been commonly used in galaxies where variations in the locally averaged ages and metallicities are expected to be minimal, but has also been performed on systems with extended star formation histories (e.g., Peletier et al., 2007; Ganda et al., 2007). In particular, this classical approach provides luminosity-weighted population parameters which are valuable for our study of the BaLROG sample: bars are prominent structures seen visually, as an additional luminous component. Therefore, we restrict our analysis in this work to the index measurements and SSP parameters derived from the former, hence analyzing the light-weighted values.

In the WiFeS study, we specifically tested the limitations of the LS analysis, summarized in the next Chapter. Furthermore, we employed a full-spectral fitting technique in order to derive star formation histories (SFH), see Sec. 3.3.3.

3.3.2 Limitations of the LS analysis

During our analyses, we dealt with various types of galaxies, most of which are suspected to be composed out of multiple stellar populations. This obviously is a drawback of the SSP analysis with line-strength indices. For certain galaxies, we therefore observed interesting behaviours in the index-index diagrams. Here we illustrate with an example of the WiFeS study some of the limitations that can be encountered using the index-index analysis.

So, in order to explain the points outside the grid for NGC 6753 seen in Fig. 6.4, we combined different single stellar population models, changing their weights, ages and metallicities, similar to Fig. 8 in Kuntschner (2000). We use the same SSP MILES models which we use for the SSP grid[2]. From the individual spectra for a certain age and metallicity for each population, we create a final spectrum which we analyze using the same line-strengths indices routine which we apply to the galaxy spectra. When combining the spectra, we impose the contribution in light per population. In the two test cases we show here, we chose two different metallicities for the young population: 0.00 and 0.22 dex, and two ages: 1.00 Gyr and 1.26 Gyrs, and the following weighting scheme:

- 100% young stars
- 50% young and 50% old stars
- 20% young and 80% old stars
- 10% young and 90% old stars

[2]http://miles.iac.es/pages/webtools/get-spectra-for-a-sfh.php

- 5% young and 95% old stars
- 1% young and 99% old stars
- 100% old stars

Fig. 3.3 summarizes the test outcome when combining an old (≈ 12.5 Gyr) population with solar metallicity (left column) with the two different young populations of each two different metallicities. On the right plot, we show the same, just with the older population having super solar metallicity.

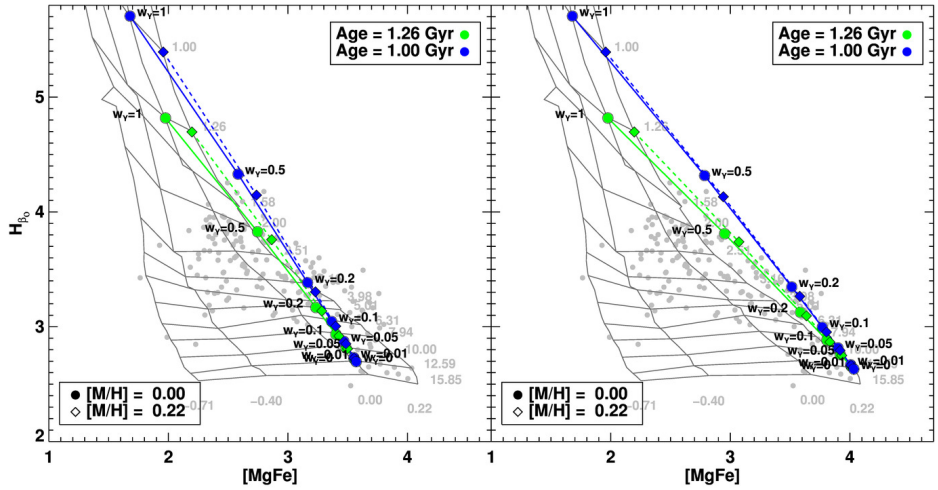

FIGURE 3.3: The influence of the combination of very different sets of stellar populations on the index results. We show model tests in colors: green and blue points indicate age, round symbols solar metallicity and rhombic symbols super solar metallicity. The different fractions of young populations are indicated next to the points, for the 1.00 Gyr population on the right, the 1.26 Gyr, on the left. In addition, we display the index measurements as obtained from NGC 6753 in grey dots. See section 3.3.2 for more details.

We also performed this same analysis weighing the spectra in mass. Here, it was much easier to move points outside the grid. Already very small mass fractions of a young population resulted in a point outside in the measurement of the combination. This is due to the fact that even a small fraction in mass of a young population (∼1-5%, depending on the exact age and its metallicity) will have a strong contribution in light and therefore outshine most of the old population. Since the index measurements are based on luminosity-weighted quantities, we foster our analysis with the L-weighted tests.

3.3.3 Full-spectral fitting

Several inversion algorithms enable the reconstruction of the stellar content from an observed spectrum (e.g. Cid Fernandes et al., 2005; Koleva et al., 2009). Full-spectral fitting techniques allow us to maximize the information encoded in a spectrum as they use the entire wavelength range and they are not limited to some specific absorption features (e.g. line-strength indices).

STECKMAP[3] (STEllar Content and Kinematics via Maximum A Posteriori likelihood, Ocvirk et al. 2006a,b) is a full-spectral fitting code that uses a Bayesian method to simultaneously recover the stellar kinematics and the stellar properties via a maximum a posteriori algorithm. It is non-parametric so it provides properties such as the stellar age distribution (SAD) with minimal constraints on their shape. In addition, the ill-conditioning of the inversion is taken into account through explicit regularization.

In practice, the code determines a linear combination of single stellar population models trying to reproduce the observed spectrum projected onto a temporal sequence of these SSP models. The weights used for the linear combination give the SSP fractions and create the according star formation history associated to the spectrum. Thus, the code does not take any a priori assumption to create the SFHs apart from imposing a smooth solution for the unknown parameters, namely the stellar age distribution, the age-metallicity relation and the line-of-sight velocity distributions or broadening function, which is supposed to avoid un-physical solutions. To achieve this, the code uses certain smoothing parameters whose choice is important, but not sufficiently enough to significantly influence the overall outcome (i.e. main features) of the SFHs, as well as the derived mean values of ages and metallicities. This has been tested in many former works, (e.g. Ocvirk et al., 2006a,b; Ocvirk, Peletier & Lançon, 2008; Koleva et al., 2008; Sánchez-Blázquez et al., 2011; Koleva et al., 2011; Sánchez-Blázquez et al., 2014a).

For this work, we use the emission-cleaned spectra coming from the GANDALF analysis following the same Voronoi scheme outlined above. We shift the spectra to rest frame according to the stellar velocity (see Sec. 6.1.1) and broadened them to 8.4 Å. We fix the stellar kinematics and fit exclusively for the stellar content in order to avoid the metallicity-velocity dispersion degeneracy reported by Sánchez-Blázquez et al. (2011).

As in the previous section, we use the MILES models as the reference templates with the following range of ages and metallicities: 63 Myrs to 17.8 Gyrs and -2.32 < [Z/H] < +0.2 respectively. We also keep using the Kroupa Universal IMF. The chosen age range can obviously lead to outputs of ages older than the age of the Universe, but in line with globular cluster ages. Several former studies have investigated this zero point problem (e.g. Vazdekis et al., 2001; Schiavon et al., 2002; Vazdekis et al., 2010; Maraston & Strömbäck, 2011) and in order to not artifially bias our outcome, we use the entire range of models available, which is also usually done in SP studies.

Once we obtain the star formation history of a given spectrum, we compute the luminosity- (L) and mass-(M) weighted age and metallicity (both represented by q) as follows:

$$\langle q \rangle_M = \sum_i mass(i) q_i / \sum_i mass(i), \tag{3.3}$$

$$\langle q \rangle_L = \sum_i flux(i) q_i / \sum_i flux(i). \tag{3.4}$$

[3] http://astro.u-strasbg.fr/?ocvirk/

In order to obtain the value of metallicity with respect to solar metallicity $Z_{\odot}$=0.02 we use:

$$[M/H]_L = -2.5 \log_{10}(Z_L/Z_{\odot}) \tag{3.5}$$

$$[M/H]_M = -2.5 \log_{10}(Z_M/Z_{\odot}) \tag{3.6}$$

The comparison of the stellar properties from the line-strength indices and the full-spectral fitting will allow us to better understand the limitations of the classical method, i.e. assess the two-fold bias of the indices results proposed by Serra & Trager (2007).

4

The BaLROG project I: The influence of bars on the kinematics [1]

Imagination is more important than knowledge.
Knowledge is limited.
Imagination encircles the world.
Albert Einstein

Unraveling the nature of bars and their influence on their host galaxies is one of the major aims of this thesis. In this Chapter, we present the results from the *BaLROG* (Bars in Low Redshift Optical Galaxies) sample, consisting of 16 morphologically distinct barred spirals, in order to characterise observationally the influence of bars on nearby galaxies. Each galaxy is a mosaic of several pointings observed with the IFU spectrograph SAURON leading to a tenfold sharper spatial resolution ($\sim$100 pc) compared to ongoing IFU surveys. In this chapter we focus on the kinematic properties. We calculate the bar strength Q_b from classical torque analysis using 3.6 μm *Spitzer* (S^4G) images, but also develop a new method based solely on the kinematics. A correlation between the two measurements is found and backed up by N-body simulations, verifying the measurement of Q_b. We find that bar strengths from ionised gas kinematics are $\sim$2.5 larger than those measured from stellar kinematics and that stronger bars have enhanced influence on inner kinematic features. We detect that stellar angular momentum 'dips' at 0.2$\pm$0.1 bar lengths and half of our sample exhibits an anti-correlation of h_3 - stellar velocity (v/σ) in these central parts. An increased flattening of the stellar σ gradient with increasing bar strength supports the notion of bar-induced orbit mixing. These measurements set important constraints on the spatial scales, namely an increasing influence in the central regions (0.1-0.5 bar lengths), revealed by kinematic signatures due to bar-driven secular evolution in present day galaxies.

[1] The majority of this chapter is based on the article: *The BaLROG project - I. Quantifying the influence of bars on the kinematics of nearby galaxies.* Seidel, M. K., J. Falcón-Barroso, I. Martínez-Valpuesta, S. Díaz-García, E. Laurikainen, H. Salo and J. H. Knapen. 2015, MNRAS, 451, 5455.

4.1 Bar strength measurements

Bar strengths have been measured in many different ways (see introduction for details). For our analysis we will concentrate on the following two methods: (1) the photometric torque Q_b taking advantage of the S^{4}G data and (2) a new measurement based on the stellar velocity maps which does not include strong model assumptions (Q_{kin}).

4.1.1 Photometric torque using 3.6 μm *Spitzer* imaging (Q_b)

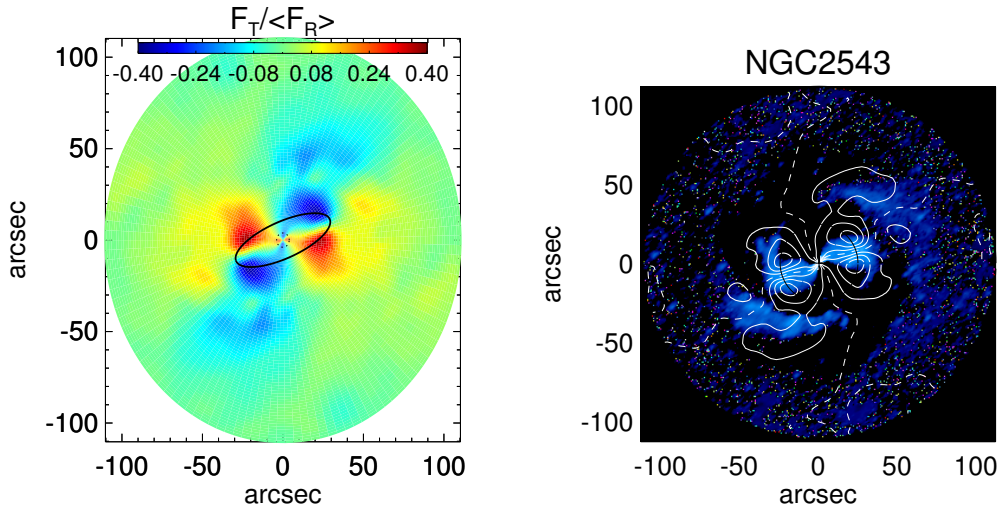

FIGURE 4.1: *Left panel*: Gravitational torque map of NGC 2543 derived from *Spitzer* image using only even Fourier components. In the top of the panel a colour bar shows the maximum and minimum Q_G; Bar length and ellipticity are traced with a black solid line; The inner dotted circle corresponds to the S^{4}G Pipeline 4 r_e of the bulge. *Right panel*: Fourier smoothed density with the axisymmetric component ($m = 0$) subtracted; Contours of equal Q_G are overplotted in white; The dotted lines indicate the regions where the tangential forces change sign.

We calculated the gravitational potential of our galaxies from the 3.6 micron images, using the NIRQB code (Laurikainen & Salo, 2002) based on the polar method developed in Salo et al. (1999). Before applying the Fourier transformation, the *Spitzer* images are rectified to face-on. Then, the even Fourier components (up to 20) of the surface density $I(r, \phi)$ are calculated within a polar grid. The gravitational potential $\Phi_m(r, \phi)$ is then inferred from the smoothed surface densities by applying a fast Fourier transformation in the azimuthal direction in combination with a direct summation over radial and vertical directions. We use a polar grid with 128 bins in the azimuthal direction, which determines an angle step-size for the azimuthal Fourier transform of $2\pi/128 = 2.8°$.

The calculation of the potential is based on the following assumptions:

1. The mass-to-light ratio is constant.
2. The disc vertical scale height h_z is constant.
3. The disc has an exponential vertical density distribution:

$$\rho_z(z) = \frac{1}{2h_z} exp(-|z/h_z|). \quad (4.1)$$

4. The vertical scale height of the disc scales with the disc size as $h_z = 0.1\ r_{k20}$, where r_{k20} is the 2MASS (Skrutskie et al., 2006) $K-$band surface brightness isophote of 20 mag arcsec^{-2}.

Tangential ($F_T(r,\phi)=\frac{1}{r}\partial\Phi(r,\phi)/\partial\phi$) and radial forces ($F_R(r,\phi)=\partial\Phi(r,\phi)/\partial r$) are obtained via integration. Non-axisymmetric forces in the galaxy are characterised by the ratio of the tangential force to the mean axisymmetric radial force field:

$$Q_G(r,\phi) = F_T(r,\phi)/\langle F_R(r)\rangle, \quad (4.2)$$

where $\langle F_R(r)\rangle$ is the azimuthally averaged radial force at a radial distance r. $Q_G(r,\phi)$ values are used to construct the gravitational torque maps of our galaxies (see example in Fig. 4.1). Typically, barred galaxies show a well-defined four-quadrant Q_G map, resembling a *butterfly pattern*, which is roughly symmetric with respect to the bar major axis. We take the even Fourier components uniquely (focusing on bi-symmetric structures) and we symmetrise our maps, reducing in this way the impact of sharp density clumps.

Based on the torque maps, and given a certain radial distance r and quadrant q, one can identify a maximum $Q_T(r)^q = \max(Q_G(r,\phi)^q)$. We calculate the radial profile of the relative strength of the non-axisymmetric perturbations throughout the galaxy, $Q_T(r)$, taking the mean of these four maxima. For additional information about the method, see Salo et al. (2010). Finally, the gravitational torque parameter (Q_b) corresponds to the maximum value of Q_T at the bar region.

The main source of uncertainty ($\approx$15%) is the poorly known vertical thickness: to account for this we have used different disc thicknesses in the calculation of the gravitational field. A small systematic error is produced by the omission of the dark halo contribution on the radial forces, but this is likely to be smaller than that associated with the vertical thickness (Díaz-García et al., submitted.)

4.1.2 Kinematic torque (Q_{kin})

In order to perform a model-independent measurement and to test the torque measure of Q_b we developed a new method solely using the kinematics, resulting in a new parameter which we call the kinematic torque Q_{kin}. The basis of this analysis is the stellar velocity field. Using this map, we extracted the radial and tangential velocities following Maciejewski, Emsellem & Krajnović (2012), using their equations 9 and 10. This method is based on assuming a thin disc geometry to obtain the two velocity components in the equatorial plane. Further assumptions in deriving these two quantities are:

1. A steady state bar, hence not in buckling phases or alike.

2. A symmetric bar with respect to its major axis.

3. A thin galaxy disc resulting in only two velocity components.

As the buckling phase is only a brief evolutionary stage of the bar (e.g. Shen & Sellwood, 2004; Martinez-Valpuesta, Shlosman & Heller, 2006), it is much more likely to observe bars in their steady state. Under the presence of spiral structure, the bar will lose its symmetry with respect to the major axis, but only at the very edges of the bar. An aspect to consider is that prominent bulges will break the third assumption in the inner regions of the bar. Following these limitations, one can conclude that the most reliable region is within the middle of the radial extension of the bar, where we expect to measure the strongest radial velocities and corresponding torques, as outlined below. In addition to these assumptions, the technique developed by Maciejewski, Emsellem & Krajnović (2012) requires the knowledge of the systemic velocity, galaxy inclination, position angle of the line-of-nodes, the bar position angle and bar length. We estimated those from the literature and close inspection of our own datasets. Furthermore, we rectified our maps to face-on in order to apply the technique.

Using the extracted radial and tangential velocities, we defined a new parameter (Q_{kin}) that measures the torque directly from the observed kinematics:

$$Q_{kin} = \frac{\max(v_{rad}(R))}{\langle abs(v_{tan,R})\rangle}, \tag{4.3}$$

where we first find the radial position of the maximum value of the radial velocity (v_{rad}), and then determine the corresponding tangential velocity (v_{tan}) as the mean value in a ring around this radius. This relation is constructed analogous to the calculation of Q_b based on the fact that v_{rad} is proportional to $F_T/F_R \times v_{rot}$ and v_{tan} roughly equal to v_{rot}. Therefore v_{rad}/v_{tan} is expected to be proportional to F_T/F_R (note that the ratios do not have to be equal, but only proportional). Figure 4.2 shows the radial (left) and tangential (right) velocity maps (top) and radial (bottom) distribution for NGC 2543 as an example. The position of the maximal radial velocity is found by evaluating the radial velocity field in rings. We expect a certain velocity modulation when tracing a circle through the four quadrants, i.e., combination of sine and cosine curves when tracing the radial velocity in a ring. This additional aspect helps us to detect and correct for outliers, i.e., unreal peaks or drops of extremely high or low values, which appear more often in the kinematic data due to higher noise levels. Hence, we avoid to simply measure the maximum which would lead to an incorrect result. A smooth version is then obtained by fitting a polynomial. In the bottom panels, we show the curves obtained when measuring the amplitudes of the modulation (red and smoothed fit in blue) compared to the individual data points (grey). It is obvious that there is a significant scatter among the individual points, but nevertheless a clear maximum can be distinguished in the radial velocity profile which is well captured with the modulation.

To further constrain the measurement, we evaluated Q_{kin} within the bar region as determined from the S^{4}G images. This is to avoid choosing areas where high values appear, either due to higher noise levels towards lower surface brightness areas, or due to spiral arms. In the example shown in the figure, the strength of the spiral arms can clearly be seen: in a central ≈20 arcsec radius, we detect the signature of the bar, but further out, the field does not become flat but shows other maxima and minima due to the torques exerted by the

spiral arms. Those strong, outer values detected in the radial velocity – and thus the measured torque – is not due to the bar but to the spiral arms in this galaxy. Similar enhancements can also be seen in Fig. 4.1 for the computation of Q_b.

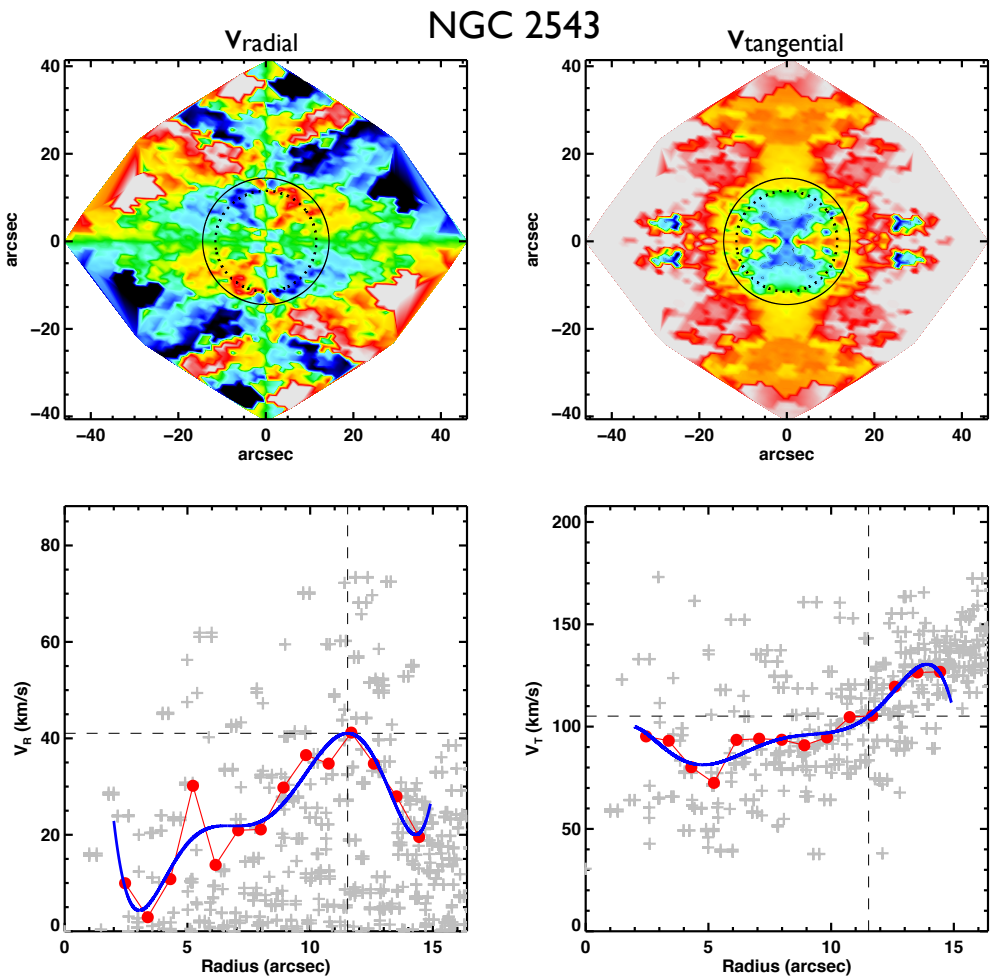

FIGURE 4.2: Radial and tangential velocities for NGC 2543. *Upper left:* radial velocity field, *upper right:* tangential velocity field; in both of them, the continuous circle indicates the bar radius and the dotted circle the radius where we measured the kinematic torque (Q_{kin}). *Lower left:* radial velocity along the radius; *lower right:* radial distribution of the tangential velocity; in both: grey crosses represent individual measurements, red points show the obtained modulation (not a fit to the gray points - see text for details) and the blue a smoothed fit to it. The dashed lines indicate the maximum found in the radial velocity and corresponding to the same radius shown for the tangential velocity (see text for details).

As the value of Q_{kin} depends on the input parameters to determine radial and tangential velocities, we chose to determine its uncertainty via a set of Monte-Carlo simulations. For each realisation, we chose a random combination of initial values of the inclination, line of nodes position angle, bar position angle and bar length, all within their uncertainties. As inclination is the most difficult to determine, we allowed an uncertainty of $\pm 10°$, whereas we chose $\pm 5°$ for the other parameters, leading to an overall uncertainty found in Tab. 4.1. Higher

values would result in simply higher uncertainties in the measured torques.

Unfortunately, the determination of Q_{kin} is only possible when the kinematic major axis and the bar position angle are neither perpendicular nor parallel (at least 5° off, while an angle of 45° would be ideal). It is only under those circumstances that the method of Maciejewski, Emsellem & Krajnović (2012) can be applied to compute the required V_{rad} and V_{tan}. From the 16 galaxies in our sample, we could only measure the kinematic torque (Q_{kin}) on the following 10 systems: NGC 2543, NGC 2712, NGC 2859, NGC 2962, NGC 3504, NGC 4245, NGC 4262, NGC 4394, NGC 5350 and NGC 5701. Results are summarised in Tab. 4.1.

4.2 Observed kinematic properties

This section summarises the different parameters extracted from the kinematic maps of stellar and ionised gas component. Figure 4.3 presents two examples of absorption-line stellar velocity maps and associated radial profiles along the major and minor axis for two galaxies in our sample, NGC 4643 (early-type) and NGC 4394 (late-type). The complete set of kinematic maps, including ionised gas kinematics and Gauss-Hermite moments h_3 and h_4 are collected in Appendix A. Overlaid in all maps, we show the isophotes of the surface brightness (in mag/arcsec^2 with an arbitrary zero point) reconstructed from the SAURON datacubes and equally spaced in intervals of 0.5 magnitudes. In this section, we concentrate on an overview of the general kinematic trends observed in our sample. We also present the bar strength measurements from these kinematics (Q_{kin}), in comparison with the ones derived from the S^{4}G imaging (Q_b).

4.2.1 Stellar and gas kinematics

We investigate the orientation of the stellar and gas kinematics, comparing them to the bar axis, as well as to features that can be linked to bar-driven secular evolution. We use the entire maps as well as cuts along different axes to better unravel certain features.

A first glance at the maps shown in Appendix A reveals that the overall rotation is not strongly affected by the bar (i.e., the kinematic major axis remains almost constant as a function of radius as determined using the method by Barrera-Ballesteros et al. 2014), implying that the bar has not changed the global rotation pattern of the galaxies. We do not detect either large velocity twists in the line-of-nodes (a kinematic feature observed in simulations). Only NGC 2712 and NGC 4394 show small deviations. The absence of this feature in our maps may be due to projection effects or simply to the limited FoV, because the twist is often visible further out, such as in NGC 936 (e.g., Maciejewski, Emsellem & Krajnović, 2012).

Along the kinematic major axis, we do detect in all cases the so-called double-hump rotation curve (local inner maximum followed by a slight drop and further rise) predicted by simulations (Bureau & Athanassoula, 2005), so far mainly confirmed in edge-on systems (e.g., Chung & Bureau, 2004). This feature can be seen in the stellar velocity maps as an enhanced area of high (low) velocity

values on both sides of the nucleus, but is obviously more apparent in the radial profiles. This double-hump is clearly visible in more than 60% of the galaxies in our sample and hints towards the existence of inner discs or rings. Along the minor kinematic axis, we also find a similar distortion in the very central parts, visible as a small-scale wiggle in the minor axis rotation profile. This profile is normally expected to be flat with a value around zero, but it appears to be present for all cases. This small feature might indicate a non-perfect estimation of the global photometric position angle of the galaxies.

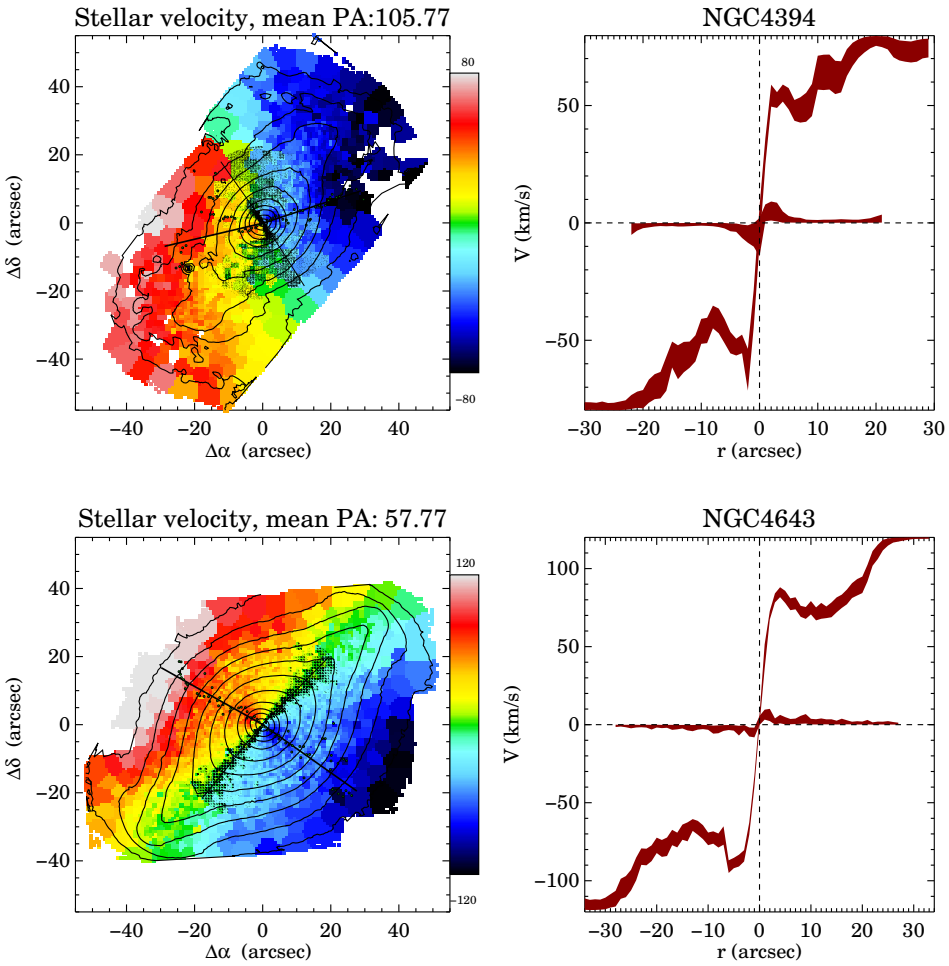

FIGURE 4.3: Stellar velocity maps and their associated major axis profile for two galaxies. The colour bars on the side each indicate the range of the parameter measured. The isophotes shown are derived from the SAURON cube reconstructed intensities and are equally spaced in steps of 0.5 magnitudes. The kinematic position angle, based on Barrera-Ballesteros et al. (2014), is given on the top. The dots indicate the bins used for determining that angle. The black lines indicate the photometric position angle, even better seen in the following figures, not demonstrating the method.

The stellar velocity dispersion maps, and radial profiles, of the two example galaxies NGC 4643 and NGC 4394 are presented in Fig. 4.4. The maps show the presence of $\sigma-$drops, a kinematic feature also predicted by simulations of barred galaxies (e.g., Wozniak et al., 2003). The fraction of galaxies in our

sample that show this behaviour is 62.5%. This is slightly elevated compared to the estimate given by previous works, stating a presence of $\sigma-$drops in up to 50% in disc galaxies (e.g Comerón, Knapen & Beckman, 2008). However, this frequency is not fully determined yet. The early types in our sample show a larger region of overall higher σ than the late types, as expected from the presence of larger central bulge structures. Peak velocity dispersion values range between 100 km s^{-1} and 220 km s^{-1} .

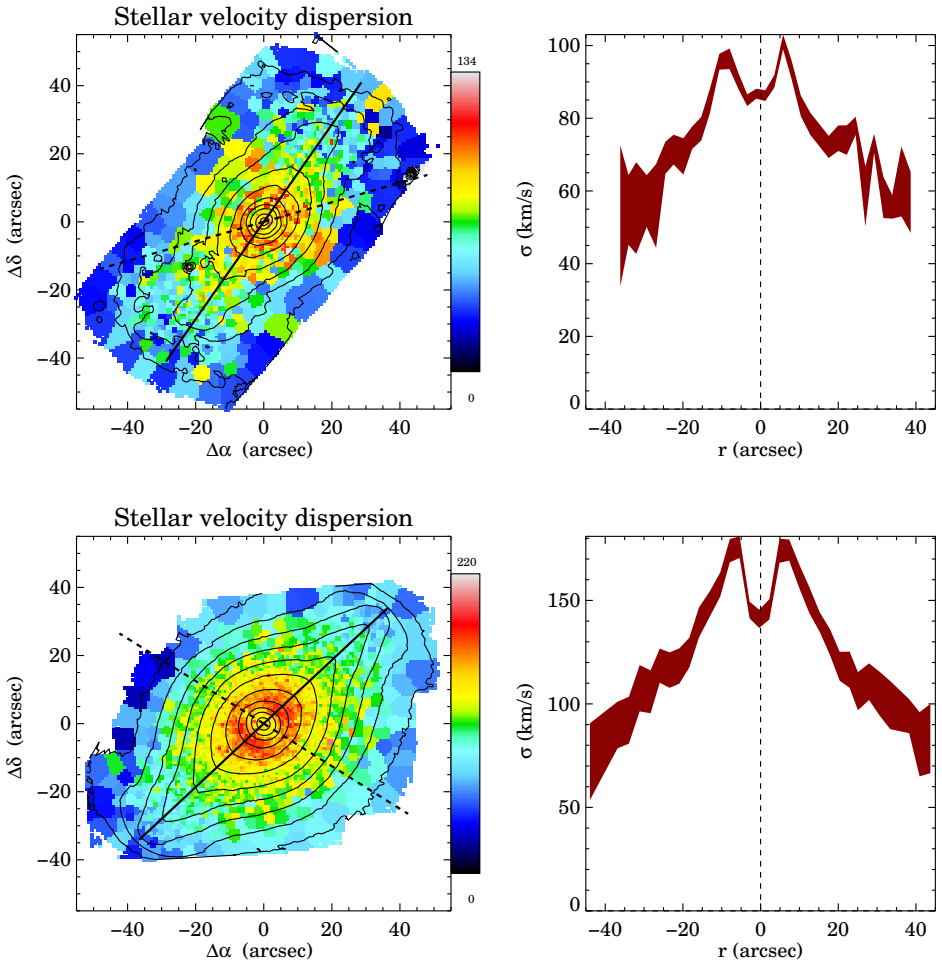

FIGURE 4.4: Stellar velocity dispersion maps and their associated profile along the bar major axis for the same two galaxies as in Fig 4.3, NGC 4394 and NGC 4643. The colour bars on the side each indicate the range of the parameter measured. The continuous black line shows the bar major axis, determined from the photometry of *Spitzer* images while the dashed line indicates the global photometric position angle found previously.

The corresponding kinematic maps (velocity and velocity dispersion) for the ionised gas are shown in Fig. 4.5 for the two example galaxies, illustrating their difference to the stellar kinematics. The ionised gas maps of the entire sample appear in general less regular with a more patchy distribution, reflecting the gas properties. We do not find gas equally distributed in all the galaxies. The absolute values of minimal and maximal rotation are generally slightly higher for the gas than for the stars in all galaxies. The kinematic major axis of the

gas velocity field has the same orientation as the stellar velocity field. Only one galaxy shows a significant change in orientation, NGC 4262, whereas two others (NGC 2962 and NGC 5701) show very mild differences only.

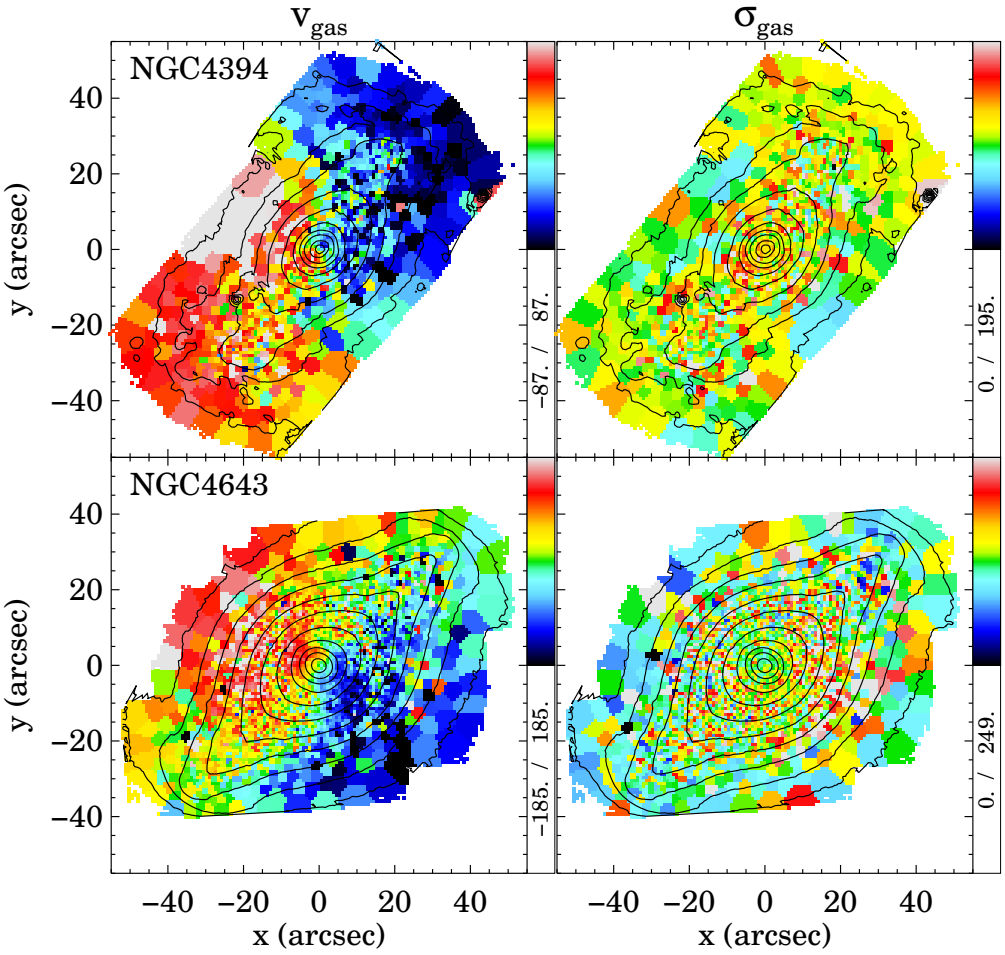

FIGURE 4.5: Velocity and velocity dispersion maps of the ionised gas component for the two examples in the BaLROG sample of galaxies.

Previous studies suggest that NGC 4262 might have been involved in an interaction (Vollmer, Huchtmeier & van Driel, 2005). The gas velocity fields also present the double-hump feature, in some cases significantly more pronounced than in the stellar maps (e.g. NGC 3504). This confirms that the gas is more susceptible to bar-driven processes (e.g., Schwarz, 1981; Ellison et al., 2011; Athanassoula, Machado & Rodionov, 2013). The ionised gas velocity dispersion differs significantly from the stellar σ. It does not show a central elevation (tracing the bulge component) but exhibits slightly higher values throughout the area inside the bar isophotes. However, the pattern is extremely patchy and we lack enough coverage of the disc for a fair comparison between the morphological components. Especially in the late-type systems, some regions display higher velocity dispersion in the gas than in the stars. These are typically associated with spiral arms (e.g. NGC 3504, NGC 4394).

We will link the investigated features to the strength of the bars in Sec. 4.3.2.

4.2.2 Gauss-Hermite moments: h_3 and h_4

In addition to the first and second moment of the LOSVD distribution (V, σ), we measured the h_3 and h_4 Gauss-Hermite moments. They help to understand the distribution of orbits along the line-of-sight and can be used to distinguish dynamically distinct regions and thus indicate whether bars influence their formation.

Mathematically, h_3 measures the skewness of the LOSVD, i.e., wings on either side of the peak deviating from the otherwise Gaussian profile, while h_4 is a measurement of the kurtosis (e.g. van der Marel & Franx, 1993). Within our sample, we find a large variety in those maps and just by visual inspection, we cannot identify a systematic pattern which could be attributed to the bars of their host galaxies.

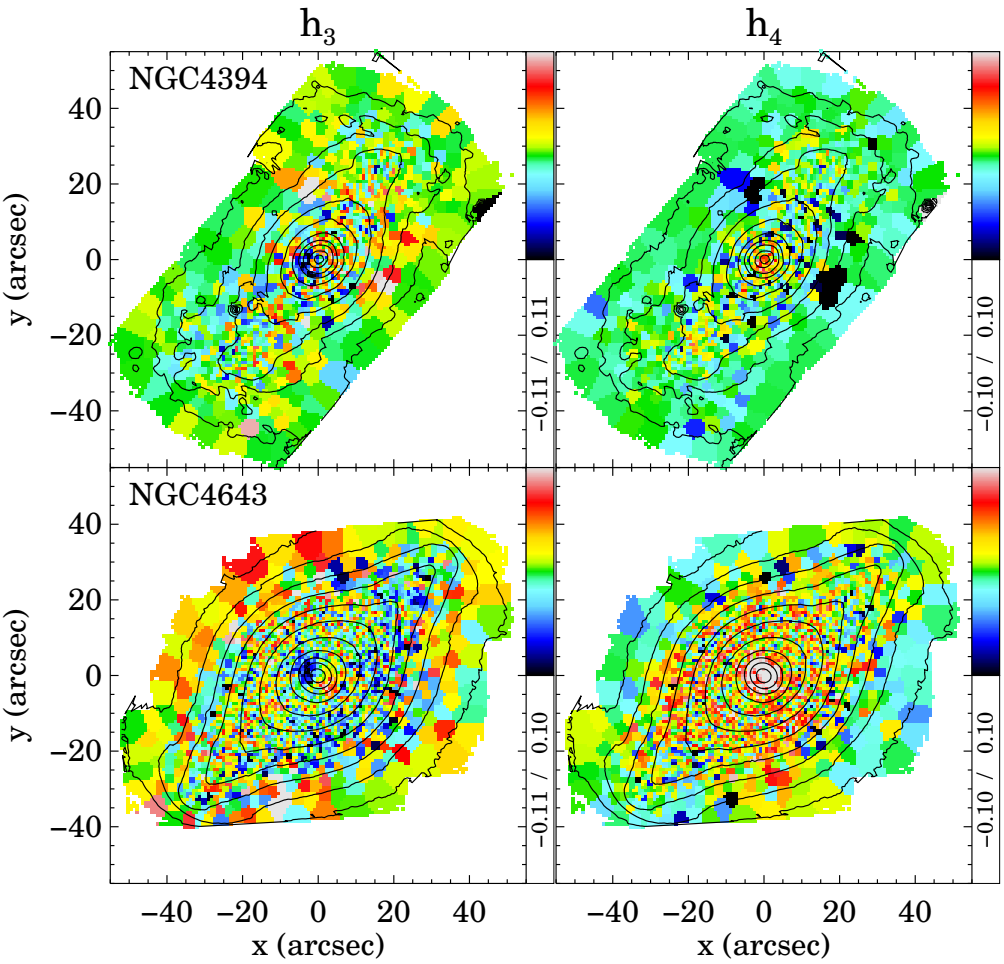

FIGURE 4.6: Gauss-Hermite maps of the stellar component for the two examples in the BaLROG sample of galaxies.

Figure 4.6 shows the two Gauss-Hermite moments h_3 and h_4 for NGC 4394 and NGC 4643. In the first galaxy, the maps appear more uniform than in the second one, which does exhibit low-level structure. However, the majority of the maps of h_3 and h_4 (see more in the appendix) show very low values (below 0.1) and are rather flat throughout the FoV. In several cases a slight anti-correlation between

the h_3 moment and the stellar velocity can be seen (NGC 1015, NGC 2959, NGC 2962, NGC 4245, NGC 4262, NGC 4643 and NGC 5350), while h_4 moments correlate in most cases with the velocity dispersion. We investigated the h_4 profiles along the bar major axis for kinematic signatures of peanut-shaped bulges (e.g., Debattista et al., 2005), but could not detect any clear evidence. This is a property of mainly very low inclined galaxies with strong peanut shapes seen in the photometry, so our sample is not an ideal selection for the detection of this characteristic. So far, only a few studies (e.g., Méndez-Abreu et al., 2008, 2014) have confirmed this prediction.

In the literature, the h_3 moment is often related to the stellar velocity and both correlations and anti-correlations are found (e.g., Bureau et al., 2004). For a more robust measure we chose to correlate h3 with V/σ, shown in Fig. 4.7, in order to compensate for different masses. However, we checked the relation correlating with the stellar velocity alone and did find very similar results. In the figure, Voronoi-binned values within the bar length are shown in black, within 0.5 times the bar length in green and within 0.1 times the bar length in red.

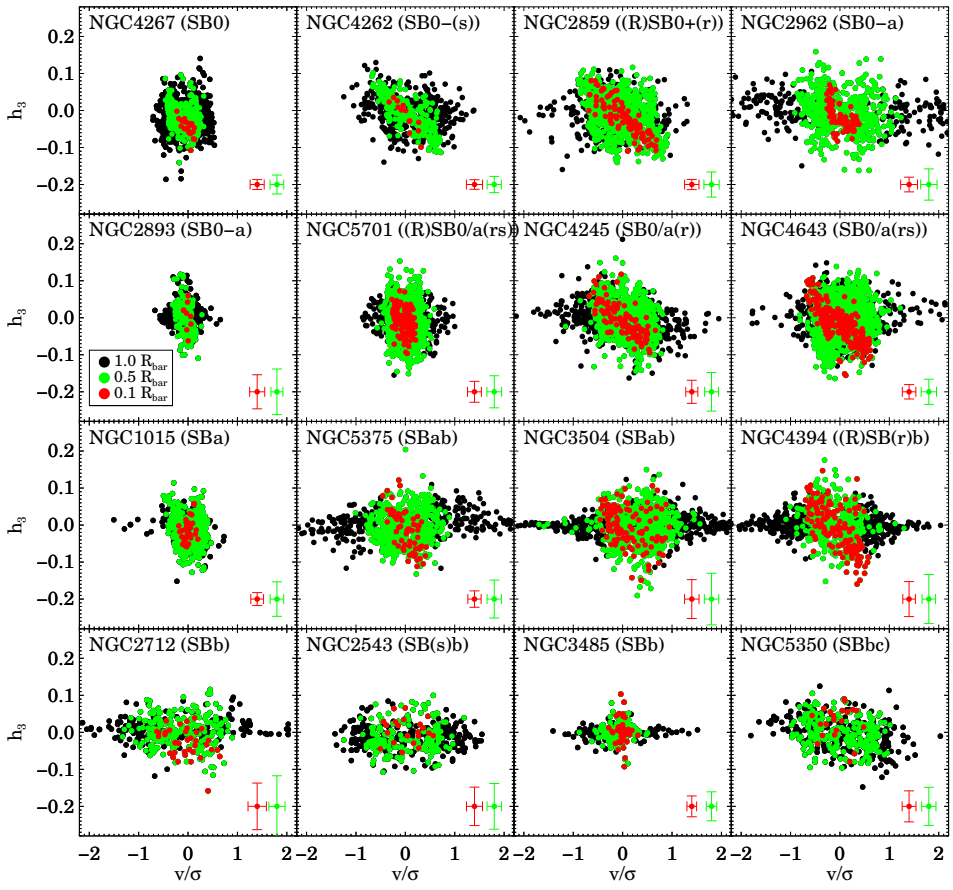

FIGURE 4.7: Individual Voronoi-binned values of h_3 versus the stellar velocity over the stellar velocity dispersion, within 1 R_{bar}, 0.5 R_{bar} and 0.1 R_{bar}. Representative error bars for the red and green regions are indicated in the lower left corner of each panel.

There is no clear (anti-)correlation for the full extent of the bar length (nor for the effective radius, which we tested for comparison, but which is not shown here). However, the more central the aperture, the stronger the anti-correlation for about 50% of our sample, clearly depicted by the red points. The other ∼50% of our sample do not show any (anti-)correlation at all, but a simple spread of h_3 values around zero. This behaviour is consistent across both measures – bar length or the effective radius – with the exception of NGC 4262. The effective radius for this galaxy is significantly smaller and captures the inner part only. Hence, as smaller apertures decreased the scatter if an anti-correlation was present, it stands out better for the effective radius measurement. In many of the other galaxies the effective radius is comparable to the bar length or at least not less than half its size. Overall, we cannot detect a tendency between late or early types, because both late types (e.g. NGC 4394) and early types (e.g. NGC 2859) show the above described behaviour, although with a mild bias towards earlier types showing stronger correlations. In the figure, we ordered the galaxies according to their Hubble type (SB0 top left to SBbc bottom right) and one can appreciate the larger scatter also amongst the innermost (red) points in the bottom row (latest types of our sample). The fact that there is no striking difference though might mean that the Hubble type is not the crucial factor, neither the bar, but the presence of significant substructures. More than 50% of those with strong central anti-correlations have confirmed substructures such as nuclear rings, nuclear lenses or nuclear ring or bar lenses (see classifications by Laurikainen et al. 2011 and Buta et al. 2015).

The influence of bars on building up a central component is supported by this h_3–V anti-correlation in the centres of about 50% of our sample of galaxies. Earlier studies have found a correlation as well as anti-correlation between the stellar velocity and h_3 moment, depending on the area and type of galaxy sampled. In edge-on barred galaxies, Bureau et al. (2004) and Bureau & Athanassoula (2005) detected an h_3–V correlation over the projected bar length, expected for a thick bar. In the centres, however, they also found an anti-correlation in more than 60% of the galaxies. This can indicate the presence of multiple components with different kinematics. Hence a significant number of barred galaxies, not only in edge-on systems but also in our sample of different inclinations, show the presence of cold and dense (quasi-)axisymmetric central stellar discs. This supports the scenario of the bar driving gas towards the centre and nourishing star formation, resulting in this additional central component. The coincidence of a steep central light profile and star-forming ionised gas discs in these same regions (e.g. Bureau & Freeman, 1999) supports this theory further. Falcón-Barroso et al. (2006) also found a link between more intense star forming regions and lower gas dispersion values.

Figure 4.8 shows similar measurements for h_4. The galaxies are again ordered by Hubble type. This parameter measures the symmetric deviation from a Gaussian profile, indicating a velocity distribution which is less (or more) peaked (negative or positive values). It is expected to correlate with the velocity dispersion (van der Marel & Franx, 1993), so we chose to plot it against σ. Overall, but especially for the early types, we observe elevated values in the central regions, most probably associated with the bulge. The presence of higher h_4 values together with an occasional $\sigma-$drop hints at the presence of components

with more recent star formation within a classical elliptical-like bulge component (Wozniak et al., 2003; Bureau & Athanassoula, 2005).

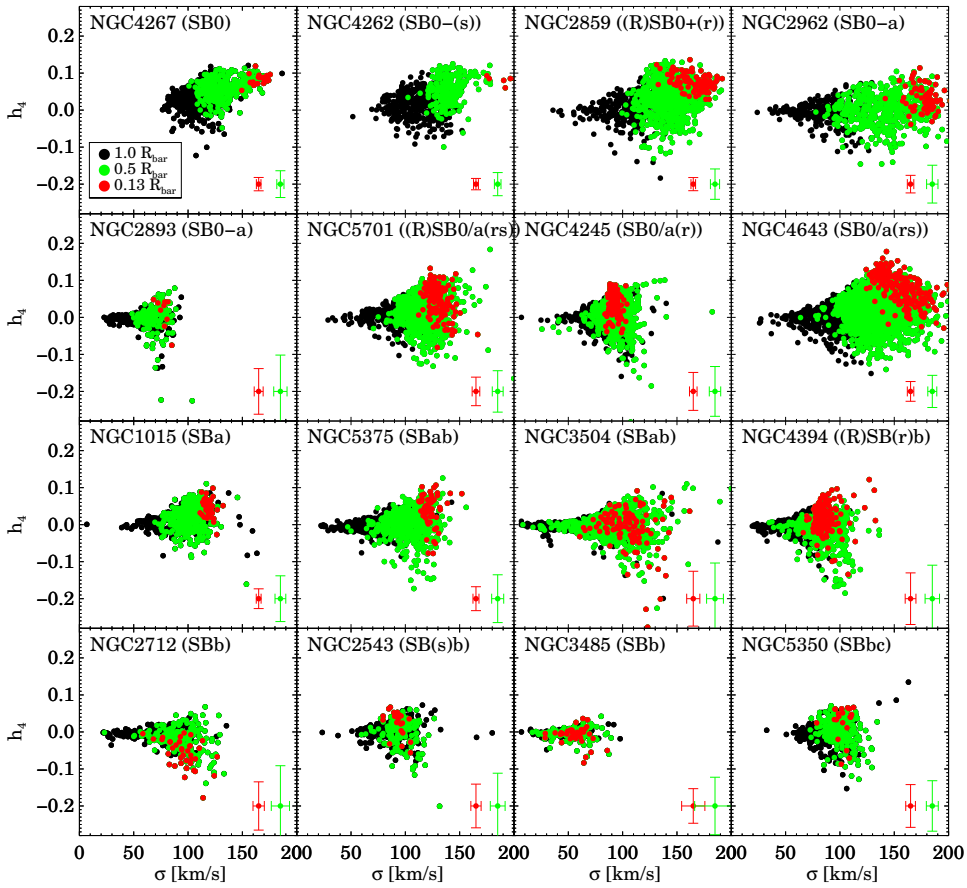

FIGURE 4.8: Individual Voronoi-binned values of h_4 versus the stellar velocity dispersion, within $1\,R_{bar}$, $0.5\,R_{bar}$ and $0.1\,R_{bar}$. Representative error bars for the red and green regions are indicated in the lower left corner of each panel.

In Fig. 4.8, this behaviour stands out even more clearly: a higher velocity dispersion is found in the centres where the red points (corresponding to most central values, i.e., within 0.1 bar lengths) also show elevated h_4 values. Later-type galaxies are clearly different. Not only does the velocity dispersion cover a larger range of values, also the h_4 values are not particularly high in the centre or even go significantly below zero (e.g. NGC 2712, NGC 3504, NGC 3485, NGC 5350, NGC 5875). The bulge in the later-type galaxies is significantly less pronounced, therefore the mixture of more components could cause this spread of h_4 values. The strongest central concentration of elevated h_4 values, at an almost constant σ and h_4, are found in NGC 1015, NGC 2859, NGC 2962, NGC 4262 and NGC 4267. These are not the galaxies showing the h_3–velocity central anti-correlation, but those to have a prominent bulge component. NGC 5701 also has a large bulge, but contains confirmed nuclear spiral structure (Erwin, 2004), which could contribute to the higher spread in h_4.

In conclusion, the analysis of Gauss-Hermite moments suggests that the cen-

ters of barred galaxies (within at least half a bar length, and even more obvious within 0.1 bar lengths) host dynamically distinct components. These could have been altered by bar-driven evolution.

4.2.3 Angular momentum: λ_R

We calculate λ_R as a measure of rotational versus pressure support following the prescription given in Emsellem et al. (2007), as bars are meant to work as engines redistributing angular momentum amongst the different components of a galaxy. This parameter is based on the first two stellar velocity moments and the corresponding flux and is defined as

$$\lambda_R = \frac{\sum_{i=1}^{N_p} F_i R_i |V_i|}{\sum_{i=1}^{N_p} F_i R_i \sqrt{V_i^2 + \sigma_i^2}} \tag{4.4}$$

for two-dimensional spectroscopy, where F_i denotes the flux, R_i the circular radius, V_i the velocity and σ_i the velocity dispersion of the ith spatial bin (going to N_p bins). As outlined in Emsellem et al. (2011), it improves the characterisation of the dynamical state of a galaxy compared to the simple measure of V/σ. It shows a clear difference, especially for non-regular rotators with irregularities in their velocity fields, whilst at the same time being correlated to the specific angular momentum of the stars.

We calculated λ_R in our sample both radially (see Fig. 4.9) as well as within one r_e (λ_{Re}, given in Tab. 4.1). We normalised the radial profiles to the bar radius to test the influence of the bar on the shape of the profile. Considering the small sample size and large variety of Hubble types and bar types, it is not surprising that we recover a variety of profiles. Yet more than 70% show a dip in λ_R at around 0.2 ± 0.1 R_{bar}. The only galaxy which shows a clear offset of this dip is NGC 4262, where the stellar and gas velocity fields are clearly misaligned.

This feature appears to be related to the double-hump in the velocity profile (Bureau & Athanassoula, 2005), in combination with the rise in σ after the $\sigma-$drop. Three galaxies (NGC 1015, NGC 2893, and NGC 5350) do not exhibit a double-hump nor a strong $\sigma-$drop. In other galaxies (NGC 2712, NGC 4267, NGC 4262, NGC 5375), the hump feature in the stellar velocity alone seems to be strong enough to produce the drop in the λ_R profile. In other cases, in particular NGC 4245, NGC 3485 and NGC 5701, the peak of the hump in the velocity profile coincides with the peak of the velocity dispersion profile (after the central drop).

Thus, despite the distinct morphologies and inclinations, we observe a common behaviour and influence on the stellar kinematics. This is likely produced by the bar, since these features seem to accumulate around a similar radius related to the bar length. This feature could probably be associated to the inner Lindblad resonance (ILR) (e.g. Elmegreen, 1994; Pfenniger & Norman, 1990). In fact, in several of our galaxies, nuclear rings have been detected at those locations: NGC 2859 (Erwin & Sparke, 2002), NGC 3504 (Buta & Crocker, 1993; Elmegreen et al., 1997), NGC 4262 and NGC 4245 (Comerón et al., 2010).

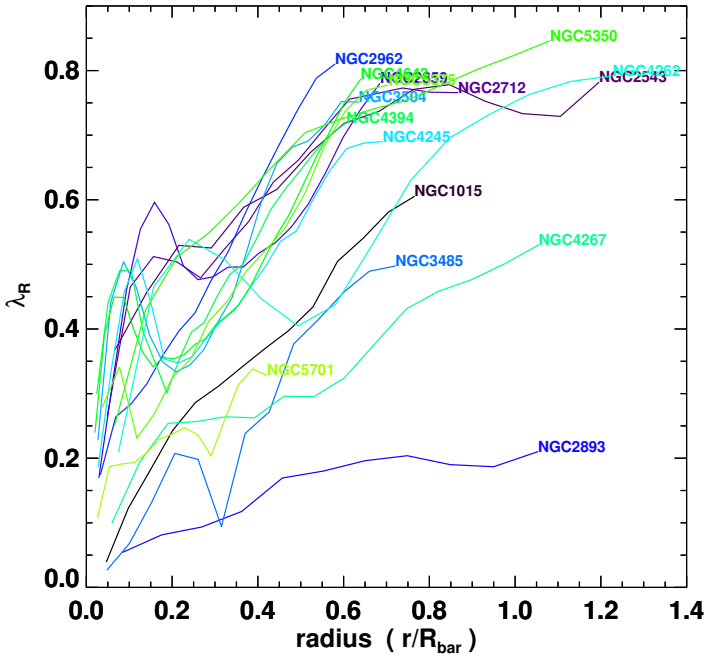

FIGURE 4.9: Radial profiles of λ_R for all galaxies, normalised to the radius of the bar. A rise and consecutive dip is observed at a similar position in the profiles of the majority of galaxies, around 0.2±0.1 R_{bar}.

We also tested the location of the dip as a function of the effective radius of the bulge and the disc scale-length (derived from the S^{4}G) but did not find any correlation. This supports our suspicion that this feature is related to the bar. Similar studies have already related outer ring radii to the bar sizes (e.g., Pérez, Aguerri & Méndez-Abreu, 2012) based on earlier studies and simulations (e.g. Byrd et al., 1994; Buta, Purcell & Crocker, 1995). Comerón et al. (2010) estimate that the maximal possible extension of a nuclear ring should be located at 0.25 bar lengths.

4.3 Contrasting bar strength measurements

In this section we compare bar strength measurements determined according to the descriptions given in Section 4.1. For the case of Q_{kin} we additionally measure it for both the stellar and ionised-gas components. This comparison will allow us to establish the ruler that will be used in Sect. 5.3 to evaluate the impact of bars of different strengths on different kinematic properties of our galaxies.

4.3.1 Q_{kin} from stars and ionised gas

We calculated the kinematic torque (Q_{kin}) from both our stellar and ionised-gas velocity maps (values given in Tab. 4.1). The comparison is shown in Fig. 4.10. The gas is expected to respond more strongly to the bar than the stars. Overall the torque derived from the gas velocity fields is significantly higher than the stellar one. For almost all galaxies it is about 2.5 times greater than the value derived from the stellar velocity maps (dotted line).

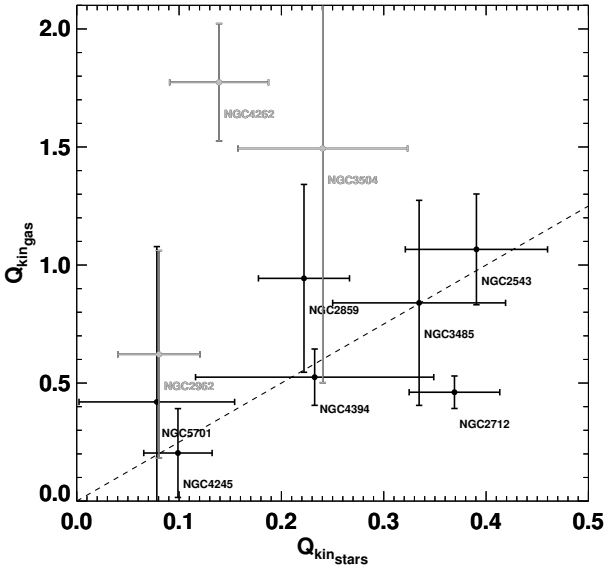

FIGURE 4.10: Kinematic gas torque versus kinematic stellar torque. The dotted line indicates a 2.5-correlation. Grey galaxies show obvious offsets between gas and stellar kinematics.

The grey points mark significantly higher values. Inspecting their gas velocity maps, we detect clear differences from the stellar velocity fields.

TABLE 4.1: Summary of the values obtained for λ_{Re} and the bar strength measurements: (1) NGC number, (2) λ_{Re}, (3) photometric torque, (4) error in the photometric torque, (5) kinematic torque, (6) error in the kinematic torque, (7) kinematic torque of the gas component, (8) error in the kinematic torque of the gas component. As the error of the measure for λ_{Re} is negligible, we do not list it here.

Galaxy	λ_{Re}	Q_b	ΔQ_b	Q_{kin}	ΔQ_{kin}	$Q_{kin,g}$	$\Delta Q_{kin,g}$
(1)	(2)	(3)	(4)	(5)	(6)	(7)	(8)
NGC 1015	0.25	0.26	0.074	-	-	-	-
NGC 2543	0.62	0.36	0.070	0.39	0.069	1.1	0.23
NGC 2712	0.65	0.28	0.044	0.37	0.044	0.46	0.07
NGC 2859	0.37	0.17	0.025	0.22	0.044	0.94	0.40
NGC 2893	0.06	0.16	0.020	-	-	-	-
NGC 2962	0.44	0.14	0.024	0.080	0.040	0.62	0.44
NGC 3485	0.52	0.38	0.064	0.33	0.084	0.84	0.43
NGC 3504	0.29	0.26	0.044	0.24	0.082	1.5	0.99
NGC 4245	0.33	0.18	0.020	0.10	0.033	0.20	0.19
NGC 4262	0.33	0.07	0.012	0.14	0.048	1.8	0.25
NGC 4267	0.24	0.04	0.013	-	-	-	-
NGC 4394	0.46	0.23	0.036	0.23	0.12	0.52	0.12
NGC 4643	0.28	0.28	0.069	-	-	-	-
NGC 5350	0.62	0.44	0.076	-	-	-	-
NGC 5375	0.47	0.23	0.044	-	-	-	-
NGC 5701	0.20	0.18	0.022	0.08	0.076	0.42	0.66

In particular NGC 4262 shows the highest value of $Q_{kin,gas}$. The gas velocity field is counter-rotating with respect to the stellar velocity field. Therefore,

a significant impact due to another process (e.g. galaxy interaction or close encounter) might be at work in this galaxy (see Vollmer, Huchtmeier & van Driel 2005). In NGC 3504, the gas velocity field shows extreme enhancements in the central regions which are not present in the stellar velocity field. It is not clear at this stage what is causing this difference. Overall, we find that the stars seem to be more stable and therefore the stellar kinematic torque agrees better with the photometric torque (see § 4.3.2), whereas the gas is more susceptible to other processes, leading to a larger number of outliers.

4.3.2 Kinematic vs photometric bar strengths

Figure 4.11 (left panel) compares the kinematic (Q_{kin}) versus the photometric (Q_b) torque measurements for the subsample of 10 galaxies, where the kinematic method was possible. Despite large uncertainties, the correlation between the two parameters is obvious. This is confirmed by a measured linear Pearson correlation coefficient of 0.83. The distribution of existing bar strengths within our limited sample is representative of larger samples of nearby galaxies (Laurikainen et al., 2004). Overall, early-type galaxies have lower values than the later types, confirming earlier results by e.g. Buta et al. (2005); Laurikainen et al. (2007). This could be a result of different factors: i) the influence of stronger spiral arms that still alter the motions within the bar region (although we tried to avoid them in our analysis), ii) the presence of more gas in later types which is more responsive to the bar could also influence the stellar motions, iii) discs in earlier types are simply hotter leading to more random versus ordered rotational motion. The dotted line in the figure indicates a one-to-one correlation.

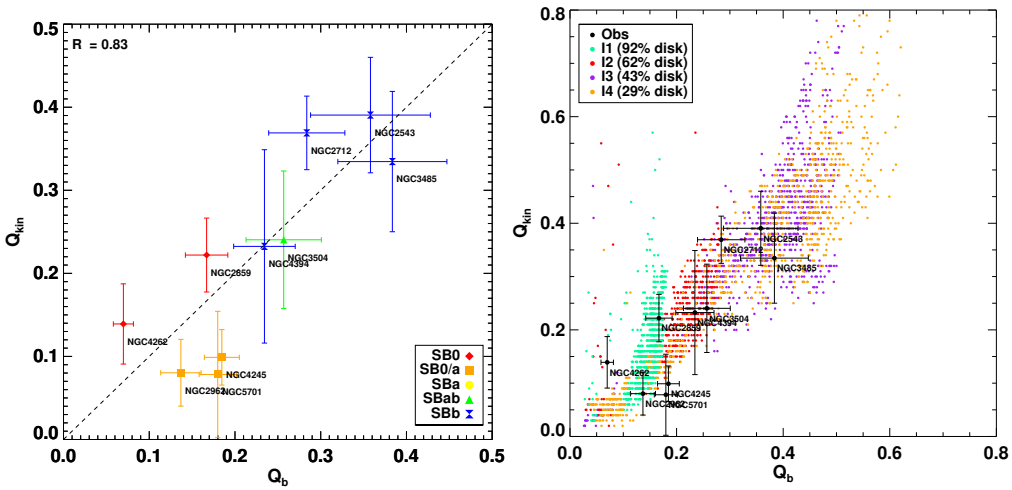

FIGURE 4.11: (*Left panel*) Kinematic versus photometric torque (Q_{kin} vs Q_b). The dotted line indicates a one-to-one correlation. Symbols are colour-coded according to Hubble type. The relation has a linear Pearson correlation coefficient of R=0.83. (*Right panel*) Comparison of Q_{kin} and Q_b for the observations (black) and the four sets of numerical simulations (I_1, I_2, I_3 and I_4). We only plot stages of the simulations that exclude the buckling phases.

To investigate further the relation between stellar Q_{kin} and Q_b, we have produced an extensive set of numerical simulations of barred galaxies following

those in Martinez-Valpuesta, Shlosman & Heller (2006) and Martinez-Valpuesta & Gerhard (2011). Here we use four simulations series, I_1, I_2, I_3 and I_4, each one with a different disc-to-total ratio: 0.92, 0.62, 0.43, 0.29 respectively. This setup allows us to explore the effect of distinct dark matter haloes on the torque parameters. We analysed 1800 snapshots taken at different points in time of the bar evolution. In addition, we also varied the inclination and the position angle of the bar relative to the galaxy's position angle to have different viewing angles and thus assess the influence of these parameters (see Appendix B.2 for more details). The bar strength measurements of the simulations are presented in Fig. 4.11 (right panel).

We analysed the simulations in the same way as the observations. We calculated Q_b from their simulated intensity distribution and Q_{kin} from their associated stellar velocity maps (see Appendix B.1 for details). Due to the lack of r_{K20} (k-band photometric parameter) to infer the scale height h_z (for the calculation of Q_b) (Speltincx, Laurikainen & Salo, 2008), we applied the de Grijs (1998) relation for intermediate type galaxies which links the scale-height to the scale-length, assuming an exponential disc without truncations. The overall trend found is consistent with what we find with the observations. Nonetheless, distinct simulation series behave systematically differently; the figure shows that higher disc fractions consistently lead to lower bar strengths, both in Q_b and Q_{kin} . Each simulation series exhibits low bar strengths, which correspond to snapshots in very early times in the bar formation. While I_1 soon seems to saturate and cannot grow stronger bars, the others do and saturate at later stages such that the strongest bars are found in the simulation series I_4, the one with the highest dark matter fraction.

Given the good agreement between Q_b and Q_{kin} for our subset of galaxies along with the large number of simulations, we will use the photometric values determined from the S^{4}G images for the bar strength values, because these are available for our entire sample. Our study also serves for verifying the technique and results of Q_b.

4.4 The effect of bar strength on galaxy properties

In this section we try to understand if stronger bars affect the properties of the host galaxy in a systematic way, focusing on whether it leads to stronger or weaker kinematic features.

4.4.1 Relation with Hubble type

Figure 4.12 (left panel) illustrates the already observed trend of Q_b with Hubble type (e.g., Laurikainen et al., 2007), resulting in a linear Pearson correlation coefficient of $R = 0.96$ for our sample (averaged values per Hubble type bin). In comparison with the observed trend found in Laurikainen et al. (2007), we cover slightly stronger bars throughout but conserving the trend, making our sample representative of rather strongly barred galaxies. For a wider study of Q_b as a function of Hubble type based on the S^{4}G sample, please refer to Díaz-García (2015, submitted).

In Fig. 4.12 (right panel) we depict the position of the dip in the λ_R profile,

depicted in Fig. 4.9, as a function of bar strength. The dip is not observed in all galaxies, therefore we only show those, which exhibit this feature. Is this dip feature related to inner structures such as nuclear rings? We plot in gray positions of rings from the AINUR sample (Comerón et al., 2010), including three galaxies (NGC 2859, NGC 3504 and NGC 4245) that we share. Evidently, ring and dip positions do not correlate and we do not find any mathematically significant trend for either sample.

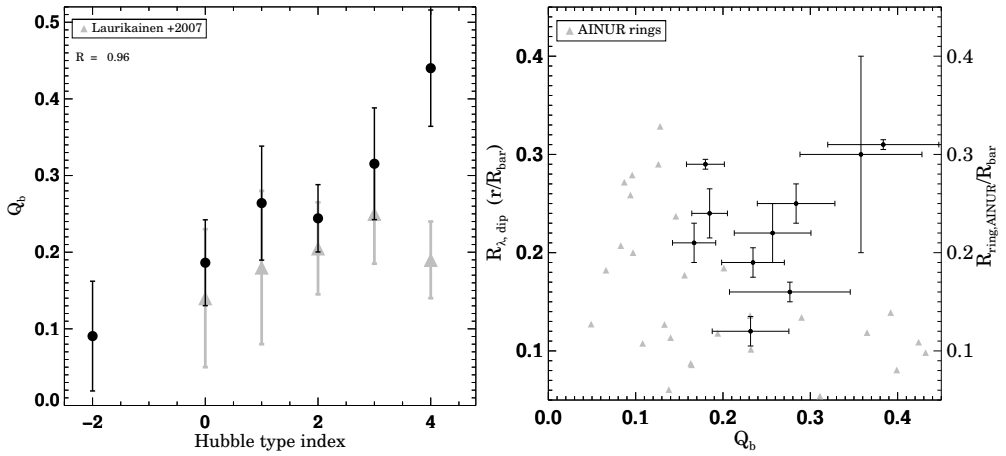

FIGURE 4.12: *Left:* Bar strength as a function Hubble type. We represent our sample averaged per Hubble type in comparison with the sample analysed in Laurikainen et al. (2007). *Right:* Position of the dip in the λ_R profile as a function of bar strength based on the profiles obtained in Fig.4.9. Grey points indicate ring positions (as bar length fractions) also as functions of the bar strength, both as measured in the AINUR sample (Comerón et al., 2010).

Fig. 4.13 shows again the position of the dip in the λ_R profile, now as a function of light concentration R_{90}/R_{50}. Apart from NGC 4262 - already found not to follow other observed trends, probably due to a recent interaction - the galaxies seem to follow a downward trend: the more concentrated the bulge, the closer is the dip feature towards the center. This could be directly related to the bulge: in our simulations with more concentrated bulges, we also find that the ILRs are located closer to the center. It could also mean that these features are more evolved in time, supporting the prediction of the migration of nuclear rings towards the center (e.g., Knapen et al., 1995; Fukuda, Habe & Wada, 2000; Regan & Teuben, 2003; van de Ven & Chang, 2009), also recently observed by Piñol-Ferrer et al. (2014).

This trend is only mildly observed for the values of the AINUR sample, taking their measured ring radii as a comparison, because no λ_R profiles are available for that data. We further determined the position of iILR and oILR by a simple linear approximation analysing Ω-curves and estimates for the bar pattern speed. Neither the position of the dip in the λ_R profile, nor the ring radius are found at the exact same position as these resonances (in a forthcoming work, we will verify this by a more robust calculation of bar pattern speeds).

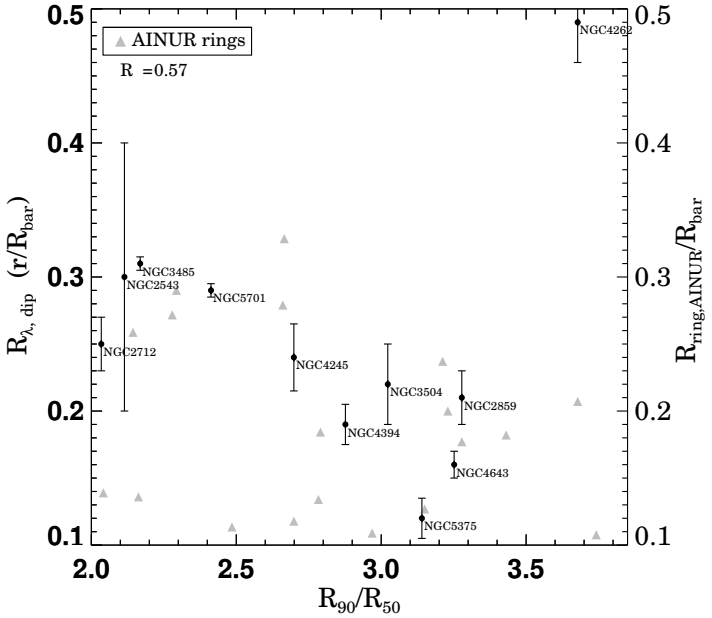

FIGURE 4.13: Position of the dip in the λ_R profile as a function of light concentration R_{90}/R_{50} based on the profiles obtained in Fig.4.9. Grey points indicate ring positions (as bar length fractions) also as functions of the concentration, derived in the same way as for our sample.

4.4.2 Influence of the bar strength on the global position angle

To quantify the influence of the bar on the global velocity map, we analysed the difference between the photometric and kinematic position angles as a function of the bar strength. We compared the photometric PA with the stellar and gas kinematic PA, as well as the difference between the stellar and gaseous components. This is shown in Fig. 4.14. We measured the kinematic PAs directly from the velocity maps following Barrera-Ballesteros et al. (2014).

No trends are observed with bar strength in any of the three cases. In previous studies including barred galaxies (e.g., Falcón-Barroso et al., 2006; Fathi et al., 2009; Krajnović et al., 2011; Barrera-Ballesteros et al., 2014), the observed misalignments were neither strong nor systematic. Misalignments were found mainly in systems with complex kinematics (non-regular rotators), systems in interaction and only in some barred galaxies, but their amplitudes largely depended on the FoV. The detailed study by Barrera-Ballesteros et al. (2014) further concludes that morphological substructures only influence the redistribution of angular momentum, but the global kinematics such as rotation are driven by the overall disc mass. Here, we also only detected one galaxy, NGC 3504, with a larger difference between the photometric and kinematic PAs. The ionised gas is known to react strongly to the bar producing a twist in the zero-velocity curve (e.g., Peterson & Huntley, 1980; Emsellem et al., 2006). However, for the gas too, we only detected large misalignments in NGC 4262. The overall misalignment is slightly larger than that for the stellar kinematic/photometric PA difference, but not significantly. Finally, the difference between the two kinematic PAs (stellar and ionised gas PA) is found to be equally small and not correlated with the bar strength, confirming the results

from earlier studies (as described above).

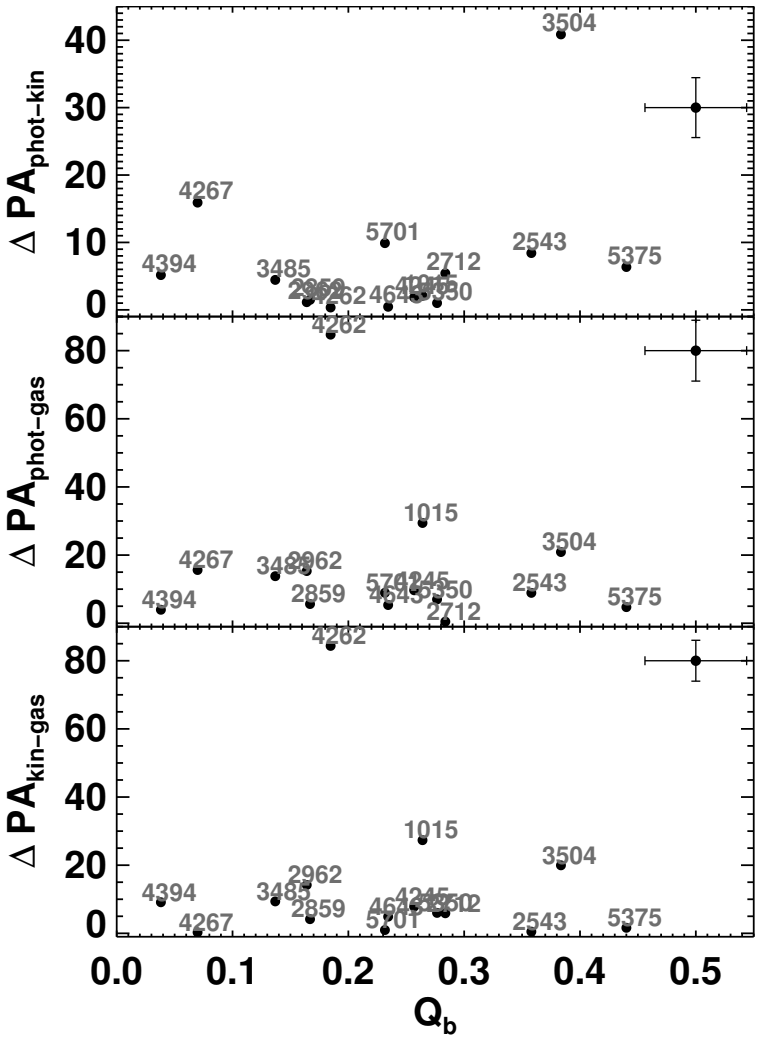

FIGURE 4.14: Photometric and kinematic position angle differences between stars and ionised gas as a function of bar strength. *Top:* difference between global photometric and stellar kinematic PA. *Middle:* difference of photometric to kinematic gas PA. *Bottom:* difference between the stellar kinematic and gas kinematic PA. Representative error bars are indicated in the top right corners.

4.4.3 Stellar kinematic features related to bar strengths

Bars can be depicted as engines that, on the one hand, drive gas towards the central regions and consequently nourish star formation (e.g. Elmegreen & Elmegreen, 1985, 1989; Erwin, 2005; Ellison et al., 2011) and, on the other hand, support radial motions of stars (e.g., Minchev & Famaey, 2010; Brunetti, Chiappini & Pfenniger, 2011). Due to these factors, they are natural triggers of changes in the centre of galaxies, and in the stellar velocity dispersion in particular. We do not find, however, any trend between the central velocity dispersion and the bar strength. This reinforces the picture that the central stellar velocity dispersion is determined by global galaxy properties. At least, it does not vary significantly due to morphological substructures in a systematic

way, except for the occasional central $\sigma-$drop.

While simulations predict and find a significant influence of the bar on the host galaxy in various ways (e.g., Martinez-Valpuesta, Shlosman & Heller, 2006; Athanassoula, Machado & Rodionov, 2013; Sellwood, 2014), we only find mild signatures on the kinematic maps in our sample, such as the proposed double-hump rotation curve and occasional $\sigma-$drops. Despite this lack of major, bar-induced alterations in global galaxy kinematic parameters, we detect some relation between those subtle kinematic features and the bar strength. It is thus logical to assume a connection between those features and the bars.

Since double-humps and $\sigma-$drops exist commonly among barred galaxies, we tested their amplitude in relation to the bar strength. In other words, would stronger bars produce stronger humps or deeper drops? We quantified the strength of the hump by the difference of its inner peak and consecutive drop, calling this parameter ΔV. We further normalised this value by the maximum rotation – corrected for inclination – that we could detect for each galaxy. We are aware that asymmetric drift could attenuate this signal slightly, but do not expect a major change for the trend observed.

For the velocity dispersion we determined the amplitude of the central $\sigma-$drop if present, again normalised by the maximum velocity dispersion (following Peletier et al. 2012). We chose to compute these quantities at the position angle where the signal was stronger. Since the hump in the velocity is seen strongest along the major axis, we took the profile along that axis. We chose to take the velocity dispersion profiles along the bar major axis, because the drop is most pronounced along that direction.

Figure 4.15 shows the results. We identified galaxies with very low inclinations in light grey, galaxies with intermediate but still low inclinations or larger uncertainties in their velocity fields in grey, and reliable points in black. As our sample is very small, we did not discard any points, but indicate that we are conscious about the bias introduced by measuring at different inclinations. As inclination effects in the velocity dispersion are very difficult to characterise (i.e., it depends on the projection of the velocity ellipsoid being probed and anisotropy), we did not attempt any correction.

We find tentative evidence that stronger bars produce stronger humps in the velocity profile. After the inclination correction, the low-inclination galaxies also follow this trend and we obtain a linear Pearson correlation coefficient of $R = 0.57$. Discarding unreliable galaxies (light gray points), the correlation coefficient increases to $R = 0.76$. As the hump could sometimes be distinguished better in the ionised gas, we also determined these parameter in the gas velocity profile (not shown here). The results follow the same trend. In the bottom row of Fig. 4.15, we show the measurement of the magnitude of the $\sigma-$drop. Stronger bars produce a stronger $\sigma-$drop features. We obtained an overall linear Pearson correlation coefficient of $R = 0.74$. All except one of the galaxies without a central dispersion drop have Q_b values below 0.15. The lack of this drop feature seems to be most evident in galaxies with weaker bars.

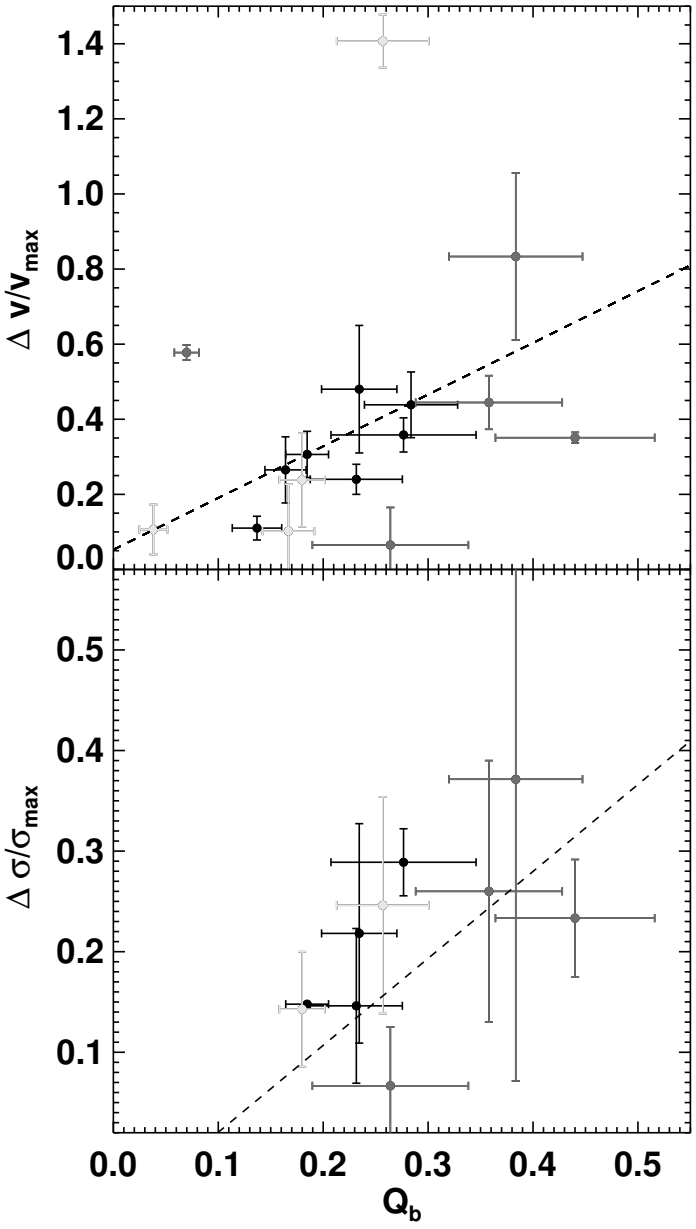

FIGURE 4.15: Different parameters detected in the kinematic maps of barred galaxies as a function of bar strength. *Top:* Magnitude of the velocity hump along the major axis rotation curve, normalised by the maximum rotation velocity and corrected for inclination (see text for details). *Bottom:* Magnitude of the $\sigma-$drop, normalised by the maximum dispersion (i.e. difference between central drop and highest surrounding velocity dispersion). In both panels, the dashed line indicates a linear fit to the black and dark gray points.

4.4.4 Stellar angular momentum as a function of bar strength

We now inspect the influence of the bar on the integrated angular momentum within one effective radii ($\lambda_{\rm Re}$). This is shown in Fig. 4.16. The values obtained for $\lambda_{\rm Re}$ are consistent with the values found in the literature for barred galaxies (e.g. Bender, Saglia & Gerhard, 1994; Krajnović et al., 2008, 2011). These studies, however, do not include bar strength measurements. We observe an increasing value of $\lambda_{\rm Re}$ with bar strength. This is somewhat connected to

Hubble type, because the later-types in our sample display the largest λ_{Re} values.

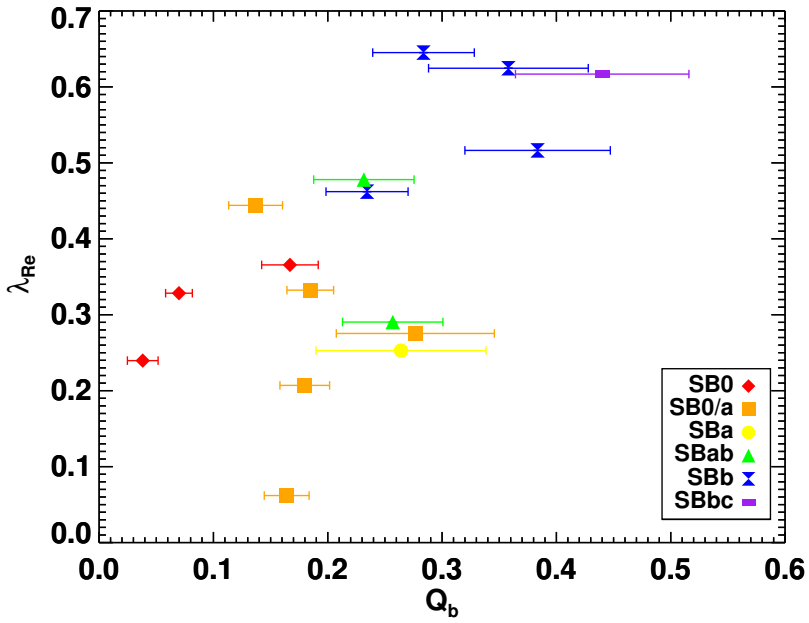

FIGURE 4.16: Apparent stellar angular momentum within one effective radius (Emsellem et al., 2007) as a function of bar strength. The different Hubble types are shown in different colours.

The high λ_{Re} values observed in the later-type galaxies are likely due to the higher fraction of the disc, and thus high rotation, included within the one effective radius aperture.

As there is angular momentum transfer between the bar, disc and outer halo (e.g., Combes & Elmegreen, 1993; Martinez-Valpuesta, Shlosman & Heller, 2006), the value of λ_{Re} should be higher in barred galaxies compared to their non-barred counterparts. Athanassoula (2003) showed, however, that while angular momentum is transferred to the disc, the bar also slows down and therefore contributes to a decrease in λ_{Re}. The current available λ_{Re} values in the ATLAS3D (Emsellem et al., 2011) or CALIFA samples (Falcón-Barroso et al., 2014) do not indicate distinct values for barred and non-barred galaxies.

4.4.5 Bars as drivers of radial motions

Bars have been studied as a major driver of radial mixing for a long time (e.g. Friedli & Benz, 1993), but spiral arms (e.g., Sellwood & Binney, 2002) or the combination of their resonance overlap (e.g., Minchev & Famaey, 2010; Shevchenko, 2011) are also held responsible for an increase of this. Investigating the latter, Brunetti, Chiappini & Pfenniger (2011) found that kinematically hot discs are not as efficient environments and exhibit less radial mixing than kinematically colder ones. We investigate the level of radial motions induced by bars in our sample by studying the radial gradients of the stellar velocity dispersion. The expectation is that barred galaxies would display flatter gradients than those measured in non-barred systems.

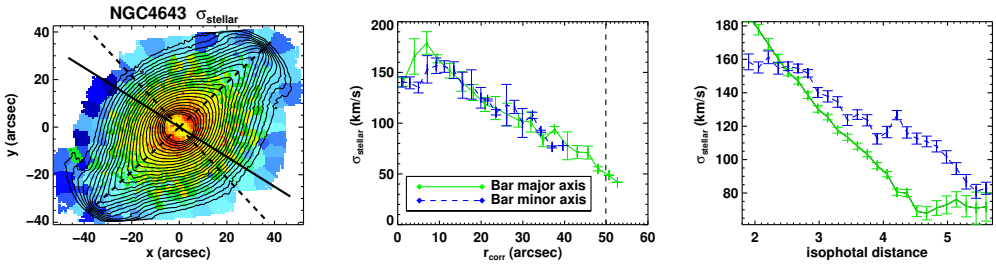

FIGURE 4.17: Stellar velocity dispersion map of NGC 4643 and associated profiles. (*Left*) Stellar velocity dispersion map with bar major and minor axes indicated with dashed lines. (*Middle*) Averaged profiles, corrected for inclination. Dashed line indicates the bar length. (*Right*) Averaged profiles along isophotes (first point corresponds to first isophote seen on the top left image).

We start by comparing velocity dispersion profiles along the major and minor axes of the bar. In earlier literature studies, velocity dispersion profiles were investigated typically only along the major axis of the bar (e.g. Pérez, Sánchez-Blázquez & Zurita, 2009). For our sample, this is shown in Fig. 4.17 for one galaxy as an example (similar plots for other galaxies are presented in Appendix A). We show the overall stellar velocity dispersion map for reference and, next to it, the radial profiles along the major and minor axes (minor axis radii are corrected for inclination) of the bar extracted from this map. The profiles along the axes are generally overlapping, hence we do not observe any increase along the bar major axis. In one third of our sample, however, we observe a mild difference around the central parts (also seen in the example), with the major axis showing a higher dispersion. This is probably linked to the aforementioned kinematic substructures such as inner discs or rings, possibly a result of barred secular evolution. The major axis profiles observed in Pérez, Sánchez-Blázquez & Zurita (2009) show a similar behavior to ours, but no minor axis measurements have been performed in that work.

As bars are structures seen in the photometry, we decided to also trace the profile comparing their points along the same isophotes. The isophotal profiles reveal a larger overall σ along of the major axis than the minor axis, and not just in the central parts. The fact that the velocity dispersion further out is higher along the minor axis, compared with the same isophote on the major axis, shows that the dispersion of the bulge – traced by the minor axis – dominates strongly, regardless of the prominent bar seen in the photometry. It shows nonetheless that the kinematics of the bar is significantly different than the bulge and it is more similar to the disc, because at the outer end of the profiles, reaching the disc, values along the major and minor axes start coinciding again.

Figure 4.18 shows a relation between the outer gradient of the stellar velocity dispersion and the bar strength. The gradient is shallower for stronger bars. Nevertheless, the trend is based on only very few points, in particular in the low bar strength regime. The presence of a bar can cause enhanced radial motions which perturb the system. Thus the orbital mixing increases which in turn can lead to higher dispersion and shallower gradients. This could be the reason for the observed flattening of the gradients with higher Q_b. Additionally, we measured the gradient not only along the major axis of the galaxy (black points),

but also along the minor axis (blue points). If the bar would significantly flatten the gradient along the major axis, the minor axis values would be expected to show steeper gradients. The results, however, show a scatter of shallower as well as steeper gradients along the minor axes compared to the points measured along the major axes and we cannot identify a systematic behavior.

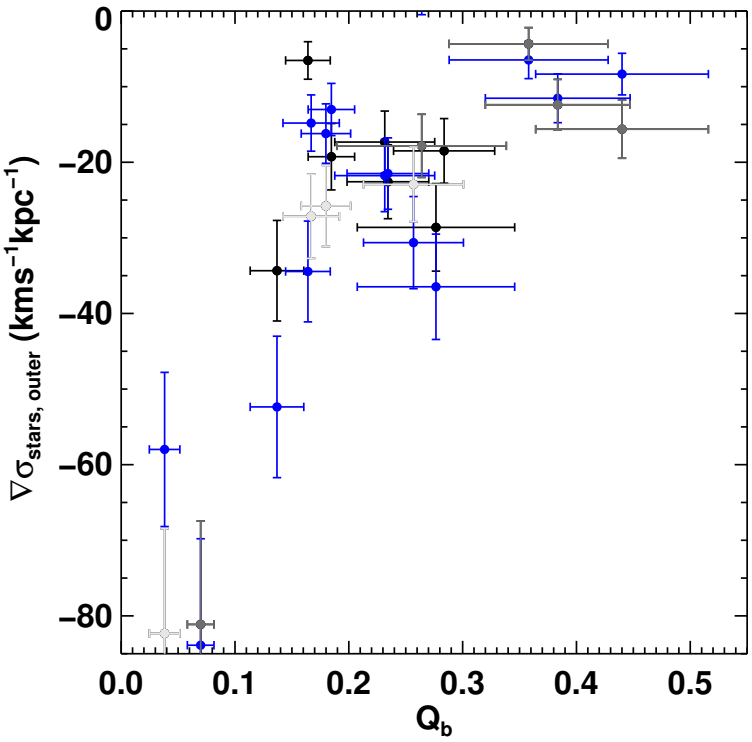

FIGURE 4.18: Gradient of the outer velocity dispersion, ignoring the central regions, as a function of bar strength. Blue points indicate profiles taken along the bar minor axis, while black points show the ones along the bar major axis.

The measurement of the maximal radial velocities that we use to calculate the kinematic torques also indicate the average radial displacement. As mentioned in previous sections, the average radial motion is much higher in the gas than for the stars. Stars move at velocities between 10 and 60 km/s radially, corresponding to about 10-60 kpc/Gyr or 0.09 - 0.88 when normalised with the rotation at $\approx r_e$, a value which is similar in magnitudes to what we find with our own simulations (e.g. in I_4 it is around 0.2) whereas the gas move at 40 - 100 km/s and in extreme cases such as NGC 4262 at more than 300 km/s. The latter is most probably due to an outer influence such as an interaction (Vollmer, Huchtmeier & van Driel, 2005). Nevertheless, the stronger effect on the gas than on the stars has been seen in numerous simulations (Athanassoula, Machado & Rodionov, 2013; Kubryk, Prantzos & Athanassoula, 2013, e.g.). Kubryk, Prantzos & Athanassoula (2014) find a particular influence of the bar-induced radial inflow on the gaseous profile. Furthermore, Maciejewski, Emsellem & Krajnović (2012) obtain values which are in the range of the ones we recover using the same method. The recent work of Goz et al. (2015) analyzing two simulations of barred galaxies resulting from N-body+SPH cos-

mological simulations, shows one case with significantly higher radial motions (around 150 km/s) whereas in the other case the magnitude is comparable to what we observe (around 30 km/s).

In a large number of simulations (e.g., Minchev et al., 2012) bars are found to be the most efficient driver of radial migration, in particular through their corotation resonance. We have not yet determined the radius of corotation for our sample, but plan to compute this in a forthcoming paper. This parameter, together with the stellar populations will further complete the picture of bar-induced mixing. In particular in the next chapter, we will assess the impact of the radial motions determined here, on the stellar population properties, which will allow us to shed light onto radial migration effects (e.g., Friedli, Benz & Kennicutt, 1994; Haywood, 2008; Roediger et al., 2012; Kubryk, Prantzos & Athanassoula, 2013).

4.5 Summary and conclusions

We present the BaLROG sample of 16 barred galaxies of different Hubble types, spanning the typical bar strengths found in the local Universe. Our large mosaics with the integral field unit SAURON cover the bars out to the radius where the disc begins to dominate, at a spatial resolution of typically 100 pc. For every galaxy we also use *Spitzer* observations from the S^4G survey of nearby galaxies (Sheth et al., 2010) to determine several photometric parameters, as well as to derive the bar strength Q_b. From the velocity maps, we calculate radial and tangential velocities to compute the bar strength based on the kinematics, Q_{kin}. Our aim is to establish a reliable yardstick, namely bar strength, to probe the influence of the bars on different parameters of the host galaxies.

In this chapter we focus on the kinematics of the galaxies, deriving stellar and gas velocities and velocity dispersions, h_3 and h_4 Gauss-Hermite moments and the stellar angular momentum λ_R and carefully comparing to a large set of N-body simulations. The analysis of our observations leads to the following results and conclusions:

- Bars do not strongly influence the global kinematics of their host galaxies, regardless of their strength. Our work confirms previous studies (e.g. Falcón-Barroso et al., 2006; Fathi et al., 2009; Krajnović et al., 2011; Barrera-Ballesteros et al., 2014) and shows the lack of strong kinematic misalignments between the galaxies' photometric and kinematic axes.

- Bars do have an influence on more subtle kinematic features, especially in the inner regions of galaxies. We detect double-hump velocity profiles and velocity dispersion drops (e.g., Bureau & Athanassoula, 2005), which increase in intensity with increasing bar strength.

- We find evidence for the presence of inner structures such as inner rings or discs in about 50% of our sample. These features are detected from the anti-correlation between h_3 and V/σ within the effective radius of the galaxies ($\approx$0.1 bar lengths).

- The derived λ_R profiles show a dip at 0.2 ± 0.1 R_{bar}, which we suggest is connected to the presence of inner substructures.

- We also derived the integrated angular momentum within one effective radius ($\lambda_{\rm Re}$) and find that galaxies with stronger bars exhibit a higher $\lambda_{\rm Re}$ value. This may be a secondary effect of late-type galaxies, because they are more rotationally supported and thus also host stronger bars.

- We developed a new method to determine the bar strength from stellar or ionised gas velocity maps ($Q_{\rm kin}$). This method relies on the extraction of the ratio of radial and tangential velocities using the technique developed by Maciejewski, Emsellem & Krajnović (2012). Values of this parameter agree well with independent measurements obtained from imaging, $Q_{\rm b}$, e.g., Laurikainen & Salo (2002), and predictions from numerical N-body simulations.

- Bar strength values measured from ionised-gas kinematic maps are a factor $\sim$2.5 larger than those determined from the stellar kinematic maps.

- We observe a flattening of the outer stellar velocity dispersion profiles with increasing bar strength.

These results suggest a complex influence of bars in nearby galaxies, especially affecting central regions. We do not observe a significant influence on global properties, but bars seem to affect only on small scales. The gas is clearly more strongly affected, reflected in higher gaseous than stellar torques. In our sample we detect a difference between bars in early and late-type galaxies hinting towards a different mechanism, maybe due to the presence of higher and lower gas fractions. To better answer these questions and determine time scales, we will investigate the stellar populations of these galaxies in detail in BaLROG II, presented in the following Chapter.

5

The BaLROG project II: The influence of bars on the stellar populations[1]

...Open mind for a different view
And nothing else matters.
Metallica

We continue the exploration of the *BaLROG* (Bars in Low Redshift Optical Galaxies) sample, consisting of 16 large mosaics of nearby barred galaxies. In this chapter we quantify the influence of bars on the composition of the stellar component. We derive line-strength indices of Hβ, Fe5015 and Mg*b*. Based on single stellar population (SSP) models, we calculate luminosity-weighted ages, metallicities and abundances ([Mg/Fe]) and their gradients along the bar major and minor axes. The high spatial resolution of our data allows us to identify breaks among all index as well as SSP profiles, commonly located at 0.13±0.06 bar length, consistent with kinematic features observed in our previous work. Inner gradients are about ten times steeper than the outer gradients. Central ages appear to be younger for stronger bars. Yet, the bar regions are usually old. We find a flattening of the iron (Fe5015) and magnesium (Mg*b*) outer gradients along the bar major axis, translating into a flattening of the metallicity gradient. This gradient is found to be 0.03±0.07 dex/kpc along the bar major axis while the mean value of the minor axis compares well with that of an extensive unbarred control sample and is significantly lower, namely -0.20±0.04 dex/kpc. These results confirm recent simulations and discern the important *localized* influence of bars. The elevated abundances of bars and bulges compared to lower values of discs suggest an early formation. Some old bars further sit inside a young star-forming disc which confirms bars as long-lived structures that survived until the present day.

[1]The majority of this chapter is based on the submitted article: *The BaLROG project II: The influence of bars on the stellar populations.* Seidel, M. K., J. Falcón-Barroso, I. Martínez-Valpuesta, I. Pérez, P. Sánchez-Blázquez, A. Vazdekis, R.Peletier. 2015, MNRAS.

5.1 Line strength indices

This section summarizes the results of the line-strength measurements of the BaLROG sample. We start by investigating global properties comparing with trends found in the literature for both, barred and unbarred galaxies. Later, we will focus on the details revealed by the two-dimensional maps, looking at specific regions and radial trends, as well as gradients. We will discuss our findings in the context of former works and their implications in section 5.3. In several parts, we only show a few maps of one galaxy as an example, but maps of our entire sample can be found in the Appendix C.1. We will use the bar length R_{bar} and fraction of it as reference points, as well as the effective radius R_{eff}.

5.1.1 Aperture absorption line index measurements

We start with a comparison of the global values obtained from the index measurements in order to situate our sample amongst statistically larger sample and detect possible offsets or outliers. We determined line strengths within different circular apertures. Figure 5.1 displays these measurements for an aperture size of one effective radius R_{eff} of the galaxy. We also computed relations for half the effective radius and for a central aperture: $R_{eff}/8$ which show similar good agreement (not shown here). This choice of apertures has been applied in various literature works, including long-slit studies (e.g., Trager et al., 2000; Thomas et al., 2005) and allows a direct comparison with the values from the ATLAS3D sample (McDermid et al., 2015) as well as spiral galaxies taken from the SAURON study of Peletier et al. (2007) and Ganda et al. (2007). These values are shown in the figure, where the ATLAS3D galaxies are shown in gray - dots for barred and triangles for unbarred galaxies and the SAURON sample is shown by open diamonds. Our own sample is colour-coded according to morphological type, where early types lie to the right exhibiting a higher central velocity dispersion. The kinematic values are determined from the BaLROG data (see our kinematic results, Seidel et al. 2015c).

The trends found with central velocity dispersion as well as with Hubble type are consistent with what is found in larger surveys, such as the ATLAS3D survey (McDermid et al. 2015). There is no difference between barred and unbarred galaxies and our sample does not reveal any outliers. Bars do not seem to have an influence on these global relations. The range of values covers a similar magnitude for early- and late-type galaxies and follows the correlations found by Trager et al. (e.g., 2000): the age-sensitive H_β index reveals a negative correlation with velocity dispersion while the metal-sentive indices show positive trends with this parameter. Even the smaller scatter for early types and larger scatter for later types (lower velocity dispersion) are reproduced by our small dataset. The correlations are clearly tighter for the high velocity dispersion end while the lower end exhibits a larger range of values. The stellar population parameters in these systems therefore might be more complex as they display a larger variety of index values at the same central velocity dispersion. This is found generally for later types, usually lower mass galaxies, than for the more massive, more early type systems.

Overall, bars seem to not affect the global trends, as they share the same aper-

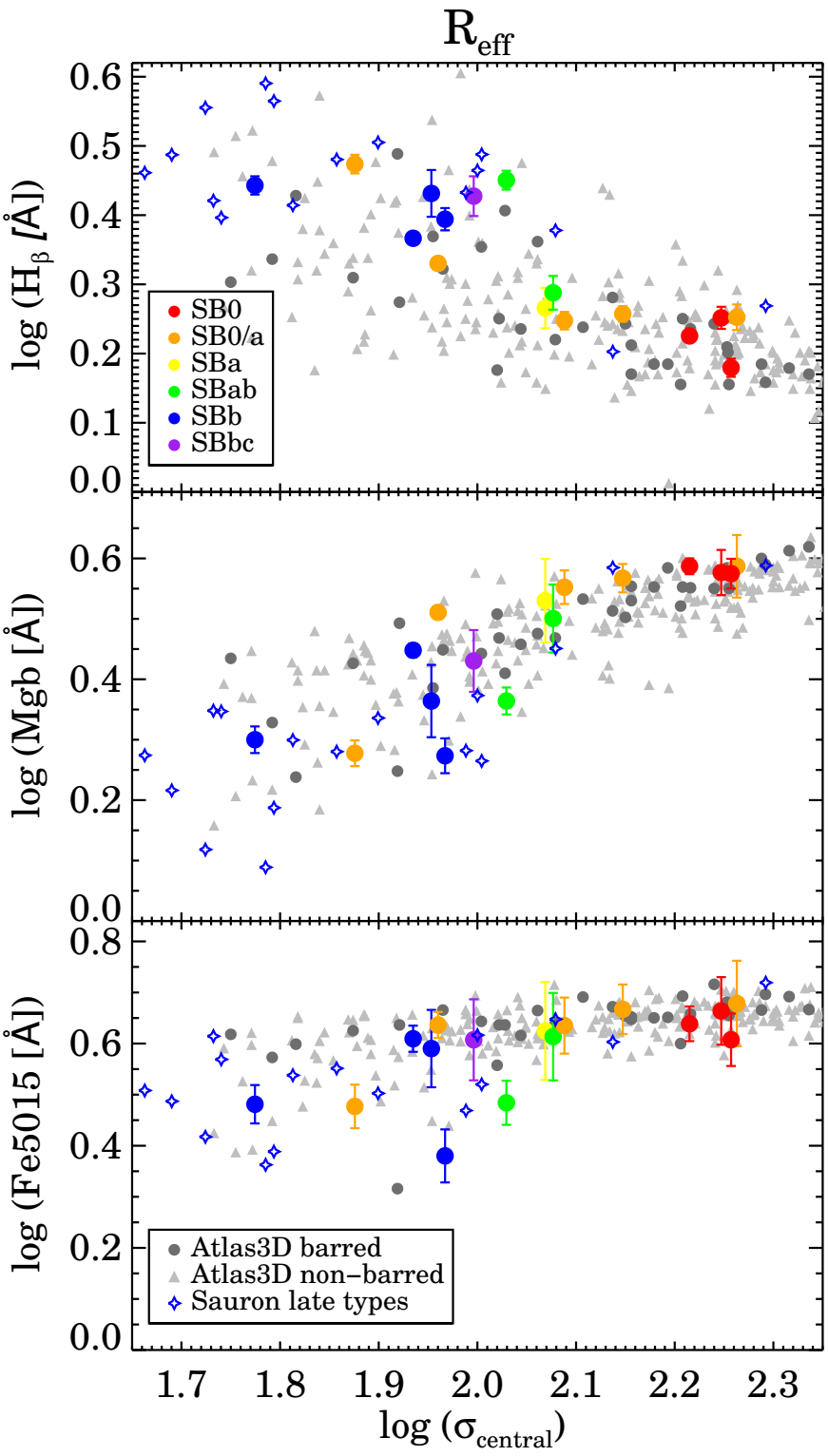

FIGURE 5.1: Index measurements within one effective radius ($R_{\rm eff}$) versus central velocity dispersion - all in logarithmic scale. Different Hubble times are colour-coded for our sample, while we show the ATLAS3D sample divided in barred and unbarred galaxies and measurements from late-type SAURON galaxies (also both barred and unbarred, but without distinction in the figure).

ture line-strength-velocity-dispersion-relations as unbarred galaxies. Locally however, we do detect their influence as outlined in the following sections.

5.1.2 Line-strength maps and profiles

In this section, we explore the details of each index map and analyse their profiles along different axes to better understand the local influence of bars on their host galaxy.

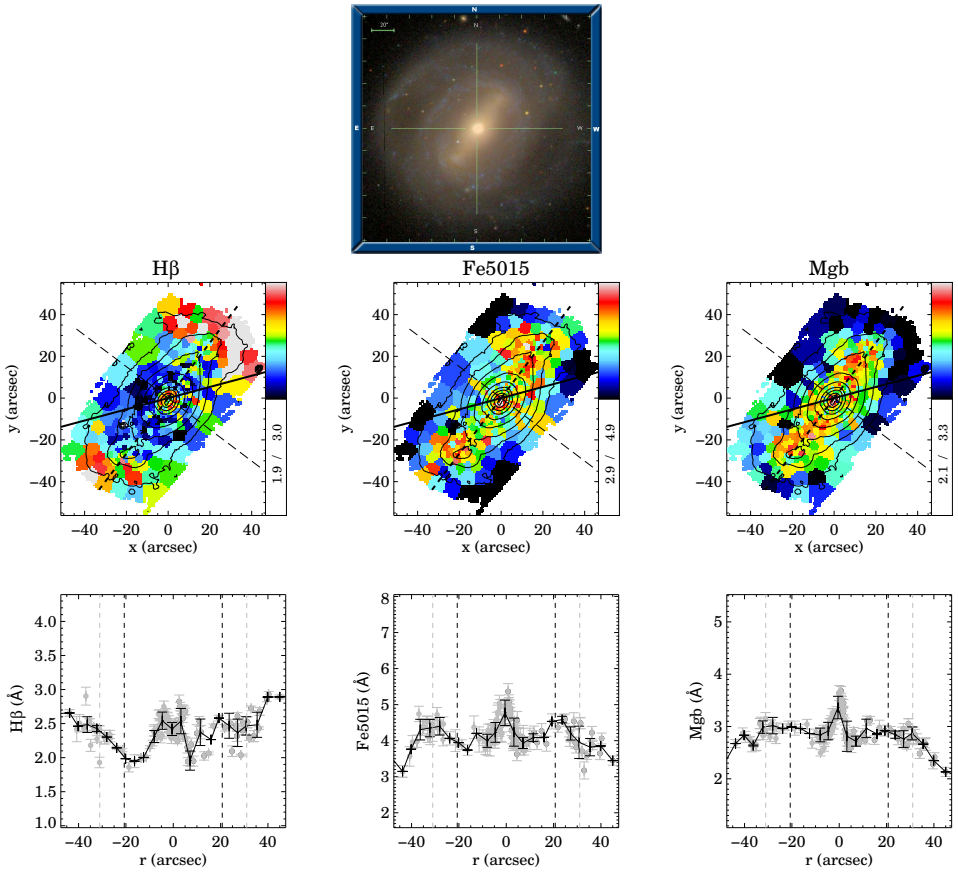

FIGURE 5.2: The top panel shows a colour SDSS image of NGC 4394. The central stellar bar is well distinguished and the colour already reveals different populations: redder (older) insider the bar and bluer in the disk and spiral arms around it. The scale of 20 arcsec is given in the left top corner of the image. Below, in the middle row, we present the index maps of our SAURON mosaic of this galaxy (in this case a composite of 6 pointings). The lines explored in our wavelength range are H_β, Fe5015 and Mg*b*. The major axis of the galaxy is indicated by a straight black line, the bar major axis by a dashed black line and the bar minor axis by a dotted-dashed line. The bottom panels show the profiles along the bar major axis directly extracted from the map with a slit of width of 3 arcsec. We show individual measurements in gray and averaged values overplotted in black. Half and three quarters of the bar length are indicated by dashed black and gray lines respectively.

Figure 5.2 shows NGC 4394 as an example of one of the galaxies in our sample. We show a colour (*ugri*) SDSS image in comparison with the line strength maps that we obtain from our SAURON data. Comparing the index measurements with the colour image, several similarities can be distinguished: the bar itself seems to be dominated by older populations as H_β is only starting to increase

towards the beginning of the disc where the spiral arms start. Nonetheless, in the very center, we can appreciate higher H_β values in the line-strength maps, unlike in the photometric image where no blue star forming region can be seen. The iron and magnesium indices also show high values in the center and along the bar. In particular Fe5015 seems to exhibit higher values towards the edges of the bar. These enhancements can be distinguished as areas of elevated (red) values. We note however, that the enhancement can also be an effect of contrast between the bulge and the bar components. Considering the high steep gradient of the inner structure and the light contribution of the bulge, compared with the flatter gradient of the bar and its light, the combination of both can make the gradient in the inner bar to be less steep, flat or even positive. In the Mg*b* map, the region seen as the photometric bar is dominated by constant elevated values, while the disc around it exhibits lower values and no bumps are seen at the edges of the bar.

Below the line strength maps, we show profiles along the major axis of the bar, in the bottom row of Fig. 5.2. We extracted the values directly from the Voronoi-binned maps taking a slit of ∼3 arcsec width (in the center slightly less and enlarging its width in a cone-like way towards the outskirts for better sampling). We show individual (gray) and averaged (black) measurements, indicating on each side half and three quarters of the bar length (vertical dashed lines, black and gray respectively).

The H_β profile nicely shows the elevated values around the center, but with a slight central dip. After the centre, we observe a steep decrease followed by increasing values towards the outside of the bar into the disc, where the spiral arms start dominating. The behaviour of the H_β profiles depends very much on the galaxy and is not systematic among our sample.

The Fe5015 profile is clearly different from the H_β index profile. Instead of a central dip, we find a central peak, dropping off steeply to either side. Following this valley, the profile reveals a the aforementioned particular feature: we find enhanced Fe5015 values at around 0.5-0.75 bar length. Inspecting the profiles among all galaxies in our sample, we can detect this feature in 7 galaxies (NGC 1015, NGC 2893, NGC 4262, NGC 4394, NGC 4643, NGC 5375 and NGC 5701). In some galaxies, it is not seen very clear and only 4 galaxies of our sample do not exhibit this feature at all. In some cases, it is more apparent in the maps while others reveal it better in the profiles. It is however not always found at the same radius - even in this galaxy, the bumps seem to be located at different distances from the center. Correcting for possible deprojection effects we could not account for the offsets. This feature is very mild - although appreciable - but based on a qualitative examination of the profiles and maps. Due to the varying location, no clear ratio of the higher areas to the lower ones could be established. With even better data in the future, using e.g. MUSE, this could be possibly better explored. We could however establish, that this feature is detected more strongly among the early types in our sample than in the later types. It does not depend on entering spiral arms (examined visually).

Mg*b*, similar to Fe5015, displays a central peak value, quickly dropping off to a stable level. No clear enhancements are seen in this index at certain regions

along the bar length. Instead, similar to Fe5015, after 0.75-1.0 bar length, the values start to decrease, when entering the disc/spiral arm regime. Overall, the Mg*b* index seems to best trace the entire bar extensions, i.e. it exhibits elevated values within the entire bar region constrained by the isophotes.

5.1.3 Analysis of distinct components

Apart from the radial trends, we also compared values of distinct regions in order to check for a common behaviour in potential resonance regions. Based on our previous analysis we divided the radial profiles in five regions relative to the bar length.

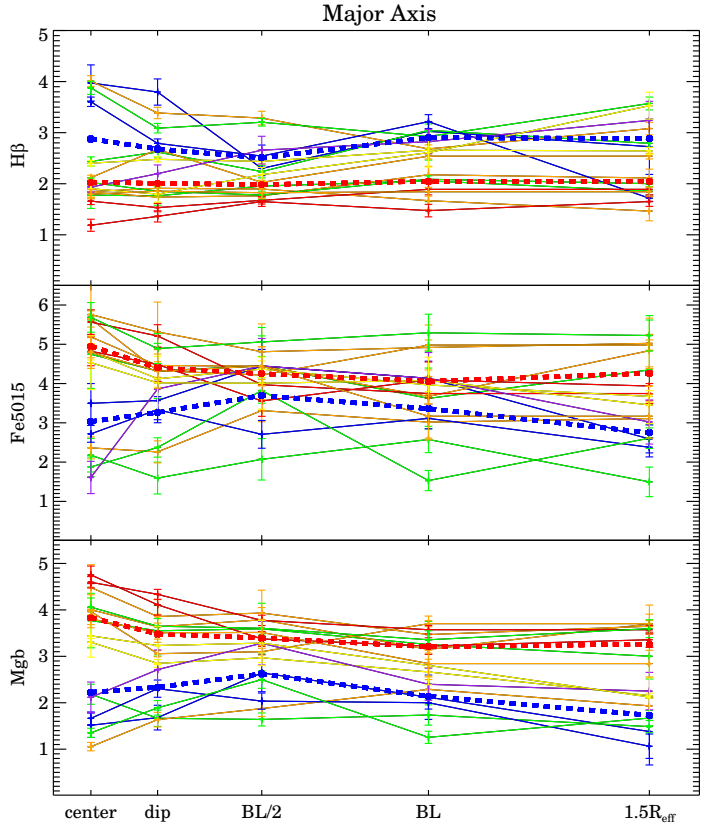

FIGURE 5.3: Index measurements within different regions along the bar major axis of the galaxies. We sample the center (within 0.01 bar length), the potential spot of bar-induced influence at around 0.13 bar length and denoted as the 'dip' as we found dips in e.g. the angular momentum profiles; then at half the bar length, full bar length and 1.5 effective radii R_{eff} (2.5 scale lengths of the disc). The individual profiles are colour-coded according to increasing bar strength, from red (weakest), over orange, yellow, green, blue up to purple (strongest). Additionally we indicate averaged profiles according to the Hubble type with dashed lines: red for early types and blue for late types among our sample.

We use the parameter of bar length R_{bar} and fraction of it as reference points as it is closely related to the corotation radius R_{CR} of the bar as shown by recent results by Aguerri et al. (2015). Using the Tremaine & Weinberg (1984) method, they determined that the mean value of the ratio R_{CR}/R_{bar} is around 1. Therefore, we use the bar length found from an analysis of *Spitzer* images

(Herrera-Endoqui et al. 2015, submitted) as an approximation. We sampled the following regions: the center (here denoted as 0.01 bar length), the potential spot of bar-induced influence at 0.13 bar length, half the bar length, full bar length and 1.5 effective radii R_{eff} (2.5 scale lengths of the disc). For some of the galaxies in our sample we do not reach this last point due to the limited extensions of the mosaic. In those cases we take the value that is the furthest into the disc.

Figure 5.3 depicts the result of our analysis. Regardless of the individual color-code, we distinguish several known trends independent of barred or unbarred galaxies, in particular for the early types (red dashed lines). As already seen in Kuntschner et al. (2006) for the original SAURON sample of early-type galaxies, we find generally negative gradients (with increasing radius) of the metal line strength maps. Similarly, we confirm flat or slightly positive trends for the H_β measurements. We also find central or circum-central elevated H_β values likely connected to recent star formation activity.

Overall, we observe a higher scatter for the central and circum-central values, than for the barred region (half or full bar length). The spread increases again at 1.5 R_{eff}. The fact that the central values as well as disc values exhibit larger scatter, implies likely a more complex star formation history with recent star formation activity in the center, given the elevated H_β strengths. Qualitatively, we do not find significant difference between major and minor axes, apart from a tentative higher scatter for the minor axis. This is however only based on a few galaxies and the limitations of our sample size are obvious.

The colour-code indicates the bar strength, starting with weak bars (red), over intermediate (from orange, yellow, green to blue) to strong bars (purple). The bar strengths are also closely coupled with Hubble type for our sample. Hence, the observed trends might be also linked to that latter parameter. Already seen in Fig. 5.1, the early types galaxies show lower H_β and higher Mg*b* values overall than the later types. Considering that bars drive fuel towards the central parts to aliment or even initiate star formation (e.g., Heller & Shlosman, 1994; Knapen et al., 1995), we do find higher values and steeper drop-off slopes in the centre and circumcentral parts for the stronger barred galaxies, seen in the top panel. Several observational studies have already related star-forming nuclear rings to bars (e.g., Allard et al., 2006; Knapen et al., 2010; van der Laan et al., 2013b) and our finding of higher H_β values in those regions for stronger barred galaxies supports this result.

From the indices alone, we could already confirm certain trends and find new evidence for bar-driven influence on the host galaxies in our sample, in particular along the bar major axis. In the following section we will now relate the indices to SSP parameters.

5.2 Single stellar populations

In this section we will relate the measured line strength values to SSP parameters deducing the luminosity-weighted age, metallicity and abundances for our sample. Since bars are structures seen prominently in the photometry, light-weighted quantities are of great interest. Similar to the index analysis, we

first present global trends and then analyse the details of the maps and radial profiles. A quantitive analysis of the profiles' gradients will be discussed in section 5.3.

5.2.1 Index-Index diagrams

Index-index diagrams intuitively relate line-strength indices with single stellar population parameters, using a grid of model predictions.

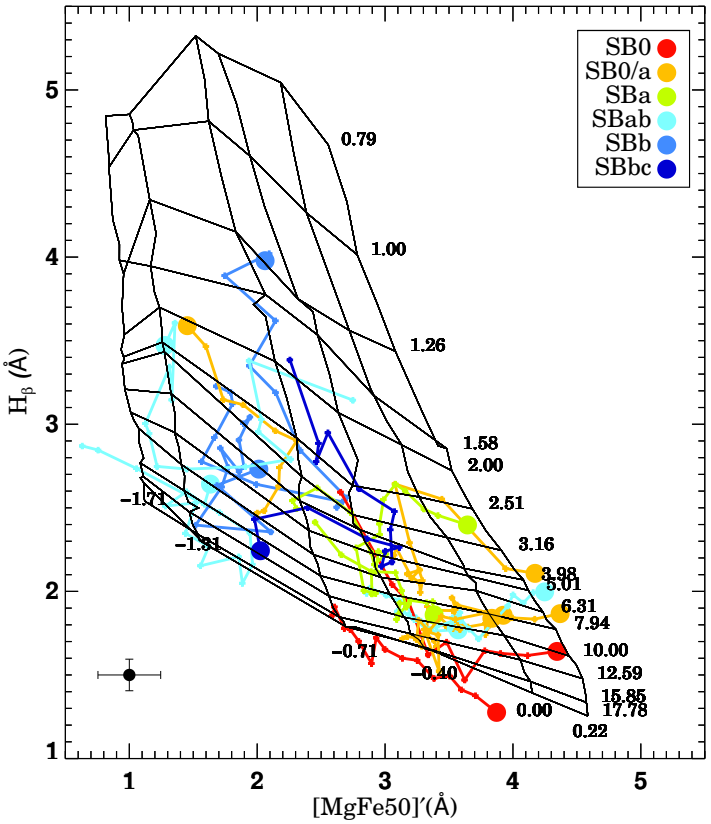

FIGURE 5.4: Index-index diagram displaying isophotal integrated radial profiles for our entire sample, colour-coded by Hubble type. Hβ is used as an age discriminator versus the combined index of [MgFe50]', employed as a proxy for metallicity. Overplotted is a model grid of single stellar populations, indicating the ages (in Gyr) and metallicities (dex) (shown on the side of this grid). In the left lower corner we indicate a typical uncertainty (weighted mean of individual errors) of the individual points with representative error bars - this error can vary depending on the galaxies and individual radial (as well as complete) index-index diagrams can be found in the appendix for each galaxy.

Figure 5.4 presents the measurements of absorption line strengths in an index-index diagram for the galaxies of our sample, showing isophotal integrated radial profiles (the individual grids per galaxy can be found in the appendix). We plot Hβ as an age indicator against the combined index of magnesium and iron, [MgFe50]' (using Mg*b* and Fe5015, see Chapter 3, Sec. 3.3.1) as a proxy for

metallicity, independent of [Mg/Fe]. A grid of MILES single stellar population models for Kroupa IMF is overplotted.

Overall, we observe a large variety of distributions within the full grid amongst our sample. Clear differences can be detected between early and late-types: most early types seem to be older and more metal-rich overall and exhibit a more confined distribution for all points while late types show a much larger spread among themselves, but also radially in the diagram. This behaviour is of course optically enhanced or even driven by the age difference due to a larger area of the grid covering young ages which makes the range more obvious and spread out than for older populations. Furthermore, we find that for a few galaxies of our sample (in the binned version in Fig. 5.4 only 3, but more in the unbinned versions (see Appendix A and below), the central spectra tend to fall slightly outside the grid (at the high metallicity end). As these are mainly the central spectra, the signal-to-noise is usually well over 100, hence the quality of the spectra should not be the scapegoat. In the appendix of Seidel et al. (2015a), we already analysed this behaviour and found that it is likely due to the complex mixture of populations present in those regions. This would be a very plausible explanation given the peculiarities already observed. In most cases, the central value is slightly younger and particularly metal-rich which hints towards a younger population formed from an already metal-enriched medium.

Within this context, we compared the inner h_3-v/σ anti-correlation explored in the previous chapter (see also Seidel et al. 2015c, Fig. 8) with the grids and found that those galaxies that show strong h_3-v/σ anti-correlations within the central 0.1 bar lengths are the same whose central index measurements are found outside the grid (mainly shifted to the right at the high metallicity end). These are: NGC 2859, NGC 2962, NGC 4245, NGC 4394, NGC 4262 and NGC 4643. Their individual point measurements can be seen in Appendix A. Most of these galaxies exhibit substantial inner components or are even double-barred (e.g., de Lorenzo-Cáceres, Falcón-Barroso & Vazdekis, 2013). In her analysis, de Lorenzo-Cáceres, Falcón-Barroso & Vazdekis (2013) find that inner bars are younger and more metal-rich than their surrounding bulges and outer bars.

Those galaxies with straight horizontal or circular accumulated h_3-v/σ relation (as seen in Fig. 8 in Seidel et al. 2015c) are corresponding to those that seem to have less spread and fall (almost) completely within the grid: NGC 1015, NGC 2893, NGC 3485 and NGC 5701. Those with very large variations in age and metallicity as seen in the grids, also show a very extensive h_3-v/σ distribution for all radial apertures: NGC 2712, NGC3504 and NGC 5350. Hence, the h_3-v/σ relation can already give qualitative hints on the present stellar population properties.

Trying to quantify this observation, we show the central age and metallicity against the linear Pearson correlation coefficient of the line (h_3-v/σ anti-correlation) in Fig. 5.5, top and bottom panels respectively. Doubtlessly, the relation exists with metallicity (linear Pearson correlation coefficient R=0.64 and p-value=0.02) and not so much with age (linear Pearson correlation coefficient R=0.48 and p-value=0.06, hence not significant). Furthermore, the

correlation seems to be stronger for earlier types, but is not entirely driven by Hubble type (colour-coded in the plot). We also analysed the slope of the h_3-v/σ anti-correlation (not shown), which seems to be steeper for higher central metallicities. This could be a hint of a connection between the dynamical parameters and their stellar populations.

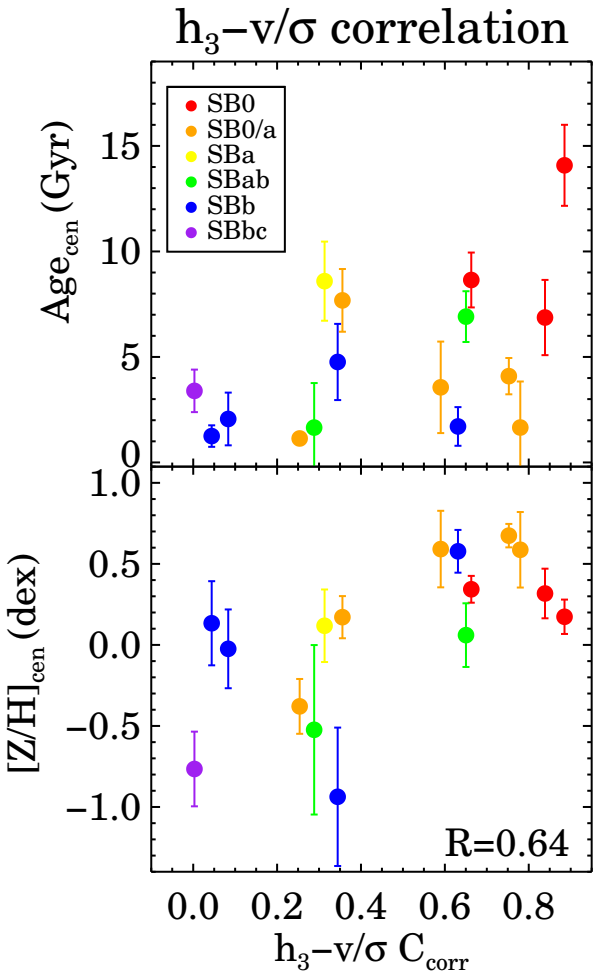

FIGURE 5.5: Central ages and metallicities, measured within the central aperture of $R_{eff}/8$, as a function of h_3-v/σ anti-correlation (analyzed in Chapter 4). We show the linear Pearson correlation coefficient of the h_3-v/σ anti-correlation on the x-axis and the central SSP parameters on the y-axis. Hubble types are indicated in colours. And the linear Pearson correlation coefficient is given for the correlation with metallicity in the lower right panel.

The overall properties of the isophotal SSP profiles as seen in the index-index diagram are still dominated by their Hubble type and no crucial global influence of the bar can be detected, apart from tentatively on the central values. Those might be influenced by substructures, such as central star formation resulting in inner rings or discs, which are enhanced by the bar's ability to provide the necessary fuel for their creation. In the following section we will further investigate central regions.

5.2.2 Central and bar values

Our previous analysis coupled with hints towards a potential influence of bars in the central regions, predicted by simulations and already seen in observations (e.g., Chung & Bureau, 2004; Fathi & Peletier, 2003), leads us to systematically test the central parameters against the strength of the bar. We use the average found within the aperture of $R_{eff}/8$.

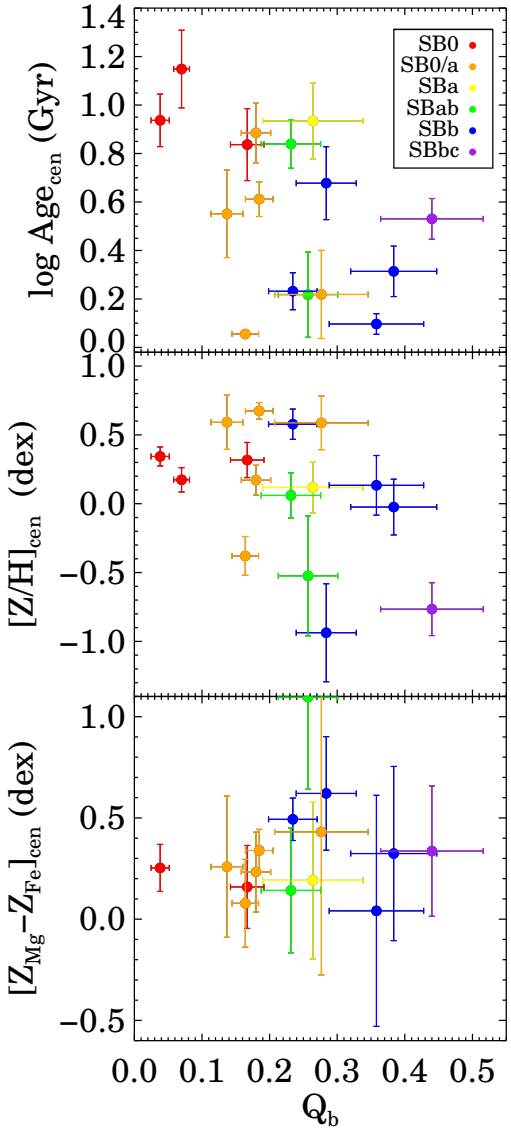

FIGURE 5.6: Central ages, metallicities and abundances, measured within the central aperture of $R_{eff}/8$, as a function of bar strength and coulor-coded by Hubble type.

Figure 5.6 shows a weak correlation of age and Q_b, such that stronger bars have younger central stellar populations (linear Pearson correlation coefficient R=0.57 and p-value=0.02). This confirms the proposed scenarios of bars funneling material to the center triggering or nourishing star formation (e.g., Knapen,

2005; Allard et al., 2006; van der Laan et al., 2013a). Very recent studies in fact found a central enhancement of the nitrogen-to-oxygen abundance and a larger star formation rate per unit area (Florido et al., 2015).

At the same time we also observe slightly lower metallicities with increasing bar strength. We notice however, that the galaxies in our sample seem to have metallicity offsets with respect to each other such that most late types have generally lower metallicities, a known Hubble type effect. Overall, the central metallicities are found to not correlate strongly with bar strength (linear Pearson correlation coefficient R=0.45 and p-value=0.08).

The very right part of the figure displays the trend with abundance. We observe again a large scatter similar to the metallicity. Our sample in this case is definitely too small to draw any firm conclusion.

The trends discussed above could also result as a consequence of different Hubble types. Apart from the trends already revealed through the colour-code in the figure, we explored the correlation with Hubble type for our barred sample and other comparison samples, only selecting unbarred galaxies. The age and metallicity trends are both found for Hubble type, too, but bars seem to lower them slightly. In particular, they seem to lower the metallicity in later types. Nevertheless, the statistics are very low and the scatter is large, probably due to yet other mechanisms that come into play in the central parts of galaxies altering these parameters.

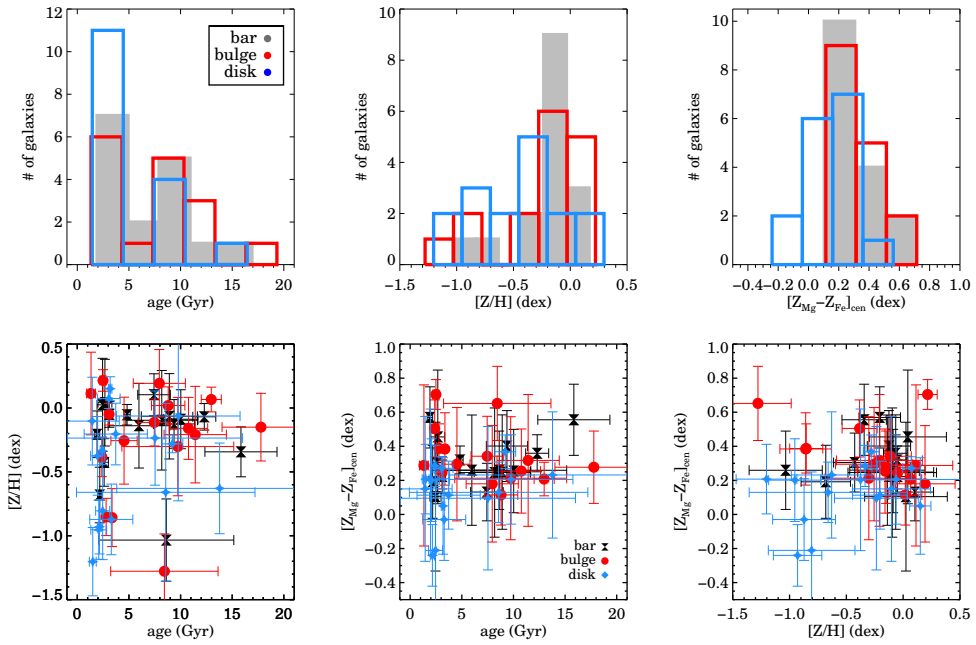

FIGURE 5.7: *Top row:* Mean ages, metallicities and abundances of the bar (gray, filled) in comparison with those of the bulge (red line) and disk (blue line) for the BaLROG sample. *Bottom row:* Correlations between ages, metallicities and abundances for the different regions.

Apart from the central values, we also calculated values at specific regions, namely for the bar (filled, gray), bulge (red lines) and disk region (blue lines),

shown in Fig. 5.7 for our sample. The top panels show histograms of the regions and the bottom panels the correlation of the different parameters. The regions are approximated as they are not based on a photometric decomposition. The bar region contains bins well outside the inner regions (from 0.35 to 0.95 barlength, averaging bins along the bar major axis). Our bulge contains bins between 0.05 up to 0.2 barlength (to avoid the center) and the disk everything further away than one full barlength.

The histograms show a similarity between bulge and bar in all three panels. The disks are also following these overall trends but are more different from the former two components, as expected (e.g., Pérez, Sánchez-Blázquez & Zurita, 2007). In particular in the abundance (right panel), they show a significant offset towards lower values compared with bulges and bars and in general a broader range of abundances.

In the age distribution, we distinguish two peaks in the distribution, one old and one at a younger age. As there remains a large number of young disks however, some of the older bars and bulges must be residing in these younger disks. Investigating the obtained maps, we find that many early-types show bars of $\sim$10 Gyr in a younger disk. Late-types are overall younger, i.e. the bar, bulge and the disk. The metallicity shows that a large fraction of bars have a common metallicity just below solar. They are slightly less metal-rich than the bulge but significantly more than the disk. Bars and bulges also seem to be very similar in their abundance while disks show significantly lower values. Table 5.1 summarizes the central and bar measurements for indices and SSP parameters.

In the bottom row of Fig. 5.7, we show the correlations between the SSP parameters of the different regions. There seems to be a tentative trend among bars and bulges. Despite being rather more metal-rich overall, they seem to get more metal-rich towards younger ages. In particular at the youngest ages, a large spread of metallicities, especially in disks, is found. The trends between abundance vs. age are as expected: older ages show higher abundances. Although some bars and bulges, despite being young, show high abundances. This can be an effect of the luminosity weighted age, which is biased towards younger populations. Furthermore, we cannot fully exclude an influence of the bulge light contributing to the bar (or vice versa). The offset between bars and bulges compared with disks is best seen in the last panel: while the former show higher metallicities coupled with higher abundance values, disks show the opposite.

5.2.3 SSP Profiles

Apart from central and regional values, we have the entire two-dimensional maps for all galaxies available. These maps and profiles for all galaxies can be found in the appendix and are displayed for NGC 4394 as an example in Fig. 5.8. As expected, the SSP maps and radial results are closely related to the indices. The age map shows younger ages corresponding to high H_β values (in the presence of spiral arms in this case). The very center seems to be young, but sitting in an older structure, as seen due to the very steep rise at both sides of it. The age of the center in fact compares well to that of the disk,

TABLE 5.1: Stellar population parameters for the BaLROG sample. - (1) Galaxy name, (2) - (4) central line-strength values and (5), (6) central age and metallicity values, (7), (8) age and metallicity of the bar region. Although errors differ, in particular between young and old populations (higher for older populations), we will give a general estimate, such that typical uncertainties for the $H_{\beta,R_{\rm eff/8}}$ values are 0.1 Å, 0.5 Å for $Fe5015_{R_{\rm eff/8}}$ and 0.2 Å for $Mgb_{R_{\rm eff/8}}$. For ages and metallicities, the uncertainties are 2.3 Gyr for $Age_{R_{\rm eff/8}}$, 0.29 dex for $[Z/H]_{R_{\rm eff/8}}$, 3.2 Gyr for $Age_{R_{\rm bar}}$ and 0.34 dex for $[Z/H]_{R_{\rm bar}}$. Objects forming part of the Virgo cluster are marked with a small v next to their name. Notes. - Line strength indices, ages and metallicities are determined in this work and values are given within $R_{\rm eff/8}$ as a central measurement.

Galaxy	$H_{\beta,R_{\rm eff/8}}$ (Å)	$Fe5015_{R_{\rm eff/8}}$ (Å)	$Mgb_{R_{\rm eff/8}}$ (Å)	$Age_{R_{\rm eff/8}}$ (Gyr)	$[Z/H]_{R_{\rm eff/8}}$ (dex)	$Age_{R_{\rm bar}}$ (Gyr)	$[Z/H]_{R_{\rm bar}}$ (dex)
(1)	(2)	(3)	(4)	(5)	(6)	(7)	(8)
NGC 1015	1.77	4.53	3.60	8.59	0.11	8.17	-0.096
NGC 2543	3.18	3.58	1.85	1.24	0.37	2.44	0.024
NGC 2712	2.49	1.77	1.83	4.76	-0.93	8.62	-1.033
NGC 2859	1.78	4.99	3.88	6.86	0.31	10.0	-0.088
NGC 2893	3.75	2.23	1.12	1.13	-0.37	2.17	-0.680
NGC 2962	1.82	5.54	4.33	3.55	0.59	8.91	-0.065
NGC 3485	2.86	3.33	2.10	2.06	-0.02	2.59	-0.426
NGC 3504	4.20	1.88	1.41	1.65	-0.52	1.91	-0.205
NGC 4245	2.18	5.24	3.72	1.02	0.67	4.81	-0.053
NGC 4262^{v}	1.19	4.72	4.72	13.0	0.17	15.8	-0.343
NGC 4267^{v}	1.61	5.28	4.35	8.64	0.34	12.2	-0.069
NGC 4394^{v}	2.58	4.35	2.92	1.70	0.57	3.10	-0.049
NGC 4643	1.97	5.55	4.01	1.65	0.58	7.42	0.103
NGC 5350	2.23	3.98	2.85	3.39	0.06	2.67	0.041
NGC 5375	1.91	4.30	3.23	6.91	0.06	5.97	-0.138
NGC 5701	1.80	4.54	3.63	7.68	0.17	9.37	-0.125

suggesting that their star formation events might have occurred at a similar epoch. However, this could also be an influence of the bar which could produce younger stellar populations at the center and at the end of the bar as predicted by Wozniak (2007). We also observe that the average age of bars in mainly our early-type galaxies is of the order of the bulge and rather old, usually up to 10 Gyr, no matter if they reside in a young, star forming disk (see Fig. 5.7 and individual maps in Appendix A). The later types host younger bars however as they are overall younger.

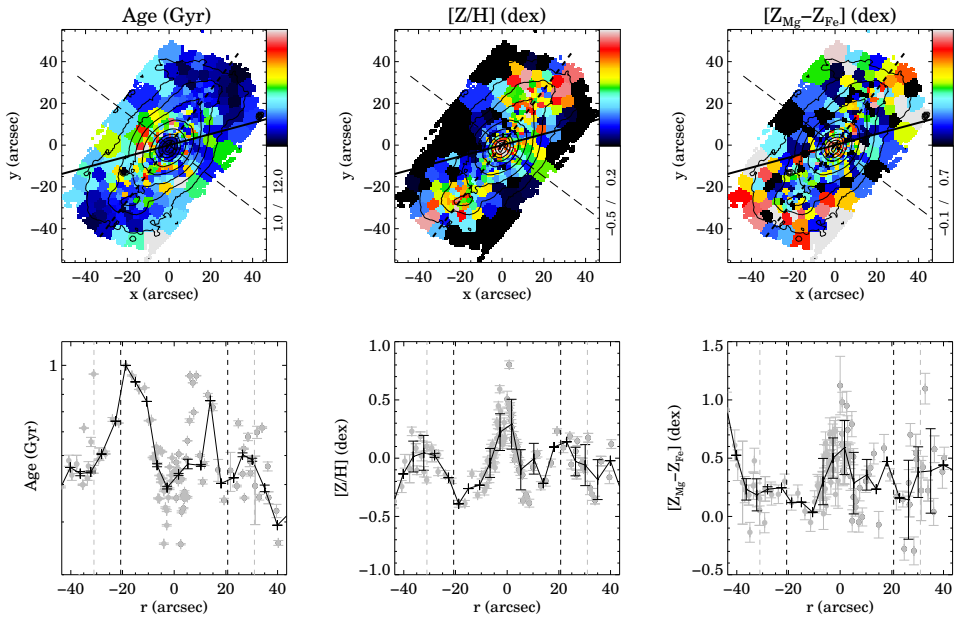

FIGURE 5.8: SSP profiles for NGC 4394. On top we present the SSP maps of age, metallicity and abundance with the major axis indicated by a straight black line, the bar major axis by a dashed black line and the bar minor axis by a dotted-dashed line. The panels below show the profile along the bar major axis directly extracted from the map with a slit of width of 3 arcsec in order to trace along the bins. We show individual measurements in gray and averaged values overplotted in black. Half and three quarters of the bar length are indicated by dashed black and gray lines respectively.

The metallicity reflects best the structure seen in the Fe5015 profiles. The central peak, as well as the peaks around half to three quarters R_{bar} are clearly visible. This is the case for several of the other galaxies, too, although some of the profiles suffer from larger scatter than the index profiles. About 40% of our sample shows higher metallicities along the major than the minor axis (in agreement with the Mg*b* and Fe5015 indices).

The abundance is very similar and agrees within error bars along both axes. The abundance map of NGC 4394 in the example figure shows indeed a clear difference between the center, the barred region and the outskirts where the spiral arms start. Within the barred region it remains practically flat and lower than for the inner and outer regions. This is not typically the case. We find a large variety showing central enhancements as well as drops amongst the galaxies of our sample.

5.3 Gradient analysis

One of the most studied aspects of bar-driven secular evolution is the effect on the stellar population gradients. Early theoretical work (e.g., Friedli, Benz & Kennicutt, 1994) suggest a significant flattening of the abundance gradients in barred galaxies. This result is further strengthened by more recent work also finding weaker metallicity gradients in the presence of a strong bar (e.g., Minchev & Famaey, 2010).

5.3.1 Break position

While observations and theory have primarily considered the overall gradient, we attempt to separate gradients and investigate their behaviour in dependence of the host galaxy's bar properties, i.e. their strength. This step is further motivated in the light of our results suggesting a noticeable bar influence in the central regions. In fact, changes in the slope of the gas-phase metallicity gradient have been distinguished and studied in numerous works (e.g., Zaritsky, 1992; Vila-Costas & Edmunds, 1992; Martin & Roy, 1995; Zahid & Bresolin, 2011). Their existence is usually attributed to variations of the gas density as a result of bar-driven large-scale mixing (Friedli & Benz, 1995).

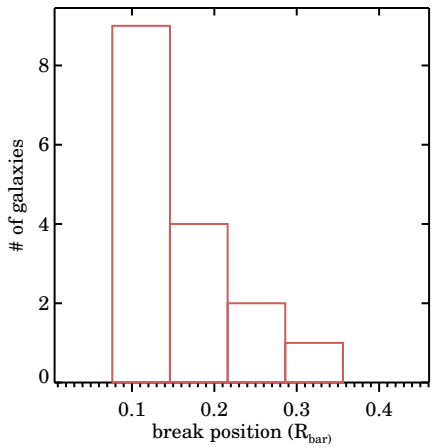

FIGURE 5.9: Location of the break position for the SSP profiles (almost identical with that for the index profiles).

Earlier works on stellar metallicity gradients such as MacArthur, González & Courteau (2009) or Pérez & Sánchez-Blázquez (2011) have also separated gradients based on a bulge-disk decomposition. In some of their profiles, this transition coincides with the innate breaks of the profiles. In other cases however, the structure of the profile itself is not taken into account and the gradients are fitted within the predetermined bulge region (bar, disc regions). Our analysis is based only on the shape of the index and SSP profiles in order to avoid biases coming from the photometry or applied bulge-disk decompositions. The work by Sánchez-Blázquez et al. (2014a) uses this same method to differentiate regions of different metallicity and metallicity gradients. This is crucial, in particular as former studies have not distinguished these breaks (e.g., Sánchez

et al., 2011). The comparison between line-strength indices and full spectral fitting results are in a good agreement, which gives particular confidence in our results. We conclude that it is important to differentiate between areas of distinct slope either by a prior decomposition or by directly observing the profiles. Both attempts bear advantages and disadvantages of course and are simply based on different assumptions.

We investigated the position of the break in the index and SSP profiles (see Fig. 5.10) which determined two regimes of different gradients. Figure 5.9 illustrates this analysis, showing the locations for the SSP profile breaks (averaged values from all profiles). They are very similar to the positions of the index profile breaks. In both cases more than 50% of the galaxies have their break at around 0.1 R_{bar}, a few up to 0.2 -0.3 R_{bar}. Summarizing our kinematic as well as population analysis, it seems that this location, around 0.13±0.06 R_{bar}, is a key location in barred galaxies.

5.3.2 Line-strength gradients as a function of bar strength

As the SSP values are based on the line strength values which are directly measured on the data, we first determine the gradients directly from the index values. In Fig. 5.10, we show the profiles with the gradients indicated for Mg*b* as an example. Doubtlessly, the break in most profiles stands out clearly for our data. At the same time we wish to point out the necessity for sufficient spatial resolution in order to resolve these profiles and thus be able to distinguish between the two gradients. This distinction is particularly important in barred galaxies as they have rich inner substructures such as inner disks or rings that could alter the overall gradient significantly (e.g Erwin & Sparke, 2002; MacArthur et al., 2004; MacArthur, González & Courteau, 2009; de Lorenzo-Cáceres, Falcón-Barroso & Vazdekis, 2013).

Figure 5.11 reveals a clear difference between the inner and outer index gradients, each consistent for major (black points) and minor axis (gray points) measurements. Apart from the major difference in magnitude, much stronger correlations with bar strength are observed for the inner gradients. In particular for the Fe5015 gradients, the correlation is found to be strong, resulting in a linear Pearson correlation coefficient of R=0.71 (p-value=0.002). For the other two indices, tentative correlations with bar strength can be observed, but among our small sample, the scatter is large and it is difficult to deduce a definite conclusion. The linear Pearson correlation coefficients are R=0.31 (p-value=0.24) for the H_β gradients and R=0.61 (p-value=0.01) for Mg*b*. Overall, the H_β gradient (as a proxy for age) seems to decrease with bar strength while the two gradients of the metallicity proxies, Fe5015 and Mg*b* seem to increase consistently.

The outer gradients are all much lower in magnitude. While the H_β outer gradients seem to correlate with bar strength, the two metallicity indicators show a scatter around zero or below. The fact that the H_β gradients seem to increase with bar strength could imply an effect of bars or a relation of them to the disk. The linear Pearson correlation coefficient in this case is R=0.62. Its p-value of 0.01 only gives a tentative significance.

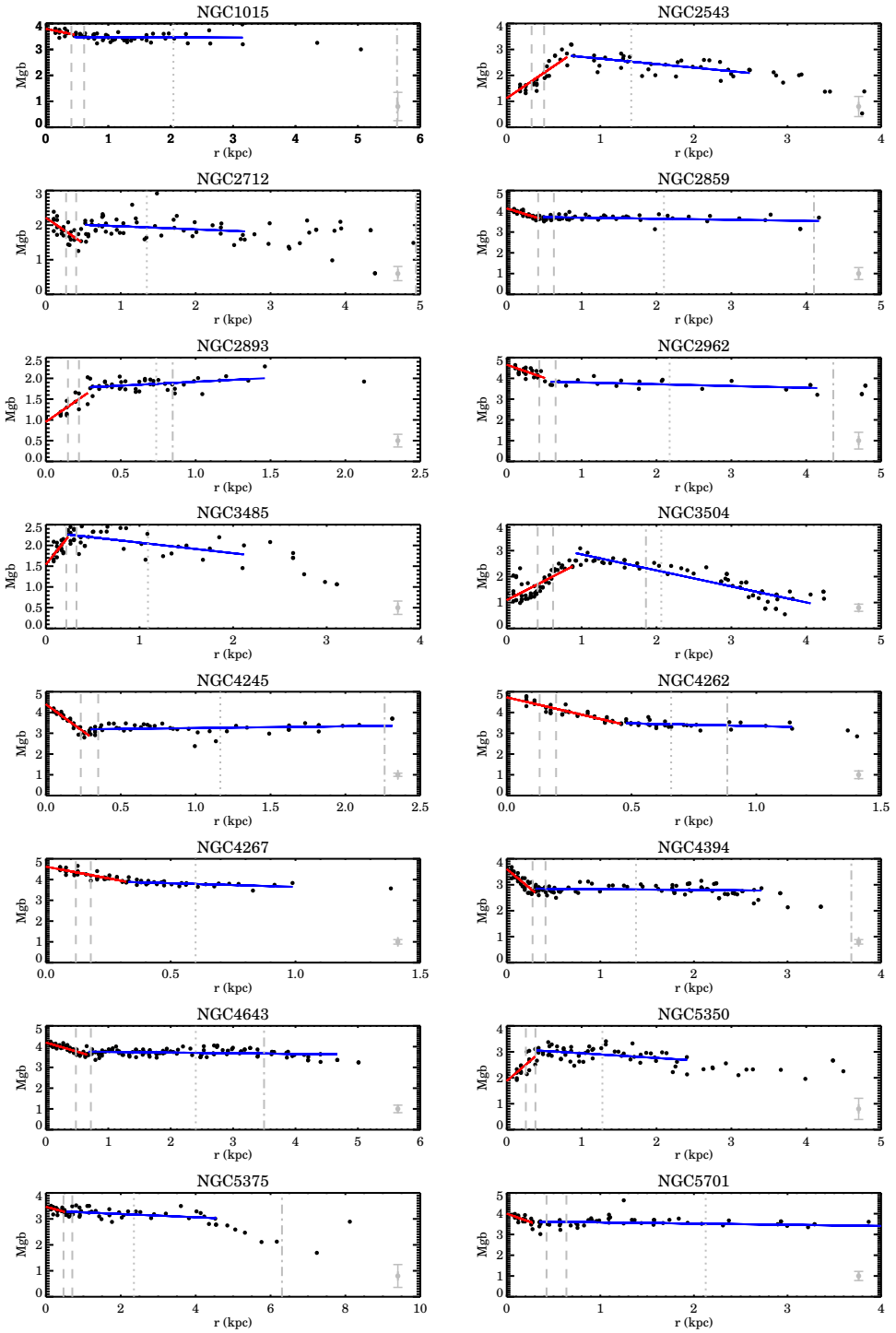

FIGURE 5.10: Major axis profiles and linear inner (red) and outer (blue) gradients of the Mg*b* index as an example of the index measurements for the entire BaLROG sample. The mean uncertainty is indicated in each panel in the lower right corner. Dashed lines indicate the region between 0.1 and 0.15 R_{bar}, dotted lines the position of 0.5 R_{bar} and dashed-dotted lines the position of 1.5 R_{eff}.

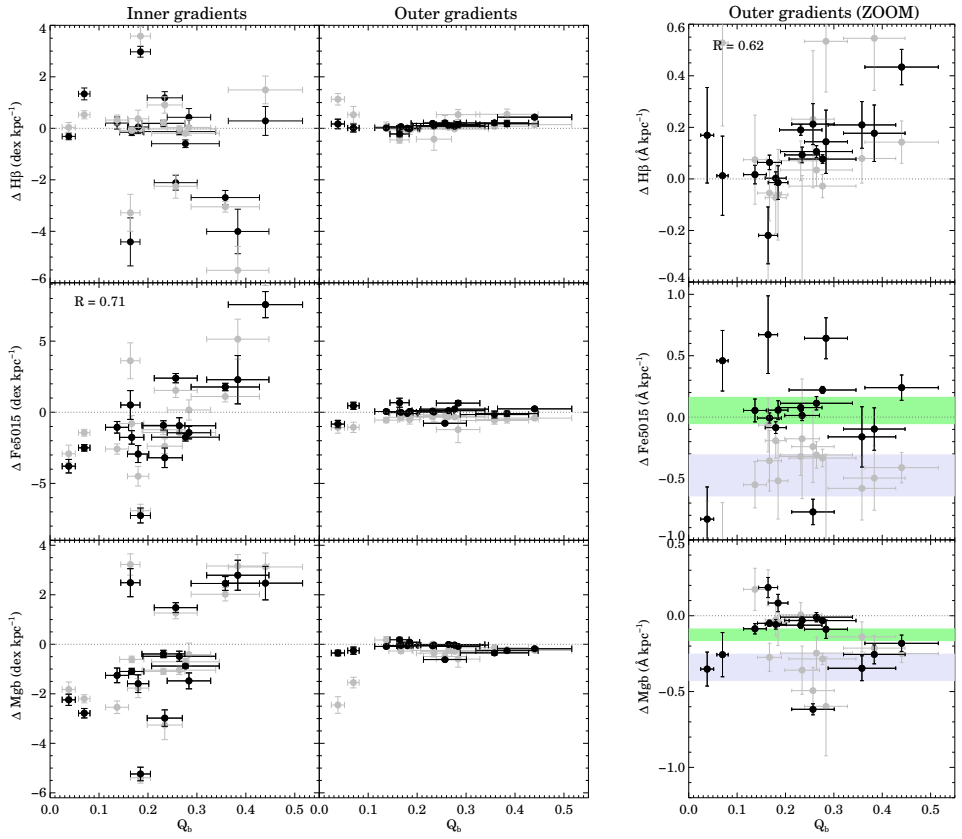

FIGURE 5.11: Inner and outer index gradients for H_β, Fe5015 and Mg*b*. We depict the outer gradient twice to 1) highlight its difference in magnitude to the inner gradient (middle panel) and 2) illustrate its values in greater detail (right). Black points represent bar major axis measurements while gray points can be attributed to the corresponding minor axis results. The linear Pearson correlation coefficient is indicated in two cases as R, for the rest it was not significant. In the right panels we furthermore indicate the averaged values (by weight) for the bar major axis measurements (green - upper bar) and for a combination of bar minor axis measurements and measurements on unbarred galaxies from the SAURON and ATLAS3D surveys (gray - lower bar).

As often, this could also be an effect of the galaxies' Hubble types. In our sample (as found in general, see, e.g. Laurikainen et al. 2007), later types exhibit stronger bars. Numerous earlier studies using colours (e.g., de Jong, 1996; Peletier & Balcells, 1996; MacArthur et al., 2004; Muñoz-Mateos et al., 2007, 2009) already found bluer outer parts in disk galaxies. This was confirmed by spectroscopic studies measuring elevated H_β (corresponding to younger ages) in the external regions (e.g., Yoachim & Dalcanton, 2008; MacArthur, González & Courteau, 2009; Sánchez-Blázquez et al., 2011; Yoachim, Roškar & Debattista, 2012; Ruiz-Lara et al., 2013; Sánchez-Blázquez et al., 2014a). Therefore, we expect to find positive values when measuring the gradient towards the edge of the bar. The value of these gradients is further expected to increase when going to later types as the disks are found to be even bluer. This effect could be enhanced by the presence of a bar due to bar-spiral coupling (e.g., Minchev & Famaey, 2010). On the one hand, the process of bar-spiral coupling is supposed to make mixing mechanisms more efficient and therefore possibly erase strong gradients. On the other hand, through the enhanced perturbations, gas

could be funneled more efficiently to these regions and star formation might be triggered easier. However, the flattening of the gradient occurs on a large time scale. The effect of recent young populations could be therefore enough to raise the luminosity weighted line-strength gradient of H_β.

For a comparison with galaxies without bars, we chose unbarred galaxies from several surveys, always matching our inclination and redshift constraints. For early-types, we took the ATLAS3D (Cappellari et al., 2011a). For early-type spirals (Sa), we chose galaxies from the SAURON (Bacon et al., 2001) studies, taking data from Peletier et al. (2007). To include later types, we also took galaxies from the late-type extension of the SAURON survey, using data from Ganda et al. (2007).

We performed our analysis analogously to the BaLROG sample on these galaxies and also obtained slopes of inner and outer gradients. When trying to detect breaks in the index gradients of the unbarred sample, we found that in some cases, they were not as obvious as in the barred galaxies, in particular for the later types. In certain cases in fact, the gradient did not exhibit a strong break, but rather showed a continuous profile as expected, leading to similar inner and outer gradients. This confirms former results, e.g., by Morelli et al. (2008) who only found very weak age gradients in a sample of unbarred galaxies. Hence, we suggest that this lack of breaks in the index profiles is not due to the outer gradients, as their magnitude remains comparable to the ones measured in BaLROG, but to the lack of inner substructures such as nuclear disks or rings. The fact that we find a strong difference of inner and outer gradients in our sample of barred galaxies confirms the influence of bars in creating those substructures, particularly by providing the fuel for subsequent star formation (e.g., Knapen, 2005; Knapen et al., 2006; Peletier et al., 2007; Comerón et al., 2010).

Comparing the value of the observed gradients in H_β, we find a stronger dependence on Hubble type than the presence of bars: our average major and minor bar gradients are practically the same, 0.10±0.07 Å/kpc and 0.11±0.16 Å/kpc respectively. The ATLAS3D sample of unbarred galaxies yields a value of 0.13±0.06 Å/kpc, the SAURON (S0 and Sa galaxies) a value of 0.14±0.11 Å/kpc and the late-type SAURON sample 0.24±0.09 Å/kpc. In context with former studies finding bluer (younger) outer regions of disk galaxies (e.g., de Jong, 1996; Peletier & Balcells, 1996; MacArthur et al., 2004), we conclude that the measured gradients are dominated by this effect: for later types the outer disk regions become increasingly bluer and hence steepen the overall H_β gradient, with or without a bar.

The gradients determined from Fe5015 as well as Mg*b* profiles however are systematically steeper along the minor bar axes compared to the major bar axis. The latter are closer to zero, in particular for Fe5015. We indicate the mean values of the bar major axis measurements for iron and magnesium in green (upper bar) in both plots. The lower gray bar is a representative value for minor axis measurements as well as unbarred galaxies where we measured iron and magnesium gradients for the same samples as for H_β. For these metallicity indicating gradients, we observe a much larger similarity of the unbarred galaxies with the bar minor axis measurements. Quantitatively, we find a mean

value for the outer gradients in Fe5015 along the bar major axis in our BaLROG sample of 0.05±0.1 Å/kpc while the minor axis shows -0.47±0.24 Å/kpc. The effect of the contrast between bulge and bar components could add to the steepening, but is not fully responsible for it. The unbarred SAURON S0-a and Sa galaxies (also within our inclination limits) show -0.55±0.23 Å/kpc and the ATLAS3D (mainly S0 and S0-a galaxies) show -0.34±0.12 Å/kpc and the late-type galaxies -0.58 ±0.12 Å/kpc . The weighted mean value of the comparison samples is -0.49 Å/kpc in comparison with 0.05 Å/kpc for the bar major axis measurements. For the Mg*b* index, we find a mean value of -0.34 Å/kpc amongst the comparison samples and a value of -0.13±0.05 Å/kpc along the bar major axis.

The results for the Fe5015 gradients are summarized in Fig. 5.12 where each curve represents the mean value and its error. The difference can clearly be appreciated. We also observe a trend that earlier types (ATLAS3D) seem to show shallower gradients than late-types. Therefore, we furthermore separated early- and late-type galaxies for the bar major axis measurements and within this sample, we actually find that the earlier types are not necessarily shallower but actually more positive. Nevertheless, the separation is small and hence we conclude that in this case, the bar is in fact the driver and not the Hubble type.

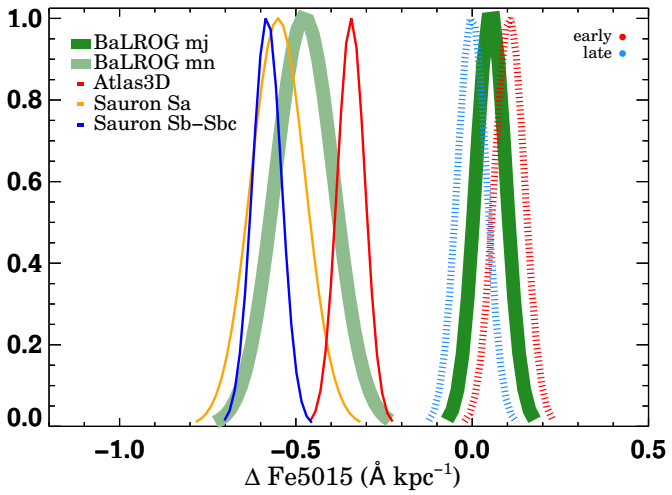

FIGURE 5.12: Mean values and their uncertainties shown as gaussians for the Fe5015 gradients for the BaLROG bar major and minor axis in comparison with the ATLAS3D, SAURON and late-type SAURON samples. Additionally, we separate early and late-types for the BaLROG galaxies .

This analysis confirms our hypothesis that bars display flatter gradients, but only along the bar major axis. A similar result was found in a pilot study by Sánchez-Blázquez et al. (2011), but only using two galaxies. Other studies have not compared profiles along these different axes nor used the distinction of inner and outer gradients based on the observed break in the index profiles. Instead the inner and outer gradients have been separated using the bulge radius which was determined from the photometry. We believe that this different methodology can lead to different results, as the differences between the gradients are

not large and can be washed out easily. In any case, the flattening of the Fe5015 and Mg*b* gradients could be a first indicator of a flattening along the bar. We will look into more details when analysing the SSP gradients in the following section.

5.3.3 SSP gradients as a function of bar strength

Similarly to the index gradients, we determined the slopes along the SSP profiles (age, metallicity and abundance), again considering two distinct regions within the bar region. An example for the metallicity is shown in Fig. C.20 in appendix C.3. The absolute values found for the outer gradients are comparable in magnitude to the ones found in previous studies, such as the recent study of CALIFA galaxies (e.g., Sánchez-Blázquez et al., 2014b). As found for the index profiles, there is a clear difference between two gradients in our SSP profiles. To make this distinction and to identify the break in the profiles is crucial for unravelling the influence of bars.

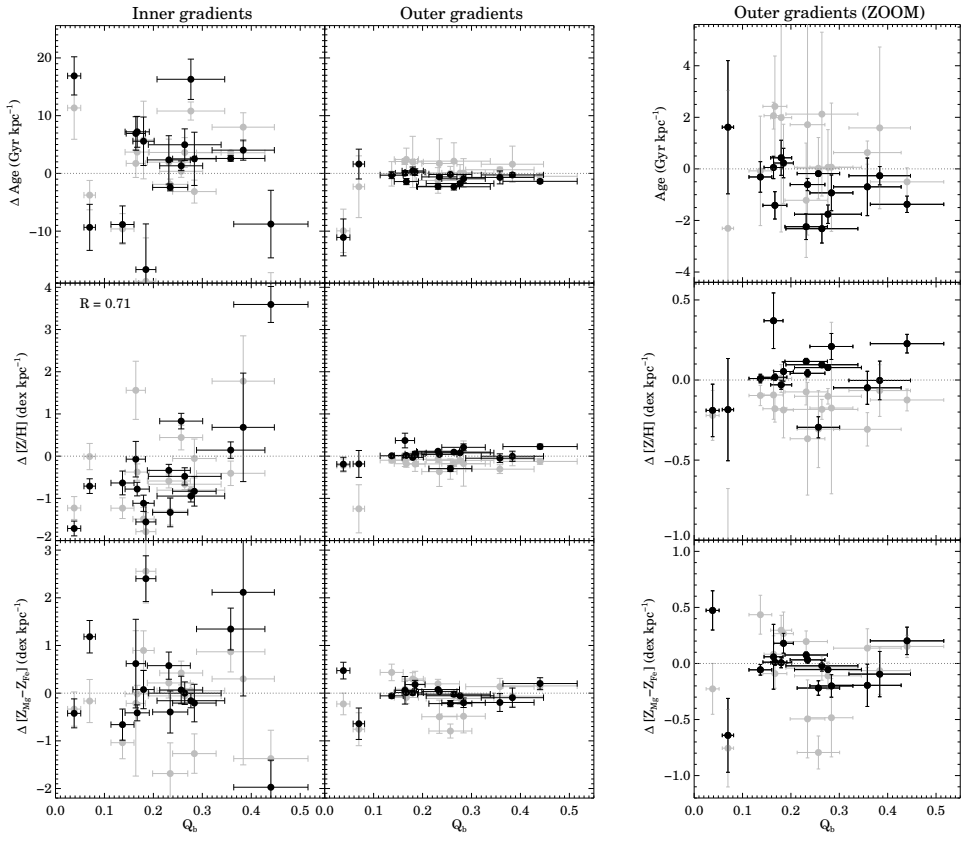

FIGURE 5.13: Inner and outer index gradients for age, metallicity and abundance. We depict the outer gradient twice to 1) highlight its difference in magnitude to the inner gradient (middle panel) and 2) illustrate its values in greater detail (right). Black and gray points represent the same as in Fig.5.11. The linear Pearson correlation coefficient is indicated in the case of the inner metallicity gradient as R=0.71, for the rest it was not significant.

As already seen for the indices, the magnitude of the inner gradients is much higher (see Fig. 5.13). This time, we only find a correlation of the inner metallicity gradients with bar strength. Weaker bars show a stronger negative metallic-

ity gradient. Supposing an initial negative metallicity gradient (e.g., Di Matteo et al., 2013), this finding implies that weak bars allow it to survive. Towards stronger bars, this gradient seems to flatten and then turns into a positive gradient in fact, such that metallicities get higher in the bar regions compared to the center. In addition, we observe once more an agreement of the results along major and minor axes. This could also suggest that the influence of the bar, if it reaches these regions, is rather quickly distributed radially around the center.

While the gradients agree for the inner regions between major and minor axes, the outer gradients along the different axes are slightly different. In the amplification of the panels on the right side of Fig. 5.13, it can be seen that the age gradients along the major axis are slightly negative. The opposite is the case for the age gradients along the bar minor axis. As our gradients stop at the maximum bar length, this could be the result of the entering spiral arms along the major axis which leads the gradients to be slightly negative, hence going towards younger populations towards the outer parts. Simulations by Wozniak (2007) suggest that young populations are indeed found at the edges of bars. Furthermore, the disc region with the spiral arms might not have been reached along the minor axis.Therefore, the gradient in those cases can result to be slightly positive, i.e. the population is younger in the inner parts.

The outer metallicity gradient exhibits a similar behaviour as the Fe5015 (and Mg*b*) index: bar major axis gradients are found to be closer to zero, while bar minor axis gradients are found to be slightly more negative. This supports the notion of increased flattening of the metallicity gradient along the bar major axis, also found for two galaxies in Sánchez-Blázquez et al. (2011). We furthermore compute metallicity gradients of three unbarred control samples already mentioned above, namely ATLAS3D (Cappellari et al., 2011a), SAURON S0 and Sa galaxies Peletier et al. (2007) and late-type SAURON galaxies Ganda et al. (2007). We use the same method as for our sample: we first derive the metallicities with `rmodel` from the line strength maps provided by the published work; then we determine the profile and identify its break to measure the two slopes. Figure 5.14 illustrates the clear difference between the outer metallicity gradient along the bar major axis and the significantly steeper metallicity gradients found along the minor axis and in all unbarred samples. Along the bar major axis we find the metallicity gradient to be 0.03±0.07 dex/kpc whereas the mean value of the minor axis and unbarred control sample is -0.20±0.04 dex/kpc. We mention once more that the contrast effect between the bulge and bar component can alter the gradient, but cannot account for the general flattening along the bar major axis. It might lead however to some of the positive gradients that we measure, which are not necessarily expected according to bar-driven secular evolution. We further note a very mild trend with Hubble types among the unbarred control samples in the sense that steeper negative gradients are found in later type galaxies. Consistent with our former results on Mg*b* and Fe5015 gradients, this trend is well within the uncertainties and the difference of barred (*along the bar major axis*) vs. unbarred (or barred, but not along the bar axis) is much higher. We therefore suggest the bar as the responsible agent for this flattening.

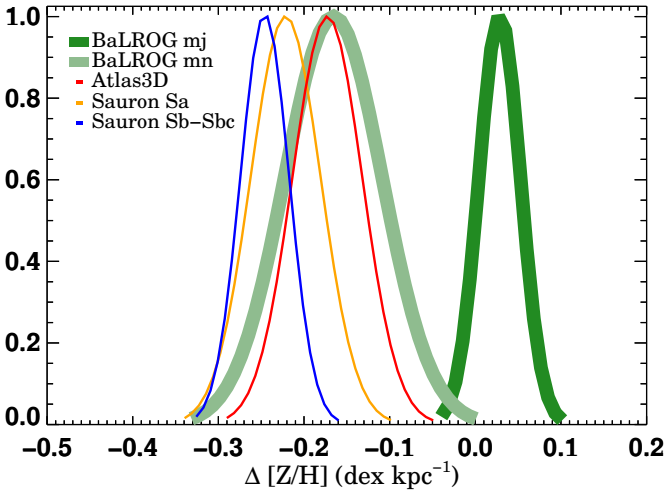

FIGURE 5.14: Mean values and their uncertainties shown as gaussians for the metallicity gradients for the BaLROG bar major and minor axis in comparison with the ATLAS3D, SAURON and late-type SAURON samples.

The abundance profiles do not reveal any tendency. We note however, that those values need to be taken with care due to the mixture of populations already revealed and observed in the index-index diagrams.

We note however, that the enhancement can also be an effect of contrast between the bulge and the bar components. Considering the high steep gradient of the inner structure and the light contribution of the bulge, compared with the flatter gradient of the bar and its light, the combination of both can make the gradient in the inner bar to be less steep, flat or even positive.

5.4 Discussion

5.4.1 Discrepancies in the literature

As already illustrated in the introduction, numerous works have been studying the influence of bars on the metallicity and abundance gradients. Simulations and theoretical studies mainly propose a flattening of these gradients, which is even stronger for older stellar populations (e.g., Friedli, Benz & Kennicutt, 1994; Minchev & Famaey, 2010). These theoretical results have only been partly found by observations. While some studies (e.g., Martin & Roy, 1994; Sánchez-Blázquez et al., 2011; Williams, Bureau & Kuntschner, 2012) confirm the flattening, others observe a large variety (e.g., Pérez, Sánchez-Blázquez & Zurita, 2009) and recent results do not find any difference in the gradients of barred or unbarred galaxies (e.g., Cacho et al., 2014; Sánchez-Blázquez et al., 2014b; Cheung et al., 2015a). There are however significant differences between the studies that could lead to this disagreement. In particular, it is crucial *where* the gradient is measured and also *along which axis* and at which possible *spatial resolution*. The last aspect is especially important to be able to distinguish different types of gradients which could be related to different drivers.

To start with, simulations disagree on the initial overall gradient and its tempo-

ral evolution. While most chemical evolution models predict an initially negative metallicity gradient that flattens in time (e.g., Mollá, Ferrini & Díaz, 1997; Mollá & Díaz, 2005; Schönrich & Binney, 2009; Fu et al., 2009) others start with flat or even initially inverted gradients that steepen with time (e.g., Samland, Hensler & Theis, 1997; Chiappini, Matteucci & Romano, 2001). The work of Pilkington et al. (2012) and Gibson et al. (2013) attribute these discrepancies to the influence of the sub-grid physics employed in the hydrodynamical codes used in cosmological simulations, where galaxy formation crucially depends on the implemented feedback schemes. Observationally, an inside-out formation scenario, leading to final overall negative metallicity gradients is commonly confirmed (e.g., de Jong, 1996; Bell & de Jong, 2000; MacArthur et al., 2004; Muñoz-Mateos et al., 2007). Our results on the outer metallicity gradients confirm this finding. We typically observe negative metallicity gradients, in particular when extending to the outer disk regions. Only when measuring the gradient along the bar major axis do we observe differences.

So, which influence can bars have and do they or not produce a flattening and if so where and why? A flattening of the overall gradient is supposed to be most obvious in the outer parts, even beyond bar corotation due to a bar-spiral coupling (e.g., Minchev, Chiappini & Martig, 2013; Di Matteo et al., 2013). This is the metallicity gradient examined in studies such as done by Sánchez-Blázquez et al. (2014b) without any hint for a flattening introduced by the bar. This result is supported by other works also studying the global (or integrated) metallicity gradients and which also do not detect any difference between barred or unbarred galaxies (e.g., Cacho et al., 2014; Cheung et al., 2015a).

However, one must distinguish between this outer (and global) and yet another inner gradient: due to the bar providing the necessary fuel to trigger central star formation in the nuclear region, abundance gradients can steepen significantly in these regions (e.g., Friedli, Benz & Kennicutt, 1994). In fact, even in unbarred galaxies, a clear break in the stellar metallicity profile has been detected and inner and outer gradients have been distinguished (e.g., Sánchez-Blázquez et al., 2014a). Furthermore, the axis along which the gradient is measured is important. Scarce former studies have compared the metallicity gradients along the bar with that perpendicular to it or along the disk major axis and detected flatter gradients along the bar major axis (Pérez, Sánchez-Blázquez & Zurita, 2009; Sánchez-Blázquez et al., 2011; Williams, Bureau & Kuntschner, 2012). This difference is predicted by simulations (e.g., Di Matteo et al., 2013; Martinez-Valpuesta & Gerhard, 2013), although the absolute value of the gradient is strongly dependent on the initial metallicity gradient in the disk. In simulations by Martinez-Valpuesta & Gerhard (2013) the initial gradient along the bar of -0.4 dex/kpc evolves to a final value of -0.26 dex/kpc, while (Friedli, 1998) starts with an inital gradient of -0.1 dex/kpc and hence also obtains a lower final value.

Our work clearly distinguishes the regions of different gradients. This allows us to differentiate between the influence of inner substructures and overall properties along the bar compared to the overall galaxy. We do observe a flattening of the metallicity gradient, but only *along the bar major axis*. This flattening is a small effect as expected from former studies that did not reach a consensus

on a difference in stellar metallicity gradients in barred or unbarred galaxies, and confirms the flattening seen along the bar major axis (Pérez, Sánchez-Blázquez & Zurita, 2007, 2009; Sánchez-Blázquez et al., 2011; Williams, Bureau & Kuntschner, 2012; Sánchez-Blázquez et al., 2014b; Cheung et al., 2015a). The implication of our finding of a flattening along the bar compared with steeper gradients observed along other axes or in unbarred galaxies is discussed in the following section.

5.4.2 The role of bars in galaxy evolution

The results obtained in our work clearly indicate an influence of bars on the stellar populations of their host galaxies. As explained above, this does not contradict former studies that claim no difference between stellar population parameters of inner regions (bulge) or metallicity gradients between barred and unbarred galaxies. Most of the differences and discrepancies between former studies arise due to different analysis techniques and/or spatial resolution effects (see above, Section 5.4.1).

Our results reveal a subtle but noticeable influence of bars in the central regions. They are able to trigger or at least favour the build-up of substructures leading to younger ages, higher metallicities and different orbital configurations. This confirms numerous former studies on central star formation, nuclear-rings and inner disks (e.g., Heller & Shlosman, 1994; Knapen et al., 1995; Allard et al., 2006; Knapen et al., 2010; van der Laan et al., 2013b).

Furthermore, we demonstrate for the first time with a representative sample of barred galaxies, compared with a large number of unbarred galaxies, that the metallicity gradients along the bar are significantly shallower than along another axis or in the unbarred control sample. Simulations of chemical evolution models investigating bar-driven secular evolution predict a flattening of the metallicity gradients of barred versus unbarred galaxies (e.g., Friedli, Benz & Kennicutt, 1994; Di Matteo et al., 2013). This has yet to be observed, in particular in the outer parts, beyond corotation, where the effect is supposed to be strongest (e.g., Brunetti, Chiappini & Pfenniger, 2011). So far, studies have found no difference (see above and Sánchez-Blázquez et al. 2014b). However, Di Matteo et al. (2013) also predicts a flattening in the inner regions of barred systems and as such the behaviour observed in Sánchez-Blázquez et al. (2011) and our study. In other words, their predictions fit our findings of bars showing higher metallicities and flatter gradients than disk stars in the same region. Simulations of the Milky Way confirm this behaviour (e.g., Martinez-Valpuesta & Gerhard, 2013).

Our interpretation of the flattened metallicity gradients along the bar (and no other axis) coupled with the absence of a difference of gradients of barred and unbarred galaxies beyond corotation (Sánchez-Blázquez et al., 2014b) or integrated (Cacho et al., 2014; Cheung et al., 2015a) is that bars seem to be confined structures, rotating as cylinders within the galaxy. Under the assumption that bars are long-lived, consistent with the latest numerical simulations (e.g., Athanassoula, Machado & Rodionov, 2013) (but proposed long ago) and observations detecting bars out to redshift z$\sim$2 (e.g., Simmons et al., 2014), we would expect to find a mixing effect if present. However, it seems that

bars mostly affect themselves and remain rather confined structures within the galactic disks without too much interaction with it. As gas is more susceptible to non-axisymmetric components, such as bars, they seem to be able to funnel it to the center and trigger the growth of circumcentral substructures. The properties along the bar however resemble the bulge properties largely (see Fig. 5.7) and additionally exhibit higher metallicities (as predicted by Di Matteo et al. e.g., 2013). The flatter metallicity gradient along the bars could hence be the result of orbital mixing - but only within the bar, as a confined structure, because it is only observed along it.

Another possibility is that the flat gradient is already produced at higher redshifts due to strong radial mixing which can be achieved by strong galaxy interactions (e.g. Rupke, Kewley & Barnes, 2010). Then, in some galaxies, bars formed from this material which already showed enhanced metallicity and flatter metallicity gradients, while in others, only the bulge remains and consists of this material. In both cases, the disk with different properties settles around the system. The similarity of bars and bulges concerning their age, metallicity and also abundance supports this idea. There could be an effect of overlap between the two components, but its effect would be minor. The clear offset in abundance to lower values for disks further underscores their distinct formation scenario and the different timescale of it. While higher abundances, such as seen in the bars and bulges of our sample, suggest short formation timescales, lower values indicate more extended formation scenarios. The fact that bars are observed up to high redshifts also enables the possibility of this scenario. Further, recent simulations also find that bars form very fast (within a few rotation timescales) and early on (e.g., Saha, 2015) as soon as a cool stellar disk is assembled around the bulge spheroid, which in turn is then altered by bar-driven secular processes. As our sample is slightly biased towards early-types, the strong connection between bars and their bulges might be even more explicit amongst this sample and could be valid in particular for bars in early-type galaxies. In particular, bars also empty the region around them, so anything that happens in the disc, does not reach the bar such that the bar is a proxy of the state of the disc when the bar formed.

In fact, the average age of bars depends on the Hubble type. However, in the early-type galaxies of our sample, it is of the order of the bulge and rather old, usually up to 10 Gyr. At the same time they often reside in a younger, star forming disk. The fact that the age of the bar in those systems is old, despite the presence of younger populations in other parts of the galaxy, argues against a recent bar formation from disk stars, but for an early formation of a bar that survived a long time, already put forward by Gadotti & de Souza (2006); Pérez, Sánchez-Blázquez & Zurita (2007); Sánchez-Blázquez et al. (2011) and supported by recent studies of the bar fraction at high redshift finding bars out to z$\sim$2, using the HST CANDELS data (Simmons et al., 2014).

Nonetheless, for both early- and late-type galaxies, we conclude that bars produce a noticeable *local* effect on their host galaxies. This is to be expected as barred and unbarred galaxies share the same large-scale dynamical properties, i.e. they both belong to the same Tully-Fisher relations (Courteau et al., 2003). This should imply that secular evolution should be a local phenomenon - as we

observe it. We summarize the most important results and conclusions in the following section.

5.5 Summary and conclusions

In this work, we explored the BaLROG (Bars in Low Redshift Optical Galaxies) sample further, focusing on the stellar populations. The sample comprises 16 large mosaics of nearby barred galaxies observed with the integral field unit SAURON. Similar to our kinematic analysis (Seidel et al. 2015c, Chapter 4), we note once again the necessity of our spatial resolution (typically 100 pc) in order to be able to detect features induced by bars.

Using the classical method of line strength index measurements, we determine SSP ages, metallicities and abundances and their gradients which lead us to the following results and conclusions:

- Bars among our sample exhibit a large variety of index measurements, and hence ages and metallicities. Global values do not seem to be influenced by the bar as already observed in larger samples (e.g., McDermid et al., 2015), but follow general galaxy trends according to Hubble type and central velocity dispersions.

- Elevated Fe5015 values are found at the edges of 7 of the bars of our sample, compared to their discs, reflected by an elevation in the metallicity profile around 0.5 to 0.75 bar lengths.

- Galaxies with their central spectra falling outside the SSP grid (towards the high metallicity end) overlap with those exhibiting a strong h_3-v/σ anti-correlation within 0.1 $R_{\rm eff}$ (found in our Paper I), suggesting a strong connection between this dynamical feature and the presence of a complex mixture of populations.

- Ages, metallicities and abundances are found to be similar in bars and bulges, while disks show offsets relative to the former two. They exhibit in particular younger ages and lower abundances than bars and bulges. Although some of the early-type bars are rather old, up to 10 Gyr, they reside in a young, star forming disk. This supports theoretical predictions that bars are long-lived structures and might have formed a long time ago and survived until the present day.

- We identify obvious breaks amongst all index as well as SSP profiles and therefore measure two different gradients. The location of the break between the two different slopes is mainly located at 0.13±0.06 bar lengths, confirming this place as a particular region already identified in Chapter 4, and possibly linked to an inner Lindblad resonance (Elmegreen, 1994).

- Inner gradients are found to be much steeper than outer gradients, for both index and SSP profiles in bar major and minor axes. Inner gradients commonly agree for bar major and minor axes,

- Outer gradients show offsets between major and minor bar axes. In particular for Fe5015, Mg*b* and metallicity, we find that major axis gradients scatter around zero while minor axis gradients are steeper and negative towards the outside. This might be a hint of flattening of these parameters along the bar major axis. This is confirmed by analyzing unbarred galaxies from the SAURON and ATLAS3D surveys that also show steeper outer gradients comparable to the minor axis gradients found in the barred galaxies. Along the bar major axis the metallicitiy gradient is found to be 0.03±0.07 dex/kpc whereas the mean value of the minor axis and the unbarred control sample is -0.20±0.04 dex/kpc. This trend was seen for 2 galaxies analysed in Sánchez-Blázquez et al. (2011) and is predicted by models (e.g., Di Matteo et al., 2013; Martinez-Valpuesta & Gerhard, 2013). We note however, that the exact values of the mean gradients are still based on a small sample and could be slightly altered due to the contrast effect of the overlying structures of bulge, disc and bar.

- We further observe a good correlation between inner Fe5015 and metallicity gradients versus bar strength, such that stronger bars have shown positive gradients, while weak bars show negative gradients. This might be an influence of the bar providing fuel for nuclear star formation. This result is supported by the increasing central H_β values and decreasing younger central ages with bar strength.

In conclusion, we reiterate our statement from the previous chapter which is that bars do not seem to alter global galaxy properties but do influence their host galaxies in a consistent way, *localized*, in different regions. In particular the region around 0.13±0.06 bar lengths seems to be a common point where this influence can be detected, but sufficient spatial resolution is needed. Furthermore, in agreement with former pilot studies (e.g., Sánchez-Blázquez et al., 2011), we find a flattening of the metallicity gradient - only along the major axis of the bar - and when taking the gradient separately from the inner slope which is clearly different. The spatial resolution coupled with the method to obtain gradients and the area where they are taken is very likely the reason for the lack of difference found in recent large statistical studies (Sánchez-Blázquez et al., 2014b; Cheung et al., 2015a). In upcoming work we will investigate in detail the resonance points in order to identify reasons for the behaviour found in kinematics and stellar populations. Furthermore, observations by even better (higher spatial and spectral resolution, larger FoV) IFUs such as MUSE will enable us to improve our understanding of substructures in galaxies, their origin and relation to large-scale structures such as bars and bulges.

6

The importance of bar-driven secular evolution in bulge formation[1]

It is not how much you do,
but how much love you put into the doing
that matters.
Anjezë Gonxha Bojaxhiu

The details of bulge formation via collapse, mergers, secular processes or their interplay remain unresolved. To start answering this question and quantify the importance of distinct mechanisms, we mapped a sample of three galactic bulges using data from the integral field spectrograph WiFeS on the ANU 2.3m telescope in Siding Spring Observatory. Its high resolution gratings (R∼7000) allow us to present a detailed kinematic and stellar population analysis of their inner structures with classical and novel techniques. The comparison of those techniques calls for inversion algorithms in order to understand complex substructures and separate populations. We use line-strength indices to derive SSP-equivalent ages and metallicities. Additionally, we use full spectral fitting methods, here the code `STECKMAP`, to extract their star formation histories. The high quality of our data allows us to study the 2D distribution of different stellar populations (i.e. young, intermediate, and old). We can identify their dominant populations based on these age-discriminated 2D light and mass contribution. In all galactic bulges studied, at least 50% of the stellar mass already existed 12 Gyrs ago, more than currently predicted by simulations. A younger component (age between ∼1 to ∼8 Gyrs) is also prominent and its present day distribution seems to be affected much more strongly by morphological structures, especially bars, than the older one. This in-depth analysis of the three bulges supports the notion of increasing complexity in their evolution, likely to be found in numerous bulge structures if studied at this level of detail, which cannot be achieved by mergers alone and require a

[1]The majority of this chapter is based on the article: *Dissecting galactic bulges in space and time I: the importance of early formation scenarios vs. secular evolution.* Seidel, M. K., R. Cacho, T. Ruiz-Lara, J. Falcón-Barroso, I. Pérez, P. Sánchez-Blázquez, F. P. A. Vogt, M. Ness, K. Freeman and S. Aniyan. 2015, MNRAS, 446, 2837.

non-negligible contribution of secular evolution.

Only very few studies have investigated galactic bulges in this great detail up to date and only few have used integral-field spectroscopy (e.g. Ganda et al., 2007; Yoachim, Roškar & Debattista, 2012; Sánchez-Blázquez et al., 2014a). While other forms of spectroscopy are equally valid, integral-field studies can often improve our understanding thanks to their two-dimensional field of view. Ocvirk, Peletier & Lançon (2008) demonstrated that a young and cold stellar population could be distinguished from an old and hot bulge using age - line-of-sight-velocity-distribution (LOSVD) diagrams. More recent attempts in the literature to achieve similar goals (using different techniques) are very scarce and usually restricted to very few, well-known multiple component systems (e.g. van der Laan et al., 2013b; Coccato et al., 2011, 2013; Johnston et al., 2013). Despite great progress, especially with the advent of large spectroscopic surveys (e.g. ATLAS3D, Cappellari et al., 2011a), we are still far from understanding galactic bulges and their subcomponents, both kinematically and from the stellar population point of view.

In this chapter, we present an in-depth study of three fundamentally different bulges using the WiFeS integral field spectrograph on the ANU 2.3m telescope in Siding Spring Observatory (see Sec. 2.1.2 for more details on the instrument). The combination of its large spectral range, high spectral resolution gratings and sufficiently large field of view allows us to explore the entire range of tools to derive stellar and gas kinematics, but also their stellar population content. In Sec. 2.3.1 and 2.3.4 we already described our target selection and observations respectively, while Sec. 2.3.5 provided details of the data reduction process. The methods employed to perform the different analyses are described in Chapter 3. Section 6.1 presents the results for the stellar and ionised-gas kinematics. Section 6.2 introduces the different stellar population results using the classical indices method and the novel technique via full-spectral fitting. These results are discussed in Sec. 6.3. Finally, Sec. 6.4 summarizes our main findings. As stated before, this chapter is based on our results already published (Seidel et al., 2015a,b).

6.1 Kinematic properties

Figures 6.1 and 6.2 present maps of the absorption and emission-line distribution and kinematics of the three galaxies in our sample. Overlaid in all maps, we show the isophotes of the total intensity reconstructed from the WiFeS spectra (in mag/arcsec^2 with an arbitrary zero point) equally spaced in intervals of 0.5 magnitudes (detailed maps are collected in Appendix D). Here, we concentrate on an overview of the general kinematic trends and results observed.

6.1.1 Stellar kinematics

NGC 5701 shows a misalignment between the galaxy's main photometric axis and the bar. The isophotes also indicate that the bar angle is clearly misaligned with respect to the major kinematic axis. The maximum absolute rotation

values reach up to $40\,\mathrm{km\,s^{-1}}$ within our FoV. The velocity dispersion is higher in the central parts ($110\,\mathrm{km\,s^{-1}}$) and drops down to $95\,\mathrm{km\,s^{-1}}$ at the edges of the FoV. The highest σ values are not found exactly in the centre, but offset by $\sim$5 arcsec, hence presenting a central σ-drop. The h_3 map reveals some level of anti-correlation in the central parts with the velocity map. This finding is consistent with the elevated h_4 values in the centre. We expect a dominant bulge in this region (Weinzirl et al., 2009), but also weak nuclear spiral arms Erwin & Sparke (2002) which could explain the non-zero h_3 and h_4 values obtained.

In NGC 6753, the photometric and kinematic axes appear to be aligned. This galaxy displays an unusually large stellar velocity rotation ($\approx$200 $\mathrm{km\,s^{-1}}$) for the assumed inclination of the galaxy ($i \sim 30°$). It also shows a very high central velocity dispersion ($\approx$214 $\mathrm{km\,s^{-1}}$) that decreases drastically within the inner kiloparsec. The dispersion map reveals an extraordinary "hot" centre embedded in a significantly colder component, i.e. the disk, with no distinct kinematic signature of the inner ring. The h_3 values anti-correlate strongly with the velocity values and so does the h_4 moment with the stellar velocity dispersion. The fact that both h_3 and h_4 values are high in the inner ring region supports the distinct kinematic properties of this substructure.

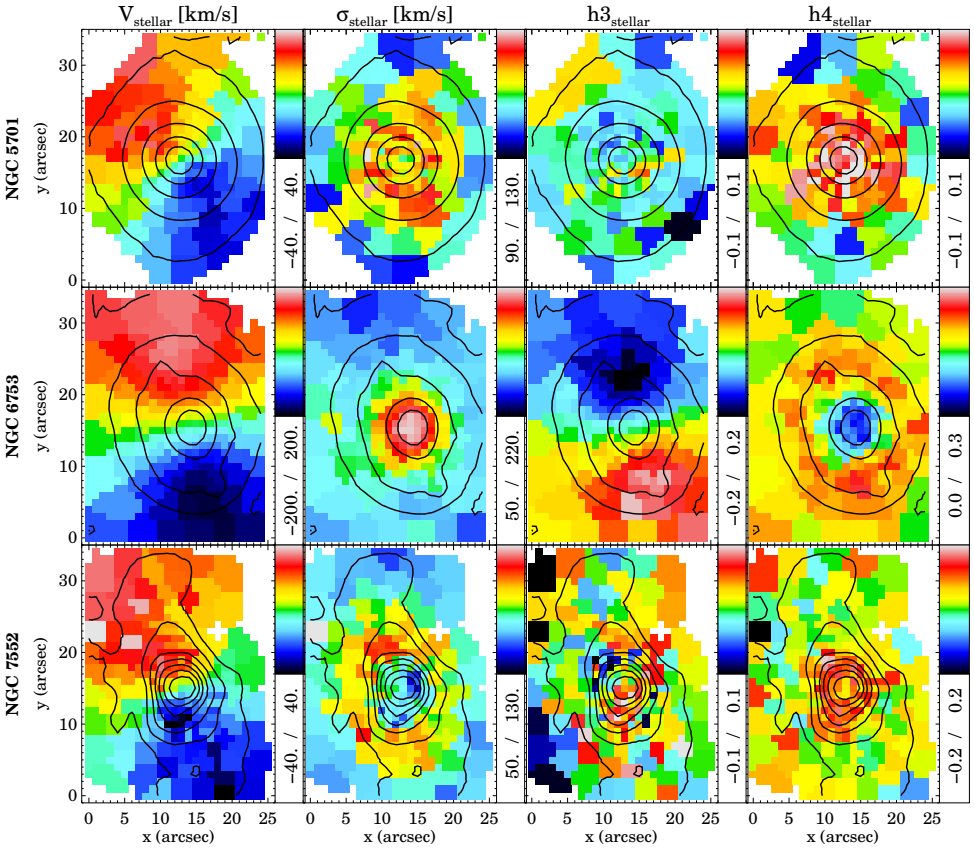

FIGURE 6.1: Stellar kinematic maps for all three galaxies, from top to bottom: NGC 5701, NGC 6753 and NGC 7552. For each one, the four panels show stellar velocity, stellar velocity dispersion, h_3 and h_4 moments. The colour bars on the side each indicate the range of the parameter measured. The isophotes shown are derived from the WiFeS cube reconstructed intensities and are equally spaced in stpdf of 0.5 magnitudes.

NGC 7552 displays a similar maximum rotation velocity to NGC 5701 within our FoV ($\approx$40 km s^{-1}). While also hosting a large-scale bar, the line of nodes is almost perpendicular to the bar's position angle, thus the rotation is along the large-scale bar and less misaligned than in NGC 5701. A closer look reveals enhancements of the rotation velocity most likely related to the bar. Hence when taking the profile, we would see the predicted double-hump rotation curve (Bureau & Athanassoula, 2005). A high velocity dispersion ring is clearly revealed outside the circumnuclear ring region. Towards the edges of the field, these values drop. In the h_3 map, only a slight anti-correlation with respect to the velocity field can be distinguished in the area where the circumnuclear ring is present. This anti-correlation is much more apparent in its velocity dispersion versus h_4 moment maps.

The three bulges in our sample display a wide range of kinematic features clearly associated to different photometric substructures, e.g. double-hump profiles σ predicted by simulations of barred galaxies (Bureau & Athanassoula, 2005). Particularly interesting is the behaviour of the Gauss-Hermite higher order moments h_3 and h_4, which are markedly different, for all galaxies, in those regions where we expect to find a mixture of populations. We will use this information in a follow-up paper (Cacho et al., in prep.) to extract the kinematic properties of the different stellar population components present in the centre of these galaxies.

6.1.2 Ionized-gas distribution and kinematics

We measured the distribution and kinematics of the following emission lines: Hγ, Hβ, [OIII] and [NI]. The resulting maps are presented in Fig. 6.2.

In NGC 5701, [OIII] is the most prominent gas component. Its flux peaks in the centre and decreases outwards until it reaches the barred component. We barely detect [NI] and H_γ. The Hβ, however, shows a weak peak in the centre, compatible with the presence of nuclear spiral structure in this galaxy (Erwin & Sparke, 2002). NGC 6753 shows a ring component in the Balmer lines, clearly visible in the Hβ line map. The upper and lower part of the ring is strongly enhanced. The [OIII] and [NI] are mostly concentrated in the nucleus. NGC 7552 shows strong central emission in all probed emission lines, being strongest in Hβ and [OIII]. The Hβ map is in agreement with the Hα and radio continuum maps of Pan et al. (2013) and Forbes et al. (1994), respectively. This comparison suggests that dust has not affected our measurements significantly. The very low [OIII]/Hβ value in the central regions (≈ 0.17) confirms that ionisation is mostly triggered by star formation (e.g. Kewley et al., 2001).

In the three galaxies, gas rotation velocities are aligned to the corresponding stellar velocity field. The ionised gas exhibits a higher rotation velocity than the stars. Conversely, the gas velocity dispersions are lower than those of the stars. This behaviour is expected given that stars exhibit higher random motions than the ionised gas. More specifically for each galaxy, we find that the gas in the centre of NGC 5701 presents lower velocity dispersion values than in its outskirts, opposite to the stellar velocity dispersion. The velocity of the

ionised gas in NGC 6753 is surprisingly close to that of the stellar kinematics. In NGC 7552, the gas velocity field shows the same twists observed in the HI and ^{12}CO (2-1) maps from Pan et al. (2013).

The velocity dispersion is high around the inner Lindblad resonance (located at a radius of 1.7 kpc, Pan et al. 2013). This region sits just outside the circumnuclear ring, which has a radius of 0.5 kpc. The elevated dispersion values are likely due to shocks induced by the gas arriving at those locations though the dust lanes along the bar. The inner Lindblad resonance of NGC 7552 is located at 0.36 bar length (taking the bar length as 4.78 kpc, Weinzirl et al. 2009) and the circumnuclear ring at 0.1 bar length. In context with Chapter 4, this could imply that rings or other features could form inside this inner Lindblad resonance which marks an outer boundary.

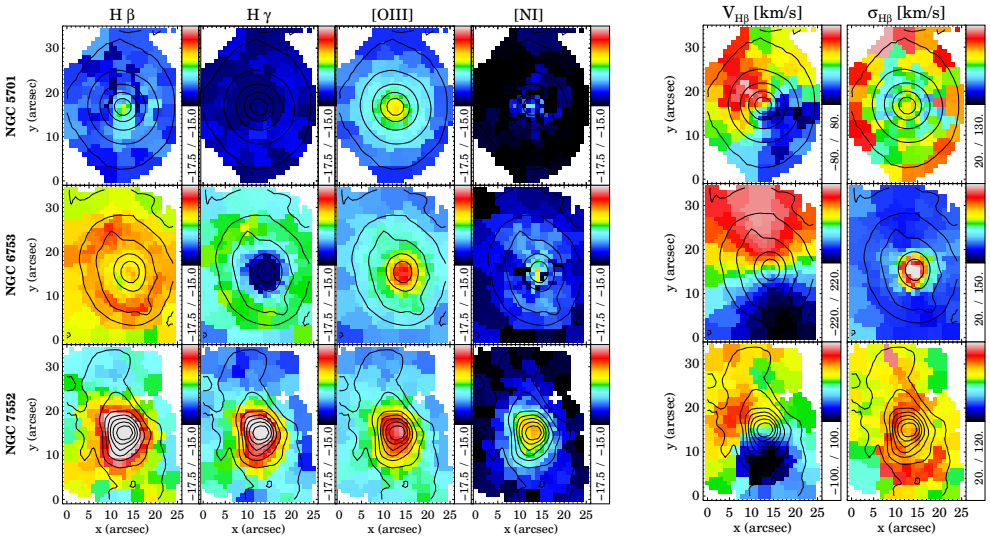

FIGURE 6.2: Gas fluxes and velocities for all three galaxies in our sample. The left four columns show the gas intensities, while we present the kinematics on the right: ionised gas rotation velocity and velocity dispersion. Each row represents one galaxy, as indicated on the left hand side. NGC 7552 has a cross of bad pixels on the right (white cross). Fluxes of the emission lines is given in erg s^{-1} cm^{-2} arcsec^{-2} and in a logarithmic scale.

6.2 Stellar populations

The rich kinematical substructure found in the previous section may suggest a similar variety in the stellar populations of our galaxies. As a first test to classify them we have compared the central properties with larger samples in the well-known line-index$-\sigma$ relation. This relation is well established for elliptical galaxies (e.g. Terlevich et al., 1981). In recent surveys, e.g. SAURON survey, this relation was confirmed for early type spirals (e.g. Peletier et al., 2007) and extended for late-type galaxies, which showed larger scatter (e.g. Ganda et al., 2007).

In order to check if our small sample could contain any atypical galaxy which would be unrepresentative of its type, we compared it to other measurements in the literature of similar galaxies. Figure 6.3 shows our measurements of central

apertures (1.5 arcsec, same aperture as in Ganda et al. 2007) in comparison with those in the literature.

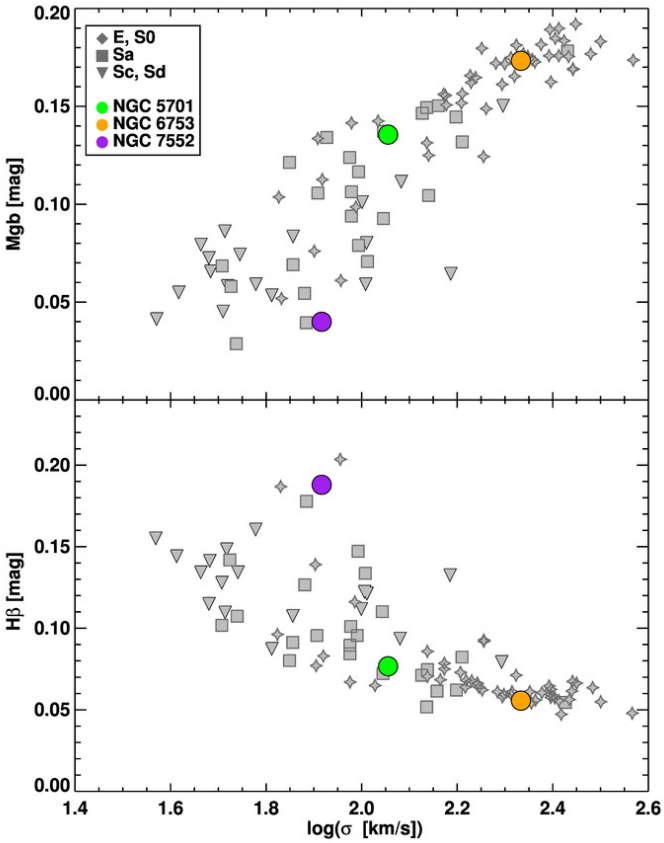

FIGURE 6.3: Line-index$-\sigma$ relations for our sample of galaxies. Central aperture measurements of all three bulges (coloured circles) are compared to values from different samples (Ganda et al., 2007; Peletier et al., 2007). Values for NGC 5701, NGC 6753 and NGC 7552 are represented by green, yellow and purple solid circles respectively. Grey symbols show literature values. The upper panel shows the Mgb, expressed in magnitudes, against central velocity dispersion, while the lower panel shows the central Hβ, also expressed in magnitudes, against velocity dispersion. For our datapoints, we have followed the conversions from Å to mag described in Kuntschner et al. (2006).

NGC 5701, indicated by a green circle, lies on the edge between the E, S0s and Sa galaxies on the relation. Despite its large-scale bar, its central bulge parameters resemble a bulge of any early-type galaxy. NGC 6753, indicated by a yellow circle, lies exactly on the cloud of E-S0 galaxies, which may be surprising given the presence of spiral structure in the inner parts. Its centre is thus similar to classical S0/Sa type bulges. NGC 7552, shown by the purple circle, follows the behaviour of late-type galaxies, likely due to the prominent central starburst. Our sample of bulges contains, at least in their central stellar content, examples of the wide population of nearby galaxies.

6.2.1 Classical index−index diagrams

Figure 6.4 presents the measurements of absorption line strengths in index-index diagrams. The top row displays the line-strength index maps for each galaxy: Hβ_o, as an age indicator, and Mgb and Fe5270 as proxies for metallicity. In the second row, we plot Hβ_o against the combined index of magnesium and iron, [MgFe]' (using Mgb, Fe5270 and Fe5335, see Sec. 3.3.1), and overplot a grid of MILES single stellar population models for Kroupa IMF.

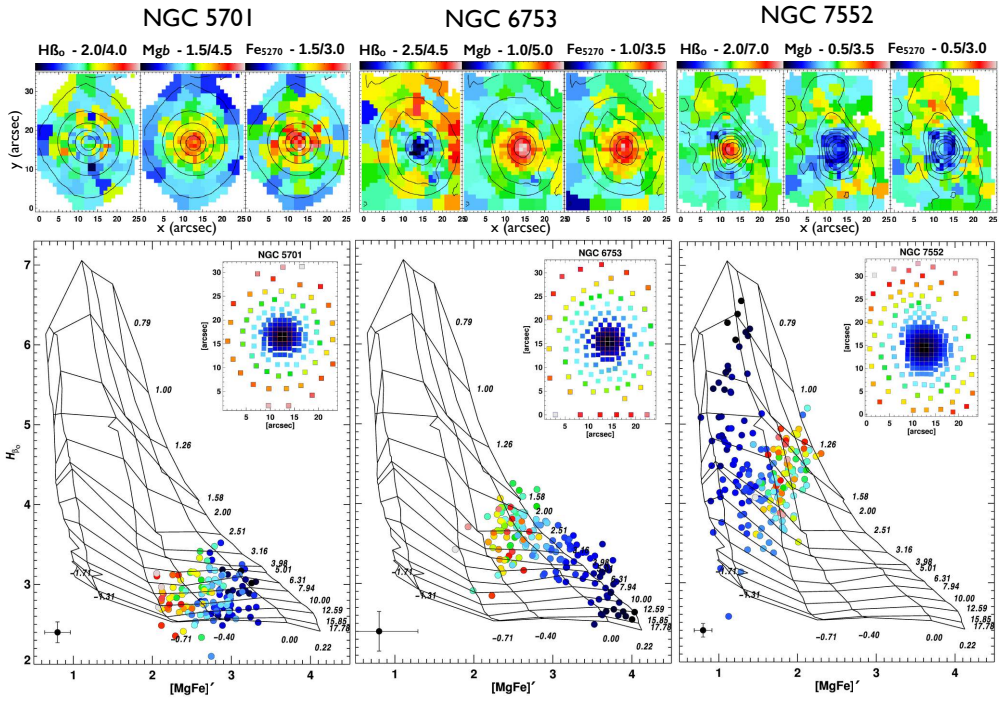

FIGURE 6.4: *Top row:* Maps of absorption line strengths for Hβ_o, Mgb and Fe5270. *Bottom row:* Hβ_o, an age discriminator, versus the combined index of [MgFe]', indicating metallicities for the galaxies NGC 5701, NGC 6753 and NGC 7552, from left to right. Overplotted is a model grid of single stellar populations, roughly indicating the ages and metallicities (shown on the side of this grid). The points are colour-coded according to the distance from the galaxy centre and the map in the top right corner of each panel indicates their position. In the left lower corner we indicate the typical uncertainty (weighted mean of individual errors) of the points with representative error bars.

NGC 5701 appears to be the oldest galaxy of the three, with a large scatter in age - from about 3 Gyr to 15 Gyr - at almost all radii. The error bar does not account for this observed spread, but the overlapping structures of bulge, bar and disk might lead to this variation. While this age spread seems to be independent of radius, the metallicity of the stars is clearly higher towards the centre, even considering the error bar. In NGC 6753, we find a steep gradient in age from the very central parts towards the ring (green points) and then an almost flat behaviour until the edges of the field. The galaxy hosts an old metal-rich population in the centre, but as soon as we enter the region dominated by the circumnuclear ring, those measurement points decrease excessively in age and most importantly fall outside of the model grid. NGC 7552 shows the opposite behaviour in the age of the central population. The central com-

ponent is very young, as expected in a starburst galaxy. The known inner ring (of about 5 arcsec radius) is so small that we cannot distinguish it from the centre. It is interesting to note two low Hβ_o regions above and below the centre. These locations correspond to the contact point of the gas and dust lanes with the inner ring. While the low values can be the result of dust affecting our measurements, it is also possible, as observed by e.g. Böker et al. (2008), that star formation is suppressed in those contact points and only enhanced once the gas enters the ring.

This classical approach of measuring stellar population parameters, while in principle valid for some of the regions in our galaxies, presents a number of important shortcomings. The most notable is the surprisingly large number of points in NGC 6753 that fall outside the grid. As we demonstrate in Chapter 3.3.2, this is likely due to the complex mixture of populations present in those regions.

Based on the tests presented in Chapter 3.3.2, we conclude that NGC 6753 presents an old, metal-rich (about solar) population, significant in mass, but whose light is mixed with a strong younger population. The old population is seen in the inner parts. Slightly further out, the young population begins to contribute more in light; according to the tests, we need approximately 20% of the light contribution coming from the young population (and only 1 to 5% in mass). Therefore, the index values that we measure move upwards and hence out of the grid. Thus, these values do not indicate a failure of our measurements, but the combination of a rather metal-rich population in combination with a low mass-fraction of young stars. This frosting of young stars has been observed despite large amount of gas available (e.g. Young et al., 2008) and is hence partly expected.

More importantly, this kind of bias implies that abundance ratios measured in the region of population mixtures will be unreliable if it is sufficiently altered by the above effect. It is hence impossible to determine accurately the stellar population parameters such as [Mg/Fe] in many locations of our galaxies. [Mg/Fe] is particularly interesting as it serves as a chemical clock to establish the speed of a star formation event (i.e. being higher for quick star formation episodes). In the remaining of this paper we will only determine and use the information provided by this ratio in areas which are mostly dominated by a single stellar population (see Sec. 6.3 for its determination).

6.2.2 α - enhancement

In Fig. 6.5 we present the results of the abundance ratio analysis for two of the three galaxies. On the left hand side, the abundance is plotted as a function of radius indicating the overall decline from the centre to the outskirts of the two galaxies, with increasing scatter in the individual values, especially for NGC 6753. On the right, the abundance versus the age is shown with colour-coded points in the same way as before: darker points are central ones and yellow, red points belong to the edges of the field.

NGC 5701 shows a separation of two clouds indicated by the horizontal line. The ages are rather homogeneously distributed. The profile of NGC 6753 reveals certain details: going outwards, we can recognize a series of bumps. We

deliberately chose to represent individual points here since averaging even in ellipses would wash out signatures of the patchy spiral structure. Comparing this profiles thus with the unsharp mask in Fig. 2.2, we can qualitatively correlate the wiggles in the profile with the spiral arms. Nevertheless, in this region the values cannot be fully trusted as pointed out before which might actually be the result of the wiggles. On the right, we indicate with the two vertical lines the different regions: to the right, we can trust the points. This narrow regime without too much scatter corresponds to the central part of the galaxy (those points which do not fall out of the grid in Fig. 6.4). In between the lines, the points start to be less reliable and to the left, we cannot fully trust them due to the mixture of different populations (the increasing scatter also hints to this problem).

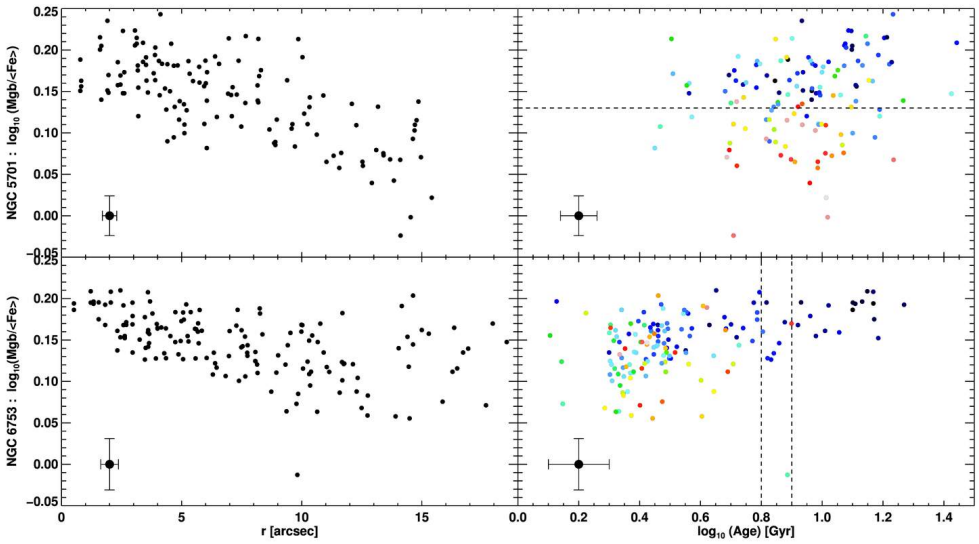

FIGURE 6.5: We show abundances as a function of radius and age for two galaxies: upper row: NGC 5701, lower row: NGC 6753. The horizontal line indicates for NGC 5701 the separation of the central bulge and the outer bar dominated region. Vertical lines (drawn at 6.31 and 7.94 Gyrs) separate the region where the values can be trusted (right side) and where, due to an obvious mixture of populations, we cannot trust the values any longer (left side); the region in the middle could be debatable. Representative error bars are given in the left lower corners.

6.2.3 Radial stellar populations from full-spectral fitting

We obtained ages and metallicities with *rmodel* from the indices as well as luminosity- and mass-weighted values from the full-spectral fitting with `STECKMAP`. For simplicity, given that the index results are similar to the light-weighted results, in this section we only present the radial profiles of the mean stellar age and metallicity measured with `STECKMAP`. In Fig. 6.6, we plot the mean stellar age and metallicity trends (both luminosity- and mass-weighted) together with the cloud of individual values in our maps. The relations are computed as the median of the individual values found in every Voronoi bin over 1 arcsec annuli. The $[M/H]$ is determined from the metallicity values that `STECKMAP` gives using a solar metallicity reference of $Z_{\odot}$=0.02.

We calculated the uncertainties in the parameters through a series of 25 Monte Carlo (MC) simulations. We tested the difference of 25 versus 250 MC simulations and found the resulting errors to be the same within 1-2% difference. In detail, the MC procedure employed is as follows: once the best fit for the best age and metallicity values is obtained, we create 25 mock spectra by adding noise to this best fit matching the S/N of the observed spectrum. Then we run STECKMAP on those mock spectra using flat first guesses for the Stellar Age Distribution (SAD). The age (metallicity) error is the standard deviation of the ages (metallicities) of the mock fits. NGC 5701 displays a rather flat age profile, both luminosity- and mass-weighted. The metallicity profile goes from solar to sub-solar values (for the luminosity-weighted values) from the centre to the outer parts. As expected, the luminosity-weighted trends found here are quite similar to the ones obtained via line-strength indices (compare with the index values, Fig. 6.4).

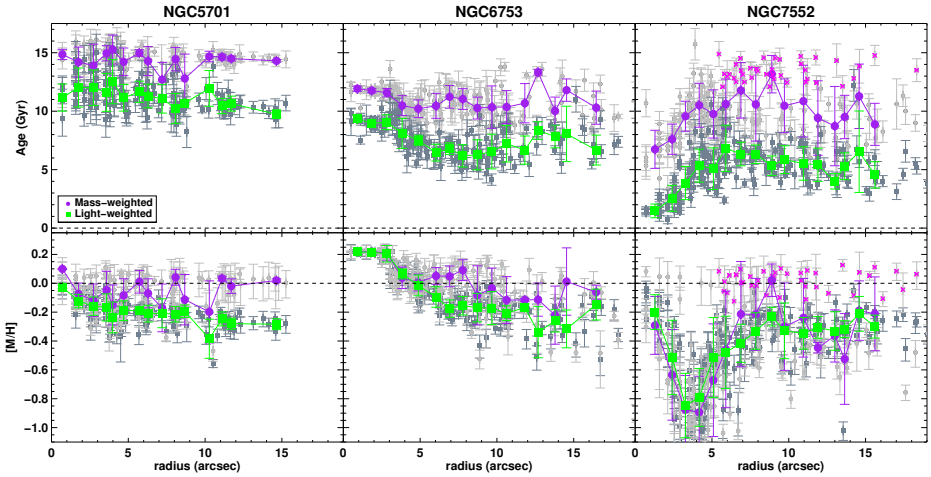

FIGURE 6.6: Stellar age and metallicity profiles for all three galaxies obtained with STECKMAP. The first row shows the age profiles. In the second row the metallicity trends. The luminosity-weighted values (green, with individual points in dark grey) and mass-weighted values (purple, with individual points in light grey) are overplotted. Errors were computed through Monte Carlo simulations. A cloud of interesting individual points for M-weighted results in NGC 7552 is marked by pink crosses (see text for details).

The comparison of those trends with the mass-weighted results suggests a uniform stellar distribution in the field of view of our data. Particularly interesting is the difference between the luminosity- and mass-weighted results in the very centre: the mass-weighted age being high, whereas the luminosity-weighted age shows a slight drop. The decrease in age could be due to the nuclear spiral structure present in that region.

NGC 6753 shows a much richer behaviour, suggesting a more complex stellar content. This galaxy contains a circumnuclear ring of young stars between 5 arcsec and 10 arcsec. The centre of this galaxy is quite old (both in the L- and M-weighted sense). The M-weighted age profile is flatter than the L-weighted. The metallicity profile saturates at the centre (i.e. 0.22 is the most metal-rich population in the MILES models) and shows a steep negative gradient until it reaches the ring, where the profile flattens ($[M/H] \sim -0.2$ for the L-weighted and solar values for the M-weighted profiles). The apparent broadening of the

lines due to the very high central velocity dispersion did not exacerbate the STECKMAP results, since the kinematics are given by ppxf and the resulting fits are very reasonable.

Young stars ($\sim$1 Gyr) are found at the centre of NGC 7552, followed by a sudden increase in age until $\sim$6 arcsec where the profile appears to flatten. The M-weighted age profile behaves similarly, but does not show such young populations in the nuclear region. The L-weighted (M-weighted) metallicity in the centre of this galaxy is below solar followed by a sudden drop to a value of $[M/H] \approx -1.0$, followed by another gradual increase towards $[M/H] \approx -0.2$ values up until $\sim$8 arcsec, from where it stays constant. The young and metal-rich stars that we find in the centre of this galaxy are consistent with the central starburst reported for this galaxy (Forbes, Kotilainen & Moorwood, 1994; Schinnerer et al., 1997; Pan et al., 2013). Outside the inner 5 arcsec, the galaxy displays values similar to those of NGC 5701 and NGC 6753 at the same radii. Our mass-weighted profile shows an interesting feature both in age and metallicity: a separate cloud of points older than 12 Gyr and around [M/H]=0.0 dex values at radii larger than 5 arcsec (marked with pink crosses in the figure). We investigated the location of these bins in our maps and they belong to regions in the ring where the velocity dispersion is large (see Fig. 6.1) and hence might represent a distinct population with clearly different kinematics.

Two of our three galaxies host known circumnuclear star-forming rings and therefore the presence of the young stars detected from our data is not unexpected. The current analysis so far has focused on average luminosity- or mass-weighted quantities and therefore does not necessarily reveal, specially in the ring-dominated regions, the presence of any underlying old stellar population. Earlier studies of the stellar populations in star-forming rings (e.g. Allard et al., 2006; van der Laan et al., 2013a) have found a non-negligible amount of old stars in the ring regions (the mass fraction of young stars in the ring is only 30-40%). In the next section we will take advantage of the possibility `STECKMAP` gives us to decompose the stellar populations of our bulges into their main constituents to establish the amount of old, intermediate and young populations present in them. We will use that information, together with evolutionary models, to set constraints on the level of secular versus merger driven processes taking place in our galaxies.

6.3 Dissecting the stellar content and its implications

The observational data clearly suggest the presence of different stellar populations and demonstrate their complexity likely present in general in galactic bulges when studied in great detail. With the aid of `STECKMAP`, we separated the different population components, both L- and M-weighted, in three age bins: young ($\lesssim$1.5 Gyr, formation redshift $z \lesssim 0.1$), intermediate (1.5 Gyr $\lesssim$ intermediate $\lesssim$ 10 Gyr, $0.1 \lesssim z \lesssim 2$) and old ($\gtrsim$ 10 Gyr, $z \gtrsim 2$). A visualization on how this is achieved can be found in the next section, Chapter 6.3.1. For the conversion between ages and formation redshift, we are using a standard ΛCDM (cold dark matter) cosmology with a Hubble constant of $H_0 = 68.14$ km/s/Mpc and a value of the matter density parameter of $\Omega_m = 0.3036$.

TABLE 6.1: Three example test results as an excerpt of our test series. Here we are using i) a constant SFR (Test example 1) ii) exponential declining SFRs (Test examples 2 and 3), producing ranges of young-intermediate-old fractions compatible with what we might expect for real galaxies. The input is given as a mass fraction and can directly be compared with the M-weighted value which we recover with `STECKMAP` in the same way as for our data. The SFR input is to be compared with the determined SFR and can be related to the L-weighted value.

Test		**Young**				**Intermediate**		
	Input (Mass)	Input (SFR)	M-weight	SFR	Input (Mass)	Input (SFR)	M-weight	SFR
1	0.05	0.27	0.04±0.01	0.29±0.04	0.44	0.53	0.40±0.13	0.47±0.10
2	0.00	0.00	0.00±0.00	0.00±0.01	0.01	0.03	0.07±0.07	0.14±0.12
3	0.03	0.38	0.03±0.02	0.32±0.06	0.26	0.32	0.27±0.15	0.33±0.13
Test		**Old**				**Extra Old**		
	Input (Mass)	Input (SFR)	M-weight	SFR	Input (Mass)	Input (SFR)	M-weight	SFR
1	0.13	0.07	0.12±0.02	0.07±0.01	0.38	0.13	0.44±0.14	0.17±0.08
2	0.03	0.04	0.06±0.04	0.09±0.04	0.96	0.93	0.87±0.10	0.77±0.15
3	0.13	0.06	0.15±0.03	0.10±0.02	0.58	0.22	0.55±0.17	0.25±0.12

Our aim is to reveal their spatial distribution within the galactic bulges and understand how different star formation epochs (associated to the distinct age cuts) influenced the evolutionary histories of these galaxies. The review on cosmic SFH (Madau & Dickinson, 2014) summarizes distinct scenarios according to different epochs, which we will discuss more in Sec. 6.3.4. We are conscious about the oldest age of SSP models exceeding the age of the universe. This has been detected in former studies (e.g. Vazdekis et al., 2001) and is mainly due to degeneracies (age, metallicity, IMF, etc.) in old systems and using these models does not change the cosmology.

We acknowledge the increasing difficulty of separating intermediate and old stellar populations, but STECKMAP has been extensively tested in different works (Ocvirk et al., 2006a,b; Ocvirk, Peletier & Lançon, 2008; Koleva et al., 2008; Sánchez-Blázquez et al., 2011; Koleva et al., 2011). The strategy and set of parameters used in this paper while running STECKMAP are the result of a series of tests following different schemes by different groups and by our own (e.g. Sánchez-Blázquez et al., 2014a). Furthermore we point out that the age cuts are an orientation and should be taken as an age range rather than a clear cut.

Additionally, we performed our own test series using combinations of model spectra according to our age cuts and recovered their L- and M-weighted age fractions within our proposed cuts with `STECKMAP`. Table 6.1 shows the quantitative results for three tests, the first using a constant SFR and the second and third using exponential SFRs. We also tested a combination of bursts using inputs similar to the mass fractions we obtained for the galaxies and also recovered those inputs. In all cases we see that a negligible mass of young population still causes an appreciable fraction in light, while the intermediate and old component are more dominant in mass. In fact if the mass of this young component is high (more than 10%), it will contribute a lot to the light and the old fraction can be underestimated (we observed this in other tests). Since the young mass fraction in none of our galaxies exceeds 4% (and this only in the centre of NGC 7552, in all the rest it is well below 1%), we assume that our measurements resemble more the test cases we show (and similar) and are therefore reliable. We point out that in the tests shown, the old population does not correspond to the entire old population (formation redshift $z>2$) but only the fraction until the extra old population ($z>4$), thus $2<z<4$.

6.3.1 Age binning and Steckmap analysis

In Fig. 6.7 we illustrate the two different processes of using `STECKMAP`, both times departing from the WiFeS spectral cube, using the emission-cleaned spectra coming from the `GANDALF` analysis, shifted to rest frame according to the stellar velocity (see Sec. 6.1.1) and broadened to 8.4 Å. In every case, we fix the stellar kinematics and fit exclusively for the stellar content avoiding the metallicity-velocity dispersion degeneracy (Sánchez-Blázquez et al., 2011).

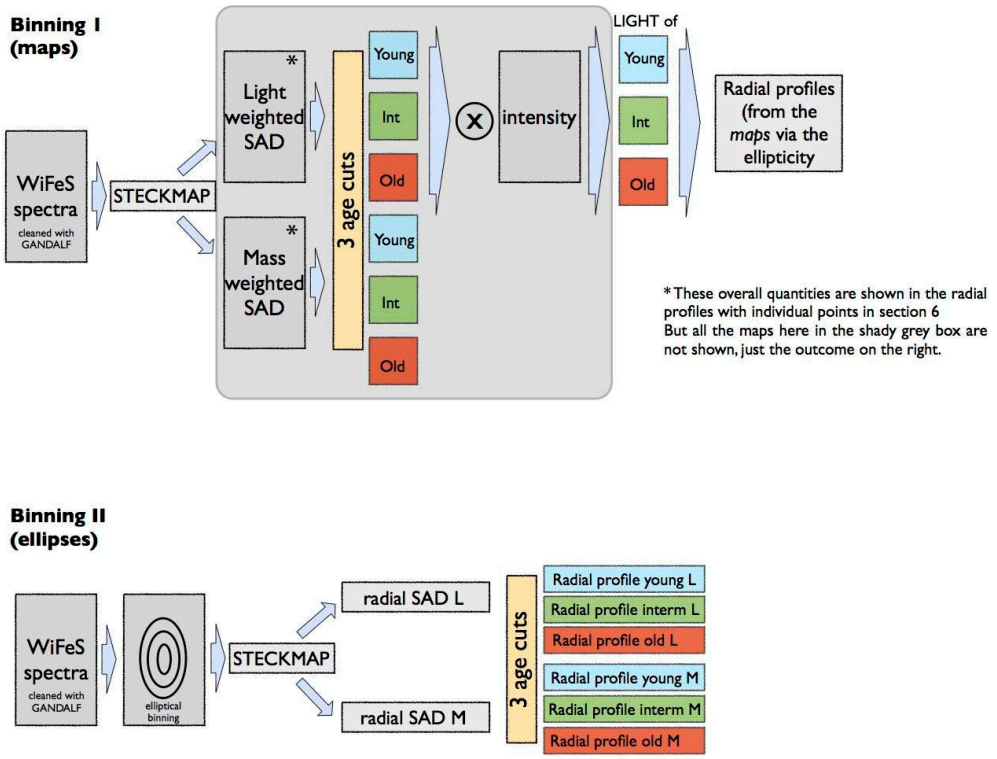

FIGURE 6.7: Visualization of the two distinct binning schemes. *Top:* Binning 1 via maps, where the grey area indicates results that we obtain during the process but do not show in the paper). The corresponding figures using this scheme are Fig. 6.6 and Fig. 6.9. *Bottom:* Binning 2 via ellipses used for the final part of our analysis, shown in Fig 6.10.

Binning 1 (maps): We use this binning, a Voronoi binning over the two-dimensional maps, almost throughout our entire analysis, starting with the kinematics, then the index analysis and later the first analysis with `STECKMAP`. Hence, from these maps we obtain with `STECKMAP` light and mass weighted stellar age distributions (SAD) and from these distributions, we obtain fractions in our three (four) defined age cuts. This process of dividing the SADs into the distinct age bins is visualized in Fig. 6.8. As shown in Fig. 6.7, we do obtain at first corresponding maps for the L- and M-weighted SADs, which we don't display in this paper due to simplicity. From those, we extract the corresponding age fractions, again in maps. Multiplying the L-weighted fractions with the overall intensity, we obtain the light maps corresponding to each of the populations. Using the ellipticity, we then plot the radial profiles directly from those maps, as shown in Fig 6.9.

Binning 2 (ellipses): This second binning scheme is only employed in the final analysis in order to raise the S/N. Here we perform an elliptical binning prior to the `STECKMAP` analysis. The radially binned spectra are then analyzed with `STECKMAP` to produce directly radial L- and M-weighted SADs from which we extract once more the fractions of young, intermediate and old populations, as shown in Fig. 6.10.

Figure 6.8 illustrates for three example spectra (one for each galaxy) the process of obtaining the different age fractions from the SADs.

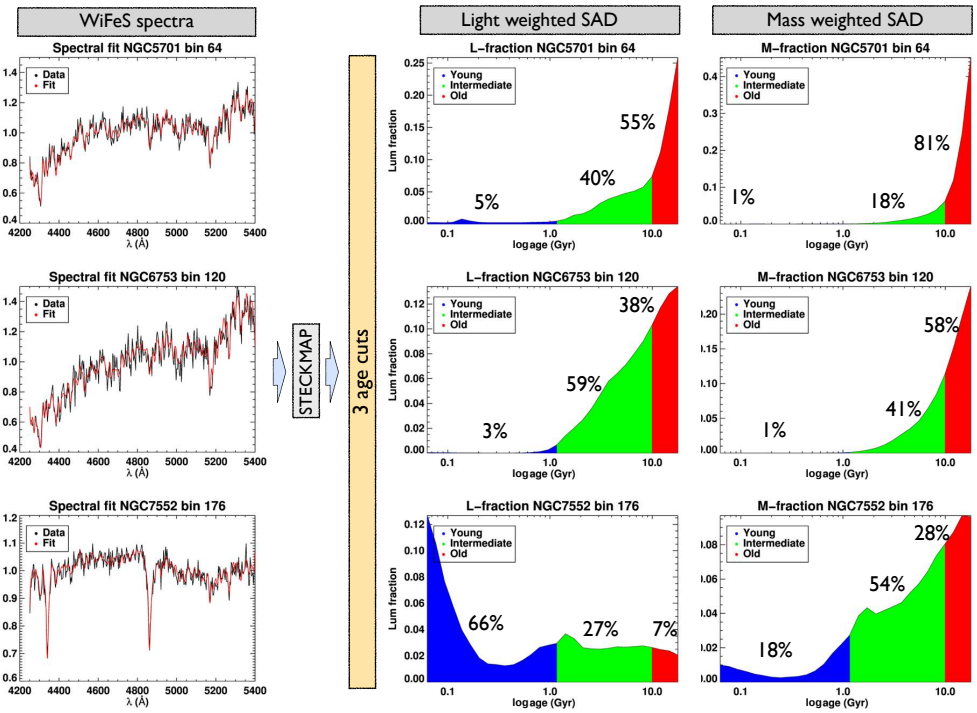

FIGURE 6.8: Visualization of the different age bins obtained from the STECKMAP SADs. *Left:* Data (black) with the STECKMAP fit (red) over plotted. *Right:* The L- and M-weighted SADs with the young (blue), intermediate (green) and old (red) (also from left to right on each plot) fractions indicated (areas under the SAD curve).

On the left we show the data and STECKMAP fit and on the right the corresponding SADs, once L- and once M-weighted. On each plot, we indicate the area under the SAD curve which corresponds to the young, intermediate and old SP. The associated fractions are given on top of these areas.

6.3.2 Surface brightness profiles for each sub-population

From the different weights of each stellar populations given by STECKMAP, we can derive their contribution to the overall light of the galaxies. We used the reconstructed surface brightness distribution and multiply with the luminosity-weighted maps for each sub-population. The result of this exercise is shown in the form of maps and radial profiles in Fig. 6.9.

NGC 5701 is dominated by the light of an old stellar population, while in its outer parts, an intermediate population gains in importance. In the maps of Fig. 6.9, we clearly detect the contribution of the central nuclear spirals in the young component (12% of the light), while the overall luminosity profile is clearly dominated by the population formed long ago. Young populations often outshine old components, but here even though a young component exists, the old remains dominant. It is already evident that the young fraction must be negligible in mass (as we will show later).

The light of NGC 6753 originates mainly from an intermediate-age population with a significant contribution in light from an old population, mostly in the

centre. As seen in the reconstructed maps, the contribution in light of the young population in the ring region is considerable (i.e. as much as the old component). At large radii no clear morphological feature can be associated to any of the populations.

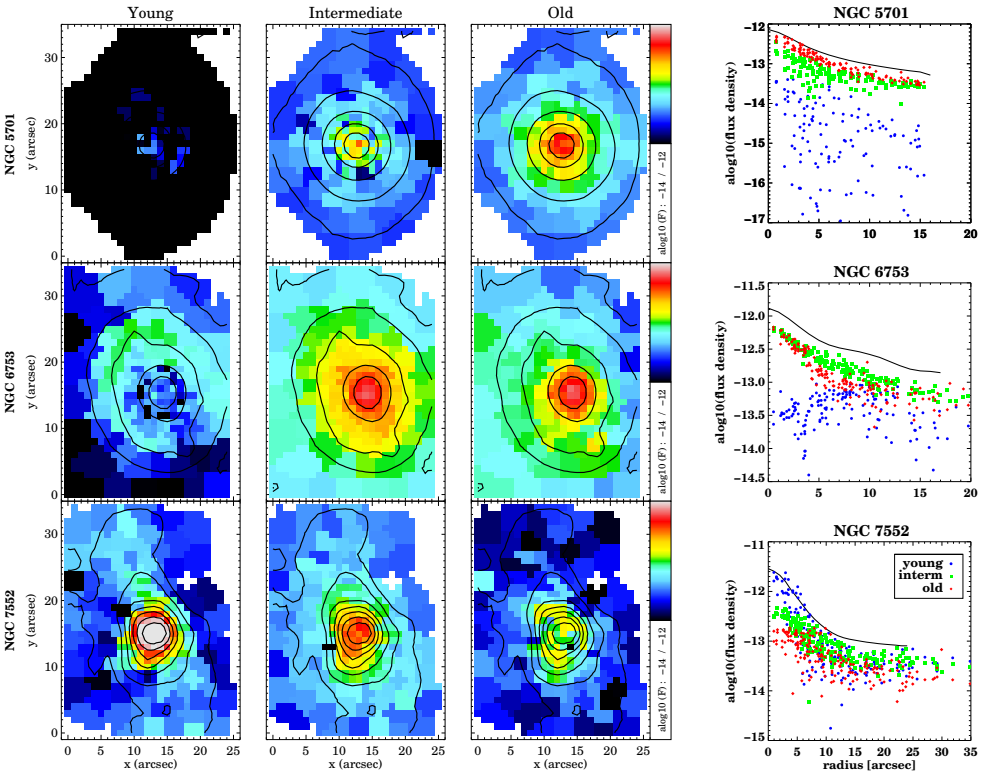

FIGURE 6.9: Surface brightness maps showing the relative contribution of young, intermediate and old stars in each spatial element throughout the galaxies and stellar luminosity profiles revealing the radial contribution of each component (young (blue circles), intermediate (green squares) and old (red diamonds). The black line indicates an ellipse fit performed with IRAF on the intensity image obtained with WiFeS. Fluxes are given in erg s^{-1} cm^{-2} $arcsec^{-2}$ and in a logarithmic scale.

NGC 7552 shows the young population as the major contributor to the surface brightness distribution, particularly in the central region but also along the bar. The contribution of the intermediate-age population is still significant, being larger than the old component at all radii. Surprisingly a non-negligible amount of old material (almost $\sim$ 30%) is organised in a ring-like structure. This is unlike the ring in NGC 6753 where most of the material in the ring comes from an intermediate-age population. The Hubble image of NGC 7552 shows that the ring is not a closed structure, being brighter North from the nucleus. This feature is also observed in our analysis as the ring exhibits an age gradient, being younger on those regions. The young populations distributed along the bar suggests that gas must have been funnelled towards the central regions sustaining star formation over a long period.

6.3.3 Stellar age distributions and mass content

Figure 6.10 displays radial profiles of the distinct age fractions, both L- and M-weighted. We separated once more into young, intermediate and old populations, additionally indicating an even older epoch by a dashed line. The motivation of this separation remains the same: the attempt to distinguish between different processes which according to theory happened at distinct epochs of the universe. The additional older age cut was motivated by the high mass fraction found in the former old age cut. We thus tried to constrain the formation redshift even further to compare with mass fractions proposed by cosmological models.

Here we binned the spectra in ellipses in order to raise the S/N in each of them to obtain radial SFHs and from those the distinct age fractions (a visualization of the two binning schemes can be found above in Chapter 6.3.1). The ellipticity was determined from reconstructed images directly from our WiFeS data cubes, using the IDL routine *find_galaxy.pro* written by Michele Cappellari and available as part of the mge_fit_sectors package[2]. Table 6.2 summarizes the fractions of each of these populations for the central and entire inner parts. We also point out that the L-weighted quantities here (Fig. 6.10) are not only obtained with a distinct binning scheme but are different measures than the computed light profiles associated to the different populations, shown in Fig. 6.9. Please see the visualization shown in Fig. 6.7 for details.

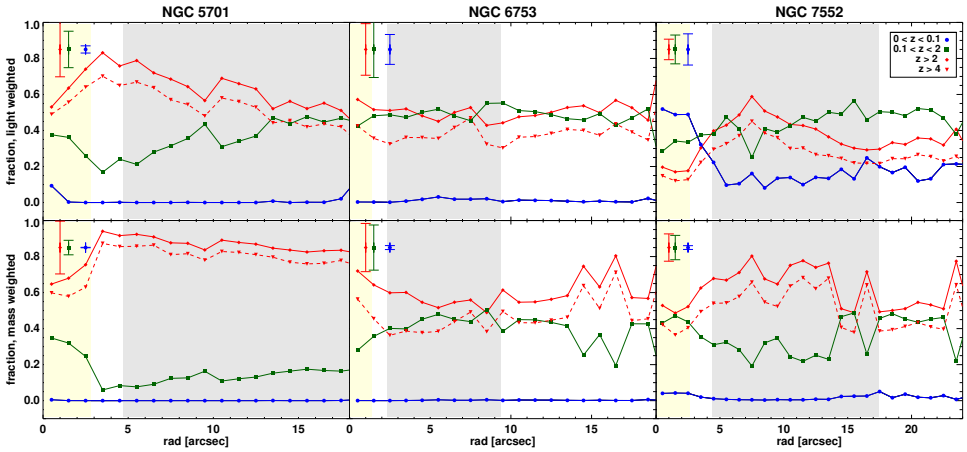

FIGURE 6.10: Fraction of young (blue dots), intermediate (green squares) and old stellar population (red rhombus, even older: red triangle and dashed line) as a function of radius. In the top left corner we indicate the corresponding uncertainties. *Top row:* L-weighted quantities; *Bottom row:* M-weighted results. Shaded regions indicate the central (< 0.3 kpc) and inner parts (0.5 kpc < r < 2 kpc) where we determine average contributions of each population (see Tab. 6.2).

The upper panel in row 1 of Fig. 6.10 already reveals at first sight that the bulge of NGC 5701 is dominated by old stars throughout. These L-weighted quantities show the old centre and at around 13 arcsec, the intermediate population starts to reach the same luminosity as the old component. A slightly younger age can only be distinguished in the central 2-3 arcsec (∼10% in the

[2]http://www-astro.physics.ox.ac.uk/∼mxc/idl/

central bin, significant enough considering the small error bar for the young population). In mass, this population of $\leq$1.4 Gyrs is negligible . This is likely the light contribution of the nuclear spiral structure. The M-weighted results show that $\sim$70-85% of the stellar mass existed in fact already at $z\sim2$. The uncertainty is large, but the fraction is significantly higher than any of the other two populations, that it comparatively dominates nevertheless. The remaining part formed from then until $z\sim0.15$, apart from the centre which is particular. Here, in the central bin, $\sim$30% is composed of the intermediate population and only $\sim$60% of the old population.

NGC 6753 demonstrates subtle differences in the M- and L-weighted results. For both, old stars dominate in the centre, but less significantly in the L-weighted values. We cannot detect any young component in either. At the expected radii of the inner ring, we do not find any major difference in young or intermediate populations. Instead we measure a radially increasing amount of intermediate populations in mass from the centre which stabilizes around 10 arcsec, and remains high ($\sim$40% in mass). Already in the colour profile obtained by Li et al. (2011), no major indication of this ring was found. In Fig. 6.9 we clearly see that the light in the ring regions originates from the intermediate component. Hence this ring has formed between $z\sim2$ and $z\sim0.15$ or maybe even earlier, like other fossil rings that have been found (Erwin, Vega Beltrán & Beckman, 2001). Furthermore, the fact that we do not detect a single enhanced region corresponding to the current position of the ring might mean that flocculent spiral structure has been present continuously throughout the last few Gyrs and thus has caused this uniform distribution of intermediate populations. Similar to NGC 5701, a significant part of this galaxy ($\sim$50-70%) has already been in place at $z\sim2$.

NGC 7552 shows a dominant young population in the centre, contributing $\sim$50% to the luminosity-weighted values. This central starburst, related to the circumnuclear ring, was reported and investigated numerous times in the literature (e.g. Schinnerer et al., 1997; Pan et al., 2013). The light of the underlying old population is only dominant in a radius between $\sim$6 and $\sim$10 arcsec, corresponding once more to the region of the high velocity dispersion ring. The mass-weighted contribution is significant over the entire FoV (up to $\sim$75%), along with the intermediate component (around $\sim$45%). In these M-weighted results, we barely detect a contribution of the young population dominating the light. Along the ring of high stellar velocity dispersion (see Fig.6.1, outside the circumnuclear ring), intermediate and especially old stars are the most significant. We might see an older component, corresponding to the higher velocity dispersion, whose central parts cannot be detected in light (lower σ) due to the dominant star burst. We report once more the existence of at least $\sim$50% to $\sim$60% of the galaxy's mass already at $z\sim2$. We also wish to note that in this figure, the main trends are nicely revealed. However, the complexity of spiral arms, starburst, dust lanes and rich substructure probably require an even higher spatial resolution to better understand their interplay.

Our finding of a dominant old component of stars older than 10 Gyrs in all bulges is consistent with studies on the Milky Way (MW) bulge. Here, colour-magnitude diagrams and spectroscopic studies reveal that the majority of bulge

stars are older than 10 Gyrs (e.g. Ortolani et al., 1995; Zoccali et al., 2006; Clarkson et al., 2008). The metal rich component of the bulge (e.g Babusiaux et al., 2010; Johnson et al., 2011; Ness et al., 2012), shows evidence for comprising stars with a range of ages (Bensby et al., 2013). This metal rich component exhibits bar-like kinematics and could be associated with the secularly evolved MW bar and compared to the younger components that we find in NGC 5701 and NGC 7552. Similar results were also found in other external galaxies where the old population dominates in mass and a younger population would make up only ∼25% (e.g. MacArthur, González & Courteau, 2009).

In all galaxies, we can see in the M-weighted results, that the mass gain in $2<z<4$ (difference of continuous and dashed red line) appears to be rather homogeneous radially, while the green curve resembles the distribution of young ages in the L-weighted values. This might be a hint to redistribution of material over a longer time, i.e. the slightly older stars are by now well-distributed, while the intermediate component has formed according to similar processes as the youngest component is forming now. Especially in the two barred galaxies, it is evident to see that in the last few Gyrs ($0.1 < z<2$), a central component has formed. In both cases, this causes a rise of up to ∼40% of the central mass. The barred structure could be responsible for driving the necessary fuel towards the centres of these galaxies in order to aliment this star formation episode. From theoretical studies we know that bars are able to remove angular momentum from the gas, driving it to the centre and enabling star formation (e.g. Combes & Sanders, 1981). We cannot identify such a central structure in NGC 6753, the unbarred galaxy in our sample. The absence of this clear central component in the $0.1<z<2$ population supports the above scenario of the bar influence in the other two galaxies. We also detect a stronger and more confined central increase in intermediate populations for NGC 5701 than for NGC 7552. This could be an indicator that in NGC 5701, secular processes have already started earlier, in concordance with this galaxy being an earlier type.

It is common practice to calculate the Mg over Fe abundance ratio as a measure of the formation time scales of stellar populations (e.g. Thomas, Maraston & Bender, 2003). It would be optimal to add this parameter to the models which are used for full-spectral fitting. However, they are not yet available. We therefore calculate it from the index-index diagrams, as it is widely done in the literature. As shown before, this value is only representative when dealing with one single prominent population. In Fig. 6.10, we detect in most cases a mixture of populations. We decided to determine the Mg over Fe abundance ratio only for NGC 5701 and the centre of NGC 6753 based on a dominant fraction of one population (please see Chapter 6.2.2 for illustrations and more details). The central values result to be very high for both, ≈0.25 for NGC 5701 and ≈0.2 for NGC 6753, indicating a very rapid formation in both cases. Towards the edges of the FoV, this value decreases. This scenario is consistent with the inside-out-growth model for galaxies where the inner parts formed before and faster than the outer parts. It also fits the picture of spatially preserved downsizing presented by e.g. Pérez et al. (2013), stating that the inner regions in more massive galaxies grow faster than the outer ones. So far, former studies found increased metallicity and lower [α/Fe] values in the central parts of external, but also in the Milky Way bulge (e.g. Jablonka, Gorgas & Goudfrooij, 2007;

Moorthy & Holtzman, 2006), while others detect a variety of different gradients (MacArthur, González & Courteau, 2009). In our study we find elevated central [α/Fe] in combination with a high metallicity.

6.3.4 Implications for bulge evolution models

Despite the small number of galaxies investigated, our analysis allows to help putting constraints on theoretical models, trying to understand the build-up and evolution of galactic bulges as: 1) we selected a representative of early and late-type spirals which seem to exhibit the typical characteristics (see Fig. 6.3) and 2) we find common results within the three galaxies hinting towards a similar origin and fundamental evolution process, across these types.

In particular, we tried to get a handle on radial stellar mass distributions in the present day Universe. Despite the differences of the three investigated bulges, we find a significant amount of old stars at all radii. Hence, at least 50% of the stellar mass was already formed at $z = 2$ and even $z = 4$ (with increasing percentage from NGC 7552 to NGC 5701 where we find more than 80%). Furthermore, we detect a significant fraction of mass in a second star formation episode below z=2. Its present day distribution is more localized and can be associated with current morphological features such as bars.

A wealth of numerical models have already explored the early formation of galaxies and their central components. The main catalysts for the first stellar formation periods have been identified as mergers (e.g. Hernquist, 1992; Bournaud, Jog & Combes, 2005; Hopkins et al., 2010), the collapse itself, e.g. in the ΛCDM (White & Rees, 1978), or high-z starbursts (e.g. Okamoto, 2013; Finkelstein et al., 2013). Independent of the model used, the maximal percentage of bulge mass formed before z=2 is usually no more than 50% and often less (ranging from 10% to 50%, see also Obreja et al. 2013). Thus, the remaining mass percentage is supposed to be attributed to later evolutionary processes, related to a second star formation peak between redshift 1 and 2 (e.g. Madau et al., 1996; Norman & Spaans, 1997; Spaans & Carollo, 1997; Daddi et al., 2010). Nonetheless, these processes might still be one of the above, but due to lower mass densities (expansion of the universe), they are more likely of secular origin. In particular when features can be associated to morphological structures such as bars, rings, (nuclear) spiral structure etc., the likelihood of internal (and/or secular) evolution increases.

In all our galaxies we detect these different components, but we always find a higher percentage of old stellar mass than found in simulations. In the very central parts (r<0.3 kpc), the old population comprises above 50% in one and around 70% in two out of the three bulges (see Tab. 6.2). This percentage is on average even higher (up to ∼85%) considering the inner parts (0.5 kpc<r<2 kpc). Hence, whichever process(es) were acting in the early life of our three galaxies, they must have produced more stellar mass as commonly predicted. This is however only revealed by recovering their mass-weighted results.

All galaxies also display regions of enhanced intermediate (and young) populations which can be associated to morphological structures. Therefore, we suggest that these populations are related to a secular origin. In the following we will briefly discuss each galaxy and speculate about their formation scenario,

TABLE 6.2: Light and mass fractions in % in the central (< 0.3 kpc) and inner (0.5 kpc<r<2 kpc) parts of young (< 1.5 Gyr, redshift z<0.1) intermediate (1.5 Gyr < intermediate < 10 Gyr, 0.1<z<2) and old (> 10 Gyr, z>2) populations. Regions are indicated in Fig. 6.10.

Galaxy	centre (< 0.3 kpc)			inner (0.5 kpc<r<2 kpc)		
	young	intermediate	old	young	intermediate	old
NGC 5701 - L-weights	0.15±0.09	36.6±3.2	63.2±8.8	0.0±0.0	38.9±8.4	61.1±9.9
NGC 6753 - L-weights	0.30±0.01	42.5±0.2	57.2±0.2	1.8±0.9	49.2±3.1	49.0±3.7
NGC 7552 - L-weights	48.5±0.5	33.4±1.7	18.1±1.3	14.0±4.7	44.6±6.6	41.4±8.5
NGC 5701 - M-weights	0.01±0.01	30.6±4.8	69.4±4.9	0.0±0.0	14.1±3.2	85.9±3.3
NGC 6753 - M-weights	0.03±0.02	28.0±0.2	72.0±0.7	0.2±0.2	44.7±3.8	55.1±4.0
NGC 7552 - M-weights	4.1±0.1	43.4±1.7	52.5±1.9	0.6±0.4	28.0±8.0	71.4±8.1

based on our results and model comparisons.

Earlier studies already report a strong influence of environment on the resulting bulge types (e.g. Kormendy et al., 2009). In high density environments mergers will more likely occur and influence the bulge formation, leading to old elliptical-like structures. None of the investigated galaxies shows signs of recent interaction and do not have close neighbours. NGC 5701 forms part of the Virgo supercluster as a member of the Virgo III Groups. Hence, it could have suffered mergers more likely than the other two galaxies leading to the highest percentage of old stellar mass of the three, both in inner and central regions.

Both, NGC 6753 and NGC 7552 show similar percentages but different distributions of old and intermediate populations. Their morphologies could be key for this. In NGC 6753 no bar is present and we can distinguish much better the centre composed of old stars, high in L- and M-weights. Along with its kinematic properties (high stellar velocity dispersion), the centre of this galaxy could present the relict of a node where the first SF occurred (e.g. Obreja et al., 2013; Barro et al., 2013)

Both NGC 5701 and NGC 7552 host large-scale bars which have affected the populations formed between z$\sim$2 and z$\sim$0.1, during the major second star formation epoch as predicted by simulations and found observationally. Here, the central parts show an increase of these intermediate stars: between 35-50% of the mass fraction. They can be attributed to the influence of the bar affecting this population (formed between z$\sim$2 and z$\sim$0.1) in particular.

We speculate that all three galaxies thus suffered a common initial stage of collapse (and/or early SF), but while NGC 5701 may have been affected also by its denser environment, the other two could retain material to form more stars in later epochs. Hence, the contribution of old stars dominating in NGC 5701 might lead to the photometric classification of a "classical bulge" (Weinzirl et al., 2009), while intermediate (and young) populations are almost equally important in NGC 6753 and NGC 7552, likely resulting in a photometric "pseudo-bulge" classfication in the same former work.

6.4 Summary and Conclusions

In this paper we present kinematic and stellar population maps of three significantly distinct bulges with the aim to quantify the importance of different populations to better constrain their evolutionary scenarios. Our data differ from most current integral field surveys, since we obtain a very high spatial (elements of $1''$x$1''$) as well as - and especially - high spectral resolution of R$\approx$7000. This combination allows us to study the inner regions in galaxies in great detail and carry out a comprehensive stellar population analysis using the full-spectral fitting code `STECKMAP` (e.g. Ocvirk et al., 2006a,b; Koleva et al., 2008; Sánchez-Blázquez et al., 2011). We employ a novel analysis method interpreting its 2D results by deriving different stellar components and their contributions to the overall mass and light profiles of the galaxy. In addition we point out clearly the limitations that a mixture of populations can cause in deriving abundance ratios using classical line-strength methods.

Analyzing the kinematics and stellar populations of the three bulges, we deduce different formation scenarios:

- NGC 5701 consists of mainly one old solar (or slightly sub solar) stellar population, where up to ∼80% of the galaxy's mass already existed at z∼4 distributed now radially almost uniformly (in our FoV), apart from the centre. The [Mg/Fe] values confirm a fast origin. The extremely weak nuclear spiral can be detected in the higher order moment maps ($h3$, $h4$) and in the stellar light contribution. Despite its stellar bar, it does not exhibit additional star formation, but shows a significant amount of intermediate populations in the central 0.5 kpc. It supports inside-out growth and appears to show a classical bulge (consistent with previous photometric analyses and increased σ) which formed almost simultaneously along with the bar.

- NGC 6753 falls into three regions: the centre is old, metal-rich, with high [Mg/Fe] values, and an extremely high stellar velocity dispersion while outside of it, σ drops and we find the presence of a significant intermediate population. We also detect an inner ring in ionised gas emission, h_4 moment and light of younger/intermediate populations. Yet, the main stellar ages vary and different populations are distributed throughout our FoV, suggesting the presence of former, short lasting ring or spiral structures producing the wide age range of intermediate (above 1.5 Gyrs) stars. Nevertheless the main component in mass is composed of old (above 12 Gyrs) stars at all radii (∼50-60%).

- NGC 7552 shows three regions: the starburst centre/circumnuclear ring, a high stellar velocity dispersion ring and an underlying disk component. The centre is dominated by the starburst and shows a young stellar component with around solar to sub-solar metallicities. At the inner side of the ring a metal-poor, old component can be found superimposed to a younger component. The outer parts of the ring present a smooth trend towards the intermediate-to-old solar stars plus younger and less metal-rich that we find in the rest of the galaxy. The central young component, extremely dominant in light, almost does not show in the mass-weighted results demonstrating its rather recent formation. Here a significant fraction (∼50-60%) of the stellar mass formed again before z∼4.

We find in all cases that most of the stellar mass has been formed long ago (before z∼4) - with a tendency to decrease for later types. We also find a strong influence of the bar on the stellar component formed between z∼2 and z∼0.1.

Comparing our results with specific simulations and models, we can confirm a two-fold formation process of galactic bulges as suggested by e.g. Obreja et al. (2013): a rapid formation of an old bulge structure in the early cosmic web initiating star formation in dense nodes (with possible influence of mergers, at least in NGC 5701) and a slower formation during the high star formation period between redshifts ∼2 and ∼1 of a younger component. Our results do not agree with the simulations on the mass fractions found. In all our cases the mass fraction of the old stellar component is larger - more than 50% and

up to 80% - than the predicted ∼30% or maximally ∼50%, pointing to higher star formation efficiencies or distinct evolutionary processes in the past. The secularly evolved component (here: intermediate populations) account for 30-40% of the stellar mass.

The limitations of our sample not only concerning its size, but also its mass range, are obvious and it cannot be regarded as representative. Nevertheless, our results point towards a common conclusion, namely the formation of already higher stellar mass fractions in the early universe than currently predicted. This work calls for even more detailed studies quantifying the importance of each process - collapse, starbursts, mergers and secular - at a given point of the lifetime of a galaxy in order to fully understand its evolutionary path. We will revisit this issue in Cacho et al. (in prep), where we extend the present work to separate the kinematics associated to each population in our sample of galaxies.

7

Conclusions and Future Work

It always seems impossible
until it's done.
Nelson Mandela

This thesis was motivated by the rising importance of *secular evolution* in the course of the evolution of a galaxy. While early formation scenarios such as interactions dominate in the early Universe, slow secular processes driven by the nature of the galaxy itself start acting later as objects are further away due to the accelerated expansion of the Universe. The exact point in time, when secular processes are becoming significant, has not been resolved yet though. Due to their significant departure from axissymmetry, *barred structures* have been predicted to be major drivers of this secular evolution and thus should produce a measurable effect on their host galaxies. Numerous studies, in particular theoretical and numerical, have already tried to investigate bars and attributed a number of features and effects to them, especially the build-up of inner structures. At the same time, an important disagreement between theory and observations, as well as within observational studies exists. While bars are theoretically predicted to significantly influence their host galaxies, most observational studies on integrated global properties between barred and unbarred galaxies have shown no differences. This is supported by the shared scaling relations between barred and unbarred galaxies, meaning that secular evolution is expected to be a *local* phenomenon. Nonetheless, clear, specific effects of bars had yet to be quantified.

This thesis presents our attempt to improve our *understanding of* ***bar-driven*** *secular evolution*. Due to the expected local effects coupled with the lack of obvious differences found between global properties of barred and unbarred galaxies, we chose to investigate a small sample of galaxies, but observed spectroscopically with very high spatial resolution. We estimated this high level of spatial detail to be necessary in order to better detect the predicted local effect of bars. On the one hand we concentrated on inner regions to particularly test the bar's capability to trigger inner substructures and on the other hand we also mapped the galaxies up to the start of their discs to probe their large-scale influence on overall gradients. This strategy in turn limited our sample size

as we decided to build large mosaics of several IFU pointings per galaxy. We conducted the observation campaign of the BaLROG (Bars in Low-Redshift Optical Galaxies) sample in several runs with the SAURON IFU at the 4.2m William-Herschel Telescope in La Palma to observe 16 barred galaxies (a total of 54 pointings, each of 1-2h). Our large mosaics cover the bars out to the radius where the disc begins to dominate, at a spatial resolution of typically 100 pc. For every galaxy we also used *Spitzer* observations from the S^4G survey of nearby galaxies. We first established a reliable yard stick, namely bar strength, conventionally via the photometry of *Spitzer* images as well as developing a new method based on the kinematics. The good agreement between the two was confirmed by using a large set of N-body simulations. This parameter allowed us to quantify the influence of bars on different parameters, kinematics as well as populations, and to ultimately answer the question: *how significant is the influence of a bar?* And thanks to the spatial detail we could further help to answer: *where do bars alter their host galaxies?*

We complemented the BaLROG project with a sample of bulges observed with very high spectral resolution gratings with the IFU WiFeS at the Siding Spring Observatory. Through an extensive analysis of their stellar and gas kinematics as well as stellar population content using state-of-the-art tools and techniques, this study helped us to set constraints on the influence of bars especially in the context of their influence on bulges and the build-up of inner structures. Furthermore, we could constrained the formation timescales of these components, giving estimates of the onset of secular evolution and its importance in the central mass build-up, hence helping to answer the questions: *when does secular evolution become important?* And: *how significant is it (in the central regions) compared to alternative scenarios such as mergers or early collapse?*

In the following, we list in detail our results and conclusions before interpreting them in a more general view.

7.1 Conclusions

Analysing stellar and gas velocities of the galaxies in the BaLROG sample, their velocity dispersions, h_3 and h_4 Gauss-Hermite moments and the stellar angular momentum λ_R and carefully comparing to a large set of N-body simulations led us to the following results and conclusions:

- **Bars do not strongly influence the global kinematics of their host galaxies**, regardless of their strength. Our work confirms previous studies (e.g. Falcón-Barroso et al., 2006; Fathi et al., 2009; Krajnović et al., 2011; Barrera-Ballesteros et al., 2014) and shows **the lack of strong kinematic misalignments between the galaxies' photometric and kinematic axes**.

- **Bars do have an influence on more subtle kinematic features**, especially in the inner regions of galaxies. We detect **double-hump velocity profiles and velocity dispersion drops** (e.g., Bureau & Athanassoula, 2005), which **increase in intensity with increasing bar strength**.

- We find evidence for the **presence of inner structures such as inner rings or discs** in about 50% of our sample. These features are detected from the anti-correlation between h_3 and V/σ within the effective radius of the galaxies ($\approx$0.1 bar lengths).

- The derived λ_R **profiles show a dip at 0.2$\pm$0.1 R_{bar}**, which we suggest is connected to the **presence of inner substructures**.

- We also derived the integrated angular momentum within one effective radius (λ_{Re}) and find that **galaxies with stronger bars exhibit a higher λ_{Re} value**. This may be a secondary effect of late-type galaxies, because they are more rotationally supported and thus also host stronger bars.

- We developed a **new method to determine the bar strength from stellar or ionised gas velocity maps (Q_{kin})**. This method relies on the extraction of the ratio of radial and tangential velocities using the technique developed by Maciejewski, Emsellem & Krajnović (2012). Values of this parameter agree well with independent measurements obtained from imaging, Q_b, e.g., Laurikainen & Salo (2002), and predictions from numerical N-body simulations.

- **Bar strength values measured from ionised-gas kinematic maps are a factor $\sim$2.5 larger than those determined from the stellar kinematic maps**.

- We observe **a flattening of the outer stellar velocity dispersion profiles with increasing bar strength**.

These results suggest a complex influence of bars in nearby galaxies, especially affecting central regions. The gas is clearly more strongly affected, reflected in higher gaseous than stellar torques. In our sample we detect a difference between bars in early and late-type galaxies, likely due to the presence of higher and lower gas fractions. To better answer some of the remaining questions and determine time scales, we investigated the stellar populations of these galaxies.

Using the classical method of line strength index measurements, we determined SSP ages, metallicities and abundances and their gradients which led us to the following results and conclusions:

- Bars among our sample exhibit **a large variety of index measurements, and hence ages and metallicities**. **Global values do not seem to be influenced by the bar** as already observed in larger samples (e.g., McDermid et al., 2015), but follow general galaxy trends according to Hubble type and central velocity dispersions.

- **Elevated Fe5015 values are found at the edges of 7 of the bars of our sample**, compared to their discs, reflected by an **elevation in the metallicity profile around 0.5 to 0.75 bar lengths**.

- Galaxies with their central spectra falling outside the SSP grid (towards the high metallicity end) overlap with those exhibiting a strong h_3-v/σ

anti-correlation within 0.1 R_{eff} (found in our Chapter 4), suggesting **a strong connection between this dynamical feature and the presence of a complex mixture of populations**.

- **Ages, metallicities and abundances are found to be similar in bars and bulges, while disks show offsets**. They exhibit in particular younger ages and lower abundances. Although some of the early-type bars are rather old, up to 10 Gyr, they reside in a young, star forming disk. This supports theoretical predictions that **bars are long-lived structures and might have formed a long time ago and survived until the present day**.

- We identify obvious **breaks among all index as well as SSP profiles** and therefore measure two different gradients. The **location of the break between the two different slopes is mainly located at 0.13±0.06 bar lengths**, confirming this place as a particular region already identified in Chapter 4, and possibly linked to an inner Lindblad resonance (Elmegreen, 1994).

- **Inner gradients are found to be much steeper than outer gradients**, for both index and SSP profiles in bar major and minor axes. Inner gradients commonly agree for bar major and minor axes.

- Outer gradients show offsets between major and minor bar axes. In particular for **Fe5015, Mg*b* and metallicity**, we find that **bar major axis gradients scatter around zero while minor axis gradients are steeper and negative towards the outside**. This might be a hint of **flattening of these parameters along the bar major axis**. This is confirmed by analyzing unbarred galaxies from the SAURON and ATLAS3D surveys that also show steeper outer gradients comparable to the minor axis gradients found in the barred galaxies. Along the bar major axis the metallicitiy gradient is found to be 0.03±0.07 dex/kpc whereas the mean value of the minor axis and the unbarred control sample is -0.20±0.04 dex/kpc. This trend was seen for 2 galaxies analysed in Sánchez-Blázquez et al. (2011) and is predicted by models (e.g., Di Matteo et al., 2013; Martinez-Valpuesta & Gerhard, 2013). We note however, that the exact values of the mean gradients are still based on a small sample and could be slightly altered due to the contrast effect of the overlying structures of bulge, disc and bar.

- We further observe a good **correlation between inner Fe5015 and metallicity gradients versus bar strength**, such that stronger bars show positive gradients, while weak bars show negative gradients. This might be an **influence of the bar providing fuel for nuclear star formation**. This result is supported by the **increasing central H_β values and decreasing younger central ages with bar strength.**

Finally, analyzing the kinematics and stellar populations of the three bulges, we deduce different formation scenarios:

- **NGC 5701** consists of mainly one old solar (or slightly sub solar) stellar population, where up to ∼80% of the galaxy's mass already existed at z∼4 distributed now radially almost uniformly (in our FoV), apart from the centre. The [Mg/Fe] values confirm a fast origin. The extremely weak nuclear spiral can be detected in the higher order moment maps (h_3, h_4) and in the stellar light contribution. Despite its stellar bar, it does not exhibit additional star formation, but shows a significant amount of intermediate populations in the central 0.5 kpc. It supports inside-out growth and appears to show a classical bulge (consistent with previous photometric analyses and increased σ) which formed almost simultaneously along with the bar.

- **NGC 6753** falls into three regions: the centre is old, metal-rich, with high [Mg/Fe] values, and an extremely high stellar velocity dispersion while outside of it, σ drops and we find the presence of a significant intermediate population. We also detect an inner ring in ionised gas emission, h_4 moment and light of younger/intermediate populations. Yet, the main stellar ages vary and different populations are distributed throughout our FoV, suggesting the presence of former, short lasting ring or spiral structures producing the wide age range of intermediate (above 1.5 Gyrs) stars. Nevertheless the main component in mass is composed of old (above 12 Gyrs) stars at all radii (∼50-60%).

- **NGC 7552** shows three regions: the starburst centre/circumnuclear ring, a high stellar velocity dispersion ring and an underlying disk component. The centre is dominated by the starburst and shows a young stellar component with around solar to sub-solar metallicities. At the inner side of the ring a metal-poor, old component can be found superimposed to a younger component. The outer parts of the ring present a smooth trend towards the intermediate-to-old solar stars plus younger and less metal-rich that we find in the rest of the galaxy. The central young component, extremely dominant in light, almost does not show in the mass-weighted results demonstrating its rather recent formation. Here a significant fraction (∼50-60%) of the stellar mass formed again before z∼4.

We further conclude that:

- We find in all cases that **most of the stellar mass has been formed long ago** (before z∼2 (and a large fraction existed already at z∼4)) - with a tendency to decrease for later types. We also find **a strong influence of the bar on the stellar component formed between z<2 and z∼0.1**.

- Comparing our results with specific simulations and models, we can confirm **a two-fold formation process of galactic bulges** as suggested by e.g. Obreja et al. (2013): a rapid formation of an old bulge structure in the early cosmic web initiating star formation in dense nodes (with possible influence of mergers, at least in NGC 5701) and a slower formation during the high star formation period between redshifts ∼2 and ∼1 of a younger component. Our results do not agree with the simulations

on the mass fractions found. In all our cases the mass fraction of the old stellar component is larger - more than 50% and up to 80% - than the predicted ∼30% or maximally ∼50%, pointing to higher star formation efficiencies or distinct evolutionary processes in the past. The secularly evolved component (here: intermediate populations) account for 30-40%.

Our conclusions and results are based on a sample of 16 barred galaxies and 3 barred and unbarred bulges. Hence, the limitations not only concerning the sample sizes, but also the mass ranges, are obvious and neither cannot be regarded as fully representative. Nevertheless, our results point towards common overall conclusions, that fit well within recent theoretical frameworks, while also proposing new constraints for both bar-driven secular evolution and the build-up of bulges.

Both studies showed that bars have a noticeable influence on galaxies, in particular on the inner parts up to circumcentral regions. The very centers however did not reveal a common behaviour, such that the influence of the bar seems to not reach beyond a certain radius. Instead, bars seem to in particular influence the region around 0.1-0.2 bar lengths. Larger statistical studies are necessary to confirm this and an orbital analysis to understand the possible resonance at this region. We also confirm that bars are not changing largely any global parameters such as galaxy or kinematic PAs. This supports the notion of secular evolution as a local phenomenon as expected from the shared scaling relations between barred and unbarred galaxies. Using our established yard stick, the bar strength, we found tentative evidence that stronger bars produce stronger features attributed to bars. However, none of the correlations was particularly striking. This points towards an even more complex picture where bars have a certain influence, but do not dominate fully over other processes or cannot alter crucially the already established galaxy properties from the early evolution. Indeed, parameters such as the total mass of a galaxy formed already at high redshift, have been proposed and found to be one of the major deciding factors on most galaxy properties observed. In fact, we found evidence for the formation of already higher stellar mass fractions in the early Universe than currently predicted. The bulge regions in our sample were mainly composed of old stars (>12 Gyr), independent of the presence of a bar. This means that the main central mass build-up likely occurred very early in the Universe, supporting an early collapse or clump merger formation scenario. As our analysis is based on galactic archeology, studies pushing the limits at high redshift would help to actually observe this mass build-up over cosmic time.

Another overall property that can influence the possible effect of bars could be the existing gas supply. This is illustrated by the stronger effect of bars in the late-types of the BaLROG sample as well as in the WiFeS sample: while we detected a build-up of inner structures in both barred galaxies in the WiFeS bulges, their magnitude is significantly different, being much larger in the gas-rich late-type. Therefore, a possible influence of a barred structure, building a secularly evolved component on top of the massive system already formed at high z, might be naturally limited to these overall properties.

Furthermore, we estimated the time when bar-driven secular evolution started to be below redshift 2. This means that it is located after the estimated peak

of the history of cosmic star formation. This supports our result that most mass had already formed by then and also could explain the minor influence of bars on global parameters of the galaxies. At the same time, it supports that bars can cause a noticeable *local influence*. The fact that galaxies exhibit different properties along the bar major axis compared to other axes implies that bars do not induce an overall mixing. Instead, they seem to behave as an auto-consistent structure, rotating as a cylinder in their host galaxies. Within this structure, stellar population gradients seem to flatten more than outside of it, due to an increased orbital mixing, but within the bar. Recent simulations and pilot observational studies on only two objects have already suggested this. The resemblance of bar and bulge as opposed to their discs, in particular in the early-types amongst our sample, further suggests an early formation of the bar along with its longevity. This has been proposed by simulations and most recent numerical studies agree that bars are long-lived structures and form early-on as soon as a disc has settled. Furthermore, simulations detected the greatest influence of the bar during its buckling phase which happens early after its formation. If this is the case, galaxy properties at that point in time could be crucial to determine the possible influence of the bar. Again, studies at higher redshift, trying to observe the buckling phase, could help us to better understand this process.

This thesis provides new insights in our understanding of bars and their influence, in particular on inner structures as well as setting constraints on the importance of bar-driven secular evolution and its onset within the major puzzle of galaxy evolution over cosmic time. This work further calls for even more detailed studies quantifying the importance of different process - collapse, starbursts, mergers and secular - at a given point of the lifetime of galaxies in order to fully understand their evolutionary path.

7.2 Plans for the future

Even though we have undertaken major efforts to better understand the formation and evolution of galaxies, in particular the nature of bars and bulges, we have only touched merely one speck of sand out of the entire desert. But at the same time, this is the beauty of it! There is still so much to be learnt and discovered and new instrumentation, telescope facilities and data analysis techniques will allow us to push the limits once more.

We have already embarked on the study of a few topics closely related to our work:

- **Dark matter**, its distribution and influence on the formation and evolution of bars. The analysis of the bar strength parameters via photometry and kinematics using N-body simulations has already given us clues on a different dark matter fraction within the bar regions of early- and late-type galaxies. The influence of the dark matter halo in galaxies has long been proposed to be a deciding factor in the formation and evolution of the barred component (e.g., Athanassoula, 2003).

- The analysis of the **exact resonance points and pattern speeds as-**

sociated to the bars in the BaLROG sample remains a pending issue. Due to the orientation of the velocity field with respect to the major axis of the bars, this is only possible in a small fraction of our sample. However, this measurement, i.e. the determination if we deal with fast or slow bars coupled with the previously mentioned dark matter fraction, will provide crucial inside on the nature of the bars. These measures can especially test the prediction that bars with $\mathcal{R}$ values (relating corotation and bar length, see Sec. 1.3.3) of 1.2 ± 0.2 must reside in maximal discs (e.g Sellwood & Debattista, 2014).

- **Lenses** as defunct bars and the possible final product of bar-driven secular evolution. A long time ago, Kormendy (1979) amongst others already proposed the transition from a bar into a lens; this last one being an elliptical shelf in the brightness distribution of a disk galaxy. In recent works, ringlenses are found to have similar sizes as bars (Laurikainen et al., 2013), but a thorough study of these scenarios is still missing. We already have observed barred lenses within the BaLROG sample and have performed more observations of unbarred lenses with the SAURON IFU and already reduced this data and started a first analysis. Nonetheless, our sample is small and it would be of interest to go for larger statistics, in particular when trying to connect bars and lenses to a common scenario.

- Further constraining the **onset of secular evolution**. We have already undertaken a pilot study using the new IFU Multi Unit Spectroscopic Explorer (MUSE) at the Very Large Telescope (VLT) in Paranal in order to better constrain when secular evolution started (Gadotti, Seidel, Sánchez-Blázquez et al., MNRAS, accepted). This study is based on the connection between the bar and inner ring component. In the future, we would like to extend the sample size in order to better understand this connection and its relevance for the importance of secular evolution overall.

- **Decoupling simultaneously the stellar populations and their kinematics**. This was the second step of our study with WiFeS and we are currently finishing the interpretation of the results (Cacho, Seidel, Ruiz-Lara et al., in prep.). As this was once again only a small pilot sample, the developed technique could be applied to larger samples that match the spectral and spatial resolution requirements in order to statistically analyse the composition of bulges and infer their formation scenarios.

As pointed out several times, the statistical significance of our results is limited due to our sample sizes. Furthermore, the BaLROG sample, while trying to be representative, still suffers a slight bias towards early-types. Therefore an obvious future improvement would be to increase the size of a sample starting with an extension towards later types, but maintaining necessary spatial and spectral resolution - or increasing it. Unfortunately, most of the analyses performed in this thesis cannot be done with current large integral field surveys, in particular due to their limited spatial resolution. In the future, instruments such as MUSE will help to resolve this problem, partly through already approved Guaranteed Time Observations (GTO) by different groups worldwide,

but also through individual proposals established within our collaborations.

Some of the hypotheses based on our results however do not necessarily require a full integral field observation, but can be done using long-slits along different axes. We already obtained spectra of two barred galaxies along major and minor bar axes with the Inamori Magellan Areal Camera and Spectrograph (IMACS) at the Magellan Telescope at Las Campanas Observatory, in the blue and red wavelength range. With those and upcoming observations, we aim to verify our results and further tackle, amongst others, the following questions:

- The **larger radial coverage** allows us to better probe the disc regions and their relation to the bar and bulge. Both studies, BaLROG and the WiFeS sample, are restricted to the inner regions and barely reach the start of the disc.

- Another short-coming of this study was the shallow depth of the analysis of the **ionised gas component**. For our future work, it could be very interesting and valuable to also consider this along with, e.g., **molecular gas** (e.g., HI kinematics), also at large scales in order to determine **streaming motions and better test the impact -and impact zone- of the bar on the gaseous component**.

- Last but not least, combining the observational effort with **simulations** can boost our understanding tremendously. However, in order for high-level numerical codes, such as **NMAGIC** (de Lorenzi et al., 2007; Morganti et al., 2013; Martinez-Valpuesta & Gerhard, 2015; Portail et al., 2015) to work, high quality data of a large enough region of the galaxy are needed.

Concerning the build-up and evolution of bulges, we further have in mind to:

- Test the recently proposed scenario of their **build-up due to the infall of large clumps at high redshift** as a possible alternative to hierarchical clustering.

- Use even **higher spatial resolution observations focusing on the centers of bulges**. Comparing a sample with and without nuclear activity, with and without bars, could help to determine their influence in these very central regions. So far, we have detected an influence at $\sim$0.13 bar length, but does it stop here? Recent studies have not found an influence of bars on AGN activity, but are higher resolution observations needed?

Last but not least, there are of course important studies that do not necessarily require the use of high spectral and spatial resolution, which is difficult to acquire in particular for large statistical studies or when moving to higher redshifts. Both are very interesting areas as bars seem to depend on their environment, too. A statistical study, even at higher redshift, would be extremely interesting to test local observations and predictions.

Unfortunately, a day only has 24 hours on this planet and a year 365 days.

The Universe still hides uncountable secrets and probably many surprises that make us reconsider and reshuffle our current understanding of the world and our place in it once more. I personally hope that my work for this thesis has contributed to our comprehension of the importance of barred structures in galaxies and the build-up of bulges and that I can continue my research on this, related and new topics in the future - - and of course, that ***you*** *enjoyed the read.*

8

Conclusiones y Trabajo Futuro

Cada vez sospecho más
que estar de acuerdo
es la peor de las ilusiones.
Julio Cortázar, Rayuela

La motivación de esta tésis reside en la creciente importancia de la *evolución secular* dentro de la evolución galáctica. Mientras que en los escenarios de formación las interacciones predominan en el Universo temprano, los procesos seculares empiezan a actuar más tarde cuando los objetos se situan más lejos entre sí debido a la expansión acelerada del Universo. Se desconoce el momento exacto en el que los procesos seculares empezaron a ser dominantes. Debido a su clara axisymetría, *las estructuras barradas* han sido propuestas como actores fundamentales en la evolución secular, debiendo producir efectos medibles en sus galaxias anfitrionas. Numerosos estudios, en particular teóricos y numéricos, ya han investigado las barras y les han atribuido un número alto de efectos, especialmente relacionados con la construcción de estructuras internas. Así mismo, existe un desacuerdo importante entre teoría y observaciones, incluso entre distintos estudios observacionales. Mientras que teóricamente se ha predicho que las barras deben influir significativamente a sus galaxias anfitrionas, la mayoría de los estudios observacionales no encuentran diferencias significativas entre galaxias barradas o no barradas. Esta falta de influencia de la barra en la galaxia anfitriona se ve reforzada por el hecho de que galaxias con y sin barra comparten las mismas relaciones de escala globales, indicando que la evolución secular se trata de un fenómeno *local*. Sin embargo, todavía existía la necesidad de cuantificar efectos específicos de las barras.

Esta tésis presenta nuestro intento de mejorar el *conocimiento de la evolución secular* ***debido a las barras***. Debido a que el efecto de la barra es de carácter local, junto a la similitud entre las propriedades globales de galaxias barradas y no barradas, hemos decidido investigar una muestra pequeña de galaxias, pero observada espectroscópicamente con muy alta resolución. Hemos estimado como necesario un nivel alto de resolución espacial para detectar los efectos locales predichos de las barras. Por un lado nos hemos enfocado en las regiones internas para medir la capacidad de la barra de iniciar subestructuras inter-

nas y por el otro lado hemos mapeado las galaxias hasta el comienzo de su disco para comprobar su influencia a una escala más grande sobre gradientes globales. Por contra, esta estrategia ha limitado el tamaño de nuestra muestra ya que habíamos decido construir grandes mosaicos usando varios apuntados. Observamos la muestra BaLROG (Bars in Low-Redshift Optical Galaxies) en varias campañas. Para ello se contó con la IFU SAURON en el telescopio de 4.2m William-Herschel Telescope, en La Palma, con el fin de obtener datos de un total de 16 galaxias barradas (en total 54 apuntados, cada uno de 1-2h). Nuestros mosaicos cubren las barras hasta el radio donde el disco empieza a dominar y están a una resolución espacial típica de 100 pc. Para cada galaxia disponemos también de observaciones de *Spitzer*, en particular, del S^{4}G survey of nearby galaxies. Primero establecimos un estándar de medición, en concreto la fuerza de barra, que medimos convencionalmente usando las imágenes de *Spitzer*. A su vez, desarrollamos un nuevo método basado únicamente en la cinemática. El buen acuerdo entre los dos se confirmó aparte usando un gran número de simulaciones de N-cuerpos. Este parámetro nos permitió cuantificar la influencia de las barras sobre distintos parámetros, tanto cinemáticos como poblacionales, respondiendo a la pregunta: *¿Cuán significativa es la influencia de una barra?* Finalmente, y gracias a la alta resolución espacial, pudimos además ayudar a responder: *¿Dónde se produce la alteración debido a la barra en la galaxia anfitriona?*

Complementamos el proyecto de BaLROG con una muestra de bulbos observados con una resolución espectral muy alta, usando las rendijas de la IFU WiFeS en el Siding Spring Observatory. Con un análisis extenso tanto de la cinemática estelar, del gas y también de las poblaciones estelares, este estudio nos ayudó a restringir la importancia de las barras, especialmente en el contexto de su influencia sobre los bulbos y la construcción de estructuras internas. Además, hemos acotado los tiempos de formación de estos componentes, dando estimaciones del comienzo de la evolución secular y de su importancia en la construcción de una masa central. Así, hemos ayudando de responder a las preguntas: *¿Cuándo empezó la evolución secular a ser importante?* Y: *¿Cuál es su importancia (en las regiones centrales) comparado con escenarios alternativos como interacciones o colapso temprano?*

La lista a continuación detalla nuestros resultados y conclusiones, antes de interpretarlas con una vista más global.

8.1 Conclusiones

Analizando las velocidades estelares y del gas de las galaxias de la muestra de BaLROG, sus dispersión de velocidades, los momentos Gauss-Hermite h_3 y h_4 y el momento angular estelar λ_R, y comparando cuidadosamente con una muestra grande de simulaciones de N-cuerpos, llegamos a los siguientes resultados y conclusiones:

- **Las barras no influyen significativamente en la cinemática global de su galaxia anfitriona**, indistintamente de su fuerza. Nuestro trabajo confirma estudios previos (e.g. Falcón-Barroso et al., 2006; Fathi et al., 2009; Krajnović et al., 2011; Barrera-Ballesteros et al., 2014) y muestra **la**

carencia de desalineamientos cinemáticos fuertes entre los ejes fotometricos y cinemáticos de las galaxias.

- **Las barras si tienen una influencia provocando características sutiles en la cinemática más**, especialmente en las regiones internas de galaxias. Detectamos **perfiles de velocidad con un doble-pico y bajadas en los perfiles de dispersion de velocidades** (e.g., Bureau & Athanassoula, 2005), que **aumentan en intensidad con la fuerza de barra**.

- Encontramos evidencias de la **presencia de estructuras internas como anillos internos o discos** en el 50% de nuestra muestra. Estas características se detectaron a través de la anti-correlación entre h_3 y V/σ dentro del radio efectivo de las galaxias ($\approx$0.1 longitud de barra).

- Los **perfiles de λ_R muestran una caída a $\mathbf{0.2\pm0.1 R_{bar}}$** lo que sugiere **la presencia de subestructuras internas**.

- Derivamos también el momento angular integrado dentro de radio efectivo (λ_{Re}) y encontramos que **las galaxias con barras más fuertes muestran un valor de λ_{Re} más alto**. Esto puede ser un efecto secundario de las galaxias de tipo tardío porque están sostenidos por rotación y por lo tanto también tienen barras más fuertes.

- Desarrollamos un **nuevo método para determinar la fuerza de la barra basado en las mapas de velocidad de las estrellas o del gas ($\mathbf{Q_{kin}}$)**. Este método está basado en la extracción del cociente entre las velocidades radiales y tangenciales, usando la técnica desarrollada por Maciejewski, Emsellem & Krajnović (2012). Los valores de este parámetro están de acuerdo con medidas independientes obtenido mediante fotometría, Q_b, e.g., Laurikainen & Salo (2002), y también con las predicciones de simulaciones numéricas de N-cuerpos.

- **La fuerza de barra medida usando la cinemática del gas supera aquella basada la cinemática de las estrellas por un factor $\sim$2.5**.

- Observamos **un aplanamiento de los perfiles de dispersión de velocidades estelar que aumenta con la fuerza de barra**.

Estos resultados sugieren una influencia compleja de las barras en galaxias cercanas, afectando especialmente a las regiones centrales. El efecto sobre el gas es claramente mayor, quedando reflejado en torques con valores más altos que en las estrellas. En nuestra muestra, detectamos una diferencia entre barras de galaxias de tipo temprano y tardío, probablemente debido a la presencia de distintas fracciones de gas. Para responder mejor a algunas de las preguntas restantes y determinar escalas de tiempo, hemos investigado las poblaciones estelares de estas galaxias..

Usando el método clásico de la medida de la fuerza de los índices de líneas espectrales hemos determinado edades, metalicidades y abundancias relacionadas con poblaciones estelares singulares (SSP) y sus gradientes. Lo que nos lleva a los siguientes resultados y conclusiones:

- En nuestra muestra las barras presentan **una gran variedad de medidas de índices, y por lo tanto de edades y metalicidades**. **Los valores globales no parecen estar alterados por la barra** como ya se ha observado en muestras más grandes (e.g., McDermid et al., 2015), pero siguen las tendencias generales de las galaxias según el tipo Hubble y la dispersión de velocidad central.

- **Los valores elevados de Fe5015 se encuentran en los bordes de 7 de las barras de nuestra muestra**, en comparación con sus discos, viéndose reflejado por **una elevación en el perfil de metalicidad alrededor de 0.5 y 0.75 de la longitud de barra**.

- Las galaxias cuyos espectros centrales se encuentran fuera del SSP grid (hacia el lado de la metalicidad más elevada) coinciden con las galaxias que muestran una anti-correlación fuerte entre h_3 y V/σ dentro de 0.1 R_{eff} (puede verse en el Capítulo 4 de la tésis). Esto sugiere **una fuerte conexión entre esta característica dinámica y la presencia de una mezcla compleja de poblaciones**.

- **Las edades, metalicidades y abundancias de las barras se parecen a las encontradas en los bulbos, mientras que los discos muestran valores más distintos.** Estos últimos parecen ser más jóvenes y presentan abundancias más bajas en comparacin con las barras y los bulbos. Sin embargo, algunas de las barras de los tipos tempranos son bastante viejas, hasta 10 Gyr, residen en un disco jóven e incluso forman estrellas. Este hecho apoya predicciones teóricas que nos señalan que **las barras son estructuras que se formaron desde hace mucho tiempo mantienendose hasta el día de hoy.**

- Identificamos **rupturas (breaks) en todos los perfiles de índices y SSP** y por ello se miden dos gradientes distintos. La **posición de estas rupturas entre los dos gradientes se encuentra en su mayor parte alrededor de 0.13±0.06 de la longitud de la barra**. Este hecho confirma esta zona como una región particular ya identificada en el Capítulo 4, posiblemente vinculada a una resonancia interna de Lindblad (Elmegreen, 1994).

- **Los gradientes internos parecen más inclinados que los gradientes externos** tanto para los perfiles de índices como para los de SSP a lo largo de los ejes mayor y menor de la barra. En general, los gradientes internos se solapan para los dos ejes.

- Los gradientes externos muestran diferencias entre el eje mayor y el eje menor de la barra. En particular para **Fe5015, Mgb y la metalicidad**, encontramos que **los gradientes a lo largo del eje mayor de la barra se encuentran en torno al cero, mientras que a lo largo del eje menor de la barra, los gradientes son más inclinados y negativos hacia fuera**. Esto podra mostrar un **aplanamiento de dichos parámetros a lo largo de la barra**. Este hecho queda confirmado al analizar una muestra de galaxias sin barra de los sondeos de SAURON y ATLAS3D que también muestran gradientes similares al observado en

el eje menor de las galaxias barradas. A lo largo del eje mayor de la barra, el gradiente de metalicidad es 0.03±0.07 dex/kpc mientras que el valor para el eje menor y la muestra control sin barras se encuentra en -0.20±0.04 dex/kpc. Esta tendencia ya se había visto para 2 galaxias analizadas por Sánchez-Blázquez et al. (2011) y estaba predicho por modelos (e.g., Di Matteo et al., 2013; Martinez-Valpuesta & Gerhard, 2013). Sin embargo, apreciamos que los valores exactos de los gradientes medianos todavía están basados en una muestra muy pequeña y podrían estar ligeramente alterados por el efecto de contraste de las estructuras que se solapan: barra, bulbo y disco.

- Además observamos una **buena correlación entre los gradientes internos de Fe5015 y metalicidad con la fuerza de barra**, refiriendonos a que las barras más fuertes muestran gradientes positivos, mientras que las barras más flojas muestran gradientes negativos. Esto puede deberse a **la influencia de la barra aportando material hacia el centro para provocar formación estelar en el núcleo**. Dicho resultado esta apoyado por **los valores centrales de H_β que aumentan y las edades centrales que disminuyen cuando la fuerza de barra aumenta**.

Finalmente, analizando la cinemática y las poblaciones estelares de nuestra muestra de tres bulbos, deducimos diferentes escenarios de formación:

- **NGC 5701** consiste mayoritariamente en una poblacion estelar solar vieja (o ligeramente sub-solar), de lo cual hasta el ∼80% de la masa de la galaxia ya existe en z∼4. Presenta una distribucin radial casi uniforme (en nuestro campo de vista), dejando aparte el centro. Los valores de [Mg/Fe] confirman un orígen de formación rápido. La espiral nuclear pequeña se puede detectar en los mapas de momento de orden superior (h_3, h_4) y en la contribución de la luz estelar. A pesar de su barra estelar, no muestra más formación estelar, solamente se ve una población de edad intermedia en los 0.5 kpc centrales. En general, esta galaxia apoya una formación de tipo 'inside-out'. Además parece mostrar un bulbo clásico (de acuerdo con los análisis fotométricos previos y σ elevados) que se formó casi simultaneamente con la barra.

- **NGC 6753** se separa en tres regiones: 1^o un centro viejo, rico en metales, con valores altos de [Mg/Fe] y una dispersión de velocidades estelar extremadamente alta mientras fuera, los valores de σ bajan y encontramos la presencia de una población intermedia. En la 2^a región, detectamos un anillo interior en la emisión de gas ionizado, en los valores del momento h_4 y en la luz de las poblaciones jóvenes e intermedias. La 3^a región se encuentra fuera de este anillo. Las edades estelares varían y dentro del campo de visión se distribuyen distintas poblaciones, sugiriendo la presencia de anillos o estructuras espirales previas de corta duración produciendo este rango ancho de estrellas de edades intermedias (más viejas de 1.5 Gyr). Por otra parte, la mayor contribucin a la masa es debida a las estrellas viejas (más viejas que 12 Gyr) en todos los radios (∼50-60%).

- **NGC 7552** muestra tres regiones: un starburst en el centro con un anillo circumnuclear, un anillo de dispersión de velocidad alta y una componente de disco subyacente. El centro está dominado por el starburst y muestra una componente estelar joven con metalicidades desde solares hasta subsolares. En el lado interior del anillo se encuentra una componente vieja y pobre en metales que esta sobrepuesta junto a otra componente joven. Los lados exteriores del anillo presentan una tendencia suave hacia las estrellas intermedias y viejas de tipo solar, junto con estrellas jóvenes y ricas en metales que encontramos en el resto de la galaxia. La componente joven central es muy dominante en luminosidad. Casi no se aprecia en los resultados pesados en masa mostrando que es una formación bastante reciente. En este caso, una fracción significante (∼50-60%) de la masa estelar se formó de nuevo antes de z∼4.

De este trabajo concluimos además que:

- Encontramos en todos los casos que **la mayor parte de la masa estelar se formo hace mucho tiempo** (antes de z∼2 (y una fracción grande ya existió a z∼4)) - con una tendencia a disminuir hacia tipos más tardíos. Encontramos también **una influencia fuerte de la barra en la componente estelar que se formó entre z<2 y z∼0.1**.

- Comparando nuestros resultados con simulaciones específicas y modelos, podemos confirmar **un proceso de formación dual de los bulbos galácticos** como ha sugerido por ejemplo Obreja et al. (2013): una formación rápida de la estructura del bulbo antiguo en la red cósmica temprana iniciando formación estelar en nodos densos (con una posible influencia de interacciones, por lo menos en el caso de NGC 5701) y una formación más lenta durante el pico de formación estelar entre redshifts ∼2 y ∼1 de una componente más joven. Nuestros resultados no están de acuerdo con simulaciones concernientes a las fracciones de masa. En todos nuestros casos, la fracción de masa de la componente estelar vieja es mayor - más que el 50% y hasta el 80% - que las predichas, que se encuentran en ∼30% o como máximo ∼50%. Este hecho apunta hacia eficiencias de formación estelar más altas o distintos procesos de evolución en el pasado. La componente que evolucionó secularmente (en este caso las poblaciones intermedias) componen 30-40%.

Nuestras conclusiones y resultados están basados en una muestra de 16 galaxias barradas y 3 bulbos barrados y no barrados. Por lo tanto, las limitaciones concernientes al tamaño de las muestras, y también a los rangos de masa, son obvias y no podemos verlas como representativas al completo. Sin embargo, nuestros resultados apuntan hacia conclusiones generales que pueden situarse bien en las teorías recientes además de proponer nuevas restricciones para la evolución secular debida a las barras y a la formación (build-up) de los bulbos.

Ambos estudios muestran que las barras tienen una influencia notable en las galaxias, en particular desde las partes interiores hasta las regiones circumcentrales. Sin embargo, los centros exactos no revelan un comportamiento común,

así que la influencia de la barra parece que no llega más allá de un radio específico. En lugar de esto, las barras parecen influir particularmente en las regiones desde 0.1 a 0.2 de las longitudes de la barra. Por ello, se hace necesario estudios más amplios con significado estadístico para confirmarlo, además de un análisis de las órbitas para entender las posibles resonancias en esta región. Confirmamos también que las barras no cambian los parámetros globales tales como los ángulos de posición global de la galaxia o de cinemática. Este hecho apoya la noción de que la evolución secular es un fenómeno local como se espera de las relaciones de escala compartidas entre galaxias barradas y no barradas. Utilizando la fuerza de barra como referencia, encontramos evidencias de que barras más fuertes producen características más fuertes atribuidas a las barras. Sin embargo, ninguna de las correlaciones aparece de forma clara. Este hecho apunta hacia un escenario más complejo donde las barras si tienen cierta influencia, pero o bien no dominan completamente los procesos o bien no pueden alterar significativamente las propiedades de la galaxia ya establecidas en su evolución temprana. Efectivamente, algunos parámetros como la masa total de la galaxia que ya se formó en su mayor parte a alto redshift, se han propuesto y encontrado como uno de los factores determinantes para muchos de los otras propiedades observadas. De hecho, hemos encontrado evidencias para la formación de fracciones de masa muy alta en el Universo temprano, mayores que las predichas. Las regiones del bulbo en nuestra muestra estaban compuestas sobre todo de estrellas viejas (>12 Gyr), independiente de la presencia de una barra. Esto significa que la formación de la masa central ocurrió ya en una fase muy temprana del Universo, apoyando una formación temprana, via un colapso temprano o via mergers de clumps. Como nuestro análisis está basado en arqueología galáctica, estudios a alto redshift ayudarían a observar esta formación de masa a lo largo del tiempo.

Otra propiedad general que puede influir al posible efecto de barras podría ser la existencia de una reserva de gas. El efecto mayor de las barras en las galaxias más tardías en ambas muestras ilustra esta sospecha: mientras que detectamos la formación de estructuras internas en ambas galaxias barradas, en la muestra de WiFeS su magnitud es muy distinta, siendo más pronunciado en el tipo tardío rico en gas. Por lo tanto, la posible influencia de una estructura barrada en formar una componente nueva a través de la evolución secular añadiendolo al sistema masivo ya formado a alto z, puede ser limitado naturalmente por estas propiedades generales.

Además, hemos estimado el tiempo del comienzo de la evolución secular de las barras situandolo por debajo de redshift 2. Esto significa que se coloca después del pico estimado de la historia de la formación estelar cósmica. Apoya nuestro resultado que la mayoría de la masa ya se formó antes y además puede explicar la menor influencia de las barras sobre parámetros globales en las galaxias. Al mismo tiempo, este hecho apoya también que las barras puedan producir una *influencia local* notable. El hecho de que las galaxias muestren distintas propiedades a lo largo del eje mayor de la barra en comparación con otros ejes, implica que las barras no inducen una mezcla global. En lugar de esto, parecen comportarse como estructuras auto-consistentes, rotando como cilindros en sus galaxias anfitrionas. Dentro de esta estructura, los gradientes de las poblaciones estelares parecen aplanarse más que fuera de ella debido al aumento de

la mezcla de órbitas, pero dentro de la barra. Simulaciones recientes y estudios observacionales piloto de solo dos objetos ya han propuesto este escenario. La similitud entre barra y bulbo en comparación con los discos, en particular para los tipos tempranos de nuestra muestra, sugiere una formación temprana de la barra y al mismo tiempo su superviviencia hasta el día de hoy. Algunas simulaciones lo han propuesto y estudios numéricos recientes están de acuerdo en que las barras se mantienen en el tiempo y que se forman temprano después de que el disco se formara. Además, las simulaciones detectaron la influencia más importante de la barra durante su fase de pandeo (buckling) que ocurre muy rápido después de su formación. Si este es el caso, las propiedades de la galaxia en este punto del tiempo podrían ser cruciales para determinar la posible influencia de la barra. De nuevo, estudios a alto redshift, intentando observar la fase de pandeo de las barras podrían ayudarnos a entender mejor este proceso.

Esta tesis presenta nuevas ideas acerca de nuestra comprensión de las barras y de su influencia, en particular sobre las estructuras internas y también ofrece restricciones acerca de la importancia de la evolución secular debido a las barras y su comienzo dentro del enorme puzzle de la evolución de galaxias en el tiempo. Este trabajo motiva también más estudios detallados para cuantificar los distintos procesos - colapso, starbursts, mergers y secular - en el punto dado dentro de la vida de una galaxia para entender mejor su camino evolutivo.

8.2 Trabajo Futuro

A pesar de nuestros grandes esfuerzos para entender mejor la formación y evolución de las galaxias, en particular la naturaleza de las barras y bulbos. Pero al mismo tiempo, esto lo hace tan bonito! Hay todavía tantas cosas por aprender y descubrir, instrumentación nueva, telescopios y desarrollos en las técnicas de análisis de datos nos permitirán desplazar los límites otra vez.

Ya hemos comenzado con varios estudios relacionados con nuestro trabajo:

- **La materia oscura**, su distribución e influencia en la formación y evolución de las barras. El análisis de los parámetros de la fuerza de barra a través de la fotometría y la cinemática usando simulaciones de N-cuerpos ya nos ha indicado las primeras estimaciones hacia una fracción distinta de materia oscura dentro del radio de barra en galaxias de tipo temprano o tardío. La influencia del halo de la materia oscura en galaxias se ha propuesto desde hace tiempo como un factor decisivo en la formación y evolución de la componente barrada (e.g., Athanassoula, 2003).

- El análisis de **los puntos exactos de resonancia y de las velocidades de patrón asociadas a las barras en la muestra de BaLROG** sigue siendo un estudio pendiente. Debido a la orientación de los campos de velocidad con respecto al eje mayor de la barra, este análisis sólo es posible en una fracción pequeña de nuestra muestra. Sin embargo, esta medida y por lo tanto la determinación de si tenemos barras rápidas o lentas junto con la fracción de materia oscura mencionada anteriormente, contiene información crucial sobre la naturaleza de las barras. Estas medidas pueden

corroborar la predicción sobre si las barras con valores de $\mathcal{R}$ (relacionando el radio de corotación y la longitud de barra, Sec. 1.3.3) de 1.2±0.2 tienen que residir en discos maximales (e.g Sellwood & Debattista, 2014).

- **Lentes** como el último estado de la evolución secular de las barras. Hace ya mucho tiempo, Kormendy (1979) y otros autores han propuesto la transición de una barra a una lente; esta última siendo una zona plana elíptica en la distribución de luminosidad de una galaxia de disco. En trabajos recientes, el tamaño de las lentes de anillo se parece al tamaño de las barras (Laurikainen et al., 2013), pero todavía no se ha realizado un estudio riguroso comprobando este escenario. Ya hemos observado lentes con barra dentro de nuestra muestra de BaLROG y hemos completado más observaciones de lentes sin barra con la IFU SAURON. Además, hemos reducido estos datos y empezado su análisis. Sin embargo, nuestra muestra es pequeña y sería interesante trabajar con una estadística más generosa, en particular cuando se intenta conectar las barras y las lentes para explicar un escenario común entre ambas.

- Restringir más **el comienzo de la evolución secular**. Ya hemos realizado un estudio piloto utilizando una nueva IFU, Multi Unit Spectroscopic Explorer (MUSE) en el Very Large Telescope (VLT) situado Paranal, con objeto de restringir mejor el momento en el que la evolución secular comenzó (Gadotti, Seidel, Sánchez-Blázquez et al., MNRAS, accepted). Este estudio está basado en la conexión entre la barra y la componente del anillo interno. En el futuro, nos gustaría extender el tamaño de la muestra para entender mejor esta conexión y su relevancia en el papel que juega dentro de la evolución secular en general.

- **Desacoplando simultaneamente las poblaciones estelares y su cinemática**. Este fue el segundo paso de nuestro estudio de WiFeS y actualmente estamos terminando la interpretación de nuestros resultados (Cacho, Seidel, Ruiz-Lara et al., in prep.). Se trato de nuevo de un estudio usando una muestra piloto pequeña. La técnica desarrollada puede ser aplicada en muestras más grandes que tienen tanto la resolución espectral como la espacial necesaria para analizar estadísticamente la composición de bulbos e inferir escenarios de formación.

Como mencionamos varias veces, la significancia estadística de nuestros resultados está limitada debido al tamaño de nuestras muestras. Además, la muestra de BaLROG, pese a que intentamos dar una muestra representativa, todavía presenta una ligera tendencia hacia tipos tempranos. Por lo tanto, una mejora obvia para el futuro sería aumentar el tamaño de la muestra comenzando con una extensión hacia tipos más tardíos, pero al mismo tiempo manteniendo la resolución espacial y espectral - o aumentándola. Desafortunadamente, la mayoría de los análisis hechos en esta tesis no se pueden repetir con los grandes sondeos de campo integral recientes, particularmente debido a su limitada resolución espacial. En el futuro, instrumentos como MUSE ayudarán a resolver este problema. Por una parte a través de tiempo ya garantizado Guaranteed Time Observations (GTO) por distintos grupos en todo el mundo, pero también

a través de propuestas individuales establecidas dentro de nuestras colaboraciones.

No obstante, algunas de nuestras hipótesis basadas en nuestros resultados no requieren necesariamente una observación de campo integral, pero podrían lograrse utilizando rendijas largas a lo largo de distintos ejes. Ya hemos obtenido espectros de dos galaxias barradas a lo largo de los ejes mayores y menores de las barras con el Inamori Magellan Areal Camera and Spectrograph (IMACS) en el Magellan Telescope at Las Campanas Observatory, en los rangos azul y rojo. Con estas observaciones y algunas más pendientes, queremos verificar nuestros resultados y además intentar responder a las siguientes preguntas, aparte de otras:

- La **extensión más larga en radio** nos permitirá comprobar con mayor precisin las regiones de disco y su relación con la barra y el bulbo. Ambos estudios, BaLROG y la muestra de WiFeS, se limitan a los regiones internas y llegan justo al disco.
- Otra limitación de nuestro estudio fue el corto análisis del **gas ionizado**. Para nuestro trabajo futuro, puede ser muy interesante y valioso considerar también esta componente junto con, e.g., **gas molecular** (e.g., de cinemática de HI), también a gran escala para determinar mejor **movimientos de streaming y comprobar con mayor finura el impacto -y la zona del impacto- de la barra sobre la componente gaseosa**.
- Por último, combinando esfuerzos observacionales con **simulaciones** se podrá mejorar en gran medida nuestra comprensión. Pero, para que funcionen códigos potentes como **NMAGIC** (de Lorenzi et al., 2007; Morganti et al., 2013; Martinez-Valpuesta & Gerhard, 2015; Portail et al., 2015), son necesarios datos de buena calidad en una región de la galaxia lo suficientemente grande.

Acerca de la formación y de la evolución de los bulbos, tenemos en mente:

- Comprobar escenarios propuestos reciéntemente, describiendo su **formación a través de la caída de trozos de masa (clumps) a redshift alto** como una posible alternativa a la agrupación jérarquica.
- Utilizar una **resolución espectral más alta enfocando a los centros de los bulbos**. Comparando una muestra con y sin actividad nuclear, con y sin barras, puede ayudar a determinar su influencia en las regiones más próximas al centro. Hasta ahora, hemos detectado una influencia de la barra a $\sim$0.13 de la longitud de la barra, pero: ¿desaparece en este punto? Estudios recientes no han encontrado una influencia de barras en la actividad de AGN, por lo que ¿necesitamos observaciones con mejor resolución?

Por último, tenemos que mencionar que hay también estudios que no requieren necesariamente ni el uso de una resolución espectral ni espacial altas, lo que es dificil de adquirir particularmente para estudios estadísticos o investigaciones a alto redshift. Ambos son áreas muy interesantes debido a que las barras también dependen del entorno en el que se encuentran. Un estudio estadístico,

incluso a alto redshift, sería muy interesante para comprobar las observaciones locales y las predicciones.

Desafortunadamente, un día solo tiene 24 horas en este planeta y un año solo 365 días. El Universo todavía esconde incontables secretos y probablemente muchas sorpresas que nos harán reconsiderar y resituar nuestra comprensión actual del mundo y nuestro sitio en él una vez más. Personalmente, espero que el trabajo de mi tesis haya contribuido a una mayor comprensión de la importancia de las estructuras barradas en galaxias y de la formación de bulbos y que puedo continuar mi investigación en ello, en temas relacionados y en otros tópicos en un futuro - - y claro, también espero que a ***usted*** *le haya gustado leer esta tesis.*

9

Zusammenfassung und Ausblick

Wissenschaft: Es ist nicht ihr Ziel,
der unendlichen Weisheit eine Tür zu öffnen,
sondern eine Grenze zu setzen dem unendlichen Irrtum.
Bertold Brecht

Die vorliegende Dissertation befasst sich mit der zunehmenden Bedeutung von *säkularer Evolution* im Laufe der Evolution einer Galaxie. Während im jungen Universum Interaktionen zwischen Galaxien dominierten, so begannen später langsame, säkulare Prozesse, beeinflusst durch die Natur der Galaxie selbst, die Evolution mehr und mehr zu bestimmen. Aufgrund der beschleunigten Expansion des Universums befinden sich die Objekte nämlich weiter voneinander entfernt, sodass Interaktionen weniger stattfinden. Der genaue Zeitpunkt, wann säkulare Prozesse bedeutsam wurden, ist bisher noch unbekannt. Aufgrund ihrer signifikanten Abweichung von einer achsensymmetrischen Struktur sind *Balkenstrukturen* als eine der Hauptaktoren von säkularer Evolution vorhergesagt worden. Deshalb wird von ihnen ein messbarer Effekt auf ihre Galaxie erwartet. Insbesondere theoretische und numerische Studien haben schon versucht, diesen Effekt zu bestimmen und haben eine Reihe von Merkmalen erkannt und vorhergesagt, die auf Balkenstrukturen zurückzuführen sind, insbesondere was den Aufbau von inneren Komponenten und Strukturen in einer Galaxie betrifft. Gleichzeitig herrscht allerdings Uneinigkeit zwischen theoretischen Studien und Beobachtungen, sowie innerhalb von Beobachtungsstudien. Während theoretische Studien einen deutlichen Einfluss der Balkenstrukturen vorhersagen, finden Beobachtungen von integrierten globalen Parametern der Galaxien keine oder nur minimale Unterschiede zwischen Balkengalaxien und anderen Galaxien (ohne Balken). Gemeinsame Skalenbeziehungen von Balken- und Nicht-Balkengalaxien unterstützen diesen Befund und deuten darauf hin, dass säkulare Evolution ein *lokales* Phänomen ist und daher kaum Unterschiede in globalen integrierten Parametern gefunden werden können. Dieser lokale Effekt von Balkenstrukturen, teils vorhergesagt, wurde allerdings noch immer nicht quantifiziert. Die vorliegende Arbeit präsentiert unseren Versuch, unser *Verständnis von durch Balken getriebene säkulare Evolution* zu verbessern. Aufgrund der Kombination vom erwarteten

lokalen Effekt und dem Fehlen von klaren globalen Unterschieden zwischen Balken- und Nicht-Balkengalaxien, haben wir uns entschlossen, unseren eigenen Datensatz spektroskopisch, sowie mit sehr guter räumlicher Auflösung zu erstellen. Nach unserer Einschätzung ist dieses hohe Maß an Detail notwendig, um die vorhergesagten Effekte der Balken zu testen. Einerseits haben wir uns auf innere Regionen konzentriert, um zu testen, ob Balkenstrukturen tatsächlich fähig sind, dort Substrukturen auszulösen. Andererseits haben wir versucht, die Galaxien bis zum Beginn ihrer Scheibe zu beobachten, um auch großräumig Gradienten messen zu können. Diese Strategie führt jedoch zu einer limitierten Größe des Datensatzes, da wir zudem beschlossen, große Mosaike von mehreren IFU-Aufnahmen pro Galaxie aufzunehmen. Die Beobachtungskampagne BaLROG (Bars in Low-Redshift Optical Galaxies) wurde in mehreren Beobachtungszeiträumen mit der IFU SAURON am 4.2m William-Herschel Telescope in La Palma durchgeführt und insgesamt haben wir 16 Balkengalaxien beobachtet (54 IFU Aufnahmen von jeweils 1-2h insgesamt). Unsere großen Mosaike decken die Balken bis zum Beginn der Scheibe komplett ab und haben üblicherweise eine räumliche Auflösung von 100 pc. Zudem haben wir für jede unserer Galaxien *Spitzer*-Aufnahmen dank der Studie des S^4G. Zu Anfang führten wir eine Art Messlatte ein, die Balkenstärke, die konventionell von photometrischen Aufnahmen gewonnen wird und die wir so über die *Spitzer*-Aufnahmen berechnen konnten. Außerdem haben wir eine neue Methode entwickelt, die Balkenstärke über die kinematischen Informationen zu gewinnen. Beide Werte stimmen gut miteinander üeberein. Dies haben wir zusätzlich mit Hilfe von zahlreichen N-body-Simulationen geprüft. Die Balkenstärke erlaubte uns, den Einfluss der Balken auf bestimmte andere Parameter zu quantifizieren, um letztlich folgende Fragen zu beantworten: *Wie bedeutend ist der Einfluss eines Balkens auf seine Galaxie?* Und dank der hohen räumlichen Auflösung konnten wir zusätzlich beantworten: *Wo genau findet sich der Einfluss des Balkens innerhalb einer Galaxie?*

Wir ergänzten das BaLROG-Projekt mit weiteren Beobachtungen von Bulgen, die wir mit spektroskopisch sehr hoch auflösenden Gittern der IFU WiFeS am Siding Spring Observatory gewinnen konnten. Eine ausführliche Analyse ihrer stellaren und interstellaren Kinematik sowie der vorhandenen Sternpopulationen dank modernster Techniken half uns, die durch Balken getriebene säkulare Evolution, insbesondere im Kontext mit ihrem Einfluss auf Bulges und dem Aufbau innerer Strukturen weiter zu beschränken. Außerdem konnten wir Zeitskalen dieser Prozesse festlegen und so eine Abschätzung dazu geben, wann der Einfluss der säkularen Evolution bedeutsam wird, also folgende Fragen beantworten: *Wann beginnt ein wesentlicher Einfluss der säkularen Evolution?* Und: *Wie bedeutsam ist dieser Einfluss (in den inneren Regionen) verglichen mit alternativen Szenarien wie Mergers oder früher Kollaps?*
Im Folgenden geben wir eine Liste unserer Resultate und Schlussfolgerungen, bevor wir diese im globalen Kontext von Galaxienevolution interpretieren.

9.1 Zusammenfassung

Nach unserer Analyse der stellaren und interstellaren Kinematik der BaLROG Daten, d.h. Rotations- und Dispersionsgeschwindigkeiten, Gauss-Hermite-Momente h_3 und h_4, stellare Drehimpulse λ_R sowie unserem Vergleich mit einer

hohen Anzahl an N-Body-Simulationen, sind wir zu folgenden Resultaten und Schlussfolgerungen gelangt:

- **Balken beeinflussen nicht die globale Kinematik ihrer Galaxien**, ungeachtet der Balkenstärke. Unsere Arbeit unterstützt somit frühere Studien (e.g. Falcón-Barroso et al., 2006; Fathi et al., 2009; Krajnović et al., 2011; Barrera-Ballesteros et al., 2014) und zeigt zudem das **Ausbleiben einer meßbaren Achsenverschiebung von Galaxienhauptachse oder kinematischer Achse** auf.

- **Balken haben Einfluss auf lokale kinematische Eigenschaften**, insbesondere in den inneren Regionen von Galaxien. Wir finden **'double-hump' Geschwindigkeitsprofile sowie zentrale Abfälle von Dispersionsgeschwindigkeiten** (e.g., Bureau & Athanassoula, 2005). Wir quantifizieren deren absolute Werte und finden, dass diese **mit der Stärke des Balkens zunehmen**.

- Wir finden Anzeichen von **Präsenz von inneren Strukturen wie inneren Ringen oder Scheiben** in ca. 50% unseres Datensatzes. Diese Eigenschaft wurde dank der Antikorrelation zwischen h_3 und V/σ innerhalb des effektiven Radius der Galaxien ($\approx$0.1 Balkenlängen) festgestellt.

- Die Drehimpulsprofile von λ_R **zeigen einen Abfall bei 0.2$\pm$0.1 R_{bar}**. Dies könnte eine Verbindung zu den **inneren Strukturen** bedeuten.

- Wir haben zudem den integrierten Drehimpuls innerhalb eines effektiven Radius (λ_{Re}) berechnet und gefunden, dass **Galaxien mit stärkerer Balkenstruktur höhere λ_{Re} Werte aufweisen**. Dies könnte allerdings ein sekundärer Effekt von späten Galaxien (late-types) sein, da diese durch Rotation zusammenhalten und so auch stärkere Balken haben können.

- Wir haben eine **neue Methode zur Berechnung der Balkenstärke entwickelt, die auf den kinematischen Informationen basiert**. Diese Methode beruht auf der Berechnung von radialen sowie tangentialen Geschwindigkeiten, die dank einer Technik, die durch Maciejewski, Emsellem & Krajnović (2012) entwickelt wurde, kalkuliert werden können. Werte dieses Parameters stimmen gut mit denen der Photometrie überein, Q_b, e.g., Laurikainen & Salo (2002), sowie mit Vorhersagen von N-body-Simulationen.

- **Die Balkenstärke der interstellaren Komponente ist $\sim$2.5 größer als die der stellaren Komponente.**

- Wir beobachten eine **Abflachung des äußeren Gradienten des Dispersionsgeschwindigkeitsprofils mit steigender Balkenstärke**.

Diese Resultate lassen auf einen komplexen Einfluss von Balken in nahen Galaxien schließen, insbesondere in ihren Zentren. Zudem ist der Effekt in der interstellaren Komponente im vorhandenen ionisierten Gas wesentlich stärker zu beobachten. Dies zeigt sich in den höheren Werten der Balkenstärken hier, im

Vergleich zu denen, die mit der stellaren Komponente gemessen wurden. Der gefundene Unterschied zwischen frühen und späten Balkengalaxien ist wahrscheinlich u.a. auf höhere Gasanteile zurückzuführen. Um einige dieser Fragen besser zu beantworten und Zeitskalen festzulegen, haben wir zudem die Sternpopulationen dieser Galaxien bestimmt.

Wir nutzten die klassische Methode der Messung der Intensität von Linienindexen, um SSP-Alter, -Metallgehalt und -Abundanzen, sowie deren Gradienten zu bestimmen. Diese Analysen führten zu folgenden Resultaten und Schlussfolgerungen:

- Die Balken in unserem Datensatz zeigen **eine Fülle verschiedener Linienindexwerte, und daher Alter und Metallgehalte** auf. **Globale Werte scheinen nicht durch den Balken beeinflusst zu sein** wie schon in früheren Studien gemessen wurde (e.g., McDermid et al., 2015). Stattdessen folgen die Messwerte generellen Trends, die auf alle Galaxien zutreffen und vom Hubbletyp und zentralen Dispersionsgeschwindigkeiten abhängen.

- **Erhöhte Fe5015 Werte finden sich an den Enden von 7 Balken in unserem Datensatz**, verglichen mit den Werten in den Scheiben. Dies reflektiert sich in **erhöhten Werten in den Metallgehaltprofilen um 0.5 bis 0.75 Balkenlängen**.

- Galaxien, deren zentrale Spektren außerhalb des SSP-Gitters fallen (auf der Seite des erhöhten Metallgehalts), stimmen mit den Galaxien überein, die eine stärkere Antikorrelation zwischen h_3 und V/σ innerhalb 0.1 R_{eff} aufweisen (siehe Kapitel 4). Dies lässt auf eine **starke Verbindung zwischen diesen dynamischen Merkmalen und der Existenz einer komplexen Mischung von Sternpopulationen schließen**.

- **Alter, Metallgehalt und Abundanzen scheinen sich zwischen Balken und Bulgen stark zu ähneln, im Gegensatz zum sehr unterschiedlichen Wert der Scheiben**. Diese sind jünger und haben niedrigere Abundanzwerte. Obwohl einige der frühen Balken sehr alt sind, bis zu 10 Gyr, sitzen sie oft in einer jungen, sternformenden Scheibe. Dies unterstützt theoretische Vorhersagen, dass **Balken langlebige Strukturen sind, die vor langer Zeit entstanden sind und bis heute überlebt haben**.

- Wir identifizieren einen deutlichen **Bruch in allen Index- und SSP-Profilen** und messen daher zwei Gradienten. Die **Position dieses Bruchs, der die zwei Gradienten trennt, befindet sich typischerweise bei 0.13±0.06 Balkenlängen**, was diesen Ort abermals als eine spezielle Region kennzeichnet, wie schon in Kapitel 4 gefunden. Sie könnte einen direkten Bezug zu einer inneren Lindblad-Resonanz haben (Elmegreen, 1994).

- **Innere Gradienten sind wesentlich steiler als die äußeren Gradient**, sowohl für Index- als auch SSP-Profile entlang der Haupt- und Nebenachse des Balkens. Innere Gradienten stimmen entlang beider Achsen zudem überein.

- Äußere Gradienten zeigen Unterschiede zwischen den beiden Achsen. Insbesondere in den Parametern **Fe5015, Mg*b* und Metallgehalt** finden wir, dass **Hauptachsengradienten sich um Null bewegen, während Nebenachsengradienten steiler und negativ (nach außen) sind**. Dies könnte ein Hinweis auf **eine Abflachung dieser Parameter entlang der Balkenhauptachse** sein. Wir bestätigen dies mit der Analyse von Gradienten in Nicht-Balkengalaxien von den Beobachtungskampagnen SAURON und ATLAS3D. Hier zeigen sich die äußeren Gradienten ebenfalls steil und sind vergleichbar mit den Nebenachsengradienten unserer Balkengalaxien. Entlang der Balkenhauptachse ist der Wert des Metallgehaltsgradienten im Schnitt 0.03±0.07 dex/kpc, während er für die Nebenachse und den Kontrolldatensatz ohne Balken -0.20±0.04 dex/kpc misst. Dieser Trend wurde schon für 2 Galaxien beobachtet (Sánchez-Blázquez et al., 2011) und wurde von Modellen vorhergesagt (e.g., Di Matteo et al., 2013; Martinez-Valpuesta & Gerhard, 2013). Wir betonen jedoch, dass die exakten Werte der durchschnittlichen Gradienten noch immer auf wenigen Datenpunkten beruhen und dass ihr absoluter Wert sich etwas ändern kann, insbesondere durch den Kontrast der sich überlappenden Strukturen (Bulge, Balken, Scheibe).

- Wir beobachten außerdem eine gute **Korrelation zwischen den inneren Fe5015- und Metallgehaltsgradienten mit der Balkenstärke**, sodass stärkere Balken positive Gradienten und schwächere Balken negative Gradienten aufzeigen. Dies könnte durch **den Transport von Material durch den Balken erreicht werden, der nukleare Sternformation hervorruft**. Dieses Resultat wird zusätzlich durch **steigende zentrale H_β-Werte und jüngere zentrale Sternpopulationen mit steigender Balkenstärke** unterstützt.

Die Analyse der Kinematik und Sternpopulationen der drei Bulges führt uns zu folgenden Evolutionsszenarien:

- **NGC 5701** setzt sich hauptsächlich aus einer alten, solaren (oder ganz leicht subsolaren) Sternpopulation zusammen, deren Masse (bis zu ∼80%) schon bei z∼4 existiert hat und die nun radial fast uniform (in unserem Blickfeld), verteilt ist - abgesehen vom Zentrum. Die [Mg/Fe]-Werte bestätigen einen rapiden Formationsprozess. Sehr schwache nukleare Spiralarme konnten in den Gauss-Hermite-Momenten (h_3, h_4) und der stellaren Lichtverteilung entdeckt werden. Trotz des stellaren Balkens finden sich ansonsten keine weiteren sternformenden Regionen. Stattdessen gibt es eine bedeutsame Menge an mittelalten Populationen in den zentralen 0.5 kpc. Dies lässt auf ein 'inside-out-growth'-Szenario schließen. Außerdem scheint der Bulge klassisch zu sein (im Einklang mit vorherigen photometrischen Analysen und erhöhten σ-Werten) und formte sich zur gleichen Zeit wie der Balken.

- **NGC 6753** kann in drei Regionen aufgeteilt werden: das Zentrum ist alt, metallreich und zeigt hohe [Mg/Fe]-Werte sowie sehr hohe Dispersionsgeschwindigkeiten. Außerhalb fallen die σ-Werte und wir finden eine bedeutsame Menge an mittelalten Sternen. Wir entdecken zudem einen

inneren Ring im ionisierten Gas, im h_4-Moment und im Licht der jungen und mittelalten Sterne. Allerdings variieren die Alter der Sternpopulationen und verschiedene Populationen verteilen sich über das gesamte Blickfeld, was auf frühere, kurzlebige Ringe und Spiralstrukturen schließen lässt, die diese Vielfalt an Populationen im mittelalten Bereich (über 1.5 Gyr) hervorgerufen haben. Nichtsdestotrotz ist die Hauptkomponente gemessen in der Masse (∼50-60%) sehr alt (über 12 Gyr) und befindet sich im kompletten Blickfeld.

- **NGC 7552** zeigt drei Regionen: einen zentralen Starburst und zentralnuklearen Ring, einen Ring außerhalb davon, der sehr hohe Dispersionsgeschwindigkeiten aufzeigt, und eine darunterliegende Scheibe. Das Zentrum ist durch den Starburst bestimmt und zeigt sehr junge Sterne mit solaren bis subsolaren Metallgehalten. An der inneren Seite des Rings befindet sich eine metallarme und alte Komponente, die sich mit einer jungen Komponente überlappt. Die äußeren Teile des Rings zeigen einen sanften Trend zu mittelalten bis alten, sowie jungen und weniger metallreichen Sternen, die wir im Rest der Galaxie finden. Die zentrale junge Komponente ist sehr lichtstark, jedoch verschwindend gering im Masseanteil, was auf einen jungen Ursprung schließen lässt. Die massereichste Komponente (∼50-60%) ist abermals alt und existierte bereits bei z∼4.

Zusammenfassend finden wir also:

- In allen Fällen **formte sich die Mehrheit der stellaren Masse vor geraumer Zeit** (vor z∼2 (und ein Großteil existiere schon bei z∼4)) - mit einer fallenden Tendenz für spätere Galaxien. Wir finden zudem einen **bedeutsamen Einfluss des Balkens auf die Sternpopulation, die sich zwischen z<2 und z∼0.1 formte**.

- Der Vergleich unserer Resultate mit Simulationen und Modellen lässt auf **einen dualen Formationsprozess von Bulges** schließen, wie z.B. von Obreja et al. (2013) beschrieben: eine rapide Phase, in der sich die alte Bulgestruktur in den Knoten des frühen kosmischen Netzes formt (mit möglichem Einfluss von Interaktionen, z.B. im Fall von NGC 5701) und eine langsamere Phase, während der sich die jüngeren Strukturen formen, während der Periode von hoher Sternformungsaktivität zwischen den Rotverschiebungen ∼2 and ∼1.

  Unsere Resultate stimmen allerdings nicht mit den Massenanteilen überein, die in Simulationen gefunden worden sind. In allen unseren Fällen finden wir, dass der Massenanteil der alten stellaren Komponente höher ist - mehr als 50% und bis zu 80% der totalen stellaren Masse - wohingegen Vorhersagen im Schnitt nur ∼30% oder maximal ∼50% betragen. Dies deutet auf eine erhöhte Effizienz von Sternformationsprozessen oder anderen evolutionären Prozessen in der Vergangenheit hin. Die säkular entwickelte Komponente (hier: die mittelalten Sterne) beinhaltet durchschnittlich 30-40% der totalen stellaren Masse.

Unsere Resultate und Schlussfolgerungen basieren auf einem Datensatz von 16 Balkengalaxien und 3 Bulgen in Balken- und Nicht-Balkengalaxien. Die

Einschränkungen aufgrund der Größe der Datensätze, aber auch aufgrund des Massenumfangs sind offensichtlich und wir können daher nicht von einer statistisch repräsentativen Studie sprechen. Nichtsdestotrotz führen unsere Resultate zu gemeinsamen und allgemeinen Schlussfolgerungen, die gut in aktuelle theoretische Rahmenbedingungen passen und gleichzeitig neue Bedingungen für durch Balken getriebene säkulare Evolution und die Entstehung von Bulgen setzen.

Beide Studien haben gezeigt, dass Balken einen bedeutsamen Einfluss auf Galaxien haben, insbesondere auf deren innere Regionen, sowie im direkten Umkreis der Zentren. Im jeweiligen Zentrum selbst wurden jedoch keine Gemeinsamkeiten entdeckt, sodass es scheint, dass der Einfluss der Balken nicht über einen bestimmten Radius hinausgeht. Stattdessen beeinflussen Balken besonders die Region um 0.1-0.2 Balkenlängen. Umfangreichere statistische Studien sind nötig, um dies zu bestätigen, sowie eine Orbitalanalyse, um die verschiedenen Resonanzpunkte besser zu verstehen. Wir bestätigen zudem, dass Balken keine globalen Parameter, wie Positionswinkel der Galaxie oder der globalen Kinematik verändern. Dies unterstützt, dass säkulare Evolution eher ein lokales Phänomen ist, wie von den geteilten Skalenbeziehungen zwischen Balken- und Nicht-Balkengalaxien zu erwarten ist. Dank unserer entwickelten Messlatte, der Balkenstärke, konnten wir tentative Korrelationen zwischen dieser und Balken-induzierten Merkmalen feststellen, jedoch war keine besonders ausgeprägt. Dies deutet auf einen noch komplizierteren Einfluss der Balken hin, in dem Sinn, dass sie nicht völlig andere Prozesse dominieren oder schon etablierte Galaxienparameter verändern können, sondern gemeinsam mit anderen Treibern kleinere Veränderungen hervorrufen. Gerade Parameter wie die Masse einer Galaxie, die sich schon im frühen Universum formt, sind schon lange als einer der entscheidenden Faktoren vorgeschlagen, die andere Galaxienparameter bestimmen. In unseren Studien finden wir auch Hinweise auf eine sehr frühe Entstehung eines Großteils der stellaren Masse, mehr als zur Zeit vorausgesagt. Die Bulge-Regionen in unseren Daten waren hauptsächlich aus alten Sternen zusammengesetzt (>12 Gyr), unabhängig von der Existenz eines Balkens. Dies bedeutet, dass die Mehrheit der zentralen Masse sich schon im jungen Universum ausbildete, was das Kollaps- oder Klumpenverschmelzungs-Szenario stützt. Da unsere Analyse auf galaktischer Archäologie beruht, wären Studien bei hohen Rotverschiebungen hilfreich um diesen Massenaufbau direkt zu beobachten.

Eine weitere allgemeine Eigenschaft, die den möglichen Einfluss von Balken behindern oder fördern kann, ist ein vorhandenes Gasreservoir. Dies wird bei dem ausgeprägteren Effekt von Balken in späteren Galaxien deutlich, sowohl im BaLROG- als auch im WiFeS-Datensatz: obwohl wir in beiden Balkengalaxien in den Bulgen des WiFeS-Datensatzes eine Entstehung von inneren Strukturen gemessen haben, ist deren Ausmaß in der späteren Galaxie deutlich größer. Daher scheint die Möglichkeit, dass eine Balkenstruktur eine säkular entwickelte Komponente aufbaut, durch diese generellen Bedingungen natürlich limitiert zu sein.

Außerdem konnten wir den Zeitpunkt, wann Balken-getriebene säkulare Evolution beginnt bedeutend zu werden, auf eine Rotverschiebung von unter 2 abschätzen. Dies zeigt, dass sie kurz nach dem geschätzten Hoch der kosmis-

chen Sternentstehungsgeschichte beginnt. Damit ist unser Ergebnis bekräftigt, dass der Großteil der Masse zu diesem Zeitpunkt schon entstanden war, was wiederum den untergeordneten Einfluss der Balken auf globale Parameter der Galaxien erklären könnte. Gleichzeitig unterstützt diese Erkenntnis, dass Balken dennoch einen spürbaren *lokalen* Einfluss haben können. Die Unterschiede zwischen den Eigenschaften entlang der Balkenachse, verglichen mit anderen Achsen, deutet darauf hin, dass Balken keine globale Vermischung erzeugen. Stattdessen scheinen sie sich als autokonsistente Struktur, die wie ein Zylinder innerhalb der Galaxie rotiert, zu verhalten. Innerhalb dieser Struktur scheinen sich Gradienten der Sternpopulationen abzuflachen aufgrund einer gesteigerten orbitalen Vermischung, allerdings immer innerhalb des Balkens. Aktuelle Simulationen sowie Pilotstudien, basierend auf nur zwei Objekten, haben dies schon angedeutet. Die Ähnlichkeit zwischen Balken und Bulge verglichen mit ihren Scheiben, insbesondere in den frühen Galaxien in unseren Daten, lässt zudem auf eine frühe Entstehung sowie Langlebigkeit des Balkens schließen. Dies wurde auch von Simulationen vorgeschlagen und mittlerweile sind sich numerische Studien über die Langlebigkeit von Balken einig, als auch über dessen Entstehung kurz nach der Entstehung der Scheibe. Simulationen zeigen außerdem, dass der stärkste Einfluss der Balken in ihrem Stauchungsstadium (buckling phase) stattfindet, welches kurz nach ihrer Entstehung stattfindet. Falls dies der Fall ist, dann wäre dieser Zeitpunkt sowie dabei herrschende Bedingungen in der Galaxie entscheidend für den möglichen Einfluss des Balkens. Abermals könnten uns Studien bei hohen Rotverschiebungen helfen, diese Stauchungsphase zu beobachten um diesen Prozess besser zu verstehen.

Die vorliegende Dissertation liefert neue Einblicke in unser Verständnis von Balken und deren Einfluss, insbesondere auf deren innere Strukturen. Auerdem wird die Beschrnkung der Tragweite von durch Balken getriebene säkularer Evolution aufgezeigt und deren Beginn innerhalb des Puzzles der Galaxienevolution. Unsere Arbeit motiviert weitere Detailstudien zu noch besserer Quantifizierung der Bedeutung verschiedener Prozesse - Kollaps, Starbursts, Mergers und säkulare Prozesse - über die Lebensdauer von Galaxien, um letztlich deren Gesamtevolution besser zu verstehen.

9.2 Ausblick

Obwohl wir bedeutsame Arbeit geleistet haben, um die Entstehung und Evolution von Galaxien besser zu verstehen, speziell die Natur von Balken und Bulgen, so haben wir nur die Spitze des Eisbergs untersucht. Dies ist allerdings gleichzeitig das Faszinierende! Immer gibt es noch mehr zu entdecken und neue Instrumente, Teleskope und Datenanalysetechniken werden uns erlauben, in Zukunft abermals einen Schritt weiterzugehen.

Jetzt schon haben wir mit einigen Studien begonnen, die einen starken Bezug zu unserer Arbeit haben:

- **Dunkle Materie**, ihre Verteilung und ihr Einfluss auf die Entstehung und Evolution von Balken. Die Analyse von Balkenstärken über die Photometrie und Kinematik mit Hilfe von N-body-Simulationen hat uns Hinweise auf einen unterschiedlichen Anteil von Dunkler Materie in frühen

und späten Galaxien gegeben. Der Einfluss von einem Halo von Dunkler Materie wurde schon lange als entscheidender Faktor bei der Entstehung und Evolution einer Balkenkomponente vorausgesagt (e.g., Athanassoula, 2003).

- Die Analyse von den **exakten Resonanzpunkten sowie der Strukturgeschwindigkeit (pattern speed) der Balken des BaLROG-Datensatzes** bleibt eine offene Studie. Aufgrund der Orientierung der Geschwindigkeitsfelder zur Hauptachse der Balken ist diese Messung allerdings nur für einen kleinen Anteil unserer Daten möglich. Nichtsdestotrotz kann sie, d.h. die Berechnung, ob unsere Balken schnell oder langsam sind, verbunden mit den Messungen der Anteile der dunklen Materie, wertvolle Hinweise auf die Natur von Balken geben. Insbesondere können wir dadurch die Vorhersage testen, ob Balken mit $\mathcal{R}$-Werten (Verbindung zwischen Corotation und Balkenlänge, Sec. 1.3.3) von 1.2 ± 0.2 sich in einer maximalen Scheibe befinden (e.g Sellwood & Debattista, 2014) - oder nicht.

- **Linsen** als mögliches Endstadium von Balken-getriebener säkularer Evolution. Schon vor geraumer Zeit haben Kormendy (1979) und weitere Autoren den Übergang von einem Balken in eine Linse vorgeschlagen; letztere definiert als 'elliptical shelf' in der Lichtverteilung einer Spiralgalaxie. Aktuelle Studien finden zudem vergleichbare Größenverhältnisse von Balken und Ringlinsen (Laurikainen et al., 2013), aber eine ausführliche Untersuchung, die die Verbindung der beiden analysiert, steht noch aus. Wir haben schon Beobachtungen von Linsen in Balkengalaxien innerhalb unseres BaLROG-Datensatzes und haben zusätzlich weitere Beobachtungen von Linsen ohne Balken an der SAURON-IFU durchgeführt. Diese Daten sind schon reduziert und die Analyse hat begonnen. Nichtsdestotrotz bleibt der Datensatz klein und es wäre wichtig, eine gute Statistik zu haben, gerade wenn wir die Verbindung von Balken und Linsen global untersuchen wollen.

- Weiter den **Beginn von säkularer Evolution beschränken**. Wir haben eine Pilotstudie mit der neuen IFU Multi Unit Spectroscopic Explorer (MUSE) am Very Large Telescope (VLT) in Paranal unternommen, um besser den Zeitpunkt festzulegen, an dem säkulare Evolution bedeutend wurde (Gadotti, Seidel, Sánchez-Blázquez et al., MNRAS, accepted). Diese Studie basiert auf der Verbindung zwischen Balken und innerem Ring. In Zukunft möchten wir die Größe des Datensatzes erweitern, um diese Verbindung und deren Relevanz in der säkularen Evolution besser zu verstehen.

- **Simultanes Bestimmen von Sternenpopulationen und deren assoziierter Kinematik**. Dies war der zweite Schritt unserer Studie mit dem WiFeS-Datensatz und wir sind dabei, die Interpretation der Resultate zu beenden (Cacho, Seidel, Ruiz-Lara et al., in prep.). Da es sich abermals um eine kleine Pilotstudie handelt, wäre es interessant, die entwickelte Technik bei größeren Datensätzen anzuwenden. Diese müssen allerdings die Bedingungen von sehr guter Auflösung sowohl spektral als

auch räumlich erfüllen. So könnten wir statistisch die Zusammensetzung von Bulgen und deren Entstehungsszenarien besser verstehen.

Wie mehrfach aufgeführt wurde, ist die statistische Bedeutung unserer Resultate aufgrund unserer Datensatzgröße limitiert. Zudem leidet der BaLROG-Datensatz, trotz unseres Versuchs repräsentativ zu sein, an einer leichten Tendenz zu früheren Galaxien. Daher wäre eine offensichtliche Verbesserung in Zukunft eine Vergrößerung des Datensatzes, insbesondere eine Extension zu späteren Galaxien - allerdings immer mit der nötigen räumlichen und spektralen Auflösung (oder besser). Leider kann die Mehrheit unserer Analysen nicht mit den Daten aktueller Integralfeld-Surveys durchgeführt werden, speziell aufgrund der limitierten räumlichen Auflösung. In Zukunft werden uns Instrumente wie MUSE dabei helfen, dieses Problem zu lösen, einerseits über schon garantierte Beobachtungszeit (Guaranteed Time Observations (GTO)) von unterschiedlichen Forschungsgruppen weltweit, als auch durch individuelle Beobachtungsproposals innerhalb unserer Kollaborationen.

Einige der hier entwickelten Hypothesen benötigen jedoch keine komplette IFU-Beobachtung, sondern können mit Schlitzbeobachtungen (long-slit) entlang unterschiedlicher Achsen der Galaxie durchgeführt werden. Wir haben jetzt schon Spektren von zwei Balkengalaxien entlang der Haupt-und Nebenachse der Balken mit dem Inamori Magellan Areal Camera and Spectrograph (IMACS) am Magellan Telescope im Las Campanas Observatory im blauen und roten Wellenlängenbereich aufgenommen. Mit diesen und weiteren Beobachtungen möchten wir unsere Resultate testen und weitere Fragen beantworten, unter anderem Folgendes:

- Die **größere Reichweite** von Schlitzbeobachtungen erlaubt uns besser die Regionen der Scheibe zu untersuchen, sowie ihre Beziehung zu Balken und Bulge. Beide Studien, BaLROG und WiFeS fokussieren sich eher auf die inneren Regionen und reichen nur bis zum Beginn der Scheibe.

- In unserer Arbeit haben wir zudem das **ionisierte Gas** nur sehr oberflächlich analysiert. In Zukunft könnte es von Interesse sein, dies mehr zu beachten und ggf. mit Analysen von **molekularem Gas** (z.B., HI, auch seine Kinematik) zu vergleichen. Diese Analysen können helfen besser, **Flussbewegungen entlang des Balkens und den Einfluss, sowie die Einflusszone des Balkens auf die interstellare Komponente zu ermitteln**.

- Die Kombination von Beobachtungen mit **Simulationen** kann unser Verständnis erheblich verbessern. Damit modernste Codes wie **NMAGIC** (de Lorenzi et al., 2007; Morganti et al., 2013; Martinez-Valpuesta & Gerhard, 2015; Portail et al., 2015) vernünftig funktionieren ist jedoch gute Datenqualität in einer weiträumigen Region der Galaxie notwendig.

Die Entstehung und Evolution von Bulgen betreffend, haben wir folgende Vorschläge:

- Das aktuelle Bulgeentstehungsmodell basierend auf **Mergers von Klumpen bei hoher Rotverschiebung** als Alternative zur hierarchischen Gruppierung testen (Beobachtungen bei hoher Rotverschiebung).

- **Beobachtungen mit noch besserer räumliche Auflösung nutzen, um die ganz zentralen Regionen von Bulges zu untersuchen**. Der Vergleich von Datensätzen mit und ohne nuklearer Aktivität und mit und ohne Balken, kann helfen deren Einfluss auf diese ganz zentralen Regionen festzulegen. Bisher haben wir den Einfluss des Balkens bei $\sim$0.13 Balkenlängen gesehen, wissen aber nicht sicher, ob er hier endet. Aktuelle Studien haben noch keinen Einfluss von Balken auf AGN Aktivität gefunden, aber gegebenenfalls sind Beobachtungen mit höherer Auflösung notwendig.

Natürlich sind auch Studien möglich, die weder gute spektrale noch gute räumliche Auflösung verlangen. Gerade wenn Statistiken erhöht werden oder Beobachtungen bei höheren Rotverschiebungen durchgeführt werden sollen, ist dies jedoch meist nur schwer möglich. Beides sind relevante Aspekte, und gerade um den Einfluss von äußeren Bedingungen wie dem Umfeld auf Balkeneigenschaften zu testen, sind statistische Studien gut. Eine statistische Studie bei hoher Rotverschiebung kann außerdem helfen, lokale Beobachtungen und Vorhersagen zu überprüfen.

Leider hat ein Tag nur 24 Stunden auf diesem Planeten und ein Jahr nur 365 Tage. Das Universum birgt noch unzählige Geheimnisse und wahrscheinlich viele Überraschungen, die uns dazu bringen werden, unser jetziges Verständnis der Welt und unseren Platz in ihr abermals zu hinterfragen und zu revidieren. Ganz persönlich hoffe ich, dass meine Arbeit für diese Dissertation zu unserem Verständnis der Bedeutung von Balkenstrukturen in Galaxien und der Entstehung von Bulgen beigetragen hat sowie dass ich weiterhin meine Forschung in diesem und in verwandten Feldern sowie zu neuen Themen in der Zukunft widmen kann - - und natürlich, dass ***Ihnen*** *das Lesen der Arbeit Freude bereitet hat.*

A

Complete kinematic maps for stars and ionised gas for the BaLROG sample

We show maps of the stellar and ionised-gas kinematics for the entire BaLROG sample of galaxies in figures A.1 to A.16. In each figure we show different maps of each galaxy, top to bottom and left to right: first row: (i) S^4G image of the galaxy with an estimate of the final SAURON mosaic and the number of pointings indicated in the left lower corner, (ii) fundamental parameters of the galaxy along with the systemic velocity, inclination, stellar angular momentum within one effective radius and the bar strengths measured; second row: (i) surface brightness derived from the SAURON cube (collapsed in wavelength, shown in logarithmic scale), (ii) stellar mean velocity V (in km s^{-1}), (iii) stellar velocity dispersion σ (in km s^{-1}); third row: (i) flux of the ionised gas, based on [OIII] (shown as square-root-scaled), (ii) mean radial ionised gas velocity, (iii) ionised gas velocity dispersion (in km s^{-1}); fourth row: (i) Gauss-Hermite moments h3 and (ii) h4; fifth row: (i) major and minor axis rotation curves of the stellar velocity, (ii) radial profile (inclination corrected) of the stellar velocity dispersion of the major and minor axis of the bar, (iii) isphotal profile of the stellar velocity dispersion along bar major and minor axis. The cut levels are indicated in a box on the right-hand side of each map.

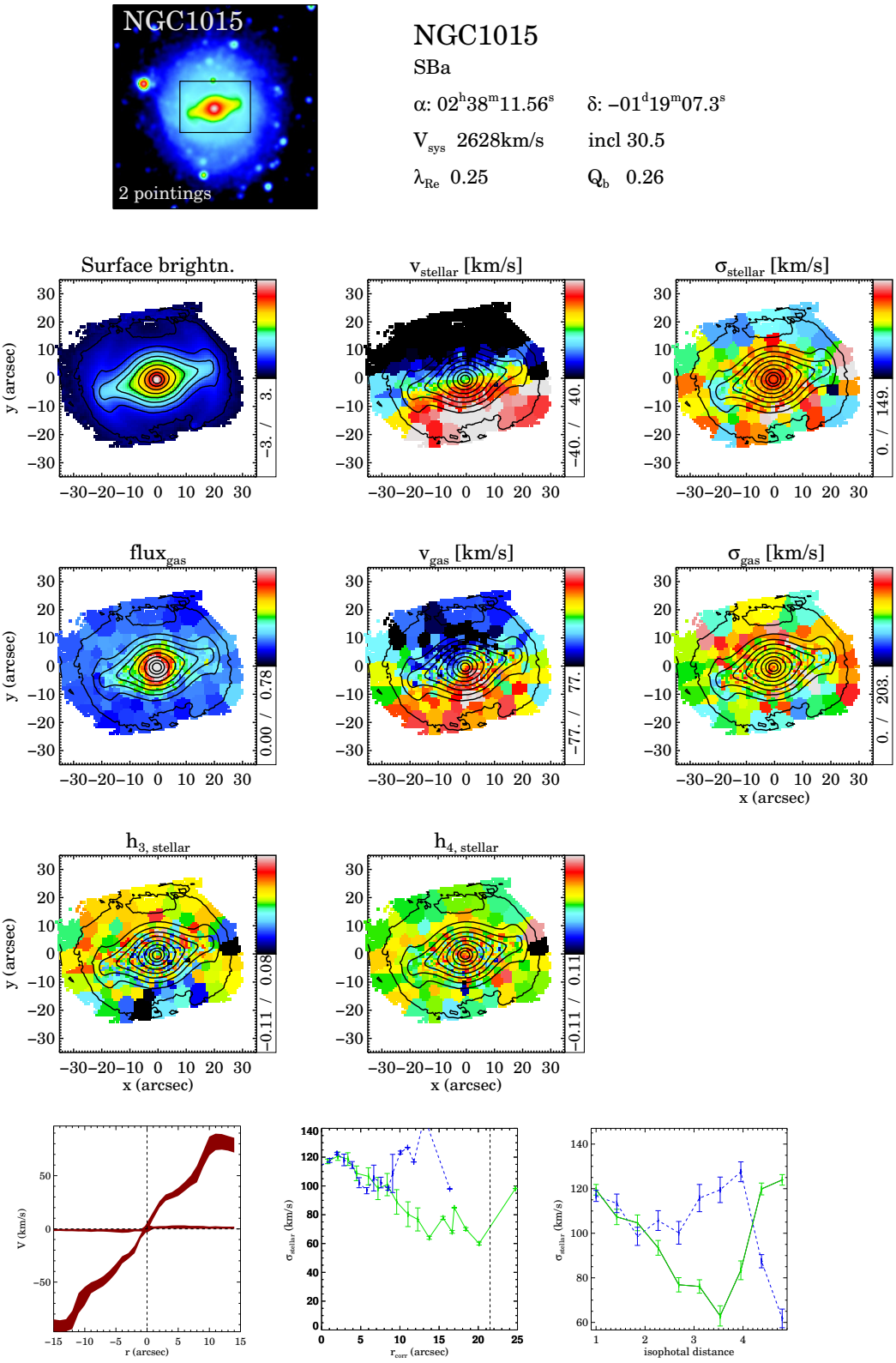

FIGURE A.1: Summary of the kinematic maps for stars and ionised gas for each galaxy.

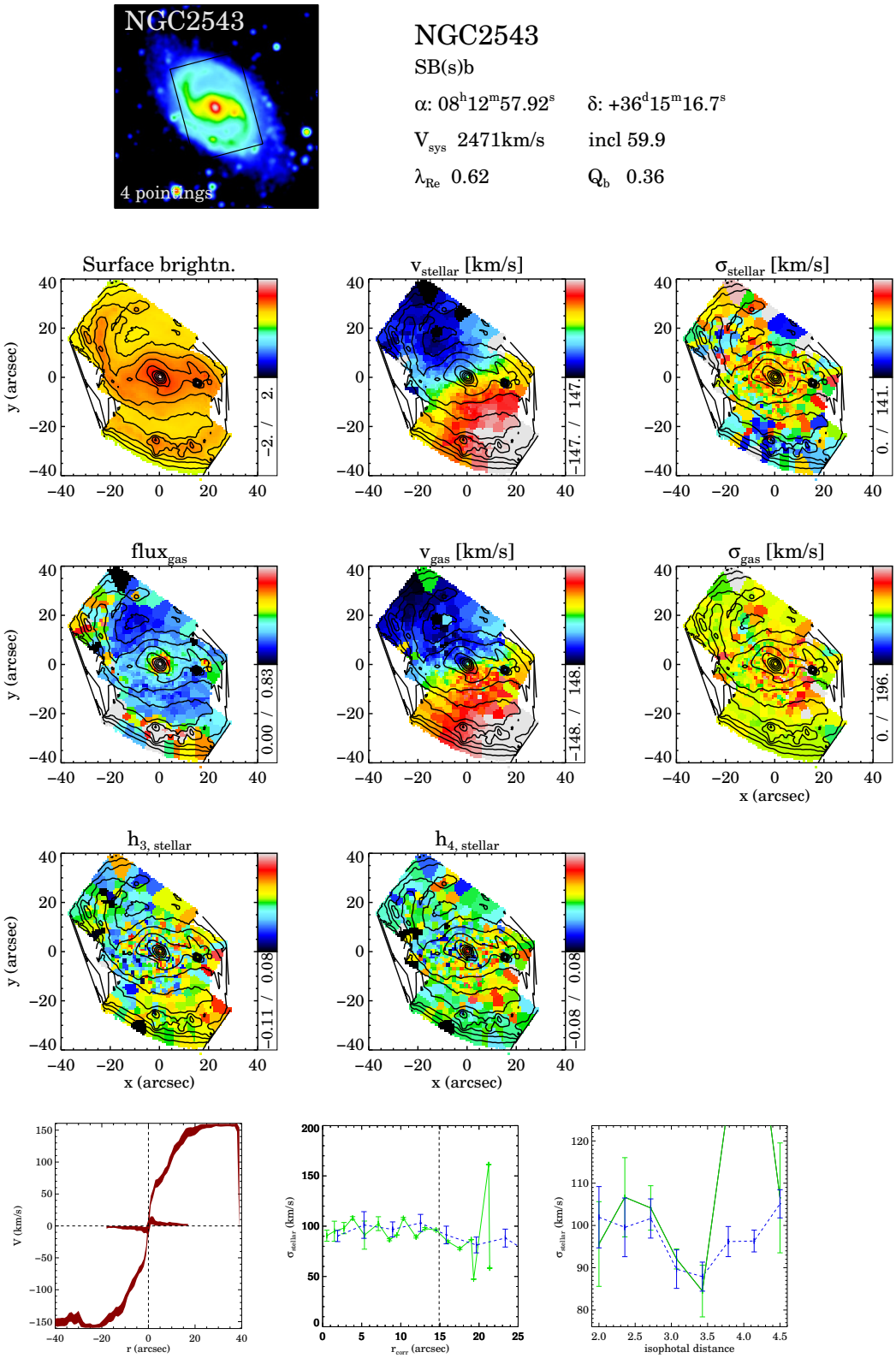

FIGURE A.2: Figure A.1 continued.

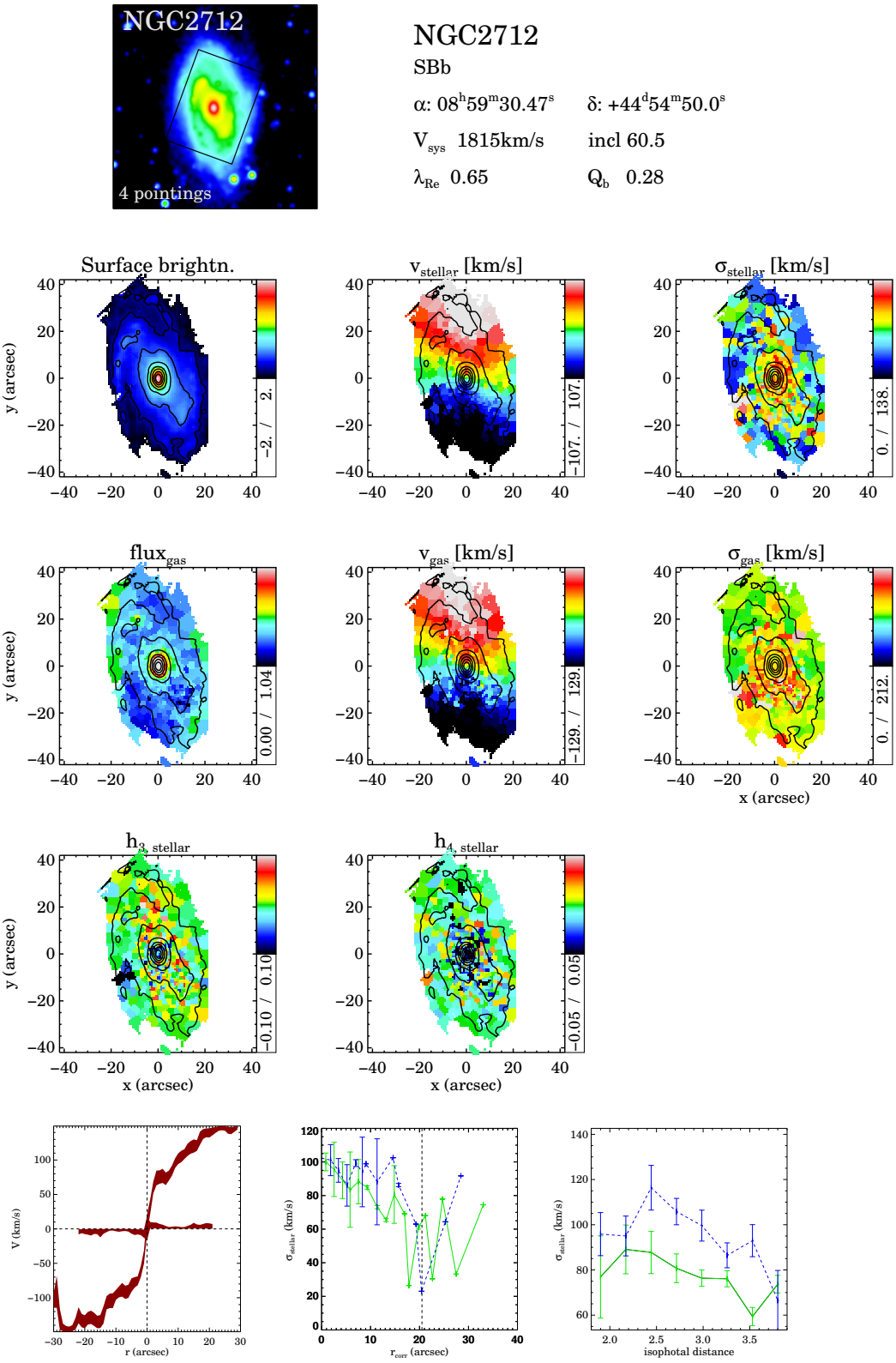

FIGURE A.3: Figure A.1 continued.

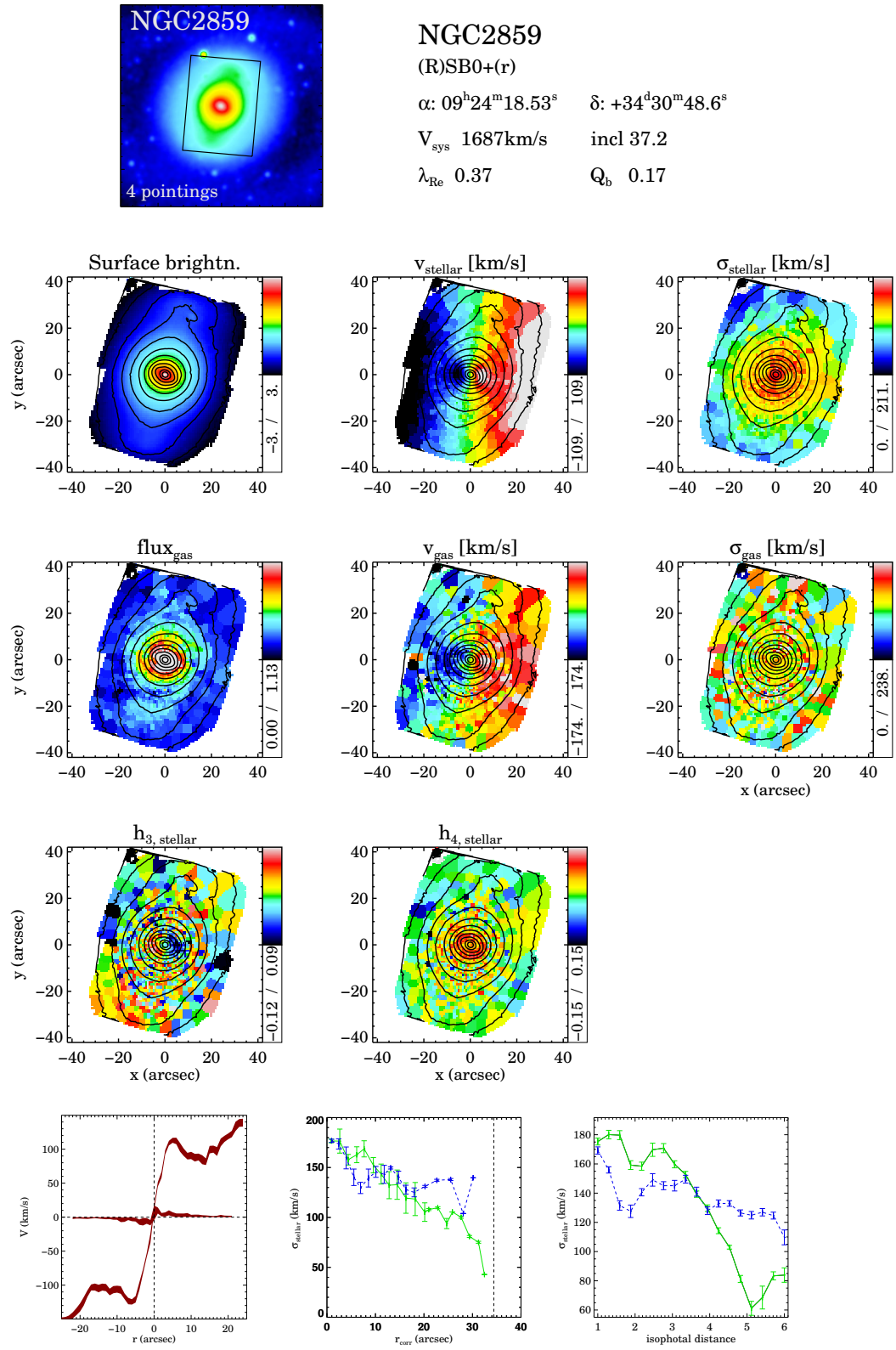

FIGURE A.4: FigureA.1 continued.

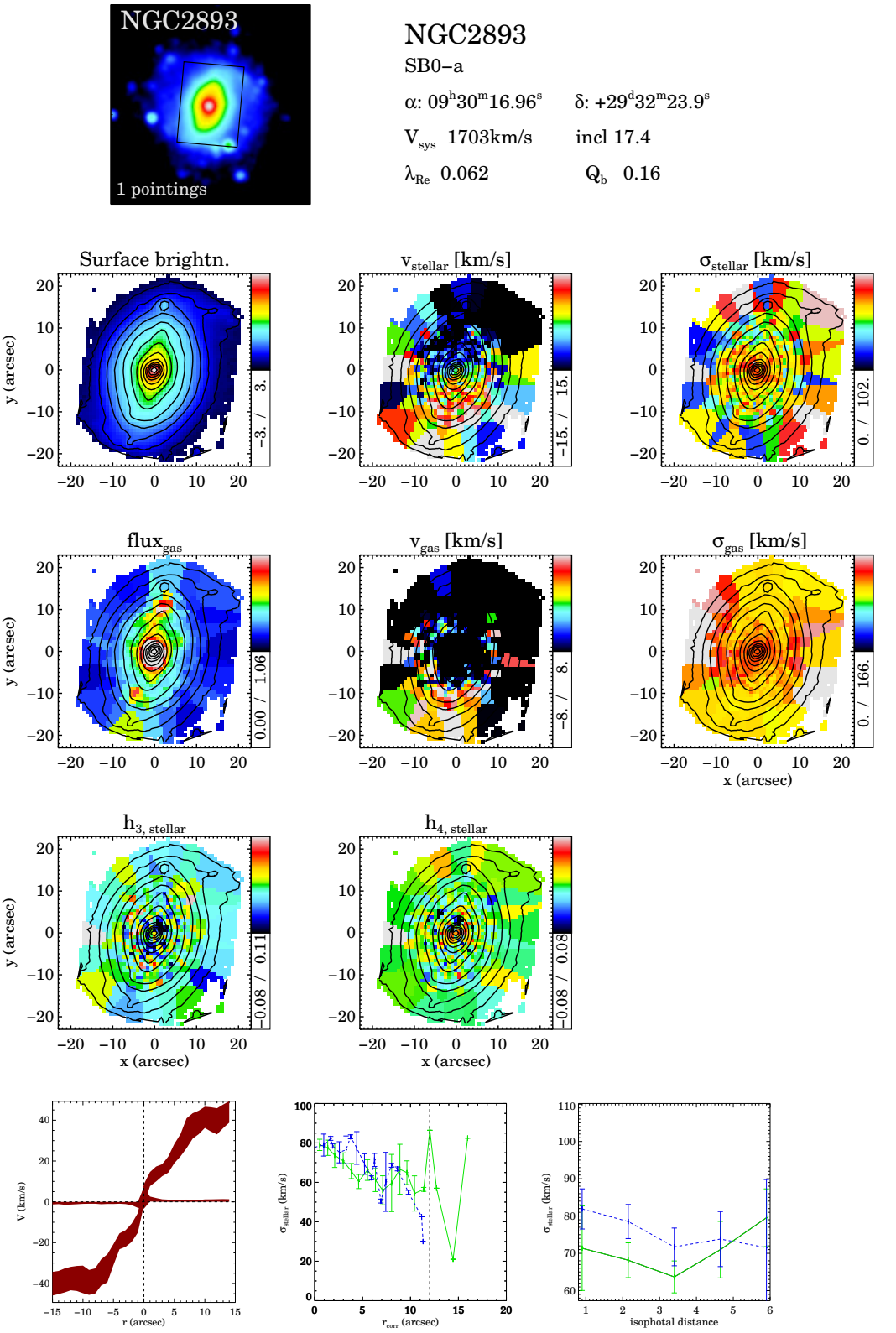

FIGURE A.5: FigureA.1 continued.

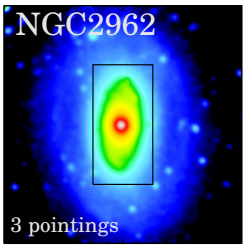

NGC2962

SB0–a

α: $09^h40^m53.93^s$ δ: $+05^d09^m56.9^s$

V_{sys} 1960km/s incl 49.0

λ_{Re} 0.44 Q_b 0.14

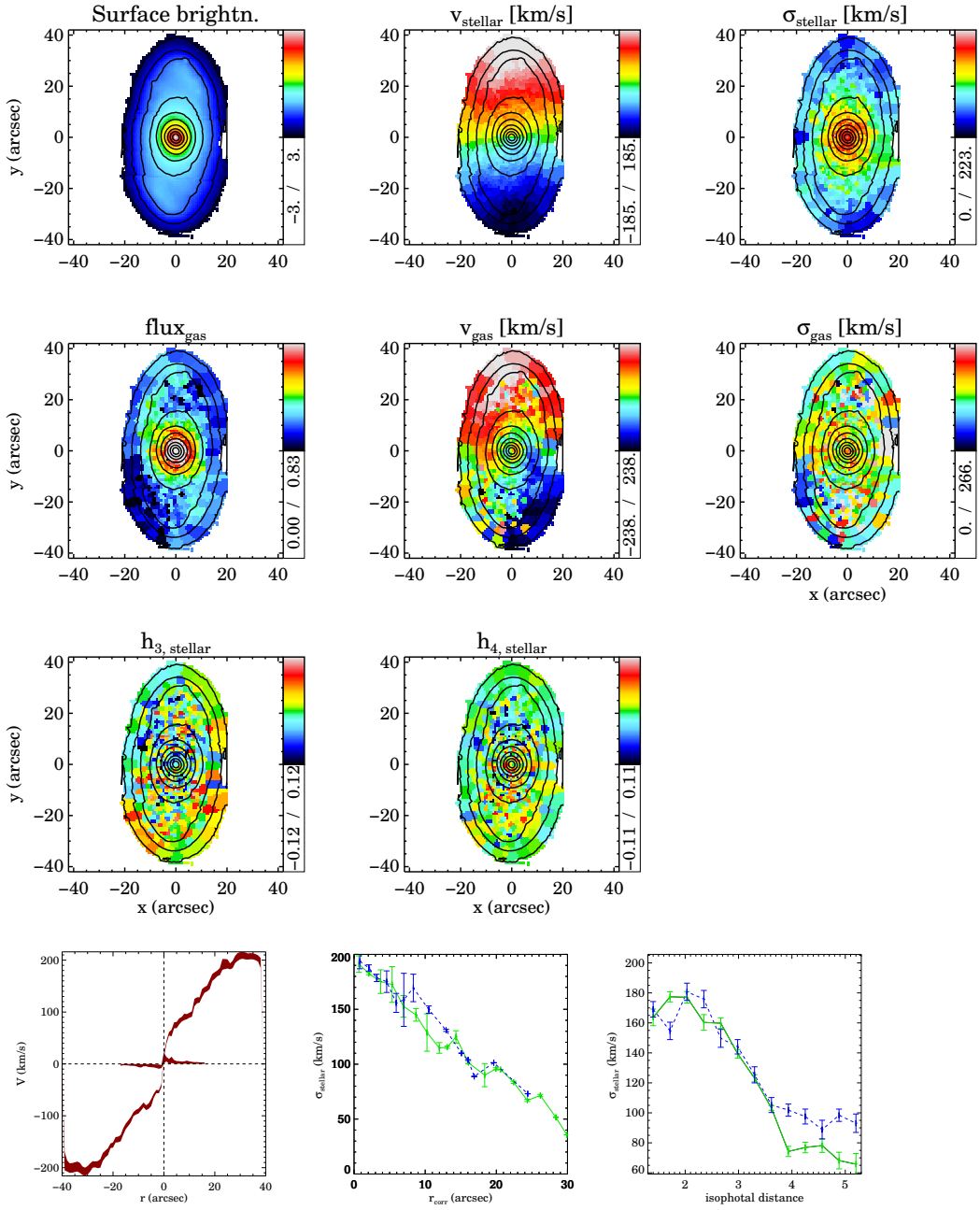

FIGURE A.6: FigureA.1 continued.

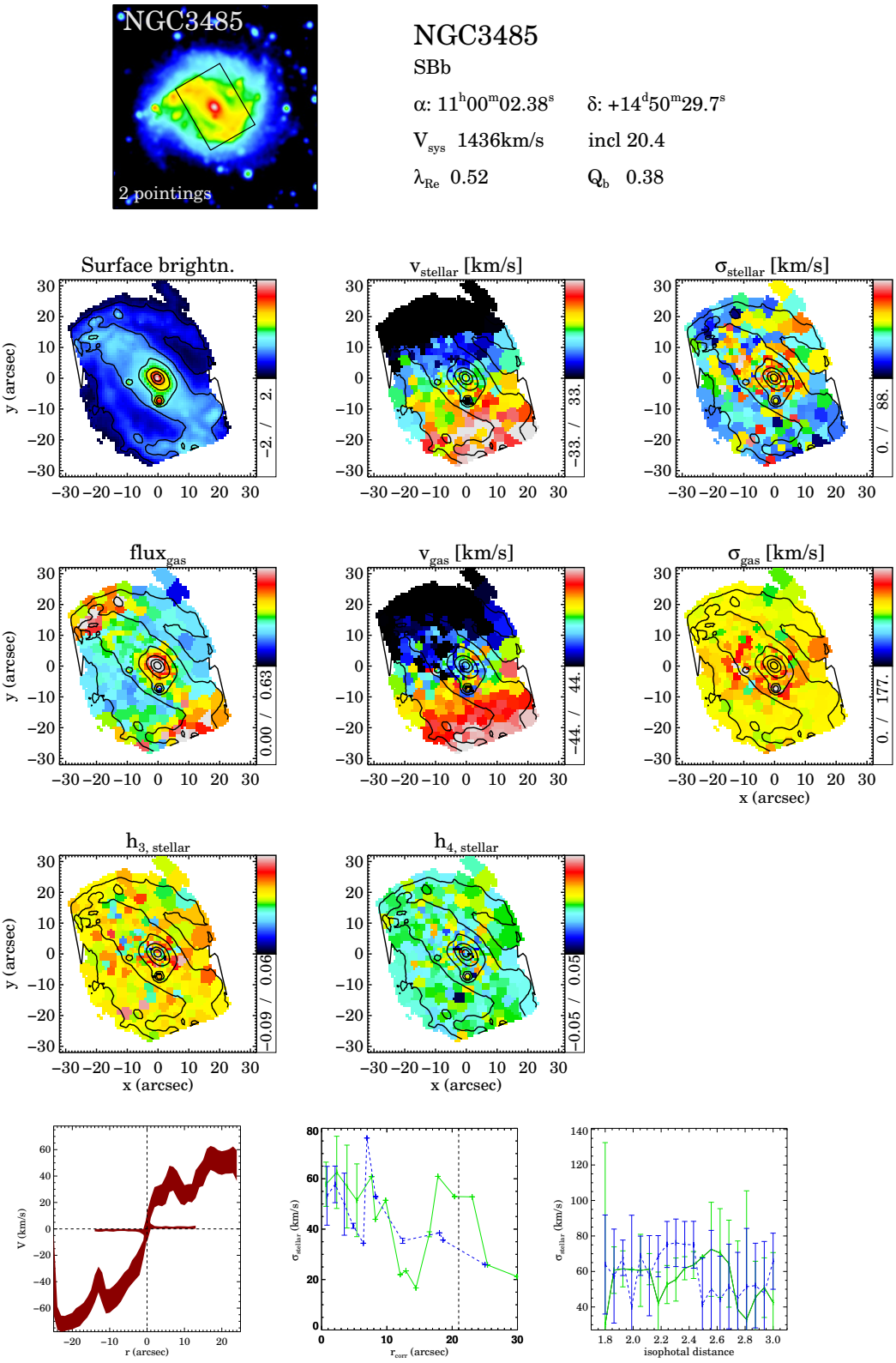

FIGURE A.7: FigureA.1 continued.

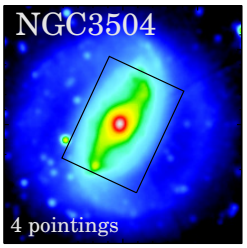

NGC3504

SBab

α: $11^h03^m11.21^s$ δ: $+27^d58^m21.0^s$

V_{sys} 1539km/s incl 12.8

λ_{Re} 0.29 Q_b 0.26

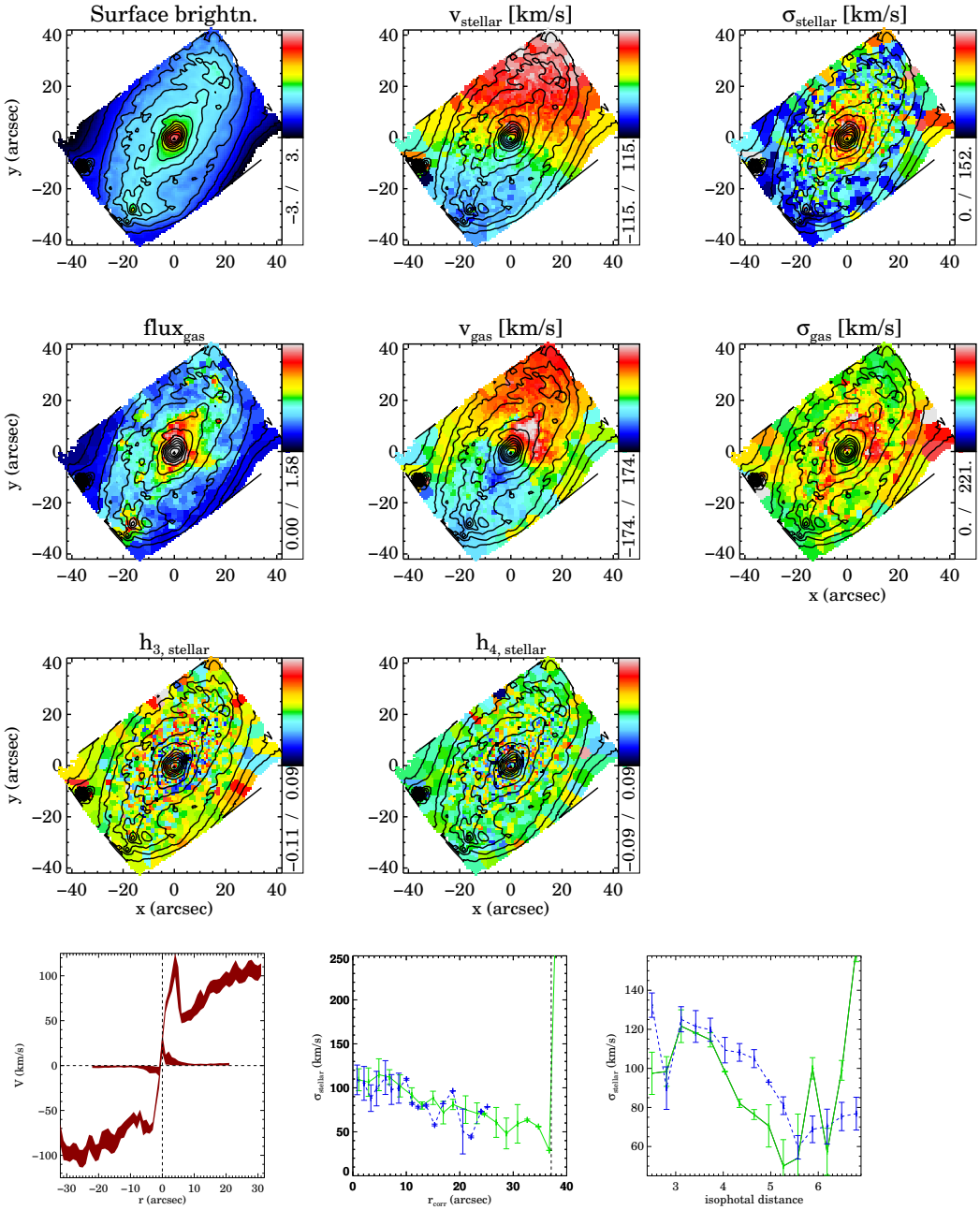

FIGURE A.8: FigureA.1 continued.

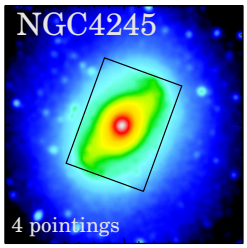

NGC4245

SB0/a(r)

α: $12^h17^m36.77^s$ δ: $+29^d36^m28.8^s$

V_{sys} 886km/s incl 33.3

λ_{Re} 0.33 Q_b 0.18

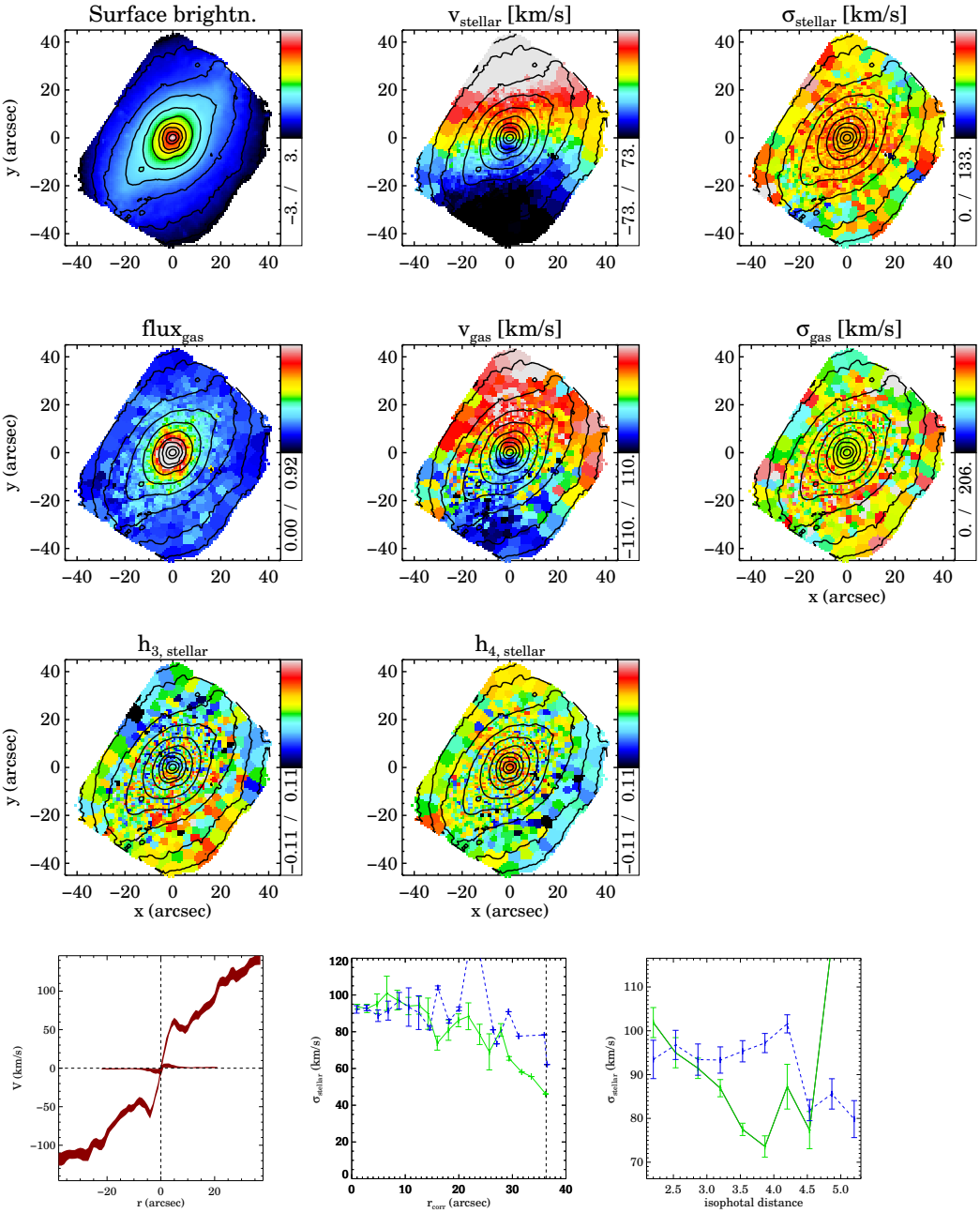

FIGURE A.9: FigureA.1 continued.

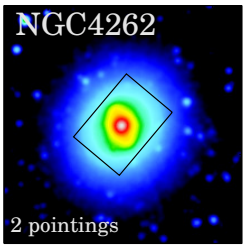

NGC4262

SB0–

α: $12^h19^m30.57^s$ δ: $+14^d52^m39.6^s$

V_{sys} 1359km/s incl 24.5

λ_{Re} 0.33 Q_b 0.069

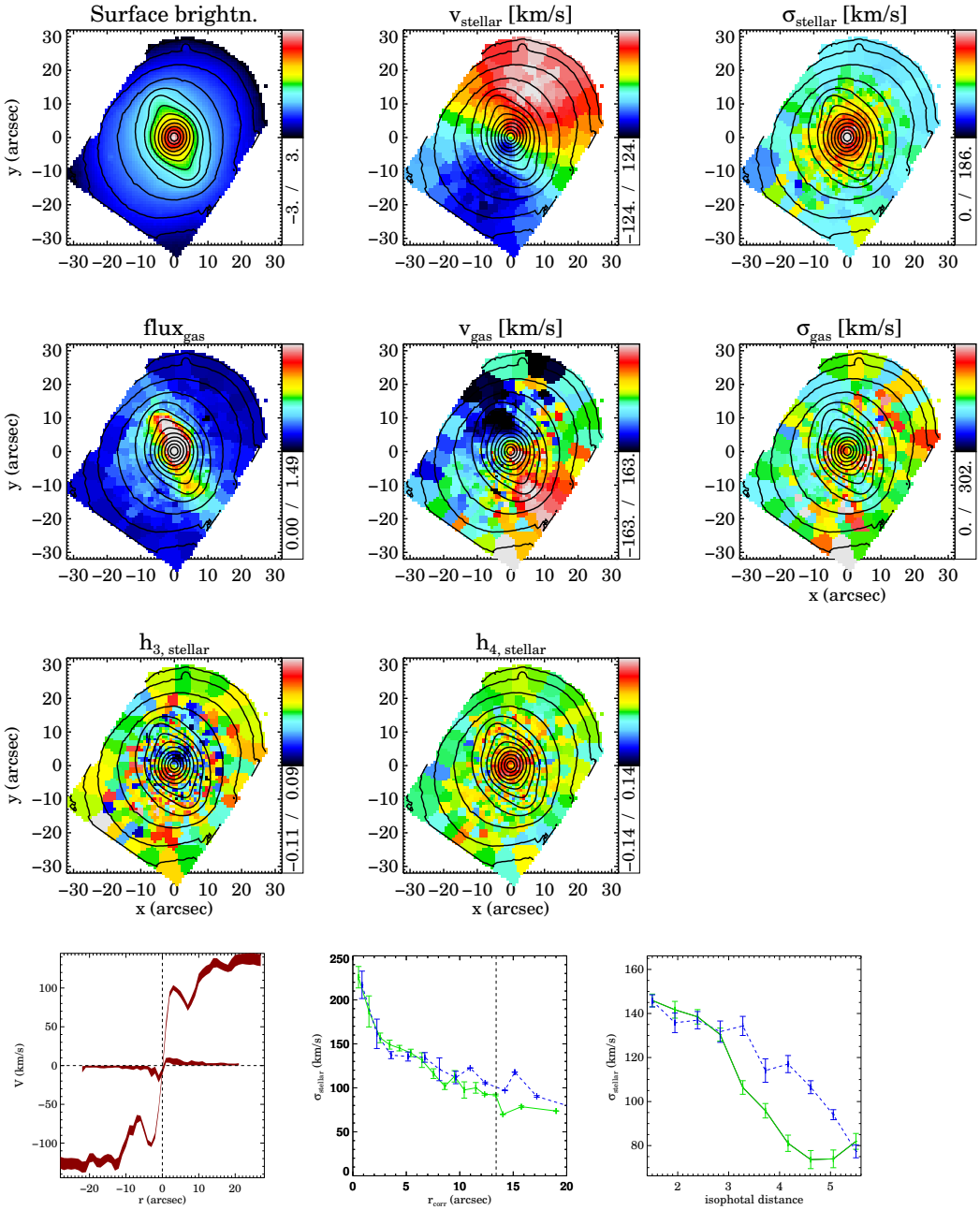

FIGURE A.10: FigureA.1 continued.

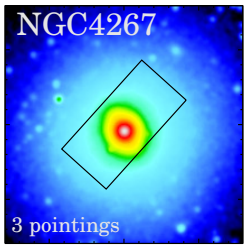

NGC4267

SB0–

α: $12^h19^m45.24^s$ δ: $+12^d47^m53.8^s$

V_{sys} 983km/s incl 11.9

λ_{Re} 0.24 Q_b 0.038

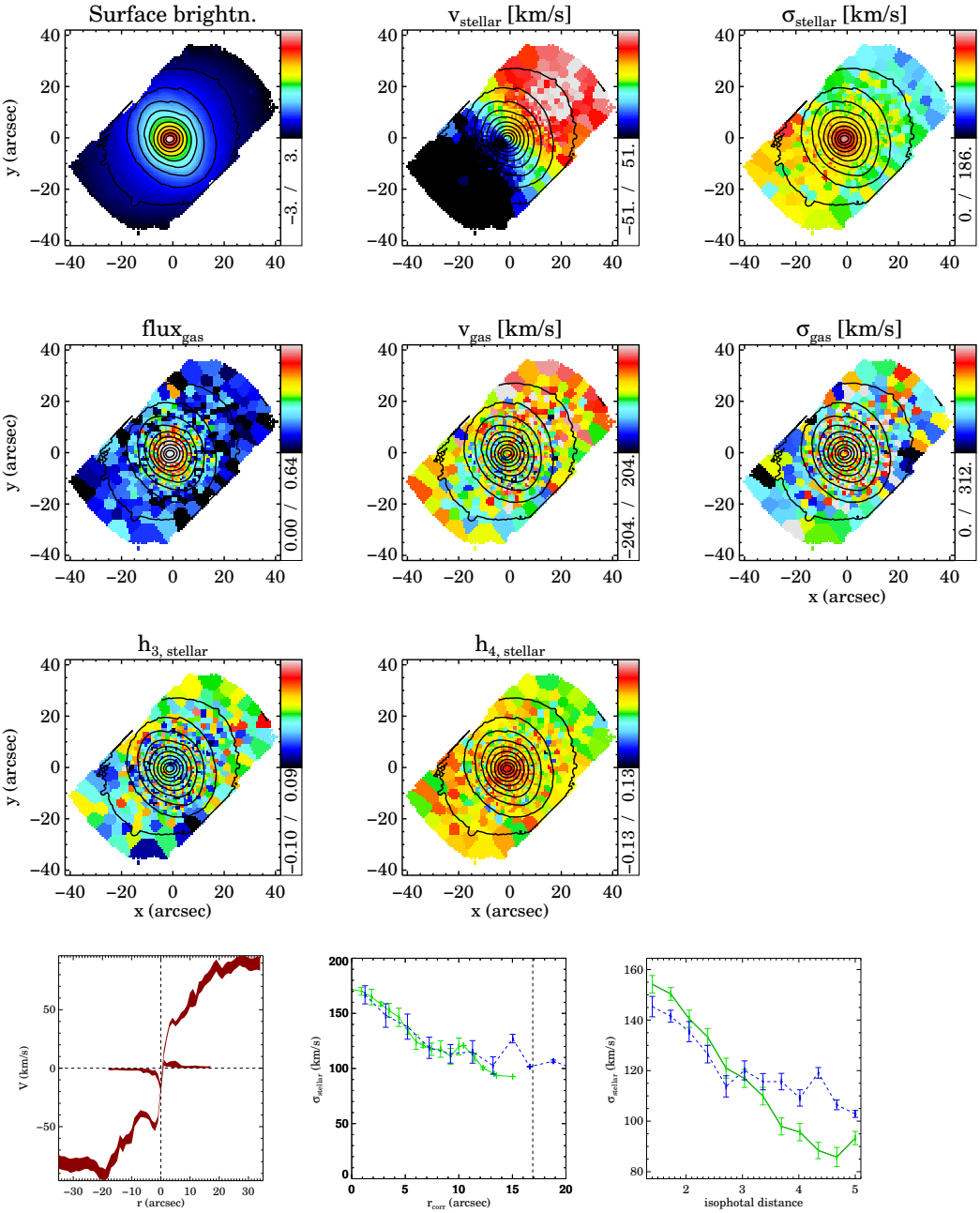

FIGURE A.11: FigureA.1 continued.

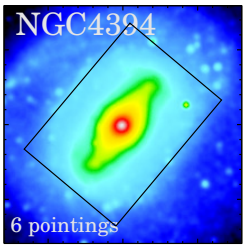

NGC4394

(R)SB(r)b

α: $12^h25^m55.53^s$ δ: $+18^d12^m50.6^s$

V_{sys} 922km/s incl 30.4

λ_{Re} 0.46 Q_b 0.234

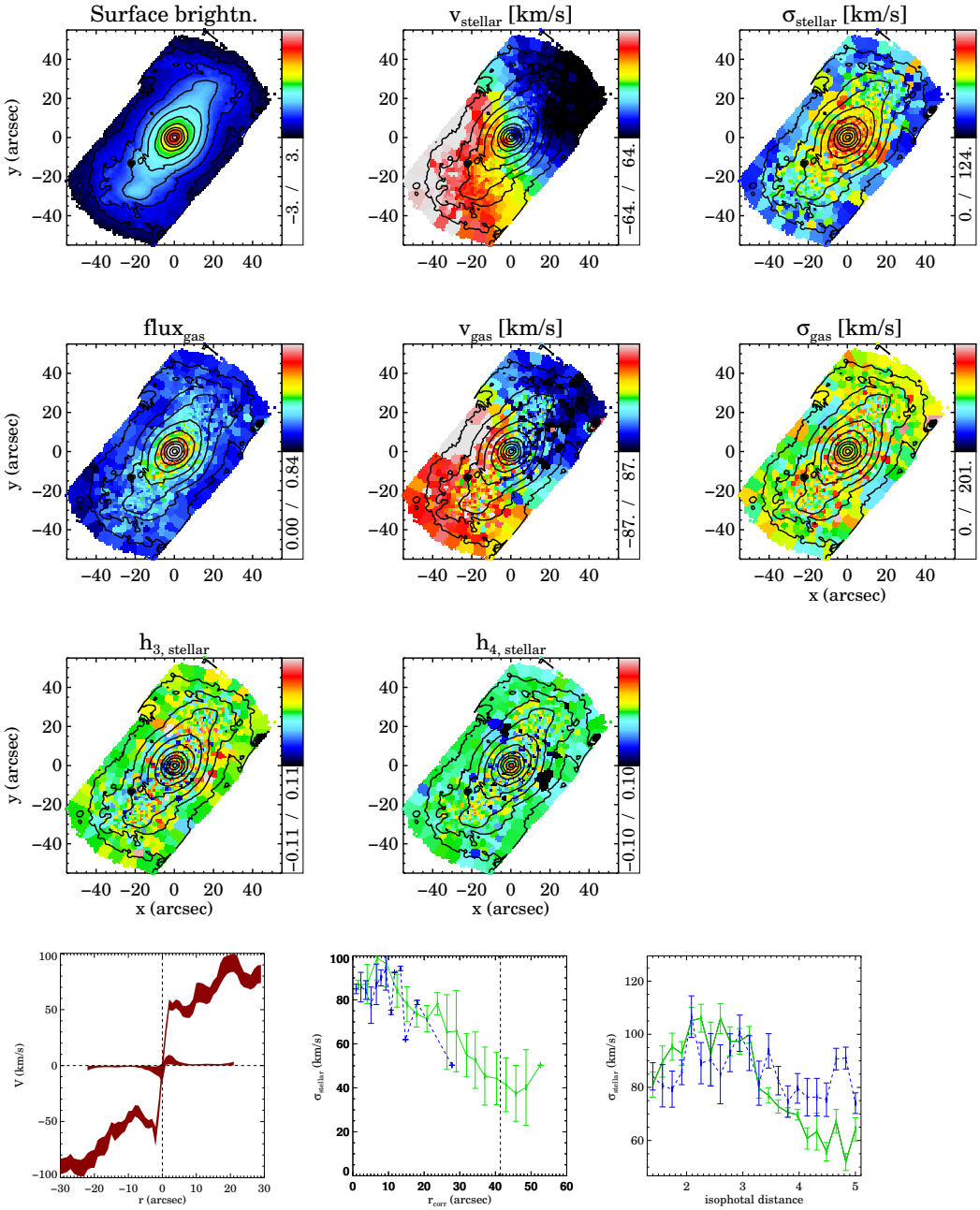

FIGURE A.12: FigureA.1 continued.

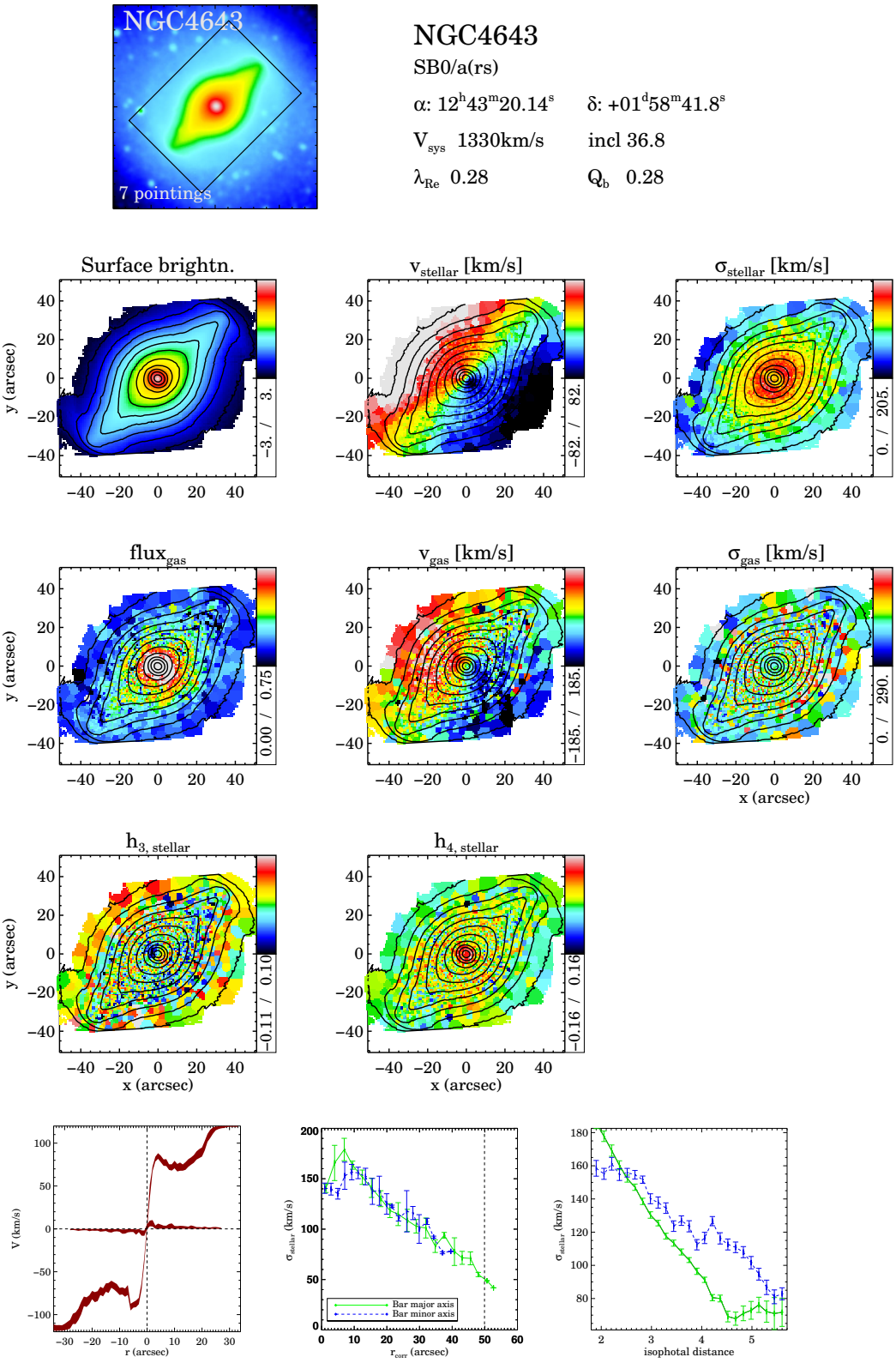

FIGURE A.13: FigureA.1 continued.

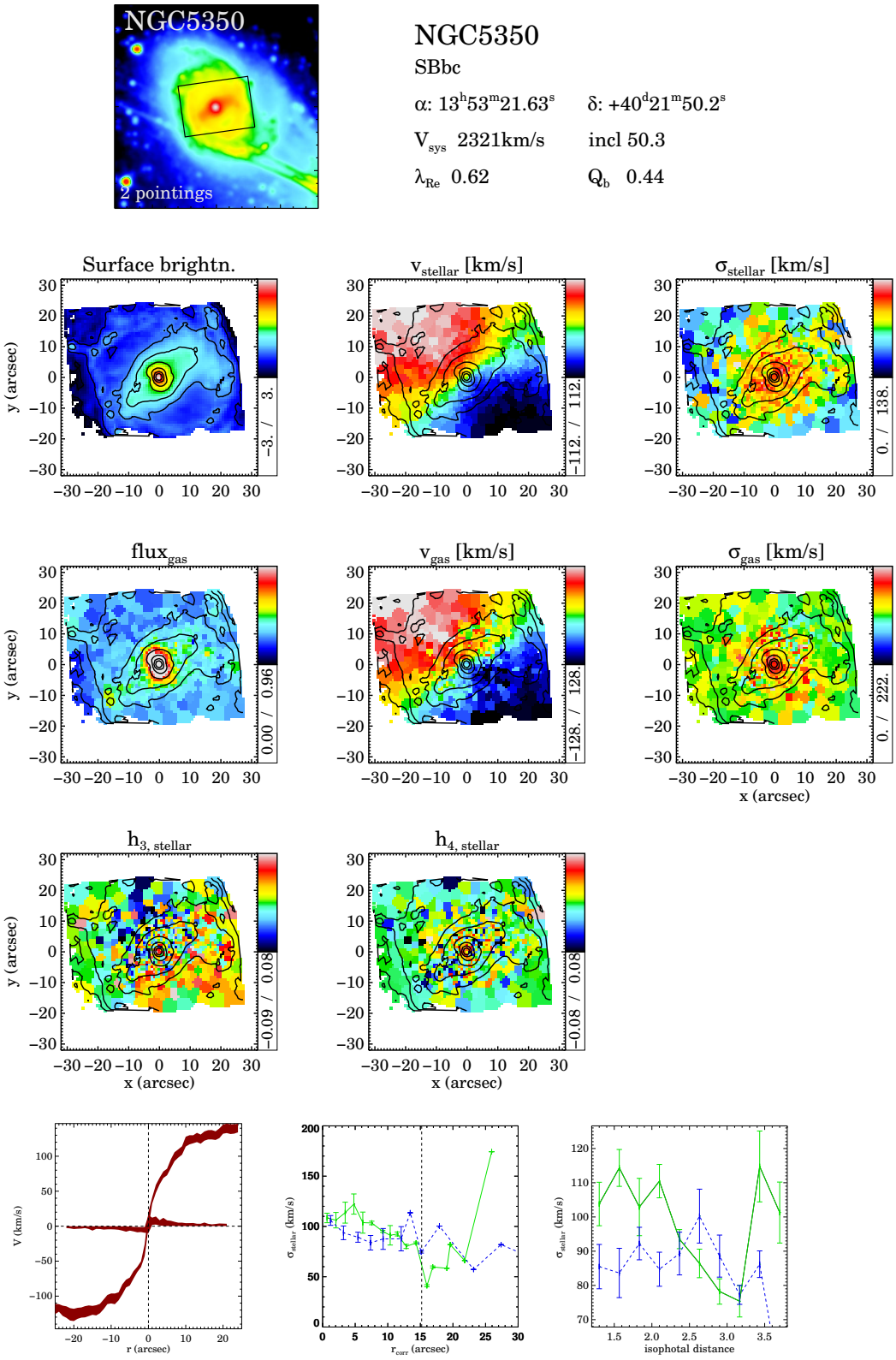

FIGURE A.14: FigureA.1 continued.

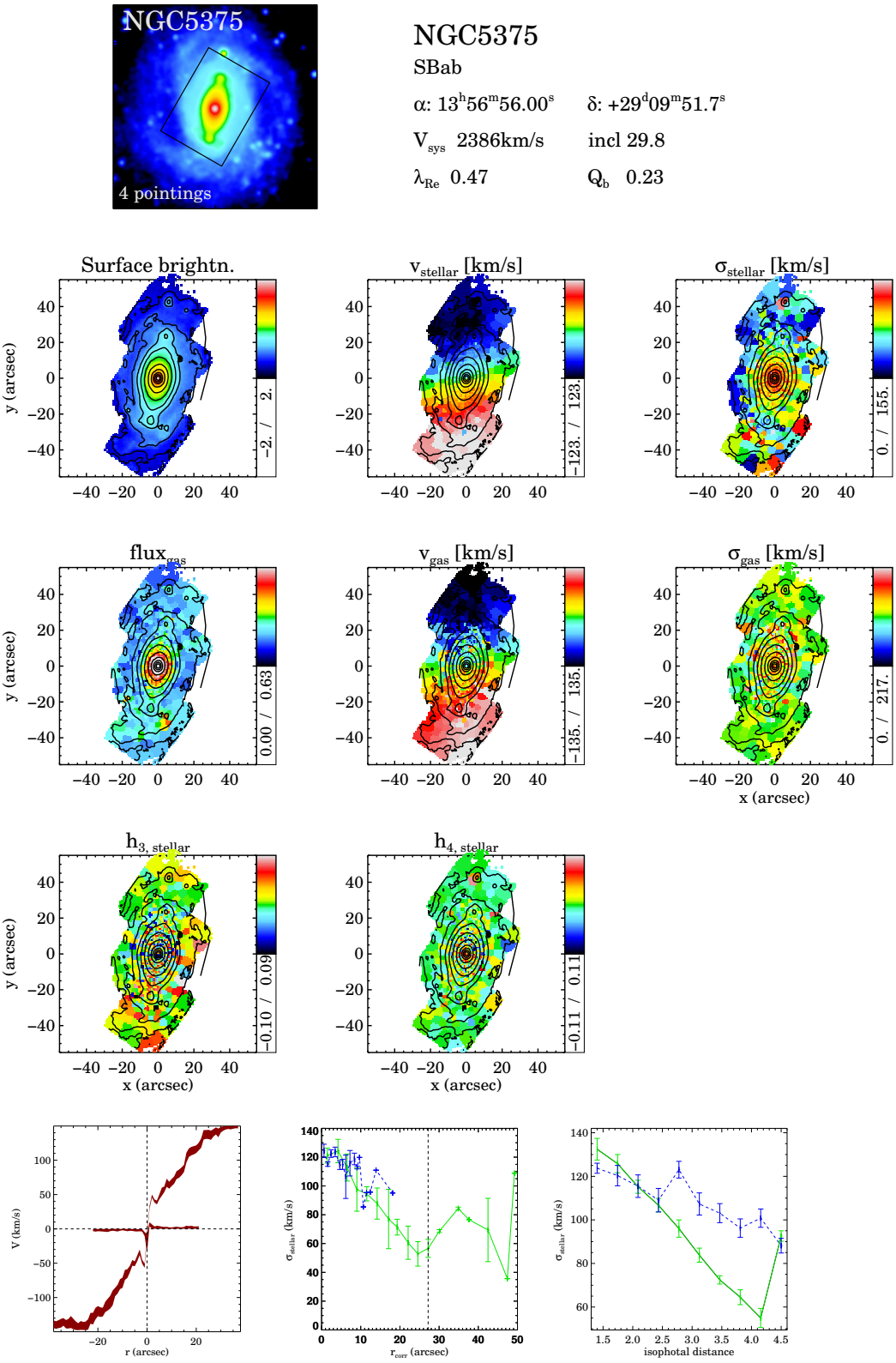

FIGURE A.15: FigureA.1 continued.

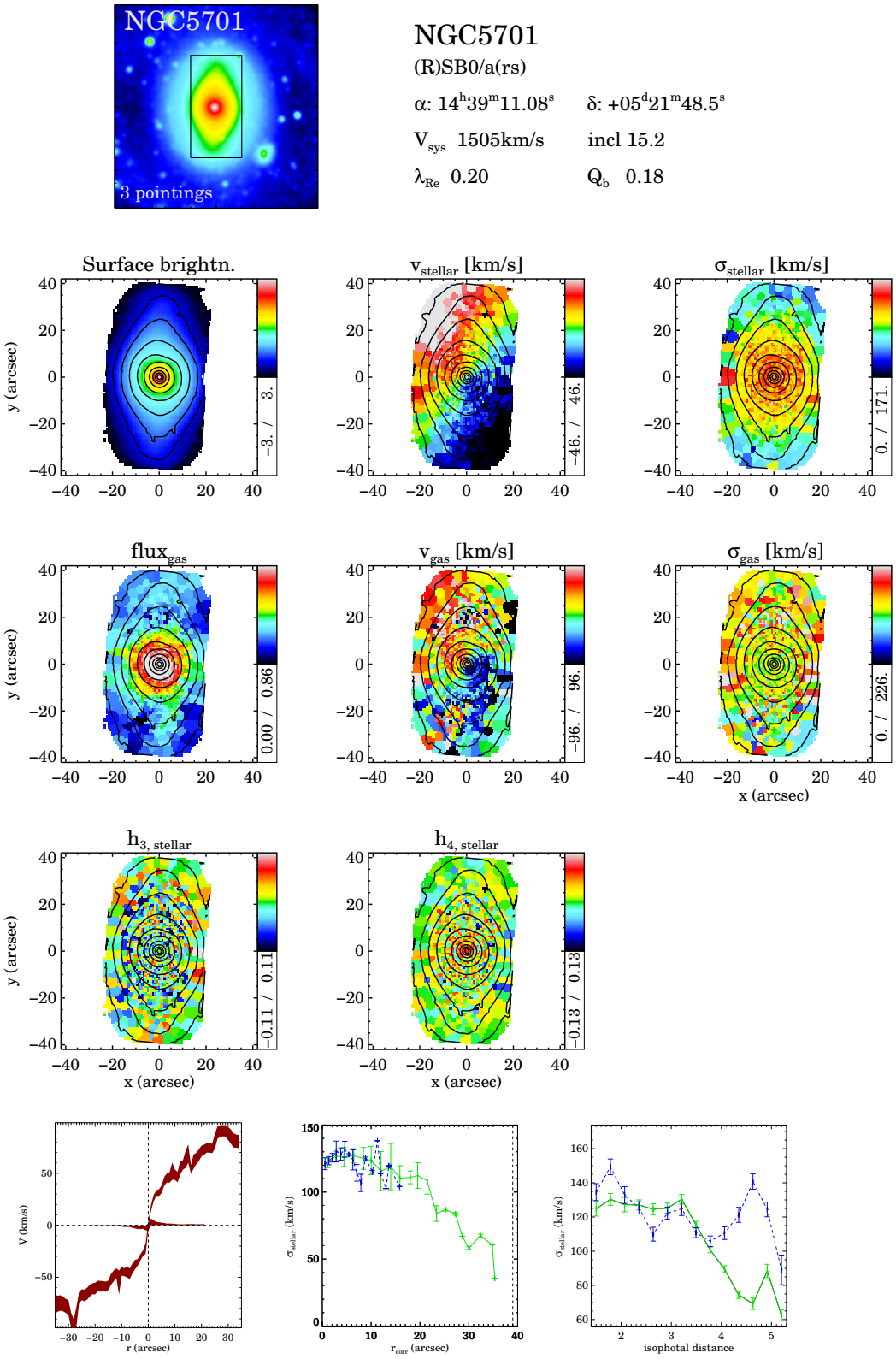

FIGURE A.16: FigureA.1 continued.

B

Simulations used in comparison with the BaLROG sample

B.1 Description of the simulations

In the following we illustrate the give a more detailed description of the simulations and how we used to obtain the torque measures. Figure B.1 shows as an example the intensity and velocity maps of one of the snapshots of the I_3 simulation at an intermediate time step, at an inclination of 30 degree and a bar-to-line-of-nodes-PA of 55 degree. Figure B.2 shows the corresponding obtained radial and tangential velocities. In Fig. B.3, the full time series (all 1800 snapshots) of this particular simulation is shown. The early very strong peak is associated with the first buckling of this bar (not stable in time). The shape of the obtained curve indicating the kinematical torque values resembles the curve of the A2 value measured during the simulation and also gives an indication on the bar strength. For the other simulations series, these measurements along with the shape of the final curve differs significantly.

The variations of Q_{kin} with inclination and PA (shown with different colors and symbols respectively in Fig. B.3 are due to the fact that the assumptions of a thin disc and stable bar are not 100% correct. This is the case especially during the buckling event of the bar and during the later stages of the evolution, which is to be expected due to the thickening of the bar. If it was a perfect measurement, all points should overlap vertically, since we simply rotate the simulated galaxy slightly in order to achieve its different orientation. Since the buckling event is a short moment during bar evolution, we can safely exclude these points from our comparison as the likelihood to find a bar in the buckling phase is rather low. Without these points and below t=200, the measurements agree rather well. A more extensive test can also be found in the Appendix B.2.

To perform the analysis for the comparison of the two torque measurements, we calculated the values of Q_b (in addition to those of Q_{kin}) for all sets of simulations in the same way as done for the observations. In Fig. 4.11 we presented the final results showing the observational measurements overlaid on the four simulations, I_1, I_2, I_3 and I_4 (level of disc-to-total ratios: 0.92, 0.62, 0.43, 0.29 respectively).

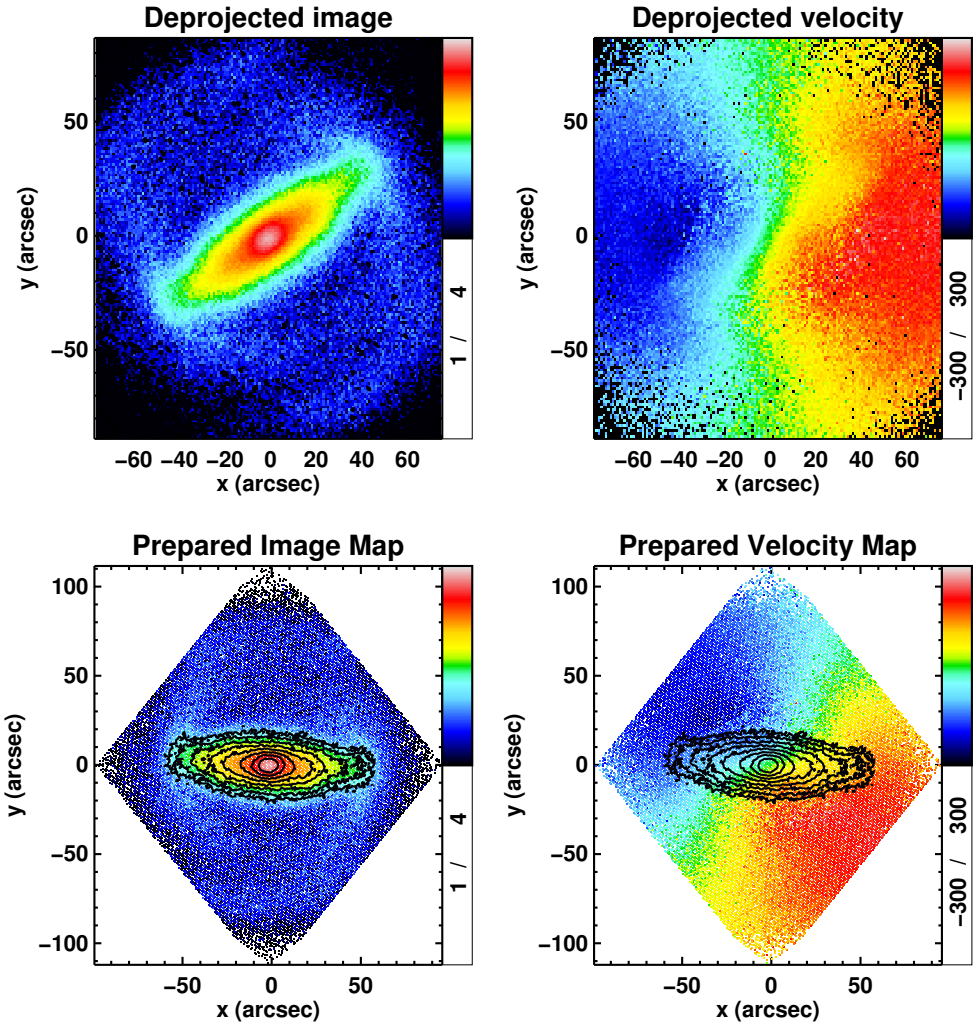

FIGURE B.1: Intensity (in logarithmic units) and velocity maps (translated in km/s) of one of the snapshots of the I_3 simulation at an intermediate point of the bar evolution t=150 at PA = 35 and inclination = 30. The bottom panels show the prepared maps which can be symmetrised by the code, with the bar in a horizontal position and adjusted field extensions. In those, we overlay the isophotes.

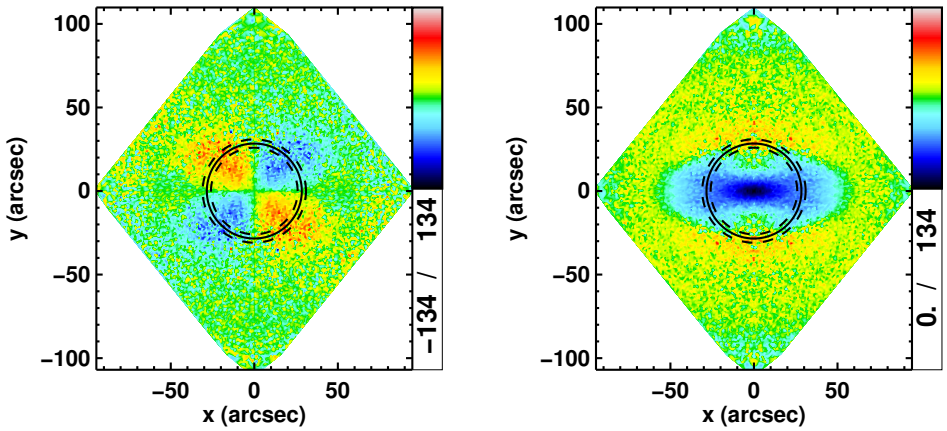

FIGURE B.2: The obtained radial and tangential velocities for the simulated galaxy above, but now symmetrised.

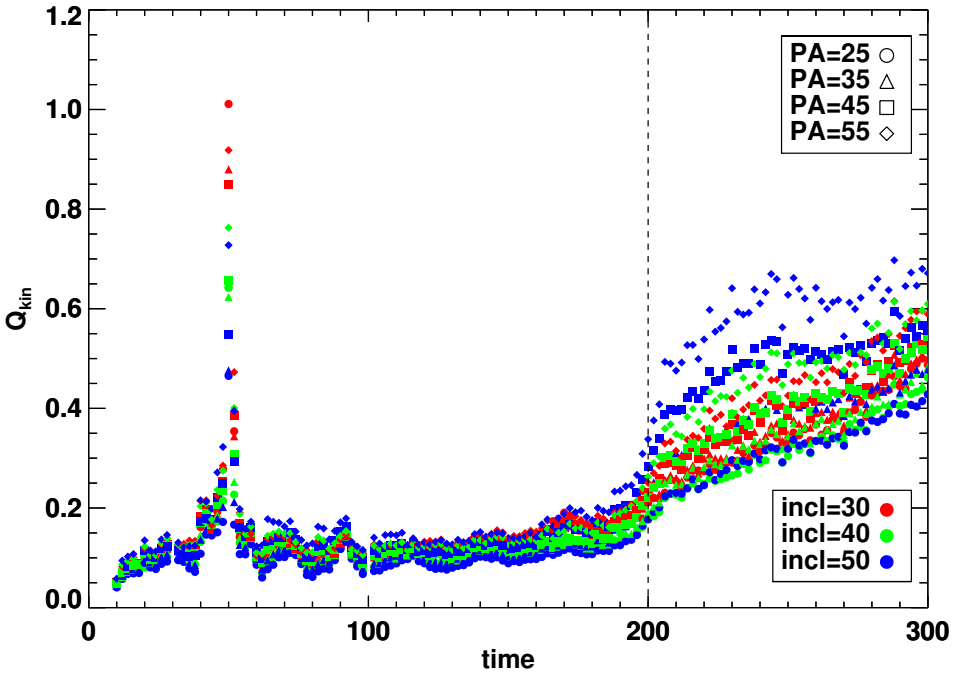

FIGURE B.3: The kinematical torque evolution for one complete simulation series, here I_3 as an example, indicating different inclinations and PAs. The dotted line indicates the point in time where the bar has reached its full strength and further evolution is not reliable, hence points to the right of it will not be considered in our analyses.

As seen in Fig. 4.11, none of the simulation series coincides perfectly with all the data points, but instead form a continuum. It is reassuring however that the simulation series fall onto the same relation found as for the observations.

Simulation I_1 (92% disk, shown by the green points) best represents the

lower bar strengths. With decreasing disc content, the both the photometric and kinematic bar strengths increase. We also distinguish a particular behavior for I_4: compared to the other sets, this series seems to adapt to all ranges starting from very weak to very strong bars. This is the simulation with the lowest disc percentage within the bar region initially and also after halo relaxation and is at every point in time submaximal. Overall, we find a trend of stronger bar development with increasing dark matter halo fraction in our simulations.

Comparing the velocity maps of the three different simulations with the observations, we find good agreement, especially in the case of I_1. Simulations I_3 and I_4 in particular develop strong distortions in the stellar velocity fields which are not as pronounced in our observations. However, the bar strength of I_1 never reaches a higher value than about 0.2-0.3, unlike the observations. To reach higher values, we needed to increase the halo fraction.

B.2 Influence of the inclination and PA on the bar strength measurements

We used four simulation sets (I_1, I_2, I_3 and I_4) to test the influence of PA and inclination on the bar strength measurements, namely Q_b, Q_{kin} and A2, on a large enough sample. Figure B.4 illustrates those tests with the example of the I_2 simulation.

In the majority of cases the influence of these two parameters causes a consistent change in any of the different bar strength measurement methods. The PA influence always shows a clear trend: larger PAs result in higher strength values overall. Furthermore it causes less spread within the distinct inclinations, especially for Q_b and A2.

The effect of inclination is two-fold: in the simulations with higher disc-percentages (I_1 and I_2), its effect is reversed for low and high PAs. For low PAs, we detect that a lower inclination results in higher values in all three parameters, whereas for higher PAs, high inclinations result in higher values overall. The spread here is less.

For the other two simulations with higher DM content (I_3 and I_4), the effect of inclination is always the same despite the distinct PAs: a lower inclination results in higher values in the three measured parameters. Again, the spread is less at higher PAs (except for Q_{kin} in I_4).

The fact that the influences are similar in spite of the different measurement methods probably helps to produce the observed relation between them. It is important to bear the influence of these parameters in mind when checking the observations: low inclinations might lead to higher values, and, depending on the PA and DM fraction, high inclinations can also lead to lower values.

We also compared Q_b with the A2 values directly from the simulations and find that Q_b resembles A2 very well.

Overall, values of Q_b are expected to be higher at lower inclinations whereas values of Q_{kin} should be higher at higher inclinations as motions can be better measured with increased inclination. Our tests, however, suggest that in almost all cases, the chosen methods indicate a lower limit for the bar strength, in particular in the case of Q_b.

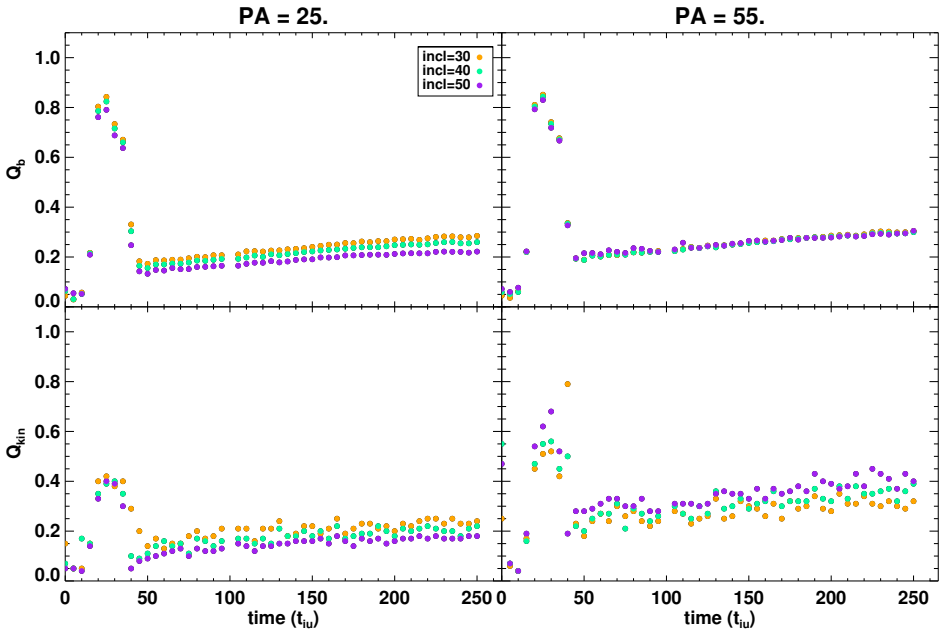

FIGURE B.4: For a simulation with 60% disc we plot Q_b and Q_{kin} versus time for different inclinations and PAs: left: PA=25, right: PA=55. Top: Q_b and bottom: Q_{kin}. The elevation at early times is due to the buckling event in the bar evolution.

C

Complete stellar population maps, index-index diagrams and profiles for the BaLROG sample

C.1 Complete set of maps of line strength indices, SSP-grids and SSP parameters for the BaLROG sample

We show maps of the obtained line strength indices and derived SSP parameters for the entire BaLROG sample of galaxies in figures C.1 to C.16. In each figure we show different maps of each galaxy in landscape format, top to bottom and left to right: top left: (i) SDSS ugri-colour image of the galaxy , (ii) parameters of the galaxy along with the inclination, the bar strengths measured, the central stellar velocity dispersion and central line strength indices for H_β, Fe5015 and Mg*b*. Bottom left: (i) index-index diagram with age-sensitive index H_β versus metallicity-sensitive combined index of MgFe50', individual measurements from each bin are shown in gray and the isophotal profile with dark blue (and larger) dots showing the central measurement going from yellow to red towards the outer parts, representative uncertainties are indicated in the right top corner for individual measurements. On the left, top to bottom we show index maps and SSP maps and their corresponding profiles along the bar major, after the maps we show the (i) major axis profile: gray values show individual Voronoi measurements while black ones indicate averaged quantities, gray dashed vertical lines indicate 3/4 of the bar length and black dashed lines half the bar length. From left to right we show (i) H_β index, (ii) Fe5015 index, (iii) Mg*b* index; below the SSP parameters: (i) age (in logarithmic units and in Gyr), (ii) metallicity (in dex), (iii) abundance (as a measure of the difference between metallicities of Mg and Fe). In all maps, isophotes are separated by half a magnitude.

C.2 Index Gradients

We determine two gradients along the index profiles for major and minor axes of our galaxies. As examples we show in the text the major axis gradients for Mg*b*. Here, we show all gradient measurements: i) H_β gradients in Fig. C.17, ii) Mg*b* gradients in Fig. C.18 and iii) Fe5015 gradients in Fig. C.19.

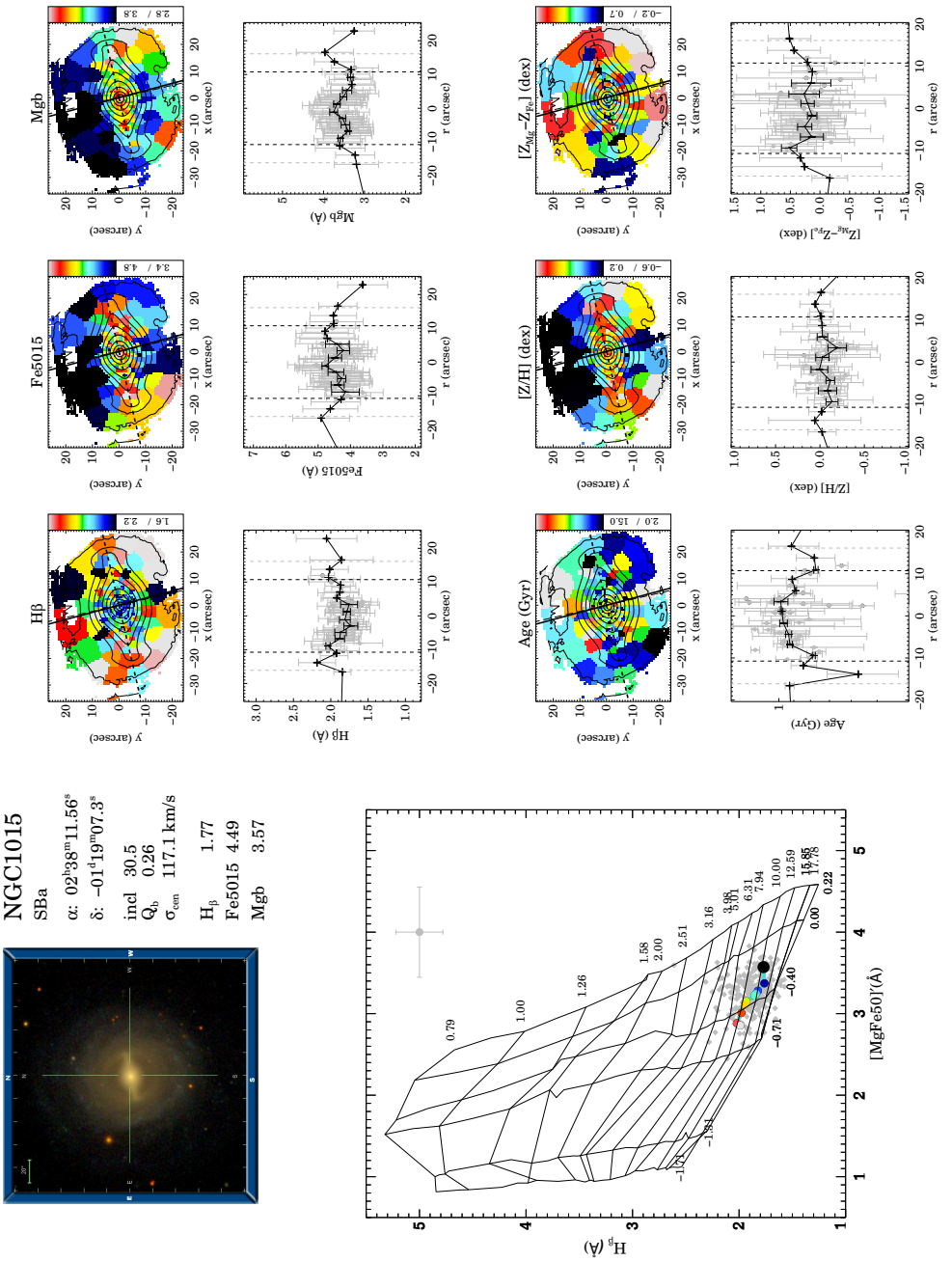

FIGURE C.1: Summary of the stellar population maps and important parameters for each galaxy. On the top left we show a colour SDSS image, below an index-index diagram and to the right index and SSP profiles. For more details please refer to the text.

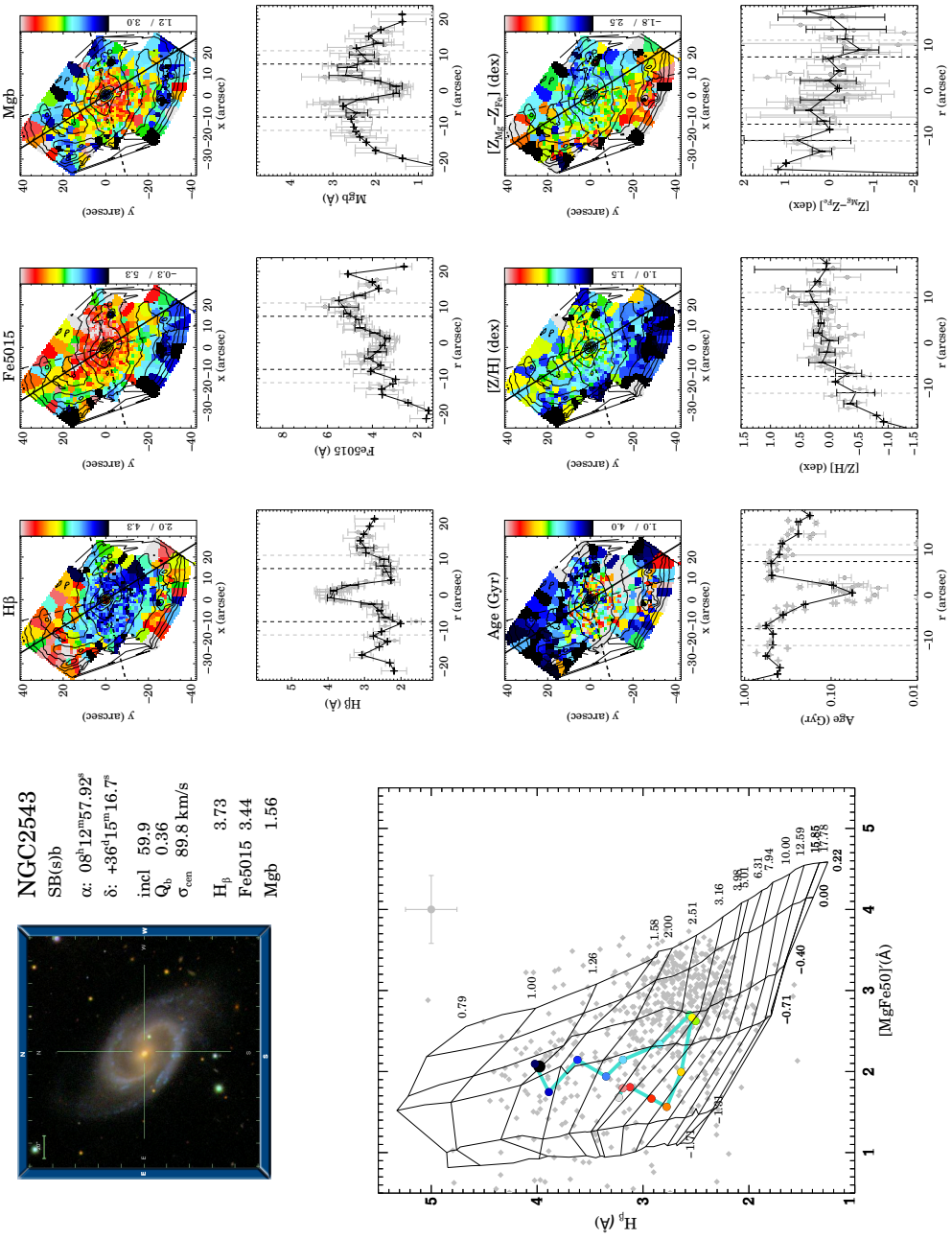

FIGURE C.2: Fig C.1 continued.

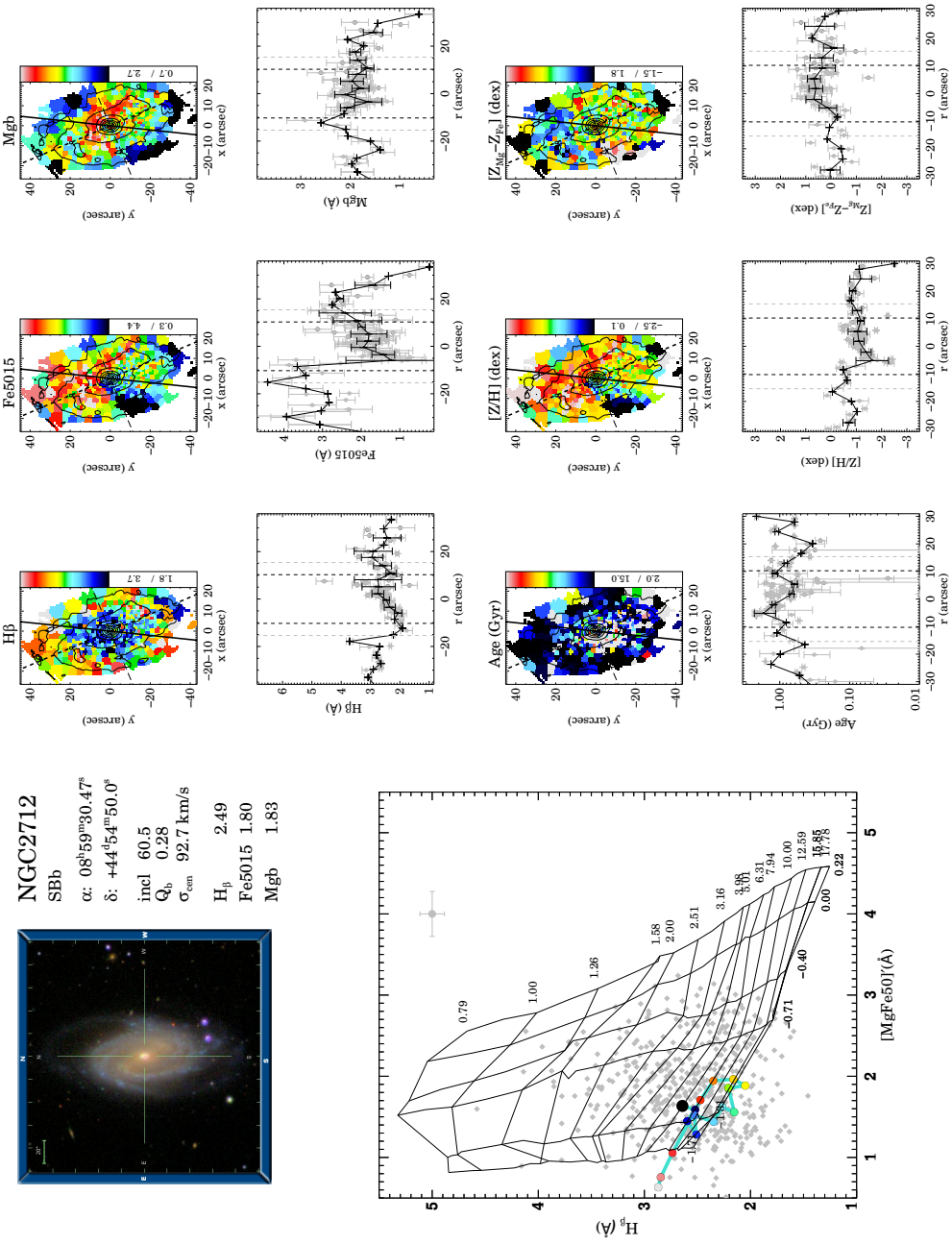

FIGURE C.3: Fig C.1 continued.

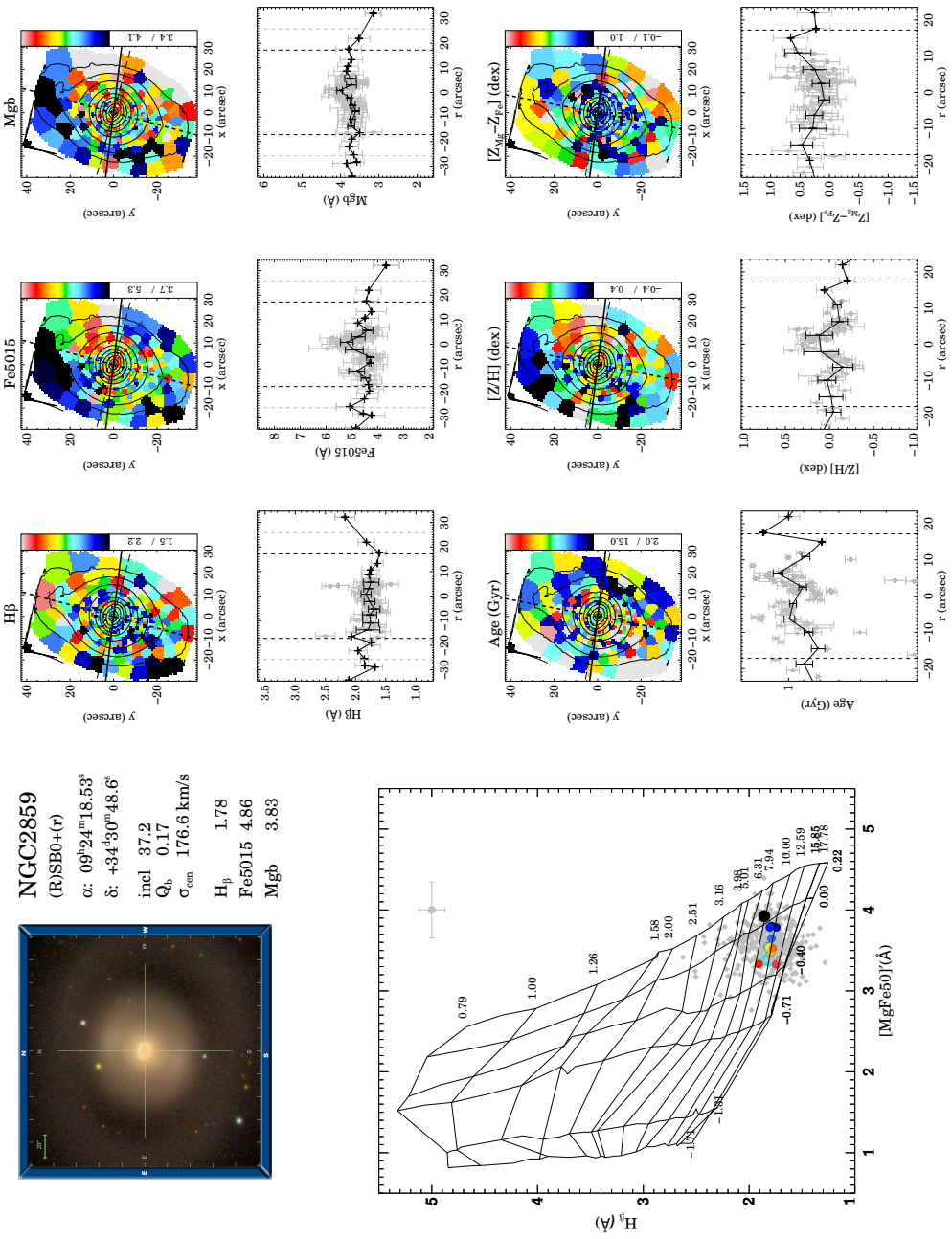

FIGURE C.4: Fig C.1 continued.

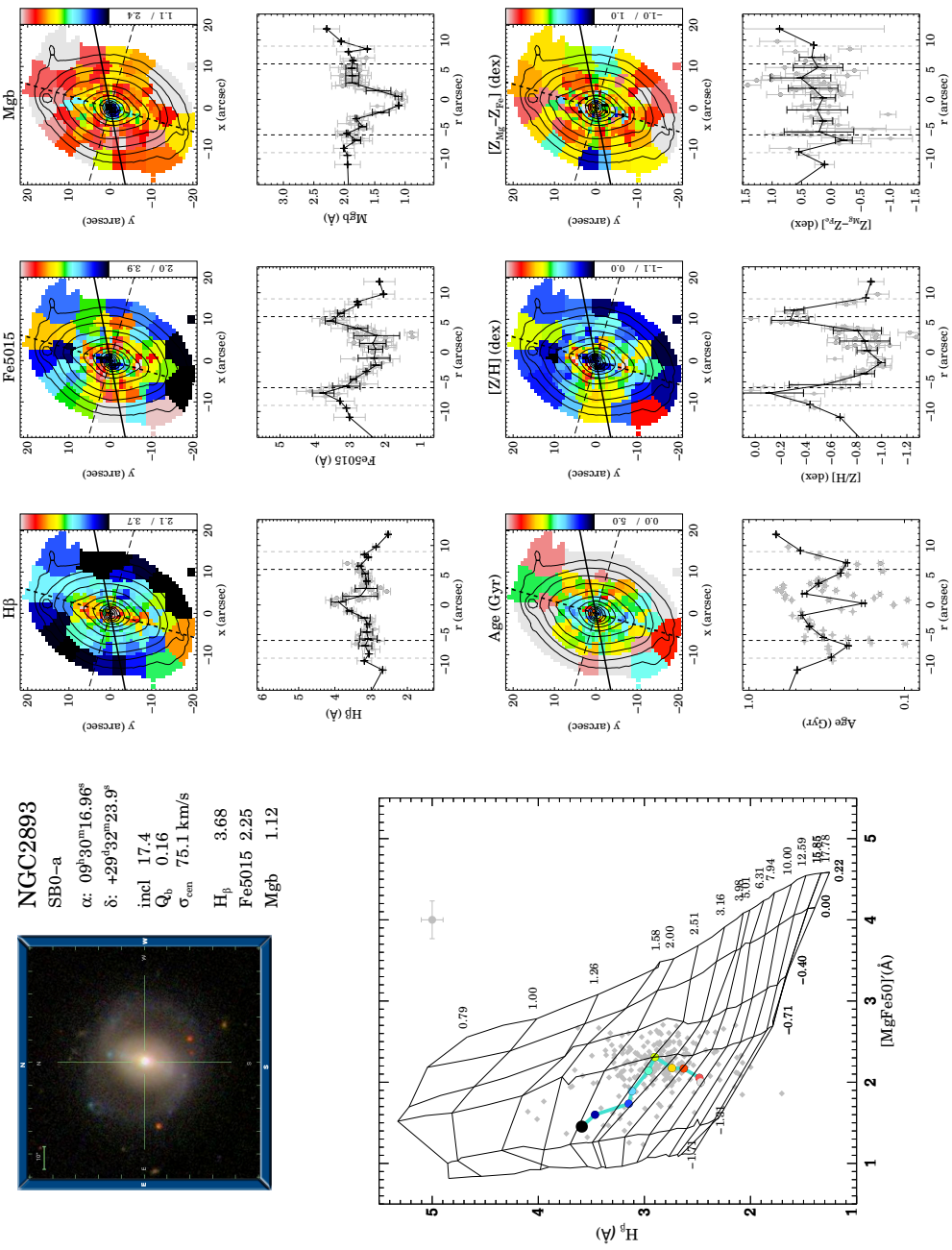

FIGURE C.5: Fig C.1 continued.

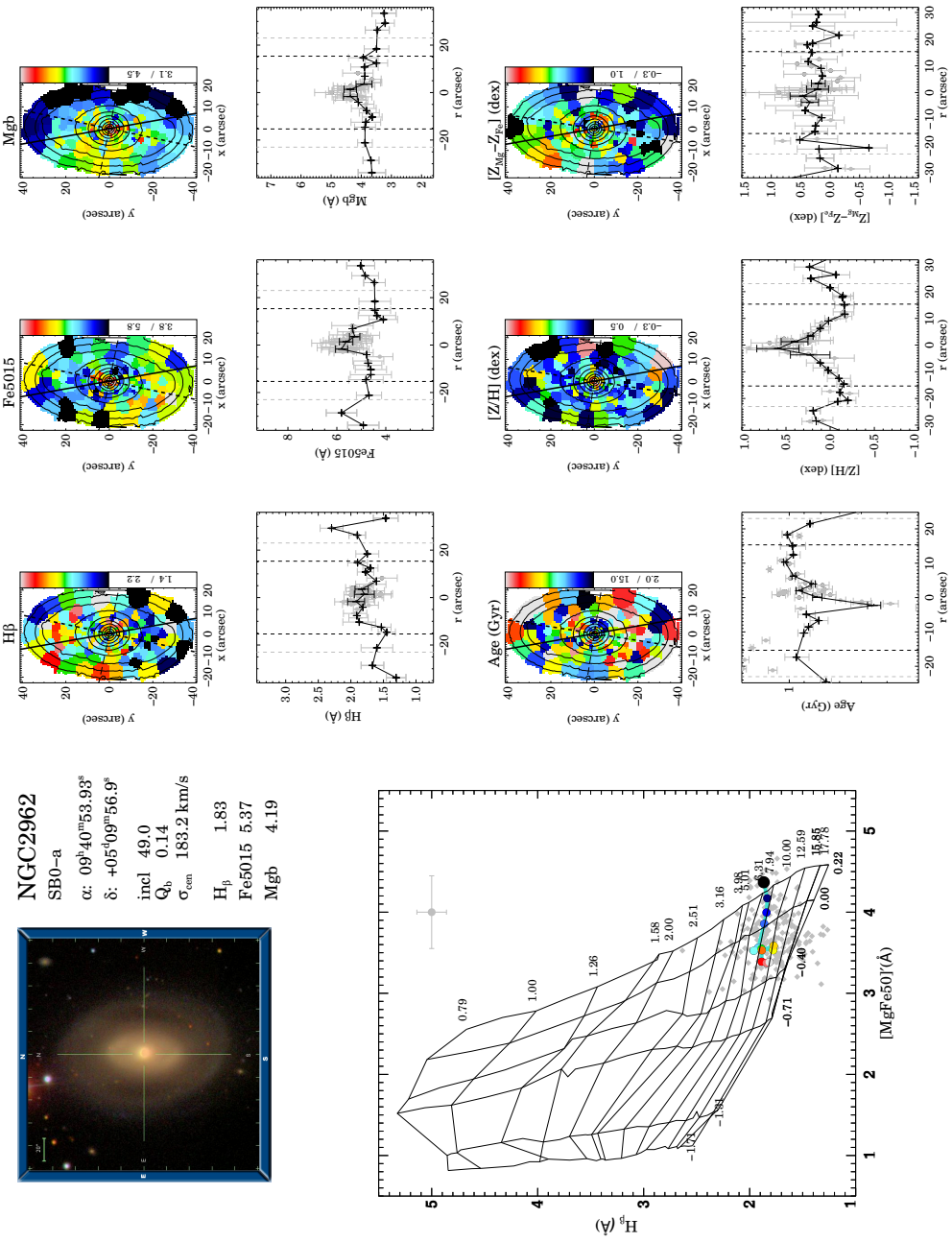

FIGURE C.6: Fig C.1 continued.

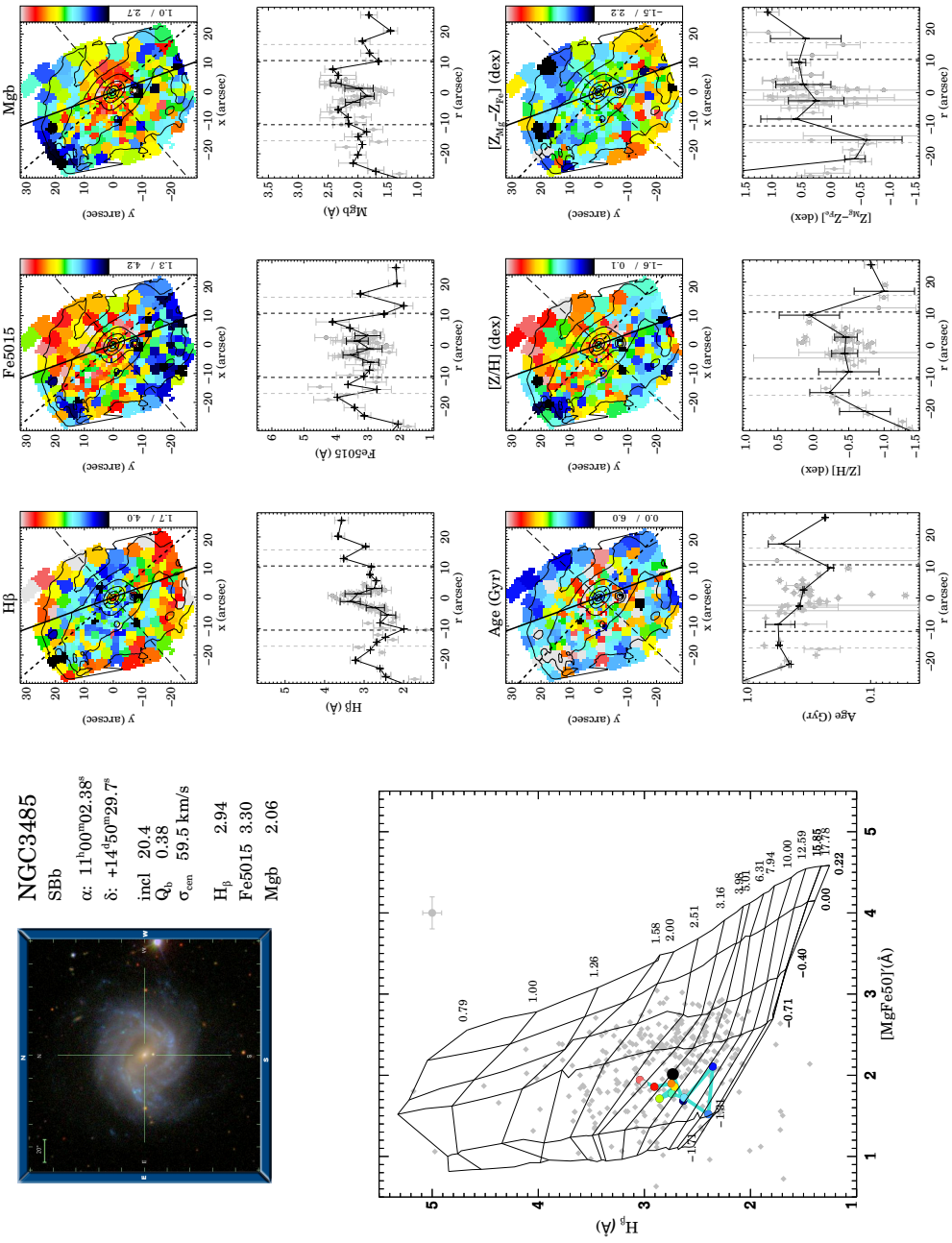

FIGURE C.7: Fig C.1 continued.

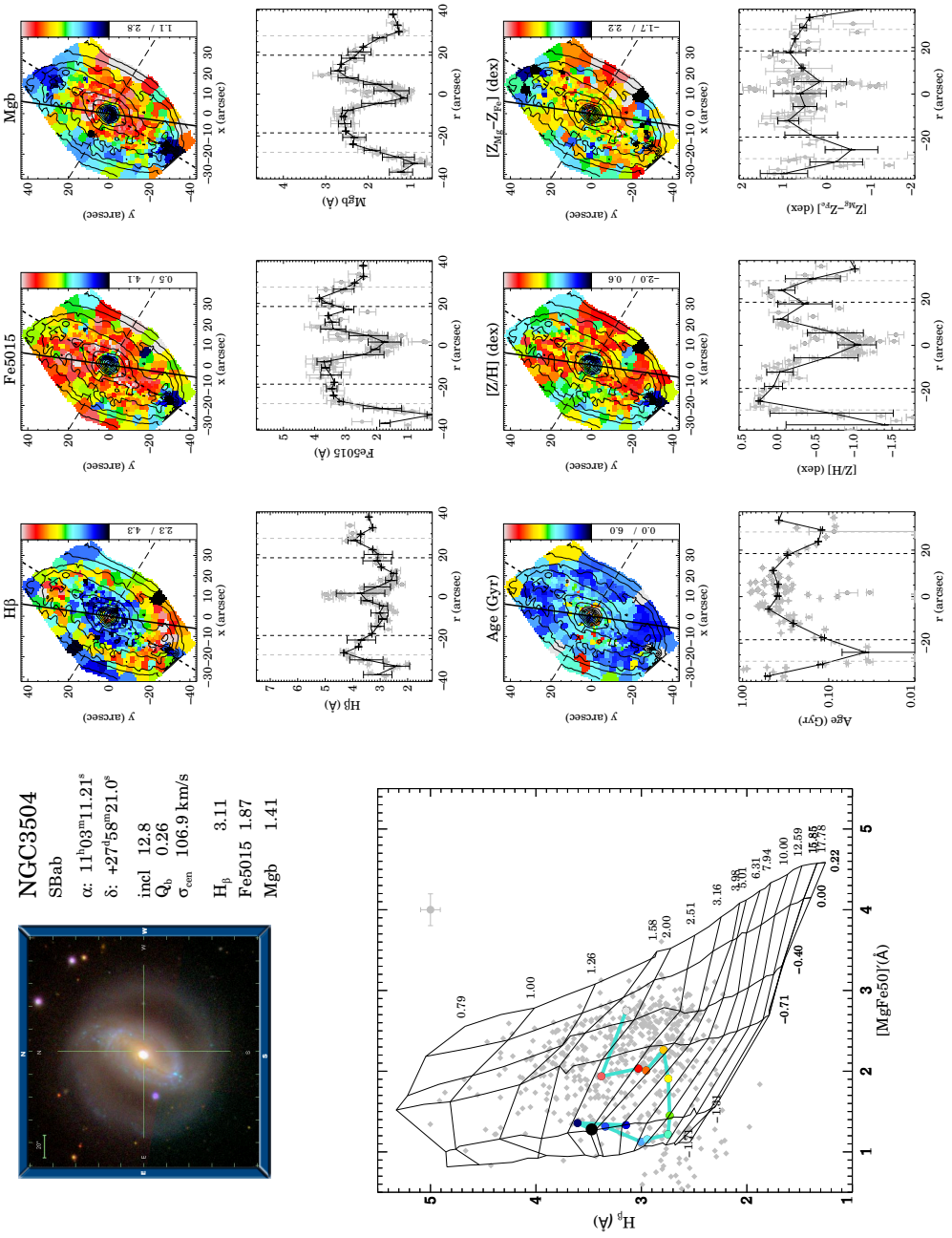

FIGURE C.8: Fig C.1 continued.

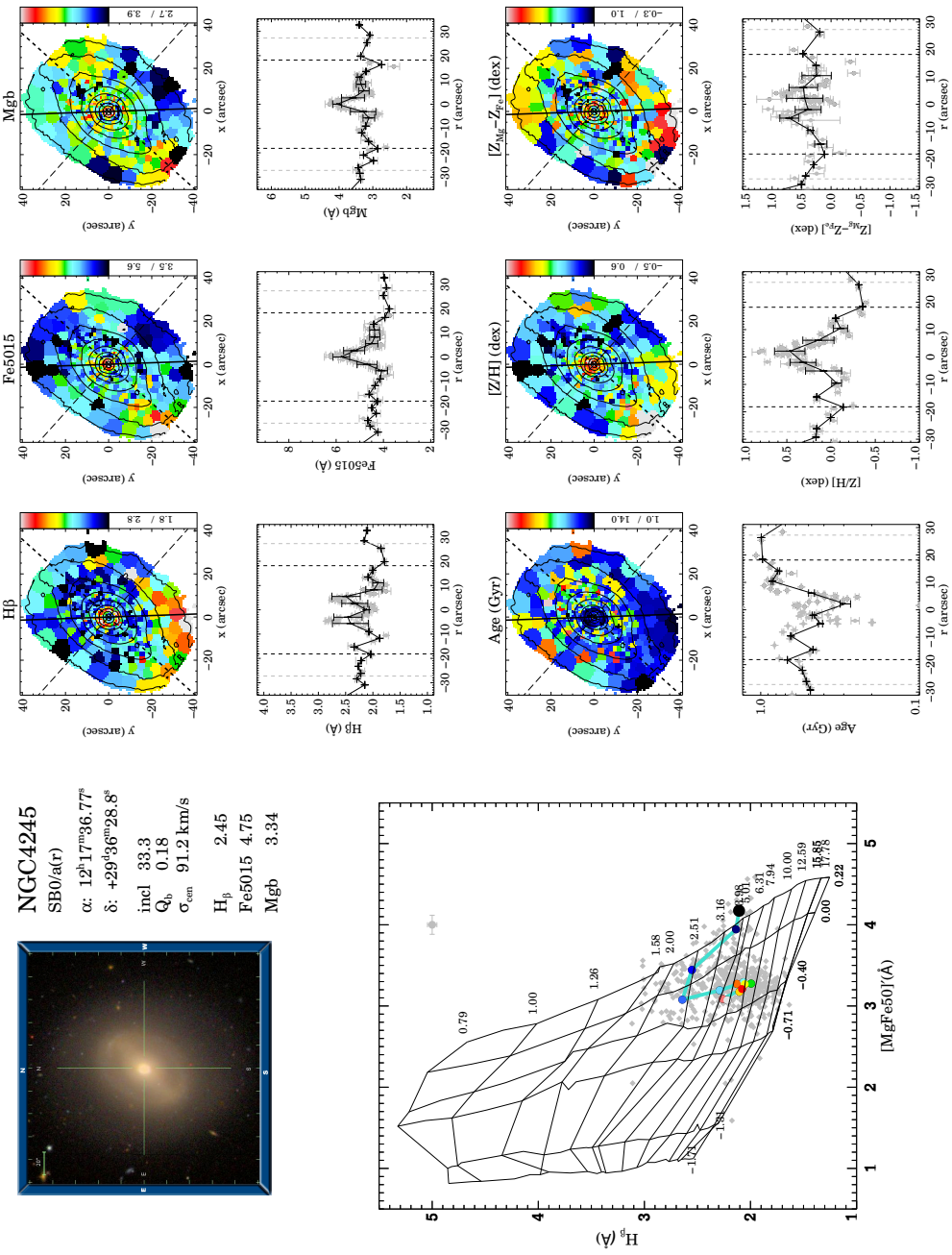

FIGURE C.9: Fig C.1 continued.

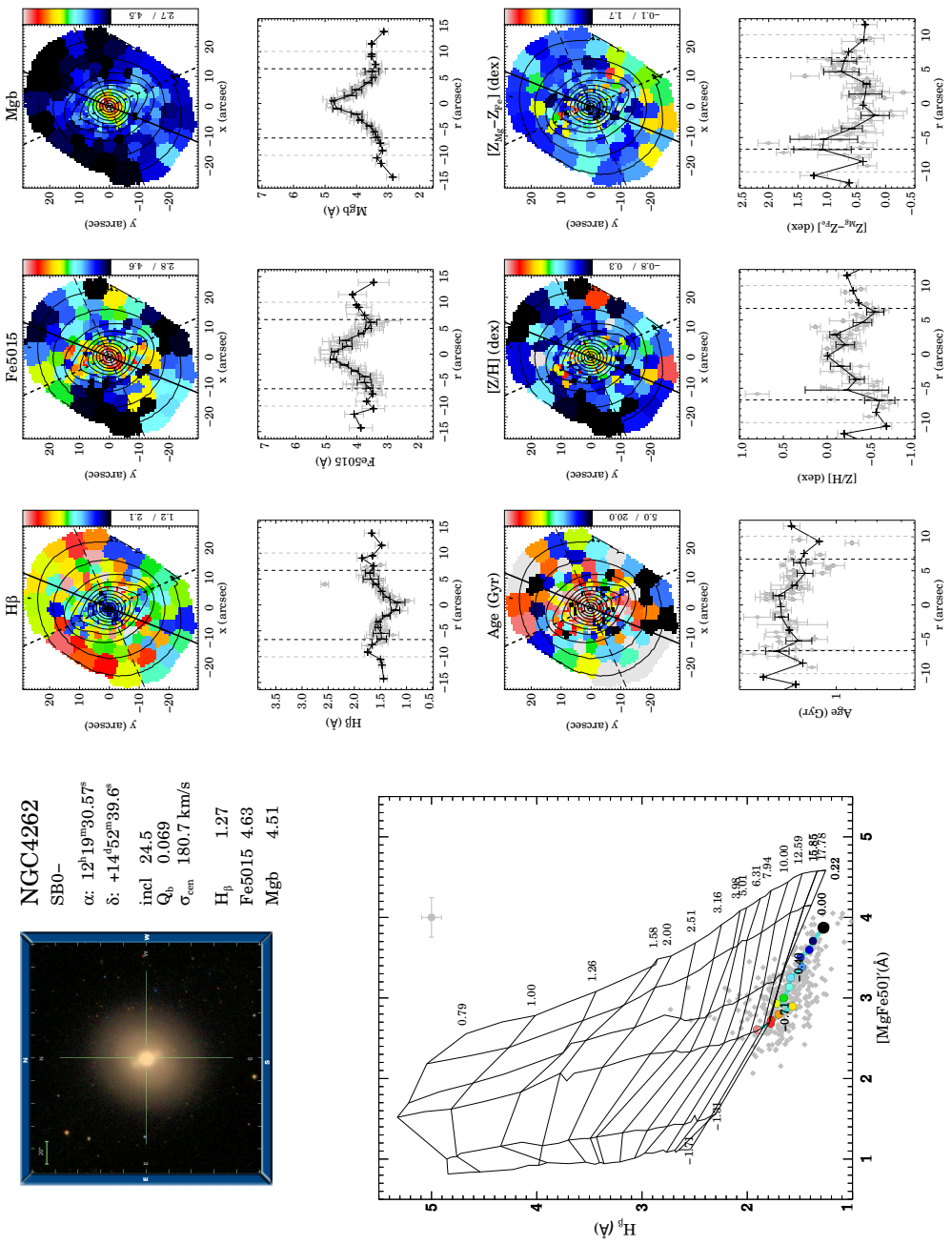

FIGURE C.10: Fig C.1 continued.

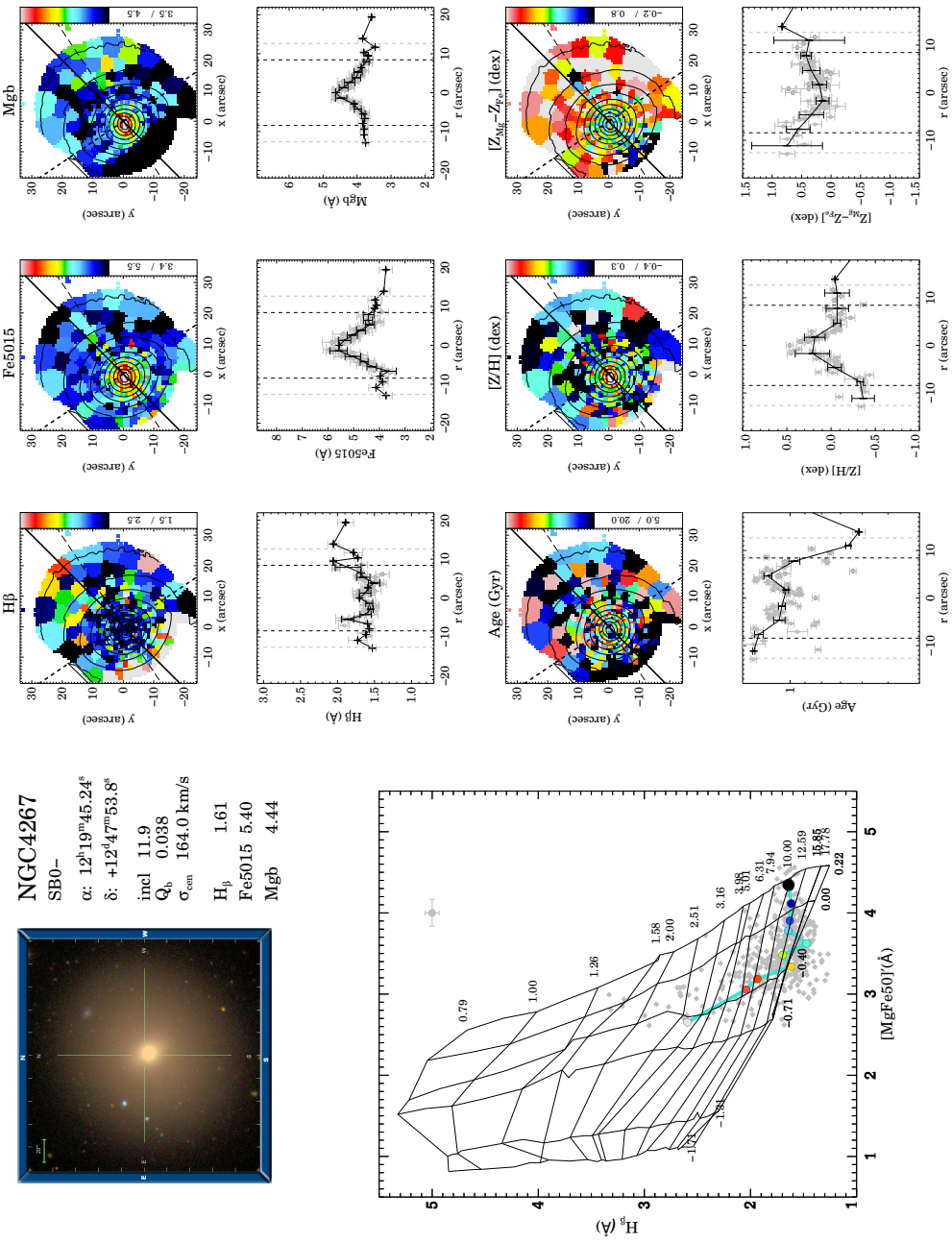

FIGURE C.11: Fig C.1 continued.

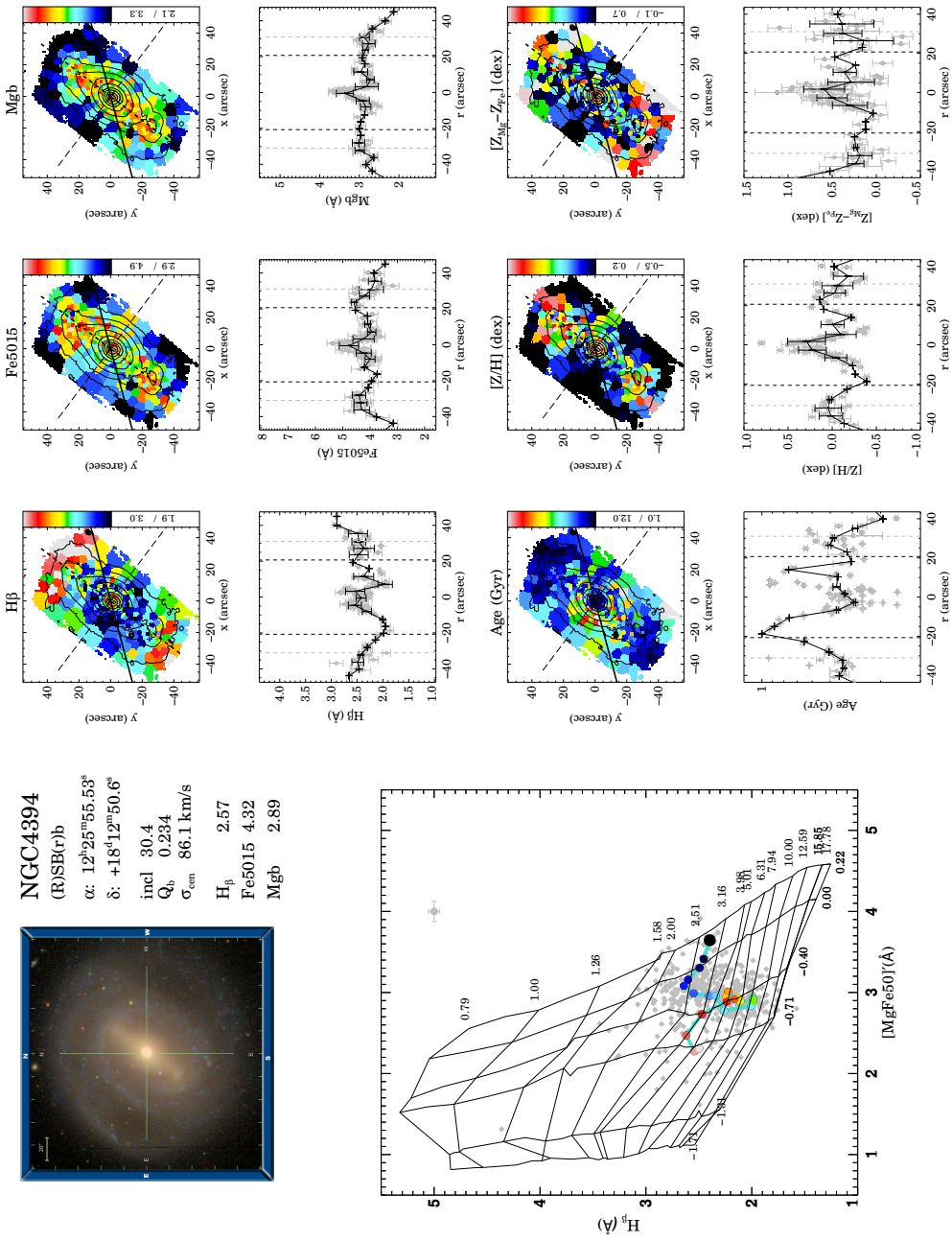

FIGURE C.12: Fig C.1 continued.

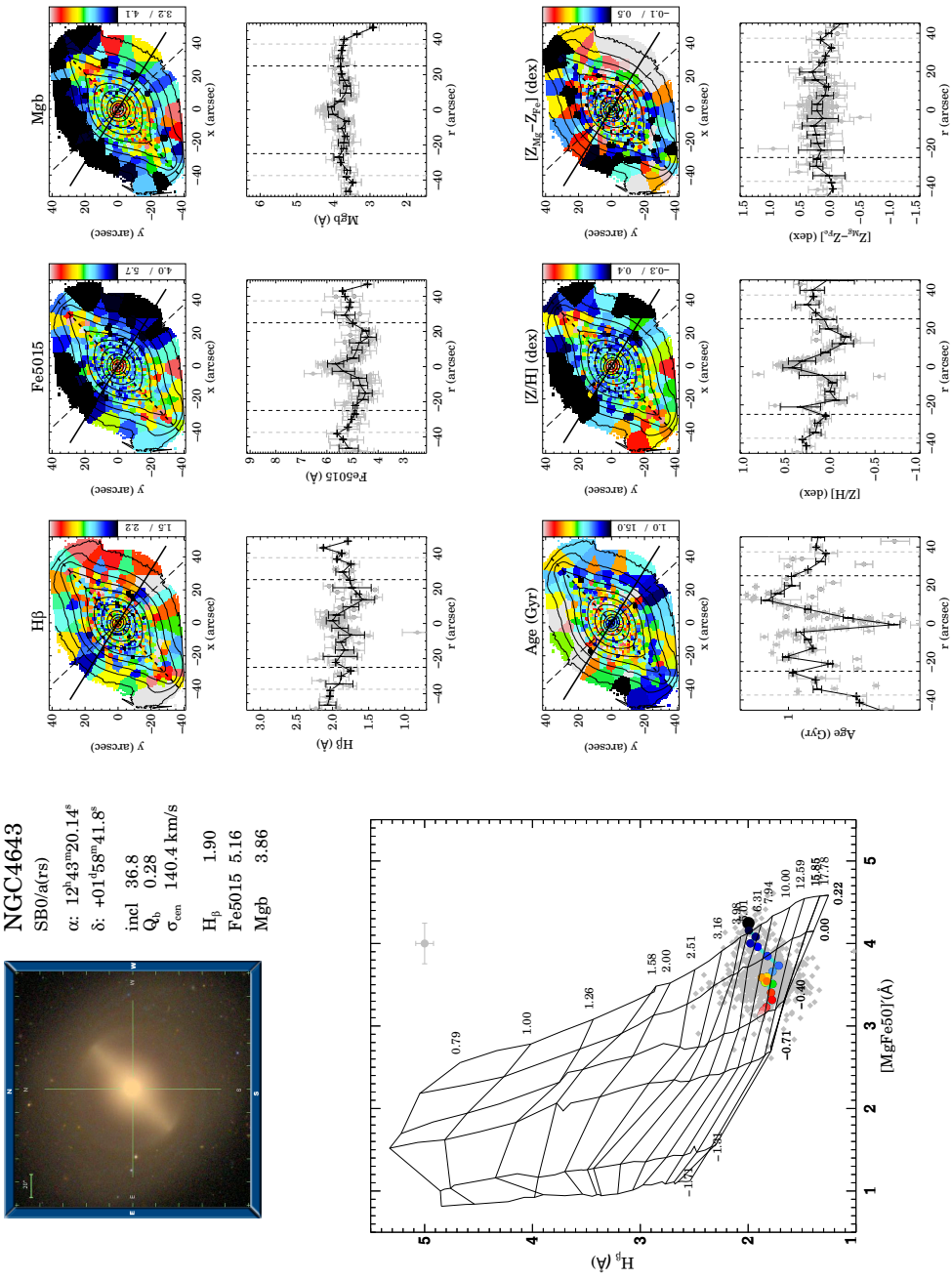

FIGURE C.13: Fig C.1 continued.

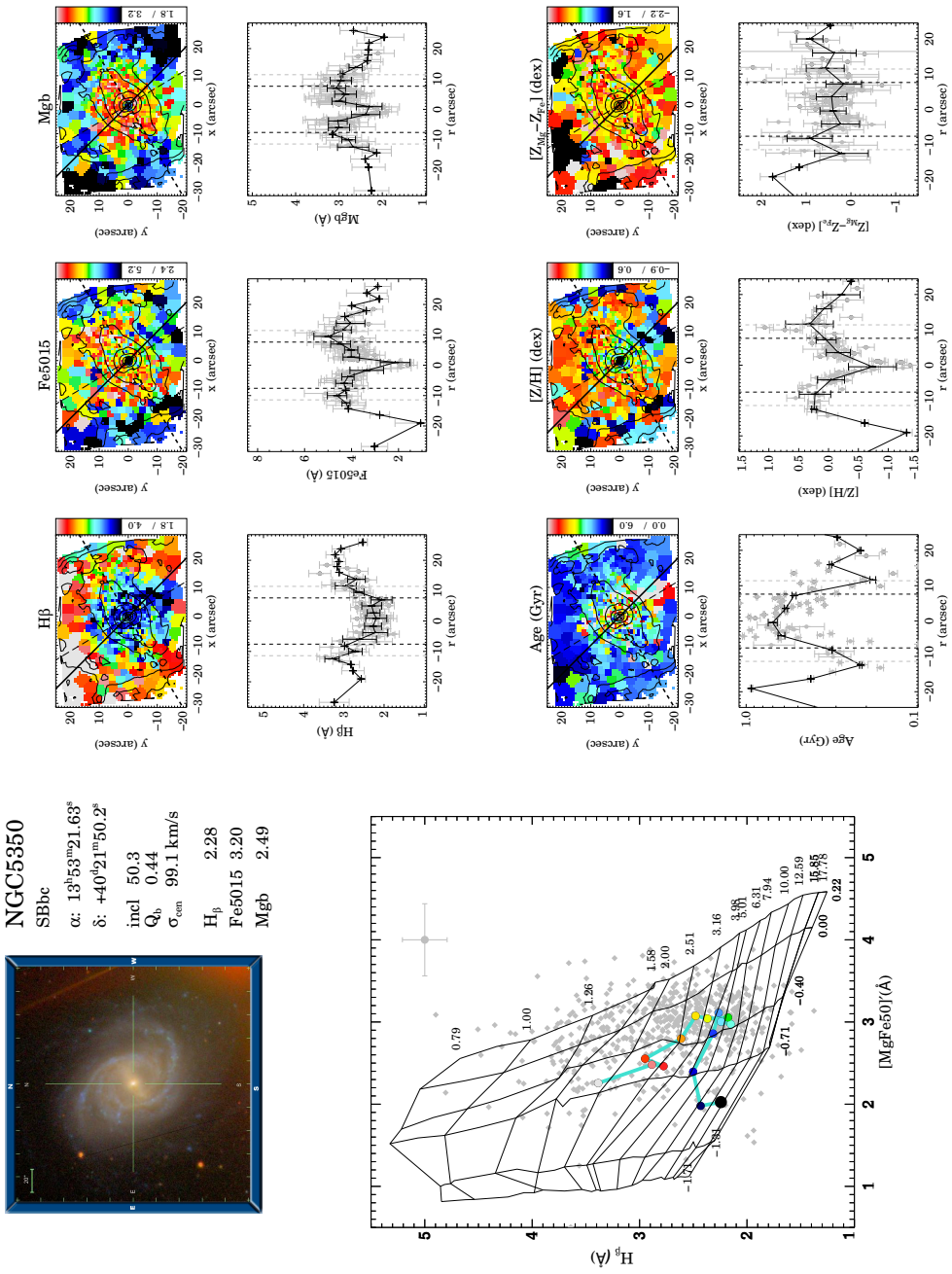

FIGURE C.14: Fig C.1 continued.

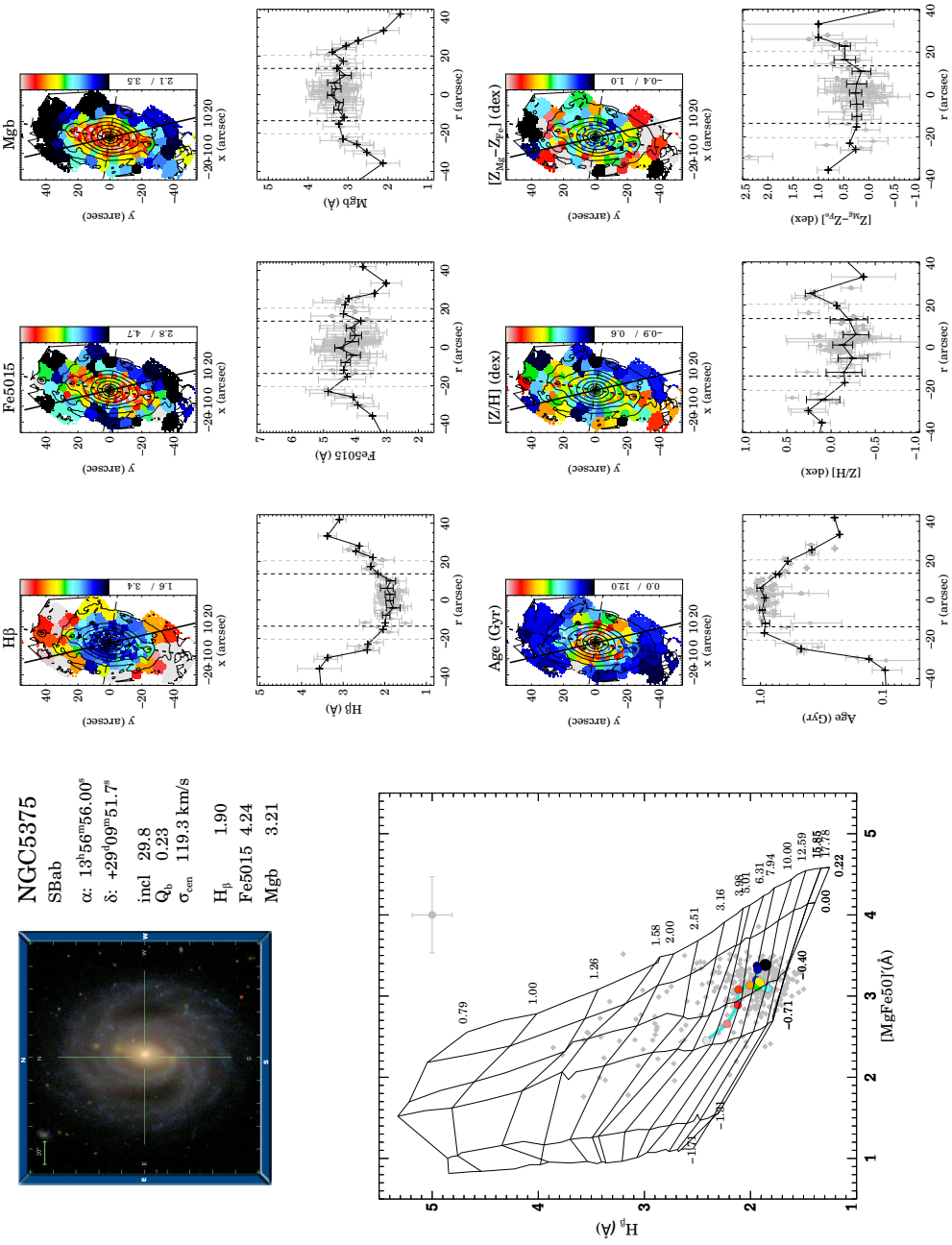

FIGURE C.15: Fig C.1 continued.

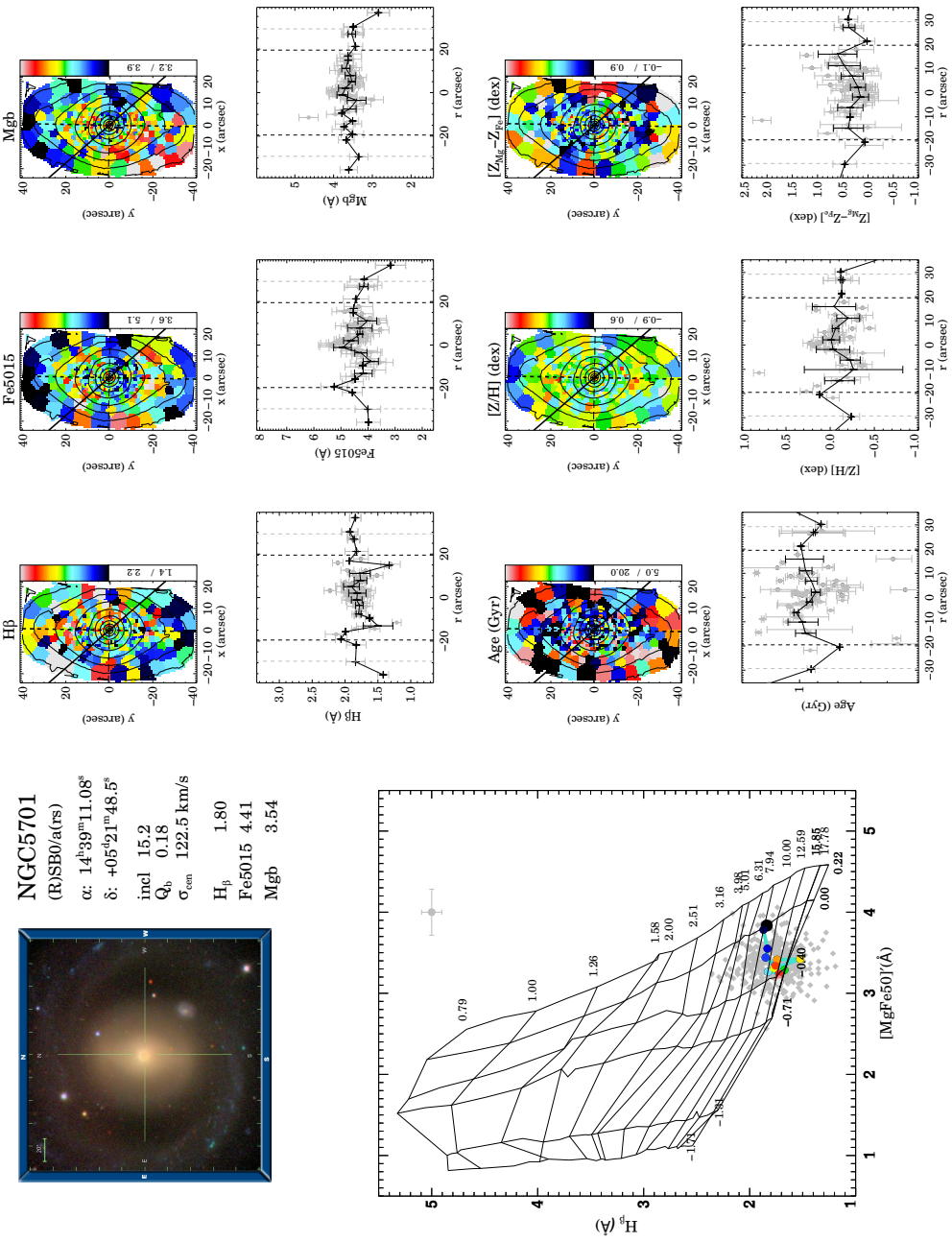

FIGURE C.16: Fig C.1 continued.

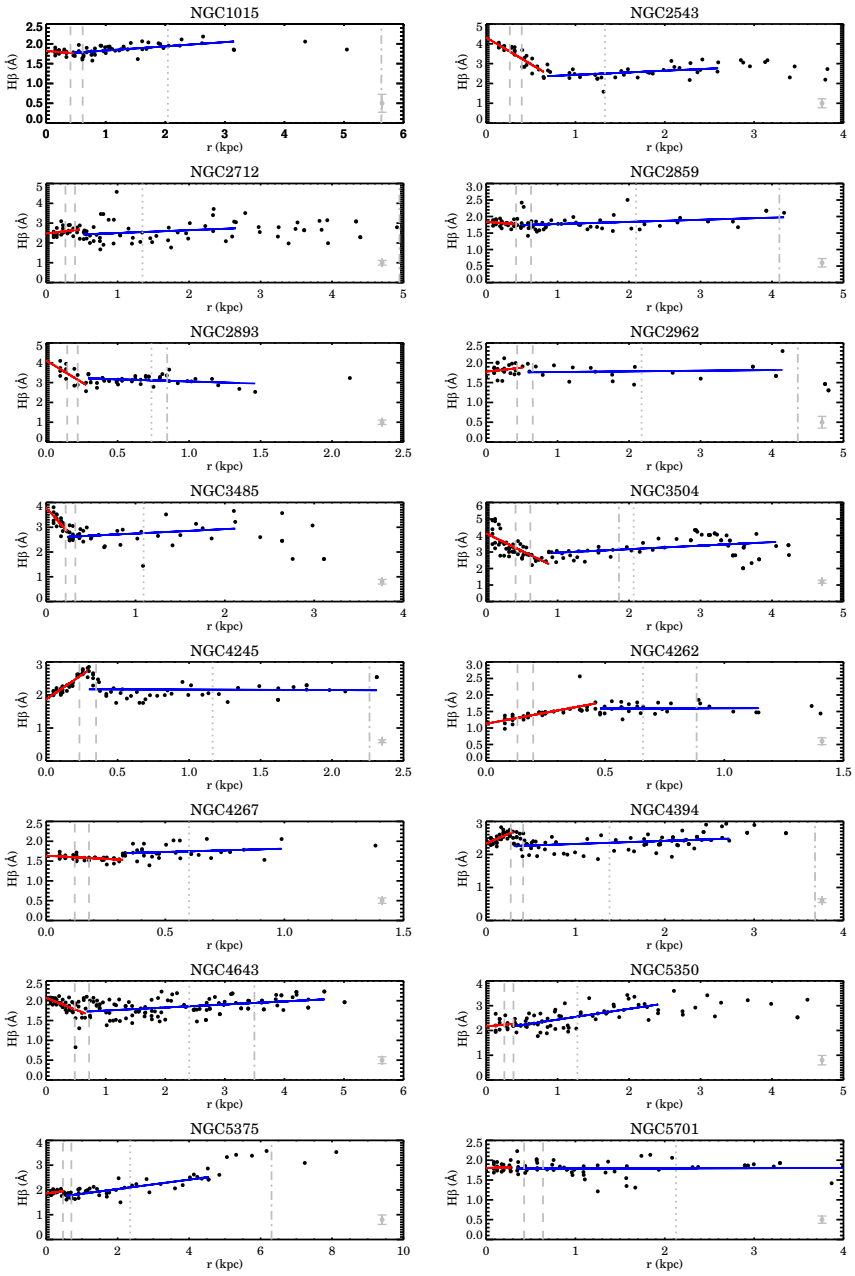

FIGURE C.17: Bar major axis profiles and linear inner (red) and outer (blue) gradients of the H_β index. The mean uncertainty is indicated in each panel in the lower right corner. Dashed lines indicate the region between 0.1 and 0.15 R_{bar}, dotted lines the position of 0.5 R_{bar} and dashed-dotted lines the position of 1.5 R_{eff}.

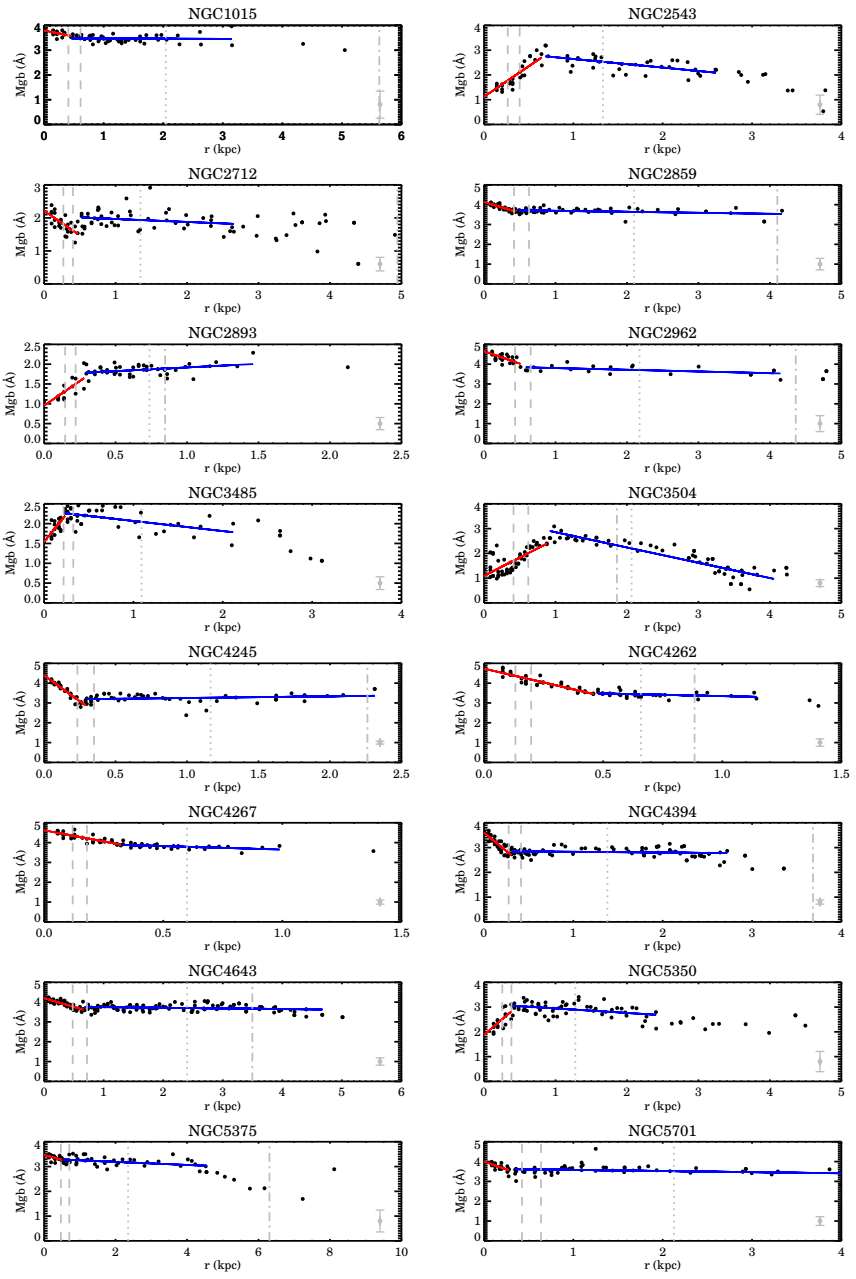

FIGURE C.18: Bar major axis profiles and linear inner (red) and outer (blue) gradients of the Mg*b* index as an example of the index measurements for the entire BaLROG sample. The mean uncertainty is indicated in each panel in the lower right corner. Dashed lines indicate the region between 0.1 and 0.15 R_{bar}, dotted lines the position of 0.5 R_{bar} and dashed-dotted lines the position of 1.5 R_{eff}.

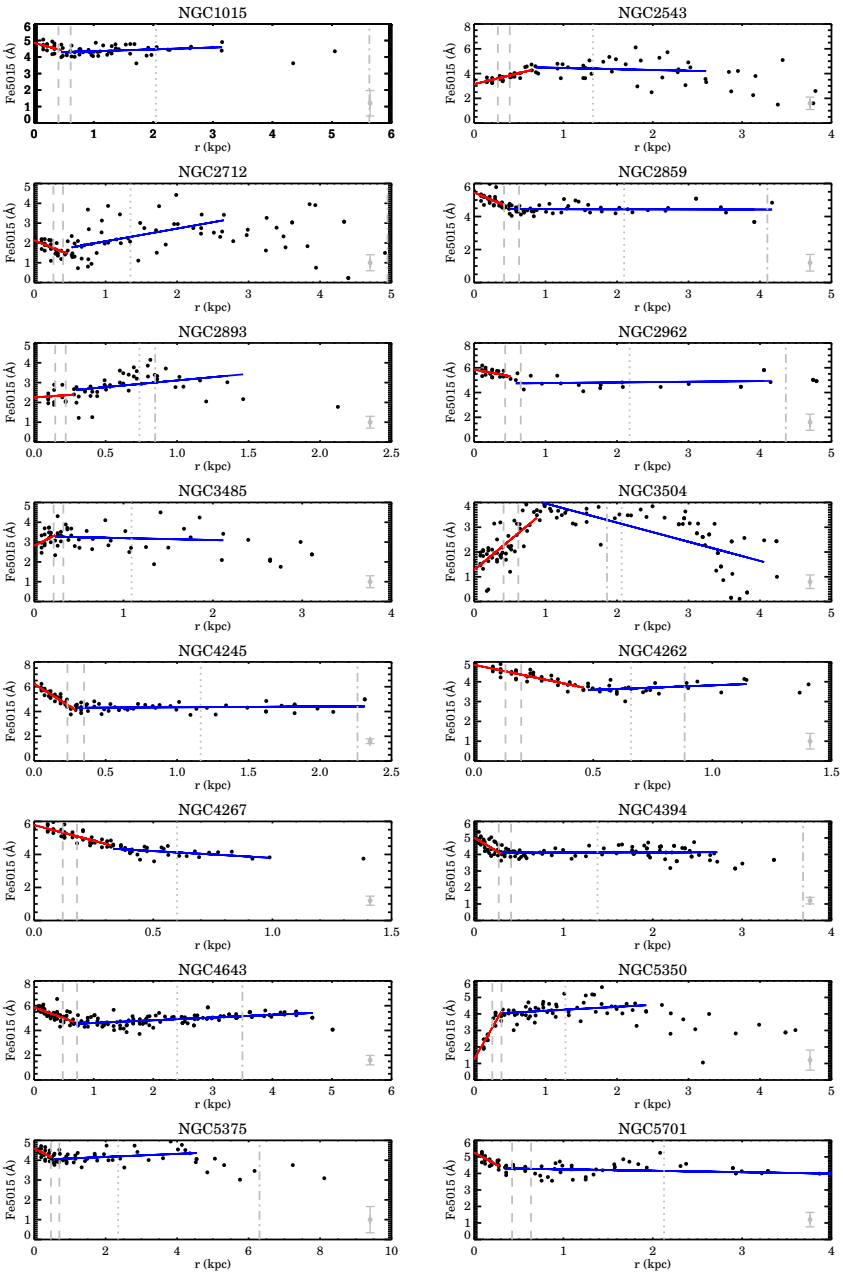

FIGURE C.19: Bar major axis profiles and linear inner (red) and outer (blue) gradients of the Fe5015 index. The mean uncertainty is indicated in each panel in the lower right corner. Dashed lines indicate the region between 0.1 and 0.15 R_{bar}, dotted lines the position of 0.5 R_{bar} and dashed-dotted lines the position of 1.5 R_{eff}.

C.3 SSP Gradients

We also determined the two gradients along the SSP profiles, shown here for the metallicity gradients in Fig. C.20, age gradients in Fig. C.21 and abundance gradients in Fig. C.22.

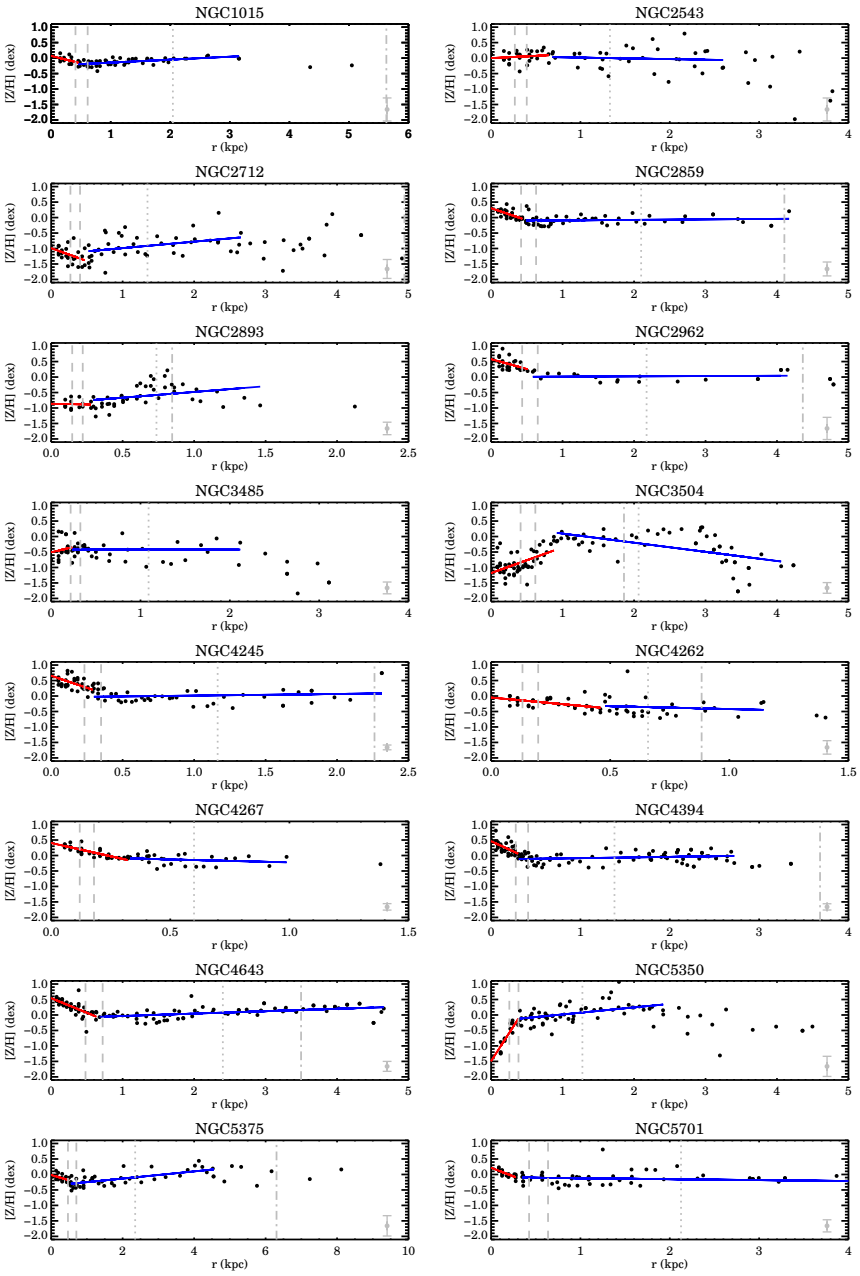

FIGURE C.20: Bar major axis profiles and linear inner (red) and outer (blue) gradients of the metallicity. The mean uncertainty is indicated in each panel in the lower right corner. Dashed lines indicate the region between 0.1 and 0.15 R_{bar}, dotted lines the position of 0.5 R_{bar} and dashed-dotted lines the position of 1.5 R_{eff}.

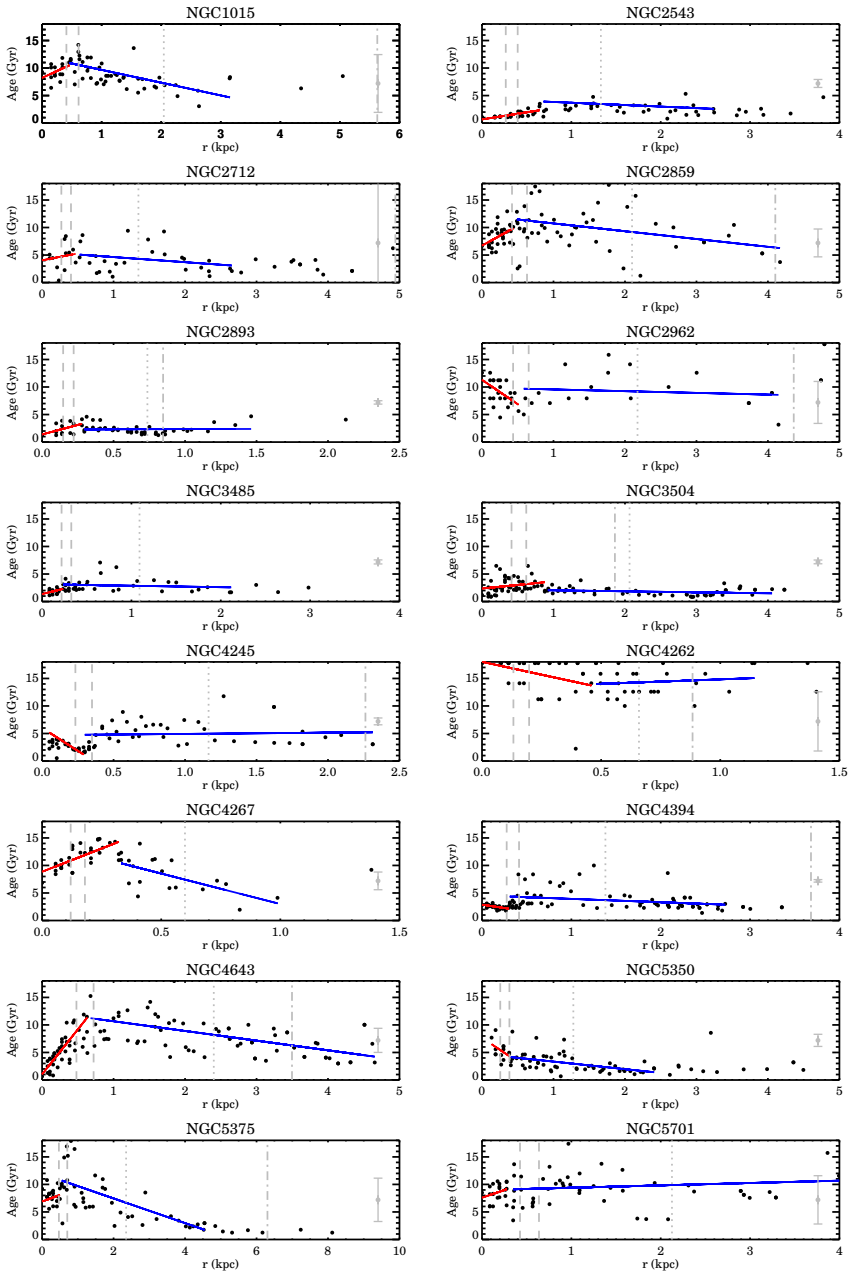

FIGURE C.21: Bar major axis profiles and linear inner (red) and outer (blue) gradients of the age. The mean uncertainty is indicated in each panel in the lower right corner. Dashed lines indicate the region between 0.1 and 0.15 R_{bar}, dotted lines the position of 0.5 R_{bar} and dashed-dotted lines the position of 1.5 R_{eff}.

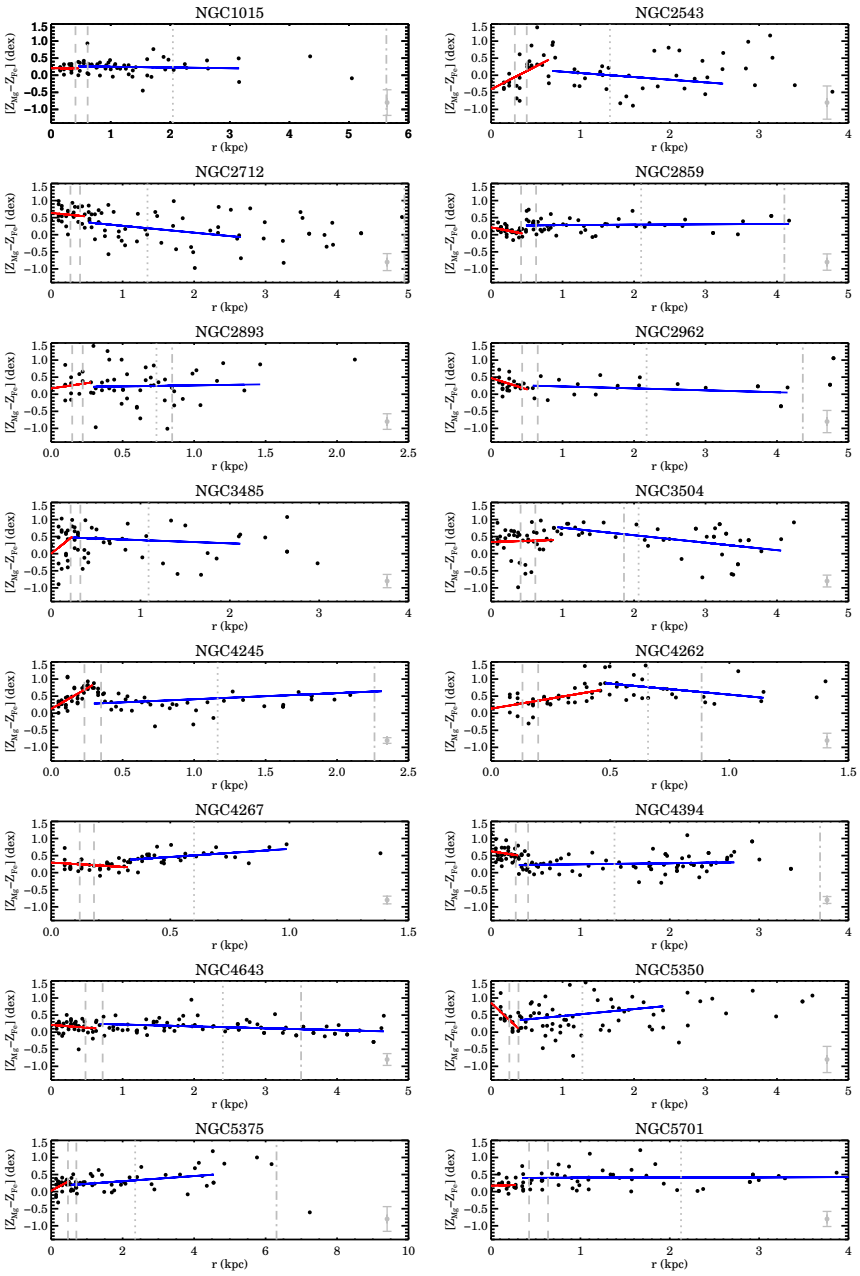

FIGURE C.22: Bar major axis profiles and linear inner (red) and outer (blue) gradients of the abundance. The mean uncertainty is indicated in each panel in the lower right corner. Dashed lines indicate the region between 0.1 and 0.15 R_{bar}, dotted lines the position of 0.5 R_{bar} and dashed-dotted lines the position of 1.5 R_{eff}.

D

Complete maps of bulges studied with WiFeS

We show maps of the stellar and ionized-gas distribution and kinematics (from the blue grating) as well as indices from the blue and red spectra for the three galaxies of this study. First row: HST or Spitzer image, its unsharp-mask and the name, Hubble type, position, absolute B-band magnitude and inclination of the galaxy. Second row: (i) stellar mean velocity V (in km s^{-1}), (ii) stellar velocity dispersion σ (in km s^{-1}), (iii) and (iv) Gauss-Hermite moments h3 and h4. Third row: (i) Hβ flux (in logarithmic scale), (ii) same for the H_γ, [OIII] and [NI] line, (v) mean radial ionised gas velocity and (vi) ionised gas velocity dispersion (in km s^{-1}). Fourth row: index maps from the blue spectra for (i) Hβ, (ii) Hβ_o, (iii) Fe5015, (iv) Mgb, (v) Ca4227 and (vi) G4300. Fifth row: index maps from the blue spectra for (i) Fe4383, (ii) Fe4668, (iii) Ca4455, (iv) Fe5270, (v) Fe5335 and (vi) Fe5406. Sixth row: index maps from the red spectra for (i) CaT, (ii) CaT*, (iii) PaT, (iv) Ca1, (v) Ca2, (vi) Ca3 - as defined in Cenarro et al. (2001a). The cut levels are indicated in a box on the right-hand side of each map.

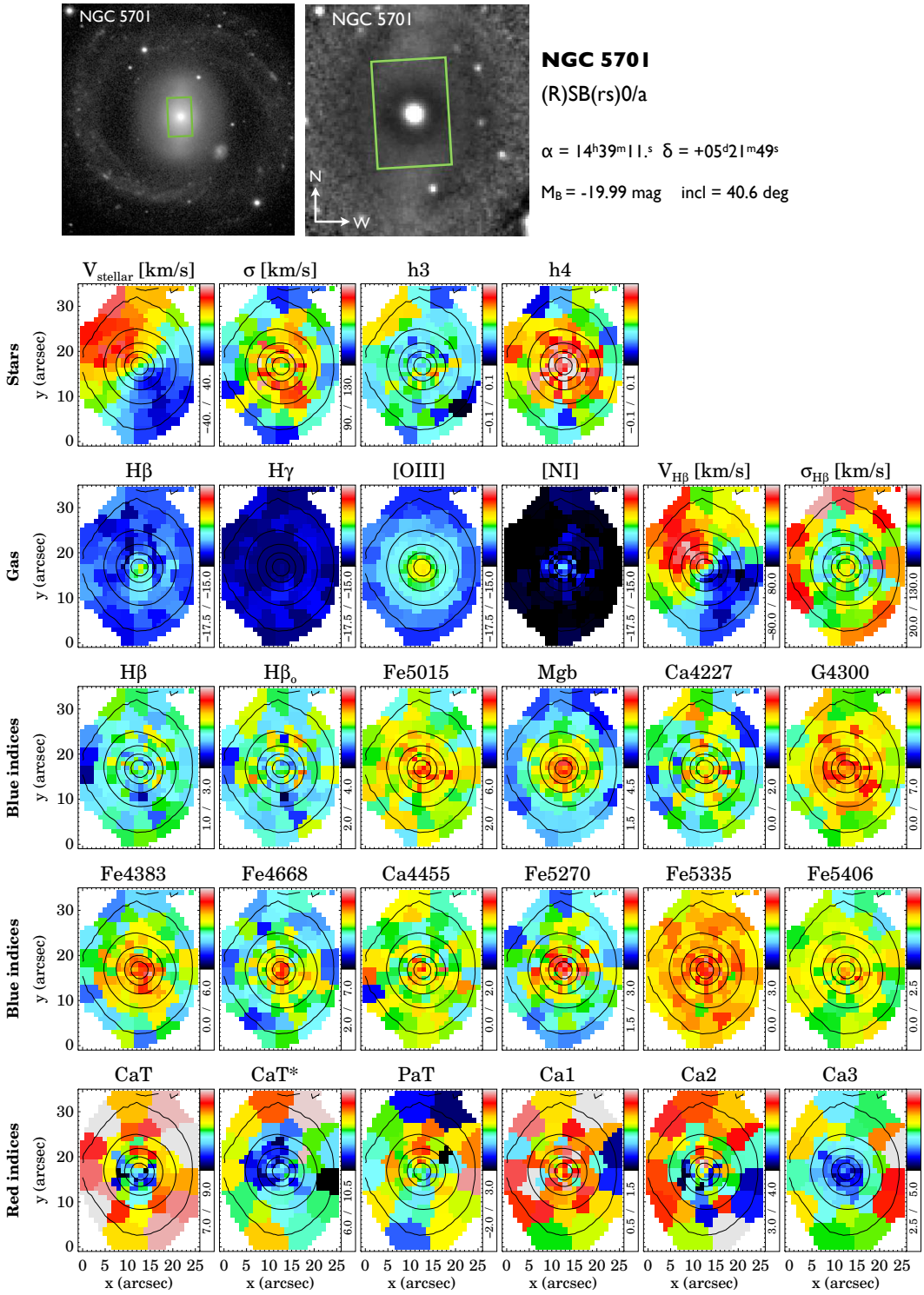

FIGURE D.1: Summarized maps for NGC 5701 from blue and red gratings. See text for details.

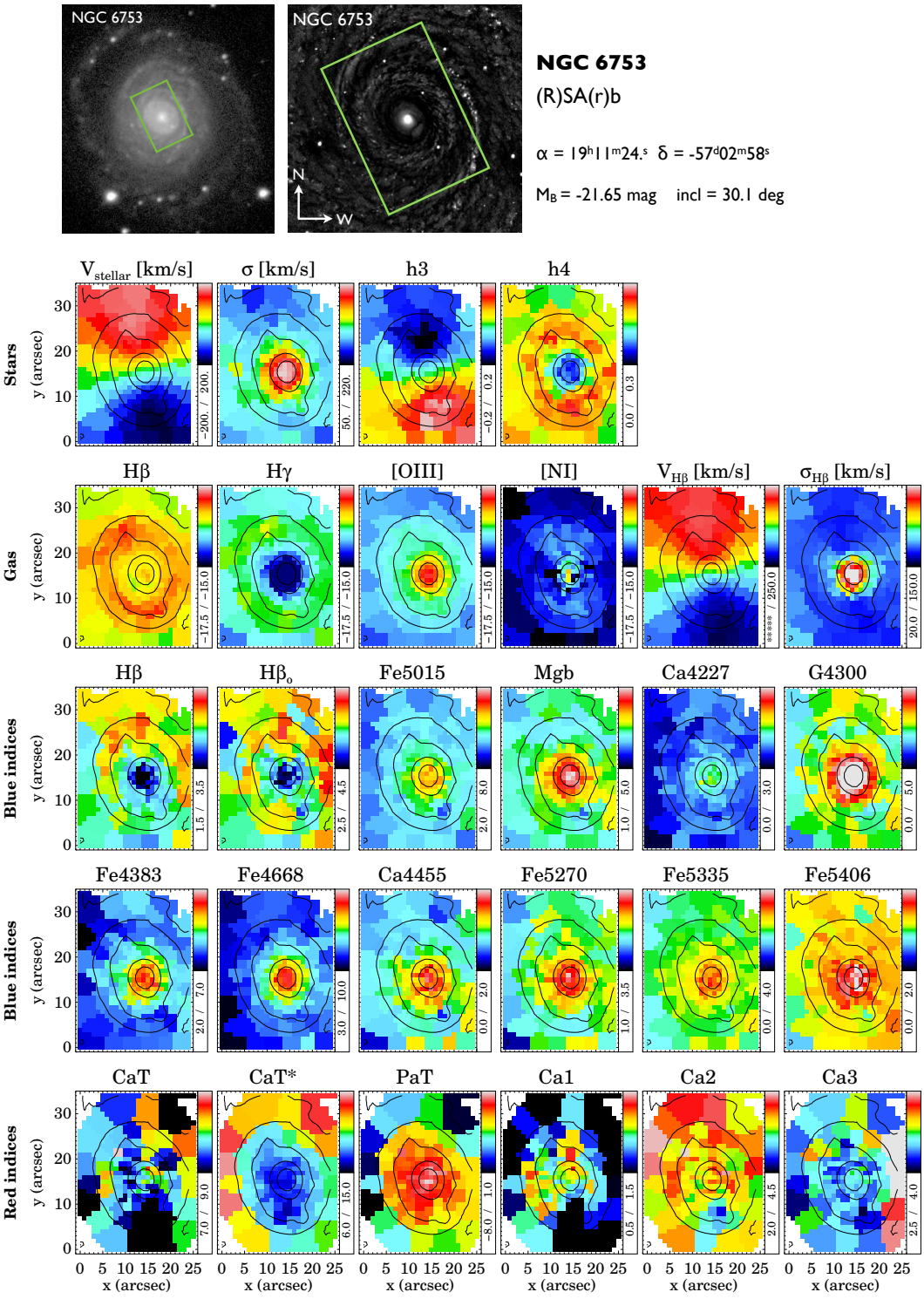

FIGURE D.2: Summarized maps for NGC 6753 from blue and red gratings. See text for details.

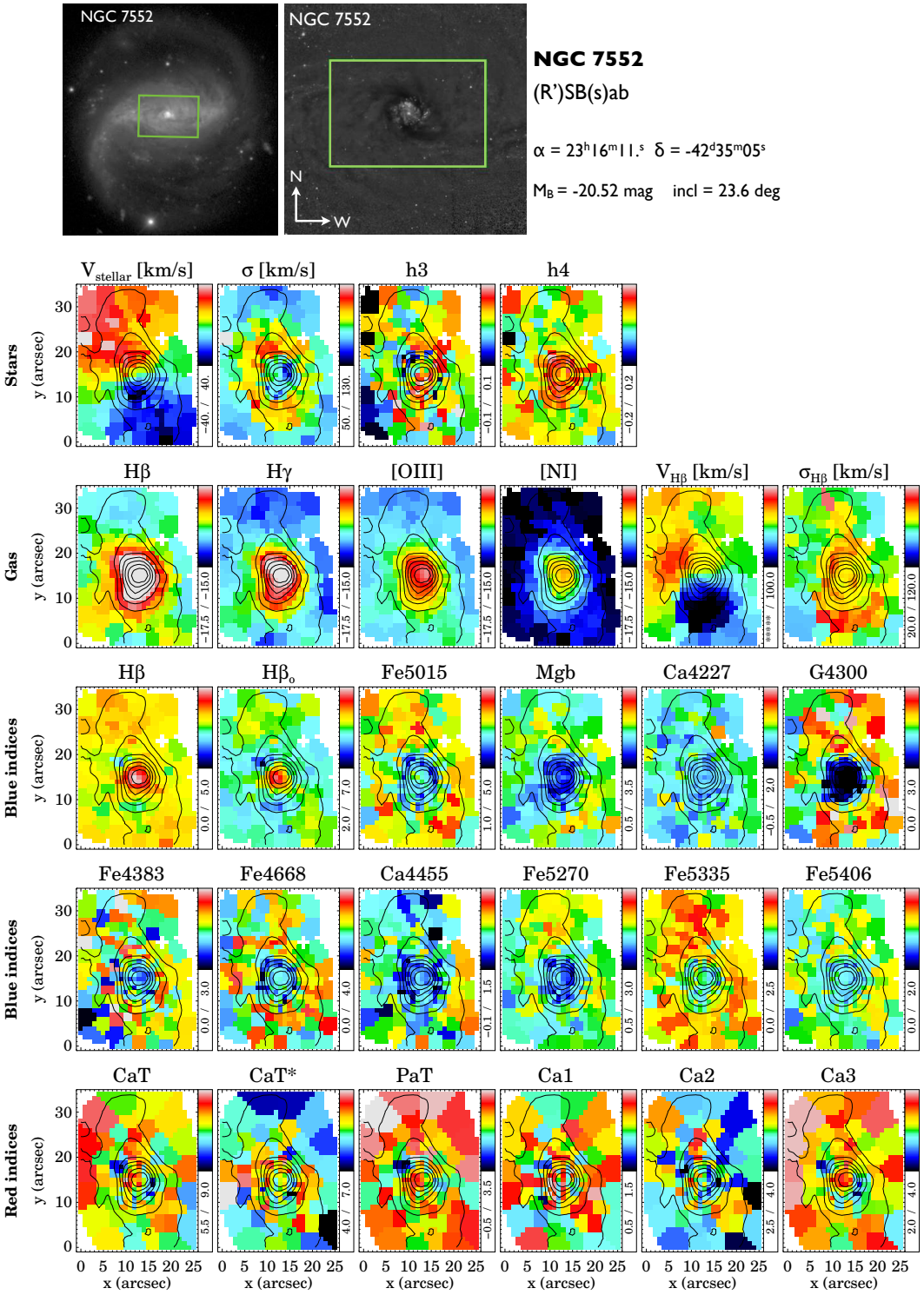

FIGURE D.3: Summarized maps for NGC 7552 from blue and red gratings. See text for details.

Acknowledgements

Doy gracias x tantas cosas

el proyecto `ANONIMAN`
Cartel de la autopista
15 de Julio 2013

Thank you. Gracias. Danke. Merci.

I have so many reasons to say *Thank You*. All this work as well as my personal survival during the last four years would not have been possible without many people. I will try to acknowledge all help here in the imposed brevity, although I could probably write yet another thesis or two on just saying *thank you all so so much*. But I bet some of you already skipped through the chapters to get to this final part. Therefore I will *try* to keep it short so you can get back to the real interesting stuff :)

In that sense, I would like to thank:
... my supervisor Jesús Falcón-Barroso. Thank you for your help and guidance throughout this thesis, starting with the observations up until this final product of the written manuscript. Thank you for your scientific advice, for your invaluable patience with my programming frustrations, for teaching me how to work with SAURON and analyse integral field data, for giving me the opportunity to go to conferences from the very beginning and for helping me to better understand the multi-facetted work of a researcher. But thank you as well for your personal side, for your understanding when I needed more time, but also for trying to push me always another step further, for tolerating my multiple journeys, for discussions on how to best survive long distance relationships during a PhD and for your belief in my scientific capabilities that I doubted so often. Thank you for being a truly fantastic supervisor!

... Inma Martínez-Valpuesta. You have been a wonderful support and your scientific advice, in particular from the theoretical point of view has been invaluable. Thank you for the numerous discussions, suggestions and feedback as well as for your support with the Journal Club.

... my amazing collaborators! I had such a chance to work with really fantastic scientists on my projects! It was a real pleasure working with each and everyone of you. Without any particular order, thank you:
- Tomás Ruíz-Lara - for your STECKMAP expertise and constant optimism
- Raúl Cacho - for your innovative skills, including improvising seat-belts in

Ken's car
- Isabel Pérez - for your incredible help putting the observation proposal together
- Patricia Sánchez-Blázquez - for your rapid feedback, suggestions and readiness to help, always
- Frédéric P. A. Vogt - for your patience explaining us how WiFeS operates in order to get the best observations possible
- Melissa Ness - for your help settling in and beautiful sunset runs
- Ken Freeman - for fantastic discussions as well as for leaving us your office, your car, a place in your house,... (Spain was in crisis)
- Suryashree Aniyan - for offering us part of her observing time
- Simón Díaz-García - for surviving late night work and early morning runs and helping us so much with the bar strength calculations
- Eija Laurikainen and Heikki Salo - for your feedback and suggestions
- Johan H. Knapen - for your very detailed comments, your advice and constant motivation
- Alexandre Vazdekis - for your never ending ideas
- Reynier Peletier - for always asking and assuring that everything went well.
This work would not have been possible without all of you!

... our research group at the IAC. I hope that I will keep seeing most of you in the future! I will definitely miss the hour(s)-long group meetings!
... Nacho (Ignacio Martín Navarro). Without you, this thesis might not exist and surely, without you, I would not exist anymore as I would not have survived this thesis. Thank you for your help and advice, scientifically and personally. I can't wait to conquer the Gran Capitan with you!
... all my fellow PhD students, our lunch group, amigo-invisible-group and my marvelous office mates -for, amongst others, teaching me that a little tequila shot during the day is not all that bad. Special thanks to Andrea for day and night walks'n talks, Alberto for being my muy mejor amigo and amongst so many other things, also for checking some of my Spanish translations for this thesis, Maria for her creative title suggestions and just being the best desk neighbour possible, Artemi for bringing the tequila (although he himself doesn't drink it!) and baking fantastic cakes, Federica for chocolate discussions and Prieto for actually bringing us chocolate, Anna (Ferré) for her invaluable help even from the distance, Tanausú for being a fantastic friend since my exchange semester and making me laugh so much, together with Andrés, Klaus for *I'm yours* and more music (and fiestas), Simone for starting the days in the mountains, Stefano for beach lunches, Jana for many beautiful postcards, Bea, Marina, Sara, Sara B., Laura, Luis, Rosa, Victor and Javi - you are great!
... the support of the fellowship of the Residente Astrofísico of the IAC. It allowed me to pursue my Master and PhD within the last four years and enjoy my life while doing great science in an extraordinary environment. Thank you so much Victor, for motivating me to apply for this grant and your help in understanding the Spanish bureaucracy involved.
... the support of the RAVET program (grants AYA2010-21322-C03-02 and AYA2013-48226-C03-01-P) from the Spanish Ministry of Economy and Competitiveness (MINECO). They allowed me to participate in conferences as well as to undertake a research stay at Mount Stromlo Observatory.

... hence, the researchers of Mount Stromlo Observatory for their friendliness, hospitality and support during my extended stay - thanks everyone who made this time unforgettable, such as Margaret Freeman for the great stories and wonderful cuisine, Elliot and Seaton for extraordinary climbing and beach excursions and Boris for teaching me latin dancing (finally - it seems one has to go to Australia for this), and my already mentioned collaborators, of course.
... Evencio for your trust in my teaching skills and for treating me as a real colleague in the ULL course on photometry. Also thanks for accepting to join my thesis committee along with Paola Di Matteo and Alfonso Aguerri - thank you all for taking the time to evaluate this work.
... my two external referees Dimitri Gadotti and Stéphane Courteau. Your comments and suggestions significantly improved this work and probably also my future works. Thank you for taking the time to read and check this thesis in depth; and also for your help and advice outside this work!
... Katey and Rhea for a great time during the winter school, continued with a true friendship
... Kartik for your advice and (occasional) mentoring - luckily I did not need it too much, but it was so good to know of your support!
... Witold for intriguing scientific dialogue as well as motivation
... my fellow seminar committee members: Cris, Victor, Mar and Matteo - it was a pleasure and honour to work with all of you!
... Martin and Marcos - so much- for their help with the Journal Club! It was not easy to start it and especially maintaining it. Your help has been vital! Keep up the fantastic work! Also thanks to the IAC for supporting this initiative via provisions as well as for the CONVIVE award.
... the Roque de los Muchachos Observatory on La Palma and the different operators of the William Herschel Telescope during our numerous runs observing the BaLROG sample, as well as observing support by Agnieszka Rys, Carolin Wittman and Thorsten Lisker. This research is based on observations obtained at the William Herschel Telescope, operated by the Isaac Newton Group in the Spanish Observatorio del Roque de los Muchachos of the Instituto de Astrof´sica de Canarias. We also used SDSS g-band images for calibration and mosaicking. Funding for the SDSS and SDSS-II has been provided by the Alfred P. Sloan Foundation and the Participating Institutions. This research made use of Montage, funded by the National Aeronautics and Space Administrations Earth Science Technology Office, Computational Technnologies Project, under Cooperative Agreement Number NCC5-626 between NASA and the California Institute of Technology.
... the Starmus-group and Garik for getting us involved in all the craziness and unique experience
... my former physics professors, especially Betti Hartmann, for all her encouragement and support
... my former supervisor Hans Deeg who also motivated me to return to Tenerife and who continuously asked if things were going well
... my future 'supervisor' Barry Madore who kept encouraging me from the start and whose support, motivation and ideas are invaluable - thank you for being a continuous source of inspiration!
... the non-scientific staff a the IAC: Lourdes, Eva, Tanja and Judith - you

have helped me so many times; the seguritas, gracias por tolerar mis horarios de trabajo fuera de horarios (tantas veces)

The chance of doing your PhD on Tenerife extends to more than just an outstanding research institute and observatories. I was extremely lucky to have met already very early on some of the most wonderful people in this Universe who have supported me so much during the last four years here and who I hope will remain one of my best friends. I wish to thank:
... Ita. Since I met you as one of the first people here on Tenerife I can't stop admiring your generosity, readiness to help and just your entire outstanding character. Thank you for some of the best times!
... Carmen for your incredible creativity, reliability and help in particular also with the astrophotos
... José Ángel for countless initiatives, help in so many ways (e.g., astrophotography) - and I will never look at a piña the same way as before knowing you
... Yaiza for the achuchar-sesiones and your incredible music
... Gabri for sharing so much the same feelings when being far away
- son un grupo de amigos increíbles y tengo tanta suerte de haberles conocido! Gracias, tanto! También a José Juan for being Gregorio at times, a Juanjo and Maria José!
... Lisa, my English/Spanish sister and peligro partner, for being up for truly anything, for many long conversations at the right times (and wrong times, i.e. when kayaking and almost being rescued) and for spreading this wonderful energy which always gets me out of the deepest tunnel. Thanks a billion!
... Moneyba, la otra loca quien nunca para de sonreír y hacerme sonreír también! Gracias por todas las locuras!
... Davi for competing together and for your spontaneity, locura, energy and constant friendship
... Silvana for making me feel at home so much, especially when painting Easter eggs or hunting them with my cousin
... Airam for climbing, acroyoga, running, swimming, taking care of me when I was sick (and when I wasn't), for making chocolate fondues on hikes and for simply being an outstanding person and friend
... David for spontaneous hikes, showing me some of the most beautiful parts of this island as well as best fruits y por rescatarme en La Laguna
... mi piso! Maño, Chipi, Judith, Tini y Rosie - fue un piso mágico para mi! Y luego con todos que vivieron aquí, Olli -tb por enseñarme el baile más divertido que he conocido hasta ahora, Marcel por ayudar en todo y siempre, Isa, Katja, Rebecca, Hans, Andrea y Luis - gracias por la coviviencia inolvidable.

... the paragliding community - in particular club norte, club termikas and equipo enminube - por el superbuen rollo siempre!
... Borja - for introducing me to hike&fly y transmitir esa magia volando juntos
... Yeray - por tu capacidad de hacerme incapaz de no reír - fue un regalo de la vida de conocerte y empezar volar contigo, gracias por las mil locuras, volando y en tierra
... David - por enseñarme con calma y ser un amigo superfiable no solo volando
... Jean-Marc - pour être le mieux frère du monde
... Basti - for inspiring me to take things lightly (most of the time;))

... Guaykie (Teguayco) for spontaneous flights wherever possible

... the climbing community - for taking care of my mental health
... Juany - for teaching me true Canarian: 'soga, baby!' and Zen-moments
... Clarisse for getting me started and being a true inspiration concerning outdoor sports
... Pablo for la locura de las animas, juntos con Moi y Moneyba, otros multipitches, bailes en el kayak y mucho más
... Alex for climbing but most of all running (and falling - and laughing - so much) in the mud after the storms in Anaga
... Roberto for taking me the first time to Ijuana
... Lisa and Carlos and their crazy Fundación en Pié for showing that we are indeed locos por la vida!

Apart from sports, I found balance in playing music with many wonderful people. Thanks to:
... El Otro for the jam sessions during my first 2 years
... Samu, Saúl, Sophia, Maño, Yaiza and more for the Crepe-jam sessions on Sundays.
... all the bands that invited me to play with them, Contratiempos, Up to 11, Freddy Matos and band, Swingvergüenzas and more.
... Alex (Sama) for the duets and for becoming an extraordinary friend - thank you so much for showing me how to live freely and always ready to help others - you are a true inspiration!
... Fede, for music, sports, talks and being one of the most positive people that I met
... to our Sandanski-group: Abo for making it all possible, Tayri for being the best roommate and redacting the funniest tutoriales, Miri for taking care of us always and driving the hotel people nuts with figs, Pablo for imitating accents and making me laugh so much that I couldn't stop, Javi for teaching us the best of all noises (plop) and Matias for transmitting this infinite joy of playing music as well as for reviewing some of my Spanish translations (and inspiring me to improve my accent ;))
... Adri, Omar, Matt, Guillo, Jacek, sin belda blues con belda ;) and more for the jam sessions at home or away
... Alba and Yanara for the anachronical plektron
... Taylan for sharing the magic of la música en la naturaleza
...and so many more. Music and especially the musicians that I met here and could play and perform with have truly helped me to find balance in my life and disconnect from the sometimes endless seeming frustrations facing my research. Without all of you, I would not have made it.

My non-Tenerifian friends have also kept me sane from the distance (or by coming to visit :)) Thank you so much:
... Kira for being my longest and be**i**stest friend, for pulling off crazy ideas, making me step outside the box with you and showing me how tough one can truly be
... Rosie for being a continuous inspiration on going your own way and being a wonderful mum - I wish I could have visited you and Sol so much more often!
... the whole Waltrop family: Muddi, Vaddi, Dave, Moritz, Lars, Jan und Lea,

Alex, Phite, Justus - auch wenn wir uns so selten sehen ist es unglaublich, wenn wir mal wieder beisammen sind! Danke für das 'Zu-Hause-Gefühl', wenn ich daheim bin!
... and my Waltrop girls: Mara und Lena - auch für's Besuchen kommen, Laura, Tine, Kirsten und Kathrin
... my Jacobs family: Franzi for being a constant inspiration on generosity, reliability and changing this world for the better, Sami for her unbelievable energy and ability to make everyone laugh around her, Anika for sharing the outdoor passion and Viki for sharing the battle of a PhD abroad
... Andra for inspiring me to reach furhter in science and go for it with all your passion
... the IniCha family, Ed, Nastya, Lukas, George, Juan, Rebecca, Joana, Cristian, Ben, Kathleen, Magali and Kyle - for being this bunch of unconventional, crazy individuals trying to make this world a better place
... Ahmed for always calling once in a while reminding me of the real troubles in life - I admire your strength!
... Steffen for your help in so many ways, before and after 2012 ;)
... Dominique for quick catch-ups which are yet so meaningful
... Taylor for having shown me that everything is possible - especially if there is enough food around ;)
... Konstantin for inspiring me to see the beauty in every moment - and if not, there is always honey :)

Last but not least, I wish to thank my parents. Danke für all die Unterstützung, Geduld und vor allem Liebe, Vertrauen und Verlässlichkeit, die ihr mir in all meinen Lebensjahren gegeben habt und ohne die ich niemals der Mensch geworden wäre, der ich jetzt bin. Ohne euch hätte ich diese Dissertation und vieles, vieles mehr nicht geschafft und wahrscheinlich gar nicht erst begonnen. Ihr habt mir so viel Kraft gegeben - und tut dies immer noch, sodass ich manchmal gar nicht weiß, wohin damit :) Danke, DANKE aus tiefstem Herzen. Ich bin so unglaublich glücklich euch als meine Familie (mit Mocki, klar ;)) zu haben.

Et finalement, como que no, merci à Charlie. Merci pour les temps joyeux et les temps difficiles, tant de temps à distance - tous nous a fait croître (j'espère ;)). Merci pour me critiquer, pour me faire reconsidérer mes points de vues quand j'étais trop bornée et merci pour m'appuyer pendant les crises, merci pour ta tendresse et ta maniére de me surprendre et surtout merci pour rêver ensemble! Et pour partager les folies! - pour être la seule personne avec qui je peux marcher toute la nuit sur des glaciers pour retourner prendre un verre et aller nager dans l'océan à moins 30 degrés dehors, qui me fais sauter des cascades et conquérir la peur, qui m'apprend á conduire un moto dans le bled en Afrique - sous la pluie -, avec qui je peux jouer la sérénade et qui organise le saxo pour le faire,... et avec qui je me sens 'at home' partout dans le monde. Quoi qu'il arrive, ces dernières années étaient tellement magiques aussi grâce à toi. Merci mille, mille fois!

Marja K. Seidel
La Laguna, August 2015

Bibliography

Abazajian K. N. et al., 2009, ApJS, 182, 543

Abraham R. G., Merrifield M. R., Ellis R. S., Tanvir N. R., Brinchmann J., 1999, MNRAS, 308, 569

Abraham R. G., van den Bergh S., Glazebrook K., Ellis R. S., Santiago B. X., Surma P., Griffiths R. E., 1996, ApJS, 107, 1

Aguerri J. A. L., Beckman J. E., Prieto M., 1998, AJ, 116, 2136

Aguerri J. A. L., Debattista V. P., Corsini E. M., 2003, MNRAS, 338, 465

Aguerri J. A. L., Elias-Rosa N., Corsini E. M., Muñoz-Tuñón C., 2005, A&A, 434, 109

Aguerri J. A. L., González-García A. C., 2009, A&A, 494, 891

Aguerri J. A. L., Hunter J. H., Prieto M., Varela A. M., Gottesman S. T., Muñoz-Tuñón C., 2001, A&A, 373, 786

Aguerri J. A. L., Méndez-Abreu J., Corsini E. M., 2009, Astronomy and Astrophysics, 495, 491

Aguerri J. A. L. et al., 2015, A&A, 576, A102

Aguerri J. A. L., Muñoz-Tuñón C., Varela A. M., Prieto M., 2000, A&A, 361, 841

Allard E. L., Knapen J. H., Peletier R. F., Sarzi M., 2006, MNRAS, 371, 1087

Andredakis Y. C., Sanders R. H., 1994, MNRAS, 267, 283

Athanassoula E., 2002, ApJ, 569, L83

—, 2003, MNRAS, 341, 1179

—, 2005, MNRAS, 358, 1477

—, 2013, Bars and secular evolution in disk galaxies: Theoretical input, Falcón-Barroso J., Knapen J. H., eds., Cambridge University Press, p. 305

Athanassoula E., Bosma A., Creze M., Schwarz M. P., 1984, A&A, 131, 175

Athanassoula E., Machado R. E. G., Rodionov S. A., 2013, MNRAS, 429, 1949

Athanassoula E., Misiriotis A., 2002, MNRAS, 330, 35

Athanassoula E., Morin S., Wozniak H., Puy D., Pierce M. J., Lombard J., Bosma A., 1990, MNRAS, 245, 130

Athanassoula E., Sellwood J. A., 1986, MNRAS, 221, 213

Babcock H. W., 1938, PASP, 50, 174

Babusiaux C. et al., 2010, A&A, 519, A77

Bacon R. et al., 1995, A&AS, 113, 347

—, 2001, MNRAS, 326, 23

Ballay U., 1990, The Astronomical Manuscripts of Nasir al-Din Tusi. Brill Publishers

Barazza F. D. et al., 2009, A&A, 497, 713

Barazza F. D., Jogee S., Marinova I., 2008, ApJ, 675, 1194

Bardeen J. M., 1975, in IAU Symposium, Vol. 69, Dynamics of the Solar Systems, Hayli A., ed., p. 297

Bardeen J. M., Bond J. R., Kaiser N., Szalay A. S., 1986, ApJ, 304, 15

Barnes J. E., Hernquist L., 1992, ARA&A, 30, 705

Barrera-Ballesteros J. K. et al., 2014, A&A, 568, A70

Barro G. et al., 2013, ApJ, 765, 104

Barway S., Wadadekar Y., Kembhavi A. K., 2011, MNRAS, 410, L18

Bell E. F., de Jong R. S., 2000, MNRAS, 312, 497

Bender R., Saglia R. P., Gerhard O. E., 1994, MNRAS, 269, 785

Bensby T. et al., 2013, A&A, 549, A147

Berendzen R., Hart R., Seeley D., 1976, Man discovers the galaxies. Science History Publications

Bertola F., Capaccioli M., 1977, ApJ, 211, 697

Binney J., Kormendy J., White S. D. M., eds., 1982, Morphology an dynamics of galaxies. Swiss Society of Astronomy and Astrophysics (SSAA)

Binney J., Tremaine S., 1987, Galactic dynamics. Princeton University Press, 1998

Binney, J. Merrifield M., 1999, Book Review: Galactic astronomy, Vol. 109. Princeton U Press, 1998, p. 46

Blitz L., Spergel D. N., 1991, ApJ, 379, 631

Block D. L., Buta R., Knapen J. H., Elmegreen D. M., Elmegreen B. G., Puerari I., 2004, AJ, 128, 183

Blumenthal G. R., Faber S. M., Primack J. R., Rees M. J., 1984, Nature, 311, 517

Böker T., Falcón-Barroso J., Schinnerer E., Knapen J. H., Ryder S., 2008, AJ, 135, 479

Bonatto C., Bica E., Alloin D., 1989, A&A, 226, 23

Bournaud F., 2015, ArXiv e-prints

Bournaud F., Combes F., Semelin B., 2005, MNRAS, 364, L18

Bournaud F., Elmegreen B. G., Elmegreen D. M., 2007, ApJ, 670, 237

Bournaud F., Jog C. J., Combes F., 2005, A&A, 437, 69

Bower R. G., Ellis R. S., Rose J. A., Sharples R. M., 1990, AJ, 99, 530

Bracher K., 1994, Mercury, 23, 7

Brunetti M., Chiappini C., Pfenniger D., 2011, A&A, 534, A75

Bureau M., Athanassoula E., 1999, ApJ, 522, 686

—, 2005, ApJ, 626, 159

Bureau M., Athanassoula E., Chung A., Aronica G., 2004, in Astrophysics and Space Science Library, Vol. 319, Penetrating Bars Through Masks of Cosmic Dust, Block D. L., Puerari I., Freeman K. C., Groess R., Block E. K., eds., p. 139

Bureau M., Freeman K. C., 1999, AJ, 118, 126

Buta R., Block D. L., 2001, ApJ, 550, 243

Buta R., Block D. L., Knapen J. H., 2003, AJ, 126, 1148

Buta R., Combes F., 1996, Fundamentals of Cosmic Physics, 17, 95

Buta R., Crocker D. A., 1993, AJ, 105, 1344

Buta R., Crocker D. A., Byrd G. G., 1999, AJ, 118, 2071

Buta R., Laurikainen E., Salo H., Knapen J. H., 2010, ApJ, 721, 259

Buta R., Purcell G. B., 1998, AJ, 115, 484

Buta R., Purcell G. B., Crocker D. A., 1995, AJ, 110, 1588

Buta R., van Driel W., Braine J., Combes F., Wakamatsu K., Sofue Y., Tomita A., 1995, ApJ, 450, 593

Buta R., Vasylyev S., Salo H., Laurikainen E., 2005, AJ, 130, 506

Buta R. J., 2013a, Galaxy Morphology, Falcón-Barroso J., Knapen J. H., eds., Cambridge University Press, p. 155

—, 2013b, Galaxy Morphology, Oswalt T. D., Keel W. C., eds., xx, p. 1

Buta R. J. et al., 2015, ApJS, 217, 32

Butcher H., Oemler, Jr. A., 1978, ApJ, 219, 18

Byrd G., Rautiainen P., Salo H., Buta R., Crocher D. A., 1994, AJ, 108, 476

Cacho R., Sánchez-Blázquez P., Gorgas J., Pérez I., 2014, MNRAS, 442, 2496

Caon N., Capaccioli M., D'Onofrio M., 1993, MNRAS, 265, 1013

Cappellari M., Copin Y., 2003, MNRAS, 342, 345

Cappellari M., Emsellem E., 2004, The Publications of the Astronomical Society of the Pacific, 116, 138

Cappellari M. et al., 2007, MNRAS, 379, 418

—, 2011a, MNRAS, 413, 813

—, 2011b, MNRAS, 416, 1680

Cardiel N., Gorgas J., Sánchez-Blázquez P., Cenarro A. J., Pedraz S., Bruzual G., Klement J., 2003, A&A, 409, 511

Carlberg R. G., 1984a, ApJ, 286, 403

—, 1984b, ApJ, 286, 416

Cenarro A. J., Cardiel N., Gorgas J., Peletier R. F., Vazdekis A., Prada F., 2001a, MNRAS, 326, 959

Cenarro A. J., Gorgas J., Cardiel N., Pedraz S., Peletier R. F., Vazdekis A., 2001b, MNRAS, 326, 981

Cepa J., Beckman J. E., 1990, ApJ, 349, 497

Cervantes J. L., Vazdekis A., 2009, MNRAS, 392, 691

Chapelon S., Contini T., Davoust E., 1999, A&A, 345, 81

Cheung E. et al., 2015a, ApJ, 807, 36

—, 2015b, MNRAS, 447, 506

Chiappini C., Matteucci F., Romano D., 2001, ApJ, 554, 1044

Childress M. J., Vogt F. P. A., Nielsen J., Sharp R. G., 2014, Ap&SS, 349, 617

Christodoulou D. M., Shlosman I., Tohline J. E., 1995, ApJ, 443, 551

Chung A., Bureau M., 2004, AJ, 127, 3192

Cid Fernandes R., Mateus A., Sodré L., Stasińska G., Gomes J. M., 2005, MNRAS, 358, 363

Cisternas M., Sheth K., Salvato M., Knapen J. H., Civano F., Santini P., 2014, ArXiv e-prints

Clarkson W. et al., 2008, ApJ, 684, 1110

Claussen M. J., Sahai R., 1992, AJ, 103, 1134

Coccato L., Morelli L., Corsini E. M., Buson L., Pizzella A., Vergani D., Bertola F., 2011, MNRAS, 412, L113

Coccato L., Morelli L., Pizzella A., Corsini E. M., Buson L. M., Dalla Bontà E., 2013, A&A, 549, A3

Coelho P., Gadotti D. A., 2011, ApJ, 743, L13

Cole S., 1991, ApJ, 367, 45

Combes F., Debbasch F., Friedli D., Pfenniger D., 1990, A&A, 233, 82

Combes F., Elmegreen B. G., 1993, A&A, 271, 391

Combes F., Sanders R. H., 1981, A&A, 96, 164

Comerón S., Knapen J. H., Beckman J. E., 2008, A&A, 485, 695

Comerón S., Knapen J. H., Beckman J. E., Laurikainen E., Salo H., Martínez-Valpuesta I., Buta R. J., 2010, MNRAS, 402, 2462

Conselice C. J., Bershady M. A., Dickinson M., Papovich C., 2003, The Astronomical Journal, 126, 1183

Contopoulos G., Grosbol P., 1989, A&A Rev., 1, 261

Contopoulos G., Papayannopoulos T., 1980, A&A, 92, 33

Corsini E. M., 2011, Memorie della Societa Astronomica Italiana Supplementi, 18, 23

Couch W. J., Ellis R. S., Sharples R. M., Smail I., 1994, ApJ, 430, 121

Courteau S., Andersen D. R., Bershady M. A., MacArthur L. A., Rix H.-W., 2003, ApJ, 594, 208

Courteau S. et al., 2014, Reviews of Modern Physics, 86, 47

Courteau S., Faber S. M., Dressler A., Willick J. A., 1993, ApJ, 412, L51

Courtes G., 1982, in Astrophysics and Space Science Library, Vol. 92, IAU Colloq. 67: Instrumentation for Astronomy with Large Optical Telescopes, Humphries C. M., ed., p. 123

Crocker D. A., Baugus P. D., Buta R., 1996, ApJS, 105, 353

Daddi E. et al., 2010, ApJ, 713, 686

Davies R. L. et al., 2001, ApJ, 548, L33

Davies R. L., Sadler E. M., Peletier R. F., 1993, MNRAS, 262, 650

Davis M., Efstathiou G., Frenk C. S., White S. D. M., 1985, ApJ, 292, 371

de Grijs R., 1998, MNRAS, 299, 595

de Jong R. S., 1996, A&AS, 118, 557

de Lorenzi F., Debattista V. P., Gerhard O., Sambhus N., 2007, MNRAS, 376, 71

de Lorenzo-Cáceres A., Falcón-Barroso J., Vazdekis A., 2013, MNRAS, 431, 2397

De Lucia G., Springel V., White S. D. M., Croton D., Kauffmann G., 2006, MNRAS, 366, 499

de Souza R. E., Gadotti D. A., dos Anjos S., 2004, ApJS, 153, 411

de Vaucouleurs G., 1948, Annales d'Astrophysique, 11, 247

—, 1959, Handbuch der Physik, 53, 275

—, 1964, in IAU Symposium, Vol. 20, The Galaxy and the Magellanic Clouds, Kerr F. J., ed., p. 269

—, 1974, in IAU Symposium, Vol. 58, The Formation and Dynamics of Galaxies, Shakeshaft J. R., ed., pp. 1–52

de Vaucouleurs G., de Vaucouleurs A., Corwin H. G., Buta R. J., Paturel G., Fouque P., 1995, VizieR Online Data Catalog, 7155, 0

de Zeeuw P. T. et al., 2002, MNRAS, 329, 513

Debattista V. P., Carollo C. M., Mayer L., Moore B., 2005, ApJ, 628, 678

Debattista V. P., Corsini E. M., Aguerri J. A. L., 2002, MNRAS, 332, 65

Debattista V. P., Sellwood J. A., 2000, ApJ, 543, 704

Debattista V. P., Williams T. B., 2001, in Astronomical Society of the Pacific Conference Series, Vol. 230, Galaxy Disks and Disk Galaxies, Funes J. G., Corsini E. M., eds., pp. 553–554

Di Matteo P. et al., 2015, A&A, 577, A1

Di Matteo P., Haywood M., Combes F., Semelin B., Snaith O. N., 2013, A&A, 553, A102

Di Matteo P. et al., 2014, A&A, 567, A122

Dopita M., Hart J., McGregor P., Oates P., Bloxham G., Jones D., 2007, Ap&SS, 310, 255

Dopita M. et al., 2010, Ap&SS, 327, 245

Dressler A., Oemler, Jr. A., Butcher H. R., Gunn J. E., 1994, ApJ, 430, 107

Dressler A. et al., 1997, ApJ, 490, 577

Durret F., Bergeron J., 1988, A&AS, 75, 273

Earn D. J. D., Lynden-Bell D., 1996, MNRAS, 278, 395

Efstathiou G., Lake G., Negroponte J., 1982, MNRAS, 199, 1069

Eggen O. J., Lynden-Bell D., Sandage A. R., 1962, ApJ, 136, 748

Eliche-Moral M. C., González-García A. C., Balcells M., Aguerri J. A. L., Gallego J., Zamorano J., Prieto M., 2011, A&A, 533, A104

Ellison S. L., Nair P., Patton D. R., Scudder J. M., Mendel J. T., Simard L., 2011, MNRAS, 416, 2182

Elmegreen B. G., 1994, ApJ, 425, L73

Elmegreen B. G., Elmegreen D. M., 1985, ApJ, 288, 438

—, 1989, ApJ, 342, 677

Elmegreen B. G., Elmegreen D. M., Fernandez M. X., Lemonias J. J., 2009, ApJ, 692, 12

Elmegreen B. G., Elmegreen D. M., Hirst A. C., 2004, ApJ, 612, 191

Elmegreen D. M., Chromey F. R., Santos M., Marshall D., 1997, AJ, 114, 1850

Elmegreen D. M., Elmegreen B. G., Ferguson T. E., 2005, ApJ, 623, L71

Elmegreen D. M., Elmegreen B. G., Ravindranath S., Coe D. A., 2007, ApJ, 658, 763

Emsellem E. et al., 2011, MNRAS, 414, 888

—, 2007, MNRAS, 379, 401

Emsellem E., Fathi K., Wozniak H., Ferruit P., Mundell C. G., Schinnerer E., 2006, MNRAS, 365, 367

England M. N., Gottesman S. T., Hunter, Jr. J. H., 1990, ApJ, 348, 456

Erwin P., 2004, A&A, 415, 941

—, 2005, MNRAS, 364, 283

Erwin P., Sparke L. S., 2002, AJ, 124, 65

Erwin P., Vega Beltrán J. C., Beckman J. E., 2001, in Astronomical Society of the Pacific Conference Series, Vol. 249, The Central Kiloparsec of Starbursts and AGN: The La Palma Connection, Knapen J. H., Beckman J. E., Shlosman I., Mahoney T. J., eds., p. 171

Eskridge P. B. et al., 2000, AJ, 119, 536

Faber S. M., 1973, ApJ, 179, 731

Falcón-Barroso J., 2015, ArXiv e-prints

Falcón-Barroso J. et al., 2006, MNRAS, 369, 529

Falcón-Barroso J., Lyubenova M., van de Ven G., the CALIFA collaboration, 2014, ArXiv e-prints

Falcón-Barroso J., Sánchez-Blázquez P., Vazdekis A., Ricciardelli E., Cardiel N., Cenarro A. J., Gorgas J., Peletier R. F., 2011, Astronomy and Astrophysics, 532, A95

Fathi K., Beckman J. E., Piñol-Ferrer N., Hernandez O., Martínez-Valpuesta I., Carignan C., 2009, ApJ, 704, 1657

Fathi K., Peletier R. F., 2003, A&A, 407, 61

Feigelson E., 2012, Classification in Astronomy: Past and Present, Way M. J., Scargle J. D., Ali K. M., Srivastava A. N., eds., Taylor & Francis Group, pp. 3–10

Feinstein C., Mendez M., Vega I., Forte J. C., 1990, A&A, 239, 90

Finkelstein S. L. et al., 2013, Nature, 502, 524

Fisher D. B., Drory N., 2008, AJ, 136, 773

—, 2010, ApJ, 716, 942

—, 2011, ApJ, 733, L47

Florido E., Zurita A., Perez I., Perez-Montero E., Coelho P. R. T., Gadotti D. A., 2015, ArXiv e-prints

Forbes D. A., Kotilainen J. K., Moorwood A. F. M., 1994, ApJ, 433, L13

Forbes D. A., Norris R. P., Williger G. M., Smith R. C., 1994, AJ, 107, 984

Förster Schreiber N. M. et al., 2011, ApJ, 739, 45

Foyle K., Courteau S., Thacker R. J., 2008, MNRAS, 386, 1821

Fragkoudi F., Athanassoula E., Bosma A., Iannuzzi F., 2015, MNRAS, 450, 229

Frebel A., Simon J. D., Geha M., Willman B., 2010, ApJ, 708, 560

Freeman K. C., 1966, MNRAS, 133, 47

—, 1970a, in IAU Symposium, Vol. 38, The Spiral Structure of our Galaxy, Becker W., Kontopoulos G. I., eds., p. 351

—, 1970b, ApJ, 160, 811

Frenk C. S., White S. D. M., Davis M., Efstathiou G., 1988, ApJ, 327, 507

Friedli D., 1998, in Astronomical Society of the Pacific Conference Series, Vol. 147, Abundance Profiles: Diagnostic Tools for Galaxy History, Friedli D., Edmunds M., Robert C., Drissen L., eds., p. 287

Friedli D., Benz W., 1993, A&A, 268, 65

—, 1995, A&A, 301, 649

Friedli D., Benz W., Kennicutt R., 1994, ApJ, 430, L105

Fu J., Hou J. L., Yin J., Chang R. X., 2009, ApJ, 696, 668

Fukuda H., Habe A., Wada K., 2000, ApJ, 529, 109

Gadotti D. A., 2008, MNRAS, 384, 420

—, 2011, MNRAS, 415, 3308

Gadotti D. A., de Souza R. E., 2003, ApJ, 583, L75

—, 2006, ApJS, 163, 270

Gadotti D. A., dos Anjos S., 2001, AJ, 122, 1298

Gadotti D. A., Sánchez-Janssen R., 2012, MNRAS, 423, 877

Ganda K., Falcón-Barroso J., Peletier R. F., Cappellari M., Emsellem E., McDermid R. M., de Zeeuw P. T., Carollo C. M., 2006, MNRAS, 367, 46

Ganda K. et al., 2007, MNRAS, 380, 506

Genel S. et al., 2014, MNRAS, 445, 175

Genzel R. et al., 2008, ApJ, 687, 59

—, 2011, ApJ, 733, 101

Gerhard O., 2002, in Astronomical Society of the Pacific Conference Series, Vol. 273, The Dynamics, Structure and History of Galaxies: A Workshop in Honour of Professor Ken Freeman, Da Costa G. S., Sadler E. M., Jerjen H., eds., p. 73

Gerhard O. E., 1993, MNRAS, 265, 213

Gerssen J., 2000, Stellar kinematics in disk galaxies. Proefschrift, Rijksuniversiteit Groningen

Gerssen J., Kuijken K., Merrifield M. R., 1999, MNRAS, 306, 926

—, 2003, MNRAS, 345, 261

Gibson B. K., Pilkington K., Brook C. B., Stinson G. S., Bailin J., 2013, A&A, 554, A47

Glyn Jones K., 1968, Journal of the British Astronomical Association, 78, 256

Goldreich P., Tremaine S., 1979, ApJ, 233, 857

Goz D., Monaco P., Murante G., Curir A., 2015, MNRAS, 447, 1774

Graham A., 2015a, Highlights of Astronomy, 16, 360

Graham A. W., 2012, ApJ, 746, 113

—, 2015b, ArXiv e-prints

Guzman R., Lucey J. R., Carter D., Terlevich R. J., 1992, MNRAS, 257, 187

Hafez I., 2010, PhD thesis, James Cook University

Hameed S., Devereux N., 1999, AJ, 118, 730

Haywood M., 2008, MNRAS, 388, 1175

Heller C. H., Shlosman I., 1994, ApJ, 424, 84

Hernandez O., Wozniak H., Carignan C., Amram P., Chemin L., Daigle O., 2005, ApJ, 632, 253

Hernquist L., 1990, ApJ, 356, 359

—, 1992, ApJ, 400, 460

Hetherington N. S., 1970, Leaflet of the Astronomical Society of the Pacific, 10, 313

Ho L. C., Filippenko A. V., Sargent W. L. W., 1997, ApJ, 487, 591

Ho L. C., Li Z.-Y., Barth A. J., Seigar M. S., Peng C. Y., 2011, ApJS, 197, 21

Hohl F., 1975, in IAU Symposium, Vol. 69, Dynamics of the Solar Systems, Hayli A., ed., p. 349

Holmberg E., 1958, Meddelanden fran Lunds Astronomiska Observatorium Serie II, 136, 1

Hopkins P. F. et al., 2010, ApJ, 715, 202

Hopkins P. F., Hernquist L., Cox T. J., Kereš D., 2008, ApJS, 175, 356

Hopkins P. F. et al., 2009, MNRAS, 397, 802

Howard C. D. et al., 2009, ApJ, 702, L153

Hoyle B. et al., 2011, MNRAS, 415, 3627

Hubble E. P., 1926, ApJ, 64, 321

—, 1927, The Observatory, 50, 276

—, 1929, ApJ, 69, 103

—, 1936, Realm of the Nebulae. New Haven: Yale University Press

Jablonka P., Gorgas J., Goudfrooij P., 2007, A&A, 474, 763

Jogee S. et al., 2004, ApJ, 615, L105

Johnson C. I., Rich R. M., Fulbright J. P., Valenti E., McWilliam A., 2011, ApJ, 732, 108

Johnson H. M., 1957, AJ, 62, 19

Johnston E. J., Merrifield M. R., Aragón-Salamanca A., Cappellari M., 2013, MNRAS, 428, 1296

Julian W. H., Toomre A., 1966, ApJ, 146, 810

Jungwiert B., Combes F., Axon D. J., 1997, A&AS, 125, 479

Kauffmann G., 1996, MNRAS, 281, 487

Kauffmann G., Charlot S., 1998, MNRAS, 294, 705

Kauffmann G., White S. D. M., 1993, MNRAS, 261, 921

Kauffmann G., White S. D. M., Guiderdoni B., 1993, MNRAS, 264, 201

Kewley L. J., Dopita M. A., Sutherland R. S., Heisler C. A., Trevena J., 2001, ApJ, 556, 121

Kim T. et al., 2014, ApJ, 782, 64

Kim W.-T., Seo W.-Y., Stone J. M., Yoon D., Teuben P. J., 2012, ApJ, 747, 60

Kim W.-T., Stone J. M., 2012, ApJ, 751, 124

Knapen J. H., 2005, A&A, 429, 141

Knapen J. H., Beckman J. E., Heller C. H., Shlosman I., de Jong R. S., 1995, ApJ, 454, 623

Knapen J. H., Mazzuca L. M., Böker T., Shlosman I., Colina L., Combes F., Axon D. J., 2006, A&A, 448, 489

Knapen J. H., Sharp R. G., Ryder S. D., Falcón-Barroso J., Fathi K., Gutiérrez L., 2010, MNRAS, 408, 797

Knapen J. H., Shlosman I., Peletier R. F., 2000, ApJ, 529, 93

Koleva M., Prugniel P., Bouchard A., Wu Y., 2009, A&A, 501, 1269

Koleva M., Prugniel P., de Rijcke S., Zeilinger W. W., 2011, MNRAS, 417, 1643

Koleva M., Prugniel P., Ocvirk P., Le Borgne D., Soubiran C., 2008, MNRAS, 385, 1998

Kormendy J., 1979, ApJ, 227, 714

—, 1982a, ed. L. Martinet & M. Mayor, Geneva Obs., Sauverny, 113

—, 1982b, in Saas-Fee Advanced Course 12: Morphology and Dynamics of Galaxies, Martinet L., Mayor M., eds., pp. 113–288

—, 1984, ApJ, 287, 577

—, 2015, ArXiv e-prints

Kormendy J., Bender R., 1996, ApJ, 464, L119

—, 2012, ApJS, 198, 2

Kormendy J., Fisher D. B., Cornell M. E., Bender R., 2009, ApJS, 182, 216

Kormendy J., Illingworth G., 1982, ApJ, 256, 460

Kormendy J., Kennicutt, Jr. R. C., 2004, Annual Review of Astronomy & Astrophysics, 42, 603

Kormendy J., Norman C. A., 1979, ApJ, 233, 539

Krajnović D. et al., 2008, MNRAS, 390, 93

—, 2011, MNRAS, 414, 2923

Kraljic K., Bournaud F., Martig M., 2012, ApJ, 757, 60

Kroupa P., 2001, MNRAS, 322, 231

Kubryk M., Prantzos N., Athanassoula E., 2013, MNRAS, 436, 1479

—, 2014, ArXiv e-prints

Kuijken K., Merrifield M. R., 1995, ApJ, 443, L13

Kuntschner H., 2000, MNRAS, 315, 184

Kuntschner H. et al., 2006, MNRAS, 369, 497

—, 2010, MNRAS, 408, 97

Lacey C., Cole S., 1993, MNRAS, 262, 627

Laine S., Heller C. H., 1999, MNRAS, 308, 557

Laine S., Shlosman I., Knapen J. H., Peletier R. F., 2002, ApJ, 567, 97

Larson R. B., 1974, MNRAS, 166, 585

Larson R. B., Tinsley B. M., 1974, ApJ, 192, 293

Laurikainen E., Salo H., 2002, MNRAS, 337, 1118

Laurikainen E., Salo H., Athanassoula E., Bosma A., Buta R., Janz J., 2013, MNRAS, 430, 3489

Laurikainen E., Salo H., Buta R., 2005, MNRAS, 362, 1319

Laurikainen E., Salo H., Buta R., Knapen J., Speltincx T., Block D., 2006, AJ, 132, 2634

Laurikainen E., Salo H., Buta R., Knapen J. H., 2007, MNRAS, 381, 401

—, 2009, ApJ, 692, L34

—, 2011, MNRAS, 418, 1452

Laurikainen E., Salo H., Buta R., Vasylyev S., 2004, MNRAS, 355, 1251

Le Borgne D., Rocca-Volmerange B., Prugniel P., Lançon A., Fioc M., Soubiran C., 2004, A&A, 425, 881

Le Borgne J.-F. et al., 2003, A&A, 402, 433

Li Z.-Y., Ho L. C., Barth A. J., Peng C. Y., 2011, ApJS, 197, 22

Lindblad P. A. B., Lindblad P. O., Athanassoula E., 1996, A&A, 313, 65

Lisker T., Debattista V. P., Ferreras I., Erwin P., 2006, MNRAS, 370, 477

Lisker T., Grebel E. K., Binggeli B., 2006, AJ, 132, 497

Łokas E. L., Athanassoula E., Debattista V. P., Valluri M., Pino A. d., Semczuk M., Gajda G., Kowalczyk K., 2014, MNRAS, 445, 1339

MacArthur L. A., Courteau S., Bell E., Holtzman J. A., 2004, ApJS, 152, 175

MacArthur L. A., González J. J., Courteau S., 2009, MNRAS, 395, 28

Maciejewski W., Emsellem E., Krajnović D., 2012, MNRAS, 427, 3427

Madau P., Dickinson M., 2014, ARA&A, 52, 415

Madau P., Ferguson H. C., Dickinson M. E., Giavalisco M., Steidel C. C., Fruchter A., 1996, MNRAS, 283, 1388

Madau P., Pozzetti L., Dickinson M., 1998, ApJ, 498, 106

Maraston C., Strömbäck G., 2011, MNRAS, 418, 2785

Marinova I., Jogee S., 2007, ApJ, 659, 1176

Marinova I. et al., 2012, ApJ, 746, 136

Márquez I. et al., 1999, A&AS, 140, 1

Martel H., Kawata D., Ellison S. L., 2013, MNRAS, 431, 2560

Martig M., Bournaud F., Croton D. J., Dekel A., Teyssier R., 2012, ApJ, 756, 26

Martin P., 1995, AJ, 109, 2428

Martin P., Roy J.-R., 1994, ApJ, 424, 599

—, 1995, ApJ, 445, 161

Martinet L., Friedli D., 1997, A&A, 323, 363

Martinez-Valpuesta I., Gerhard O., 2011, ApJ, 734, L20

—, 2013, ApJ, 766, L3

—, 2015, Highlights of Astronomy, 16, 351

Martinez-Valpuesta I., Knapen J. H., Buta R., 2007, AJ, 134, 1863

Martinez-Valpuesta I., Shlosman I., Heller C., 2006, ApJ, 637, 214

Masters K. L. et al., 2011, MNRAS, 411, 2026

Matteucci F., 2003, Ap&SS, 284, 539

McDermid R. M. et al., 2015, ArXiv e-prints

Mebold U., Goss W. M., Siegman B., van Woerden H., Hawarden T. G., 1979, A&A, 74, 100

Méndez-Abreu J., Aguerri J. A. L., Zarattini S., Sánchez-Janssen R., Corsini E. M., 2010, in Astronomical Society of the Pacific Conference Series, Vol. 421, Galaxies in Isolation: Exploring Nature Versus Nurture, Verdes-Montenegro L., Del Olmo A., Sulentic J., eds., p. 269

Méndez-Abreu J., Corsini E. M., Debattista V. P., De Rijcke S., Aguerri J. A. L., Pizzella A., 2008, ApJ, 679, L73

Méndez-Abreu J., Debattista V. P., Corsini E. M., Aguerri J. A. L., 2014, A&A, 572, A25

Méndez-Abreu J., Sánchez-Janssen R., Aguerri J. A. L., 2010, ApJ, 711, L61

Menéndez-Delmestre K., Sheth K., S4G Team, 2015, IAU General Assembly, 22, 58286

Menéndez-Delmestre K., Sheth K., Schinnerer E., Jarrett T. H., Scoville N. Z., 2007, ApJ, 657, 790

Merrifield M. R., 2004, in Astronomical Society of the Pacific Conference Series, Vol. 317, Milky Way Surveys: The Structure and Evolution of our Galaxy, Clemens D., Shah R., Brainerd T., eds., p. 289

Merrifield M. R., Kuijken K., 1995, MNRAS, 274, 933

Micheau F., 1996, Roshdi Rashed & Rgis Morelon (1996), Encyclopedia of the History of Arabic Science, 985

Minchev I., Chiappini C., Martig M., 2013, A&A, 558, A9

Minchev I., Famaey B., 2010, ApJ, 722, 112

Minchev I., Famaey B., Quillen A. C., Di Matteo P., Combes F., Vlajić M., Erwin P., Bland-Hawthorn J., 2012, A&A, 548, A126

Miwa T., Noguchi M., 1998, ApJ, 499, 149

Mo H., van den Bosch F. C., White S., 2010, Galaxy Formation and Evolution. Cambridge University Press

Mollá M., Díaz A. I., 2005, MNRAS, 358, 521

Mollá M., Ferrini F., Díaz A. I., 1997, ApJ, 475, 519

Moore B., Katz N., Lake G., Dressler A., Oemler A., 1996, Nature, 379, 613

Moore B., Quinn T., Governato F., Stadel J., Lake G., 1999, MNRAS, 310, 1147

Moorthy B. K., Holtzman J. A., 2006, MNRAS, 371, 583

Morelli L. et al., 2008, MNRAS, 389, 341

Morgan W. W., 1971, AJ, 76, 1000

Morganti L., Gerhard O., Coccato L., Martinez-Valpuesta I., Arnaboldi M., 2013, MNRAS, 431, 3570

Muñoz-Mateos J. C., Gil de Paz A., Boissier S., Zamorano J., Jarrett T., Gallego J., Madore B. F., 2007, ApJ, 658, 1006

Muñoz-Mateos J. C. et al., 2009, ApJ, 703, 1569

Nair P. B., Abraham R. G., 2010, ApJ, 714, L260

Nakada Y., Onaka T., Yamamura I., Deguchi S., Hashimoto O., Izumiura H., Sekiguchi K., 1991, Nature, 353, 140

Navarro J. F., Frenk C. S., White S. D. M., 1995, MNRAS, 275, 56

—, 1996, ApJ, 462, 563

Navarro J. F. et al., 2010, MNRAS, 402, 21

Ness M. et al., 2013, MNRAS, 432, 2092

—, 2012, ApJ, 756, 22

Noguchi M., 1987, MNRAS, 228, 635

Norman C. A., Spaans M., 1997, ApJ, 480, 145

Obreja A., Domínguez-Tenreiro R., Brook C., Martínez-Serrano F. J., Doménech-Moral M., Serna A., Mollá M., Stinson G., 2013, ApJ, 763, 26

Ocvirk P., Peletier R., Lançon A., 2008, Astronomische Nachrichten, 329, 980

Ocvirk P., Pichon C., Lançon A., Thiébaut E., 2006a, MNRAS, 365, 74

—, 2006b, MNRAS, 365, 46

Oemler, Jr. A., Dressler A., Butcher H. R., 1997, ApJ, 474, 561

Oh S., Oh K., Yi S. K., 2012, ApJS, 198, 4

Okamoto T., 2013, MNRAS, 428, 718

Ortolani S., Renzini A., Gilmozzi R., Marconi G., Barbuy B., Bica E., Rich R. M., 1995, Nature, 377, 701

Osterbrock D. E., Ferland G. J., 2006, Astrophysics of gaseous nebulae and active galactic nuclei. CA: University Science Books

Ostriker J. P., Peebles P. J. E., 1973, ApJ, 186, 467

Pan H.-A., Lim J., Matsushita S., Wong T., Ryder S., 2013, ApJ, 768, 57

Pease F. G., 1918, Proceedings of the National Academy of Science, 4, 21

Peeples M. S., Martini P., 2006, ApJ, 652, 1097

Peletier R. F., Balcells M., 1996, AJ, 111, 2238

Peletier R. F. et al., 2007, MNRAS, 379, 445

—, 2012, MNRAS, 419, 2031

Pellet A., 1976, A&A, 50, 421

Pérez E. et al., 2013, ApJ, 764, L1

Pérez I., Aguerri J. A. L., Méndez-Abreu J., 2012, A&A, 540, A103

Pérez I., Sánchez-Blázquez P., 2011, A&A, 529, A64

Pérez I., Sánchez-Blázquez P., Zurita A., 2007, A&A, 465, L9

—, 2009, A&A, 495, 775

Peterson C. J., Huntley J. M., 1980, ApJ, 242, 913

Pfenniger D., 1984, A&A, 134, 373

Pfenniger D., Friedli D., 1991, A&A, 252, 75

Pfenniger D., Norman C., 1990, ApJ, 363, 391

Piñol-Ferrer N., Fathi K., Carignan C., Font J., Hernandez O., Karlsson R., van de Ven G., 2014, MNRAS, 438, 971

Pilkington K. et al., 2012, A&A, 540, A56

Planck Collaboration et al., 2014, A&A, 571, A16

Poggianti B. M., van Gorkom J. H., 2001, in Astronomical Society of the Pacific Conference Series, Vol. 240, Gas and Galaxy Evolution, Hibbard J. E., Rupen M., van Gorkom J. H., eds., p. 599

Polyachenko E. V., 2013, Astronomy Letters, 39, 72

Portail M., Wegg C., Gerhard O., Martinez-Valpuesta I., 2015, MNRAS, 448, 713

Press W. H., Schechter P., 1974, ApJ, 187, 425

Prieto M., Aguerri J. A. L., Varela A. M., Muñoz-Tuñón C., 2001, A&A, 367, 405

Prieto M., Gottesman S. T., Aguerri J.-A. L., Varela A.-M., 1997, AJ, 114, 1413

Proctor R. N., Sansom A. E., 2002, MNRAS, 333, 517

Regan M. W., Teuben P., 2003, ApJ, 582, 723

Roediger J. C., Courteau S., Sánchez-Blázquez P., McDonald M., 2012, ApJ, 758, 41

Rose J. A., Bower R. G., Caldwell N., Ellis R. S., Sharples R. M., Teague P., 1994, AJ, 108, 2054

Rubin V. C., Ford, Jr. W. K., Krishna Kumar C., 1973, ApJ, 181, 61

Ruiz-Lara T., Florido E., Pérez I., Sánchez-Blázquez P., Falcón-Barroso J., Cacho R., 2013, in Highlights of Spanish Astrophysics VII, Guirado J. C., Lara L. M., Quilis V., Gorgas J., eds., pp. 367–372

Rupke D. S. N., Kewley L. J., Barnes J. E., 2010, ApJ, 710, L156

Saha K., 2015, ApJ, 806, L29

Saha K., Naab T., 2013, MNRAS, 434, 1287

Sakamoto K., Okumura S. K., Ishizuki S., Scoville N. Z., 1999, ApJ, 525, 691

Salo H., Laurikainen E., Buta R., Knapen J. H., 2010, ApJ, 715, L56

Salo H., Rautiainen P., Buta R., Purcell G. B., Cobb M. L., Crocker D. A., Laurikainen E., 1999, AJ, 117, 792

Samland M., Hensler G., Theis C., 1997, ApJ, 476, 544

Sánchez S. F., García-Lorenzo B., Jahnke K., Mediavilla E., González-Serrano J. I., Christensen L., Wisotzki L., 2006, New Astronomy Reviews, 49, 501

Sánchez S. F. et al., 2012, A&A, 538, A8

Sánchez S. F., Rosales-Ortega F. F., Kennicutt R. C., Johnson B. D., Diaz A. I., Pasquali A., Hao C. N., 2011, MNRAS, 410, 313

Sánchez-Blázquez P., Gorgas J., Cardiel N., González J. J., 2006a, A&A, 457, 787

Sánchez-Blázquez P., Ocvirk P., Gibson B. K., Pérez I., Peletier R. F., 2011, MNRAS, 415, 709

Sánchez-Blázquez P. et al., 2006b, MNRAS, 371, 703

Sánchez-Blázquez P., Rosales-Ortega F., Diaz A., Sánchez S. F., 2014a, MNRAS, 437, 1534

Sánchez-Blázquez P. et al., 2014b, A&A, 570, A6

Sánchez-Janssen R., Gadotti D. A., 2013, MNRAS, 432, L56

Sandage A., Freeman K. C., Stokes N. R., 1970, ApJ, 160, 831

Sansom A. E., Proctor R. N., Reid N., 1998, in Astronomical Society of the Pacific Conference Series, Vol. 147, Abundance Profiles: Diagnostic Tools for Galaxy History, Friedli D., Edmunds M., Robert C., Drissen L., eds., p. 26

Sarzi M. et al., 2006, MNRAS, 366, 1151

Schaye J. et al., 2015, MNRAS, 446, 521

Schiavon R. P., Faber S. M., Rose J. A., Castilho B. V., 2002, ApJ, 580, 873

Schinnerer E., Eckart A., Quirrenbach A., Boker T., Tacconi-Garman L. E., Krabbe A., Sternberg A., 1997, ApJ, 488, 174

Schönrich R., Binney J., 2009, MNRAS, 396, 203

Schwarz M. P., 1981, ApJ, 247, 77

Schweizer F., 1982, ApJ, 252, 455

Seidel M. K. et al., 2015a, MNRAS, 446, 2837

—, 2015b, in IAU Symposium, Vol. 309, IAU Symposium, Ziegler B. L., Combes F., Dannerbauer H., Verdugo M., eds., pp. 163–164

Seidel M. K., Falcón-Barroso J., Martínez-Valpuesta I., Díaz-García S., Laurikainen E., Salo H., Knapen J. H., 2015c, MNRAS, 451, 5455

Seidengart J., 1996, in Journées 1996 - Systèmes de Référence Spatio-Temporels: Deux Siècles d'Évolution du Système du Monde, Capitaine N., ed., pp. 211–217

Sellwood J. A., 2010, ArXiv e-prints

—, 2014, Reviews of Modern Physics, 86, 1

Sellwood J. A., Binney J. J., 2002, MNRAS, 336, 785

Sellwood J. A., Debattista V. P., 2014, ArXiv e-prints

Sellwood J. A., Evans N. W., 2001, ApJ, 546, 176

Sellwood J. A., Wilkinson A., 1993, Reports on Progress in Physics, 56, 173

Serra P., Trager S. C., 2007, MNRAS, 374, 769

Serra P., Trager S. C., van der Hulst J. M., Oosterloo T. A., Morganti R., 2006, A&A, 453, 493

Sersic J. L., 1968, Atlas de galaxias australes. Observatorio Astronomico, Universidad Nacional de Cordoba

Shapley H., Curtis H. D., 1921, Bulletin of the National Research Council, Vol. 2, Part 3, No. 11, p. 171-217, 2, 171

Shen J., Sellwood J. A., 2004, ApJ, 604, 614

Sheth K. et al., 2008, ApJ, 675, 1141

—, 2010, PASP, 122, 1397

Sheth K., Regan M. W., Scoville N. Z., Strubbe L. E., 2003, ApJ, 592, L13

Sheth K., Vogel S. N., Regan M. W., Thornley M. D., Teuben P. J., 2005, ApJ, 632, 217

Shevchenko I. I., 2011, ApJ, 733, 39

Simmons B. D. et al., 2014, MNRAS, 445, 3466

Skrutskie M. F. et al., 2006, AJ, 131, 1163

Spaans M., Carollo C. M., 1997, ApJ, 482, L93

Sparke L. S., Sellwood J. A., 1987, MNRAS, 225, 653

Speltincx T., Laurikainen E., Salo H., 2008, MNRAS, 383, 317

Springel V., Frenk C. S., White S. D. M., 2006, Nature, 440, 1137

Strauss M. A. et al., 2002, AJ, 124, 1810

Strohmaier G., 1984, Die Sterne des Abd AR Rahman as-Sufi. Hanau/Main: Mueller Kiepenheuer, —c1984

Terlevich A. I., Kuntschner H., Bower R. G., Caldwell N., Sharples R. M., 1999, MNRAS, 310, 445

Terlevich R., Davies R. L., Faber S. M., Burstein D., 1981, MNRAS, 196, 381

Thomas D., Maraston C., Bender R., 2003, MNRAS, 343, 279

Thomas D., Maraston C., Bender R., Mendes de Oliveira C., 2005, ApJ, 621, 673

Tody D., 1993, in Astronomical Society of the Pacific Conference Series, Vol. 52, Astronomical Data Analysis Software and Systems II, Hanisch R. J., Brissenden R. J. V., Barnes J., eds., p. 173

Tolstoy E., Hill V., Tosi M., 2009, ARA&A, 47, 371

Toomre A., 1964, ApJ, 139, 1217

—, 1977, in Evolution of Galaxies and Stellar Populations, Tinsley B. M., Larson D. Campbell R. B. G., eds., p. 401

—, 1981, in Structure and Evolution of Normal Galaxies, Fall S. M., Lynden-Bell D., eds., pp. 111–136

Toomre A., Toomre J., 1972, ApJ, 178, 623

Trager S. C., Faber S. M., Worthey G., González J. J., 2000, AJ, 120, 165

Tremaine S., Weinberg M. D., 1984, ApJ, 282, L5

Trimble V., 1995, PASP, 107, 1133

Valdes F., Gupta R., Rose J. A., Singh H. P., Bell D. J., 2004, ApJS, 152, 251

van Albada T. S., 1982, MNRAS, 201, 939

van de Ven G., Chang P., 2009, ApJ, 697, 619

van den Bergh S., 1960a, ApJ, 131, 558

—, 1960b, ApJ, 131, 215

—, 1976, ApJ, 206, 883

van der Kruit P. C., Freeman K. C., 2011, ARA&A, 49, 301

van der Laan T. P. R., Schinnerer E., Emsellem E., Hunt L. K., McDermid R. M., Liu G., 2013a, A&A, 551, A81

van der Laan T. P. R. et al., 2013b, A&A, 556, A98

van der Marel R. P., Franx M., 1993, ApJ, 407, 525

van Dokkum P. G., Franx M., Fabricant D., Kelson D. D., Illingworth G. D., 1999, ApJ, 520, L95

van Dokkum P. G. et al., 2008, ApJ, 677, L5

Vanderriest C., 1980, PASP, 92, 858

Vazdekis A., 1999, ApJ, 513, 224

Vazdekis A., Salaris M., Arimoto N., Rose J. A., 2001, ApJ, 549, 274

Vazdekis A., Sánchez-Blázquez P., Falcón-Barroso J., Cenarro A. J., Beasley M. A., Cardiel N., Gorgas J., Peletier R. F., 2010, MNRAS, 404, 1639

Vila-Costas M. B., Edmunds M. G., 1992, MNRAS, 259, 121

Vogelsberger M. et al., 2014, MNRAS, 444, 1518

Vollmer B., Huchtmeier W., van Driel W., 2005, A&A, 439, 921

Weinzirl T., Jogee S., Khochfar S., Burkert A., Kormendy J., 2009, ApJ, 696, 411

White S. D. M., Negroponte J., 1982, MNRAS, 201, 401

White S. D. M., Rees M. J., 1978, MNRAS, 183, 341

Whyte L. F., Abraham R. G., Merrifield M. R., Eskridge P. B., Frogel J. A., Pogge R. W., 2002, MNRAS, 336, 1281

Williams M. J., Bureau M., Kuntschner H., 2012, MNRAS, 427, L99

Worthey G., Faber S. M., Gonzalez J. J., Burstein D., 1994, ApJS, 94, 687

Wozniak H., 2007, A&A, 465, L1

Wozniak H., Combes F., Emsellem E., Friedli D., 2003, A&A, 409, 469

Wozniak H., Friedli D., Martinet L., Martin P., Bratschi P., 1995, A&AS, 111, 115

Wozniak H., Pierce M. J., 1991, A&AS, 88, 325

Wyse R. F. G., Gilmore G., Franx M., 1997, ARA&A, 35, 637

Yoachim P., Dalcanton J. J., 2008, ApJ, 683, 707

Yoachim P., Roškar R., Debattista V. P., 2012, ApJ, 752, 97

Young L., Bureau M., Crocker A., Combes F., 2008, in IAU Symposium, Vol. 245, IAU Symposium, Bureau M., Athanassoula E., Barbuy B., eds., pp. 173–176

Zahid H. J., Bresolin F., 2011, AJ, 141, 192

Zaritsky D., 1992, ApJ, 390, L73

Zimmer P., Rand R. J., McGraw J. T., 2004, ApJ, 607, 285

Zoccali M. et al., 2006, A&A, 457, L1

Zwicky F., 1957, Morphological astronomy. Berlin: Springer, 1957